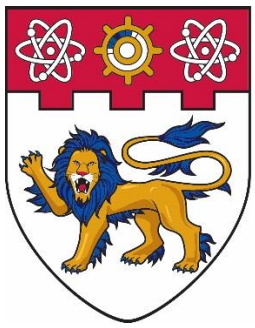

NANYANG TECHNOLOGICAL UNIVERSITY
SINGAPORE

ENZYMATIC AND STRUCTURAL INSIGHTS INTO THE MYCOBACTERIAL ALKYLHYDROPEROXIDE REDUCTASE SUBUNIT C AND REPURPOSING OF AN ANTIMALARIA COMPOUND INHIBITING THE MYCOBACTERIAL CYTOCHROME *BCC* OXIDASE FOR TUBERCULOSIS DISEASE

CHONG SHI MIN SHERILYN

Interdisciplinary Graduate School
NTU Institute for Health Technologies
(HealthTech NTU)

2020

ENZYMATIC AND STRUCTURAL INSIGHTS INTO THE MYCOBACTERIAL ALKYLHYDROPEROXIDE REDUCTASE SUBUNIT C AND REPURPOSING OF AN ANTIMALARIA COMPOUND INHIBITING THE MYCOBACTERIAL CYTOCHROME *BCC* OXIDASE FOR TUBERCULOSIS DISEASE

CHONG SHI MIN SHERILYN

Interdisciplinary Graduate School
NTU Institute for Health Technologies
(HealthTech NTU)

A thesis submitted to the Nanyang Technological University in partial fulfilment of the requirement for the degree of
Doctor of Philosophy

2020

Statement of Originality

I hereby certify that the work embodied in this thesis is the result of original research, is free of plagiarised materials, and has not been submitted for a higher degree to any other University or Institution.

11th Sept 2020
Date

Chong Shi Min Sherilyn

Supervisor Declaration Statement

I have reviewed the content and presentation style of this thesis and declare it is free of plagiarism and of sufficient grammatical clarity to be examined. To the best of my knowledge, the research and writing are those of the candidate except as acknowledged in the Author Attribution Statement. I confirm that the investigations were conducted in accord with the ethics policies and integrity standards of Nanyang Technological University and that the research data are presented honestly and without prejudice.

13th Sep. 2020
. . . . . .
Date

. . . . . .
Prof. Dr. Gerhard Grüber

Authorship Attribution Statement

This thesis contains material from 2 papers published in the following peer-reviewed journal(s) where I was the first and/or corresponding author.

Chapter 3 is published as **Chong, S. S. M.;** Kamariah, N.; Grüber, G., Critical residues of helix α2 for catalytic efficiency of Mycobacterial Alkylhydroperoxide reductase subunit C. Febs Letters. 2020.

The contributions of the co-authors are as follows:

- Chong, S.M.S., Kamariah, N., and Grüber, G. conceived and designed the experiments.
- Chong, S.M.S., and Kamariah, N. performed the experiments and analyzed the data.
- Chong, S.M.S., Kamariah, N., and Grüber, G. wrote the paper.

Chapter 5 is published as **Chong, S. S. M.;** Malathy S. S. M.; Sarathy, J. P.; Williams, Z. C.; Harold, L. K.; Cook, G. M.; Dick, T.; Pethe, K.; Bates, R. W.; Grüber, G., Anti-tuberculosis activity of the anti-malaria cytochrome *bcc* oxidase inhibitor SCR0911. ACS infectious diseases, 2020.

The contributions of the co-authors are as follows:

- Chong, S.M.S., Malathy, S.S.M., Cook, G.M., Dick, T., Pethe, K., and Grüber, G. conceived and designed the experiments.
- Chong, S.M.S., Malathy, S.S.M., Sarathy, J.P., Willams, Z.C., and Harold, L.K. performed the experiments and analyzed the data.
- Chong, S.M.S., Malathy, S.S.M., and Grüber, G. wrote the paper with contribution from other authors.

11th Sept 2020
. . . . . .
Date

. . . . . .
Chong Shi Min Sherilyn

Acknowledgements

My heart is filled with gratitude to everyone who have accompanied me through my PhD journey. The completion of this research would not have been possible without the contribution of many individuals.

First and foremost, I would like to extend my sincerest gratitude to my main supervisor, Prof. Gerhard Grüber. His valuable advice, encouragement, and insightful comments have provided a rewarding learning experience. I appreciate the life lessons, many of which will be carried with me throughout my whole life.

I am extremely grateful to Prof. Roderick Wayland Bates. Prof. Bates first sparked my interest in research during my first year of my undergraduate studies. His patience, immense knowledge, and unwavering support have played a big role to where I am today.

I would like to thank my mentor, Prof. Thomas Dick, and Prof. Kevin Pethe, for their valuable suggestions and advice. Special thanks to their students, Mr. Jickky Palmae Sarathy, Ms. Lee Bei Shi, and Ms. Ekaterina Sviriaeva, for the enjoyable moments where we exchanged ideas and experiences.

I am very thankful to Ms. Saw Wuan Geok, who guided me since I first joined the biology lab. Her constant encouragement, eagerness, and advice have broadened my perspective. I would also like to thank Dr. Malathy Sony Subramanian Manimekalai for sharing her expertise in X-ray crystallography and computational docking, Dr. Neelagandan Kamariah, for his advice in enzymatic kinetics assays, and Dr. Shin Joon for his guidance in protein NMR. I would like to additionally thank Dr. Priya Ragunathan, Dr. Ardina Grüber, and Dr. Amaravadhi Venkata Krishna Harikishore for their valuable advice during this journey.

It has been incredible to work alongside many wonderful colleagues in the School of Biological Sciences. To Dr. Ankita Pan, Dr. Bharti Singal, Ms. Wong Chui Fann, Mr. Lau Aik Meng, and Dr. Nebojsa Bogdanovič, I appreciate all the discussions we had and thank you all for brightening up my days in the lab.

To the peers in the School of Physical and Mathematical Sciences, Dr. See Yang Feng Anders, Ms. Annabel Ho Xuan Ying, and Ms. Ko Weiting. Thank you for easing my transition back to chemistry. I am grateful for all the help you guys offered in times of need and I truly enjoyed the time we spent together. To Mr. Lin Hong Xuan, Mr. Pham Thang Loi, Ms. Patcharaporn Sae-Lao, Mr. Seankongsuk Pattarakiat, and Ms. Toh Hui Min Hannah, thank you for making the lab such a fun environment to work in.

Additionally, I would like to thank the staff of beamline 13B1 at NSRRC for their technical assistance. In addition, I would like to acknowledge all the academic and technical staffs and facilities at the Interdisciplinary Graduate School, School of Biological Sciences, and School of Physical and Mathematical Sciences. Special thanks to Ms. Suriani Binte Rabu for her assistance throughout the past four years. The research in the past four years has been supported by the Academic Research Fund (AcRF) Tier 1 ID889 Ministry of Education (MOE) Singapore, the National Research Foundation (NRF) Singapore, and NRF Competitive Research Programme (CRP), Grant Award Number NRF-CRP18-2017-01).

Words fall short to express my gratitude to two of my closest friends, Bernice and Connie, for being such incredible and supportive friends.

Lastly, I would like to express my deepest gratitude to my father, mother, brother, and husband, for their unconditional love and being my pillar of support. Thank you for seeing greater things in me, than I did in myself.

Table of Contents

List of Figures

Introduction

Materials and Methods

Results

Discussion

Results

Conclusion

List of Tables

Materials and methods

Results

Results

Abbreviations

Å	Angstrom
ACMA	9-Amino-6-Chloro-2-Methoxyacridine
ADC	Albumin–dextrose–catalase
ADP	Adenosine diphosphate
AhpC	Alkyl Hydroperoxide Reductase subunit C
AhpD	Alkyl Hydroperoxide Reductase subunit D
AhpF	Alkyl Hydroperoxide Reductase subunit F
ATP	Adenosine triphosphate
Ax	*Ampjibacillus xylanus*
BCA	Bicinchoninic acid assay
BCG	Bacillus Calmette–Guérin
BDQ	Bedaquiline
Cys-SOH	Sulfenic acid
Cys-S_pH	Peroxidatic cysteine
Cys-S_RH	Resolving cysteine
cyt-*aa_3*	Cytochrome *aa_3*
cyt-*bcc*	Cytochrome *bcc*
cyt-*bd*	Cytochrome *bd*
DBU	1,8-Diazabicyclo(5.4.0)undec-7-ene
DCM	Dichloromethane
D_H	Hydrodynamic diameter
DLS	Dynamic Light Scattering

DMAP	4- (Dimethylamino)pyridine
DMSO	Dimethyl sulfoxide
DNA	Deoxyribonucleic acid
DTH	delayed-type hypersentivity
DTT	Dithiothreitol
E. coli	*Escherichia coli*
EDCI	*N*-(3-Dimethylaminopropyl)-*N*'-ethylcarbodiimide hydrochloride
EDTA	Ethylenediaminetetraacetic acid
EGCG	Epigallocatechin gallate
EM	Electron microscopy
ETC	Electron transport chain
FDA	Food and Drug Administration
FF	Fully folded
FOX	Ferrous Oxidation-Xylenol Orange
GMQE	Global model quality estimate
HIV	Human Immunodeficiency Virus
HRMS	High resolution mass spectrometry
HTS	High-throughput screen
IFN-γ	Interferon gamma
IMV	Inverted membrane vesicle
INH	Isoniazid
InhA	Enoyl ACP reductase
IPTG	Isopropyl-β-D-thiogalactoside

IR	Infrared spectroscopy
KatG	Catalase-peroxidase
K_{cat}	catalytic turnover number
K_m	Michaelis-Menten constant
LB	Luria-Bertani
LTBI	Latent tuberculosis infection
LU	Locally unfolded
M. bovis	*Mycobacterium bovis*
M. leprae	*Mycobacterium leprae*
M. smegmatis	*Mycobacterium smegmatis*
MDR-TB	Multi-drug resistant tuberculosis
MIC	Minimal inhibitory concentration
MK	Menaquinone
MKH_2	Menaquinol
MS	Mass spectrometry
Mtb	*Mycobacterium tuberculosis*
NADH	Nicotinamide adenine dinucleotide
NADPH	Nicotinamide adenine dinucleotide phosphate
NDH	NADH dehydrogenase
Ni-NTA	Nickel-nitrilotriacetic acid
NIS	*n*-Iodosuccinimide
NMR	Nuclear magnetic resonance
Nox2	NADPH oxidase

NSRRC	National Synchrotron Radiation Research Center
P. falciparum	*Plasmodium falciparum*
PCC	Pyridinium chlorochromate
PCR	Polymerase chain reaction
PDB	Protein Data Bank
PMF	Proton motive force
PMV	Inside-out plasma membrane vesicles
PRSAF1	Prokaryotic respiratory supercomplex association factor 1
Prxs	Peroxiredoxins
PZA	Pyrazinamide
QSQE	Quaternary structure quality estimate
RLU	Relative Light Units
RNA	Ribonucleic acid
ROS	Reactive oxygen species
S. typhimurium	*Salmonella typhimurium*
SAR	Structure-activity relationship
SDH	Succinate dehydrogenase
SEC	Size exclusion chromatography
Sod	Superoxide dismutase
TB	Tuberculosis
THF	Tetrahydrofuran
THZ	Thioridazine
TLC	Thin layer chromatography

TNF	Tumour necrosis factor alpha
Trx	Thioredoxin
TrxR	Thioredoxin reductase
WHO	World Health Organization
WT	Wild type
XDR-TB	Extensively drug-resistant TB

Abstract

Tuberculosis (TB) is one of the leading contagious diseases that results in mortality. Treatment with antibiotics has been applied for TB however, with new forms of antibiotic resistance emerging, difficulty in treatment of TB was detected. In this study, alkylhydroperoxide reductase subunit C (*Mt*AhpC), involved in the antioxidant defense system of mycobacterial species against reaction oxygen species (ROS), and cytochrome *bcc*, complex III of the electron transport chain (ETC), where most endogenous ROS is generated, were investigated.

*Mt*AhpC possesses several distinctive features, allowing it to serve as a good drug target. The importance of *Mt*AhpC has been highlighted in isoniazid-resistant strains, the primary antibiotic for TB treatment, where an increased expression in *Mt*AhpC was revealed. One unique feature of *Mt*AhpC was discovered from its crystal structure, where a cavity within *Mt*AhpC was observed, not present in its bacterial counterparts. This was postulated to be a result of a helical displacement. Here, the importance of the helical movement was demonstrated by performing mutagenesis studies, along with enzymatic assays. Additional biophysical assays provided evidence into the oligomeric state of the mutants. To gain structural insights into the catalytic efficiency of the protein, the crystallographic structure of the *Mt*AhpC mutant was determined at 3.3 Å. The reported crystal data provided insights into the effect of the mutation on the helix, which consequently impacts the oligomeric interface.

Cytochrome *bcc* plays a major role in the production of the proton motive force (PMF) for ATP synthesis, as well as ROS. With the concept of drug repurposing, SCR0911, an antimalaria compound, was envisioned for use in mycobacterial species as it was postulated to bind to cytochrome *bcc*, and more specifically, the Q_i site. Previous studies have revealed that inhibitors at the Q_i site expedite the formation of endogenous superoxides. The synthesis of SCR0911 was carried out and subjected to antimicrobial susceptibility testing and on-target activity assays. Towards improving the activity of SCR0911, docking studies along with synthesis of analogs were performed.

These results provide valuable insights into the helical displacement of *Mt*AhpC, thus allowing the establishment of a foothold in drug design, for the application of molecular docking to identify a ligand that can target *Mt*AhpC specifically. Additionally, SCR0911 was identified to possess anti-TB properties. This enables future works into an improved binding of SCR0911

analog at the Q_i site of cytochrome *bcc*, which could stimulate *Mtb* to produce an excess of endogenous superoxides.

Introduction

Outlook of Tuberculosis Disease

1. Introduction

1.1 Tuberculosis Disease

Tuberculosis (TB) is the leading contagious disease that results in mortality and is one of the top ten causes of death worldwide, caused by a single infectious agent, *Mycobacterium tuberculosis* (*Mtb*) [1]. Each year, approximately 10.4 million people are diagnosed with active TB, with 1.7 million cases of death [1, 2]. Countries from Asia, such as India, Indonesia, China, the Philippines, and Pakistan, constitute about 56% of the total TB cases globally [1]. Treatment of TB is of critical importance, as without treatment for active TB, as much as half the population with active TB succumbed to the disease [3]. Following the discovery of streptomycin in the 1940s that was first effective against TB, isoniazid (INH) and pyrazinamide (PZA) were later introduced, which led to the belief that TB could be eradicated [4]. However, despite the emergence of these remedies, TB remains a pressing concern in this day.

1.1.1 TB – a global health challenge

One reason for the difficulty in eradicating TB is due to the large number of people with latent TB. Recently, it has been estimated that a quarter of the world's population are latently infected with TB, suggesting that a very large number of people are susceptible to the progression of active TB [5]. Approximately 5 to 10% of the latent TB cases develop to active TB, and this risk factor is increased if the patient is immunocompromised [6, 7]. Furthermore, challenges have been found in diagnosing and predicting the development of latent to active TB, which could hinder the overall control of the disease [8, 9].

Another cause is due to the escalating prevalence of Human Immunodeficiency Virus 1 (HIV-1), giving rise to a vulnerable population, as TB is the highest cause of death in HIV patients and approximately one in three HIV death is correlated to TB [10, 11]. A correlation between HIV and TB has been established, and it was discovered that HIV patients are more susceptible to contracting TB, and at the same time, leads to a faster progression towards active TB [12-14]. Due to this correlation, the large number of populations with latent TB, along with the upward trend of HIV-1, increases the prevalence of active TB. Diagnosing TB in HIV patients has proven to be more challenging as both the sputum smear microscopy and chest x-rays, commonly used for detecting active TB, have a higher inclination to provide false negative results [15, 16]. Additionally, higher drug intolerance to the standard TB treatment is present in

HIV-patients, and alongside the drug interactions and additive toxicity profiles between the TB and HIV treatments, it becomes more complicated for the treatment of TB in HIV patients [17, 18].

Lastly, the emergence of drug-resistant TB has further threatened the current TB situation [19]. Drug-resistant TB mainly results from the inconsistent use and inappropriate administration due to the long-term therapy of antibiotics, or the lack of medical supervision [10, 20, 21]. The treatment of latent TB requires up to nine months of self-administered INH, while the standard regimen for active TB uses a combination of INH, rifampicin, ethambutol, and PZA for six to nine months [22-24]. These long-term treatments tend to result in poor patient compliance. Strains of *Mtb* that are resistant to rifampicin and INH have resulted in Multidrug-resistant TB (MDR-TB). On the other hand, extensively drug-resistant TB (XDR-TB) have emerged from *Mtb* that is not only MDR, but is also resistant to any fluoroquinolone classes and at least one of the three injectable drugs; kanamycin, capreomycin, and amikacin [25]. Approximately 490,000 people were infected with MDR-TB in 2016 worldwide, and it was predicted that the mortality rate of individuals with MDR-TB is 40% [1, 26].

1.1.2 TB – End TB Strategy

Following the current TB epidemic, an "End TB Strategy" was put in place by the World Health Organization (WHO) in 2015 [27]. The "End TB Strategy" aims to decrease TB incidence by 90%, with a 95% decrease in death caused by TB by 2035, as compared to that in 2015. Targets were outlined for every five years, and in the year 2020, they envisioned a 75% decrease in TB death, as compared to that in 2015, with a 50% less occurrence of TB infections. To accomplish this goal, three different pillars for the End TB Strategy are in place. The three approaches are "integrated, patient-centered care and prevention", "bold policies and supportive systems", and "intensified research and innovation", which aims to improve on patient support and accessibility of treatment, reinforce health and social sector policies, and to encourage research and innovations that can aid in the prevention, diagnosis, or treatment of TB disease [27, 28].

1.1.3 Current treatment for TB

As mentioned previously, the current treatment for TB uses a combination of INH, rifampicin, ethambutol, and PZA for up to nine months [22-24]. INH has the ability to eliminate 95% of the

bacteria within the first two days of initial treatment, portraying its importance and effectiveness in the TB regimen [29]. The introduction of rifampicin reduces the treatment duration that lasts from 1 to 2 years to less than 12 months, while the addition of PZA has revealed to decrease the relapse rate from 22% to 8%, further shortening the chemotherapy duration [29]. Ethambutol, although not shown to be able to decrease the duration of the therapy, has demonstrated its ability in preventing the emergence of drug resistance [30].

To realize the End TB Strategy by 2035, a breakthrough must be made by 2025. However, since the third pillar of the End TB Strategy has been put in place, not much progress has been attained [1]. Currently, 17 drugs are in trials for TB treatment, with two drugs, bedaquiline (BDQ) and delamanid that have received conditional or accelerated approval [1]. Both BDQ and delamanid are effective against both drug-susceptible TB and MDR-TB with an acceptable safety profile [31, 32]. Nevertheless, despite the recent introduction of these drugs, resistance strains against BDQ and delamanid have emerged [33, 34].

Hence, further research for the search of an ideal drug must continue. The characteristics of an ideal drug include: (I) a decrease in treatment duration, (II) a decrease in dosing frequency, (III) an ability to treat MDR/XDR TB, (IV) oral availability for easy administration, (V) a good safety profile, (VI) effectiveness for latent TB treatment, and (VII) minimum drug interaction with HIV treatments [24].

1.1.4 Pathogenesis of TB Disease

TB can affect any organ system, however, it most commonly affects the lungs, known as pulmonary TB [35]. TB that affects the other organs systems is known as extrapulmonary TB. They are non-contagious as the spread of TB is usually due to the spread of aerosol droplets containing *Mtb* that usually occurs during coughing or sneezing [36]. Hence, in patients with exclusively extrapulmonary TB, the bacteria were not found in the lungs that allow the spread of disease through these aerosol droplets. The ideal situation when an individual comes into contact with *Mtb*, would be for the individual to be resistant to the bacteria or is able to eliminate the bacteria in the early stages [37]. If the bacteria managed to infect the individual, the person could acquire latent TB that persists in the body, and this could develop into active TB.

TB infection happens in three stages [38]. First, transmission of TB occurs when aerosol droplets containing the infectious disease is inhaled by a non-infected person [7]. This allows the entry of the bacteria into the alveoli and gets ingested by the macrophages [39]. Here, the

macrophages could be successful in eradicating the bacteria, or *Mtb* managed to infect and multiply within these macrophages, creating a temporary residence for themselves [40].

In the second stage, growth of *Mtb* continues within these macrophages until these macrophages burst [41]. As the bacteria are released, other macrophages, such as those from peripheral blood, enter and ingest the bacteria. However, these macrophages are not activated, and instead they form a symbiotic relationship with the bacteria, allowing the bacteria to multiply within [40-42]. At this stage, the host begins activation of the delayed-type hypersensitivity (DTH) immune response, and begins recruitment of $CD4^+$ and $CD8^+$ T-cells [43, 44]. These $CD4^+$ and $CD8^+$ T-cells produce interferon gamma (IFN-γ), tumour necrosis factor alpha (TNFα), and macrophage colony-stimulating factor, which activates macrophages to produce ROS to eradicate the bacteria [17, 18]. It additionally brings in and activates more macrophages to the site of infection and initiates cytotoxic cells to inhibit *Mtb*'s growth [45, 46]. Eventually, this leads to the formation of a granuloma, which mainly consists of macrophages, mononuclear phagocytes, foam cells and lymphocytes [47]. Maturation of the granuloma occurs with the development of a fibrous capsule, with lymphocytes relocating to the peripheral of the granuloma, resulting in granuloma necrosis [48, 49]. Within the granuloma, the *Mtb* bacteria exist in a hypoxic environment, and they remain in the dormant state, effectively containing the bacteria [38]. If this situation persists, the person is said to have latent TB infection (LTBI) [50].

Rupturing of the granuloma marks the final stage of the TB infection, where the necrosis of the granuloma progressively increases, till liquefaction of the center occurs, releasing bacteria into the airway [51, 52]. The risk of granuloma rupturing increases in immunocompromised individuals [53]. The disintegration of the granuloma signifies the start of active TB [3, 45]. With the release of the bacteria, *Mtb* can spread within the lungs, causing the development of more lesions and even to other tissues in the central nervous system, the skin, internal organs, and genitourinary tract [39, 54].

Patients diagnosed with LTBI, although carrying *Mtb*, are able to contain the disease, and at the same time, present no symptoms and do not transmit the disease [3]. INH preventive therapy can be given to individuals who have LTBI, after assessing that the risk for reactivation is higher than the risk of the therapy [55]. Approximately 5 to 10% of people with LTBI will progress to active TB, with risk factors such as age, administration of corticosteroids, malnutrition, co-infection with HIV, or any other factors that cause immunosuppression [46]. This progression

from LTBI to active TB can occur at any moment, although if treatments are successful in containing the TB infection, the progression from LTBI to active TB is seldom observed [56].

Active TB, on the other hand, depends greatly if the patients have pulmonary TB or extrapulmonary TB. Approximately 60 to 80% of patients with active TB develop pulmonary TB [57]. Patients with pulmonary TB are able to infect others, with symptoms such as persistent coughing, which may include blood in their sputum, chest pain, and fever [58].

1.1.5 Exogeneous and endogeneous ROS

ROS released by the macrophages during an infection is generated from a phagocyte NADPH oxidase (Nox2) [59, 60]. Nox2 reduces molecular oxygen to superoxide anions ($O_2^{\bullet-}$), which successively forms other ROS, such as hydrogen peroxide (H_2O_2) and hydroxyl radicals ($OH^{\bullet}$) [61]. The importance of ROS as a host defense mechanism was outlined by individuals with defects in their Nox2 being highly susceptible to various bacterial and fungal infections [62]. On a more relatable note, individuals with mutations in the $gp91^{phox}$ subunit of the Nox2 are more vulnerable to mycobacterial diseases [63].

ROS generation is detrimental to cells by causing protein damage, DNA damage, or lipid damage [64]. Protein damage such as carbonylation of proline, arginine, lysine, and threonine [65] and oxidation of histidine [66] could result in the loss of structure or inactivation of the protein [67]. DNA oxidation leads to modification of DNA and RNA, along with oxidation to the nucleotide pool [68]. Guanine is the most susceptible DNA base to oxidation due to its low redox potential, and its oxidation results in mismatched base-pairing and double strand breaks, which are lethal to the cell [69]. ROS also causes lipid peroxidation due to the oxidation on the unsaturated fatty acids on the cell membranes, leading to destabilization of the organism [64].

Other than an exogenous source of ROS, *Mtb* produces an endogenous source of ROS. A major endogenous ROS source is generated at the ETC [70]. During the electron transfer process within the ETC, FAD^+ first receives a hydride anion, and it transfers the electron obtained to redox moieties within the complex, such as the iron-sulfur cluster. During this process, if oxygen comes into contact with $FADH_2$ before it passes on its electrons, molecular oxygen gets reduced to $O_2^{\bullet-}$ (Fig. 1.1) [70, 71]. This process generates ROS within the cytoplasm.

$O_2^{\bullet-}$ in the periplasm is produced mainly by the cytochrome *bcc*, complex III of the ETC [70]. Within the cytochrome *bcc* complex, an electron carrier, menaquinol, carries and transfers two electrons within the complex towards complex IV. In the intermediate state where one electron is

transferred, menaquinol gets oxidized to menasemiquinone, a highly reactive species that is able to reduce molecular oxygen [70]. The presence of superoxide dismutase (Sod) in the periplasm and its close proximity to the cytochrome *bcc* complex further substantiates the production of superoxides by the cytochrome *bcc* complex [72, 73]. Sod serves to reduce $O_2^{\bullet -}$ to H_2O_2 and molecular oxygen [7].

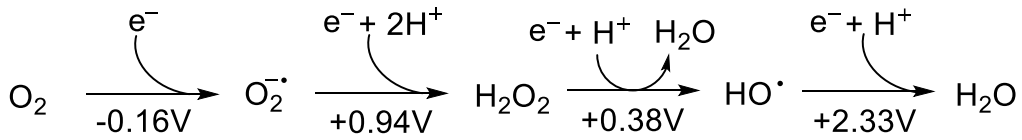

Figure 1.1: From molecular oxygen to ROS. The reduction potential for each step is shown.

Hence, for *Mtb* to protect itself from both endogenous and exogenous ROS, it possesses a comprehensive antioxidant defense system comprising of catalyase and peroxiredoxins to reduce peroxides, along with Sod [7]. Here, we look at AhpC, a peroxiredoxin that carries out antioxidant defense activity, and the cytochrome *bcc* complex that is a major source of endogenous ROS.

Enzymatic and Structural Insights into the *Mtb* Alkylhydroperoxide Reductase Subunit C

1.2 Enzymatic and Structural Insights into the *Mt*AhpC

1.2.1 INH-Resistant TB

Since 1952, INH has been used as one of the frontline antibiotics for the treatment of TB due to its effectiveness [25, 74]. However, in recent years, INH-resistant strains have been increasingly prevalent, and it is found in approximately 8% of the TB strains worldwide, while in Eastern Europe, it comprises approximately 45% of the total TB cases [1, 75]. INH functions as a prodrug that first enters the bacteria by passive diffusion, followed by activation from *Mtb*'s catalase-peroxidase *(*KatG) [76].

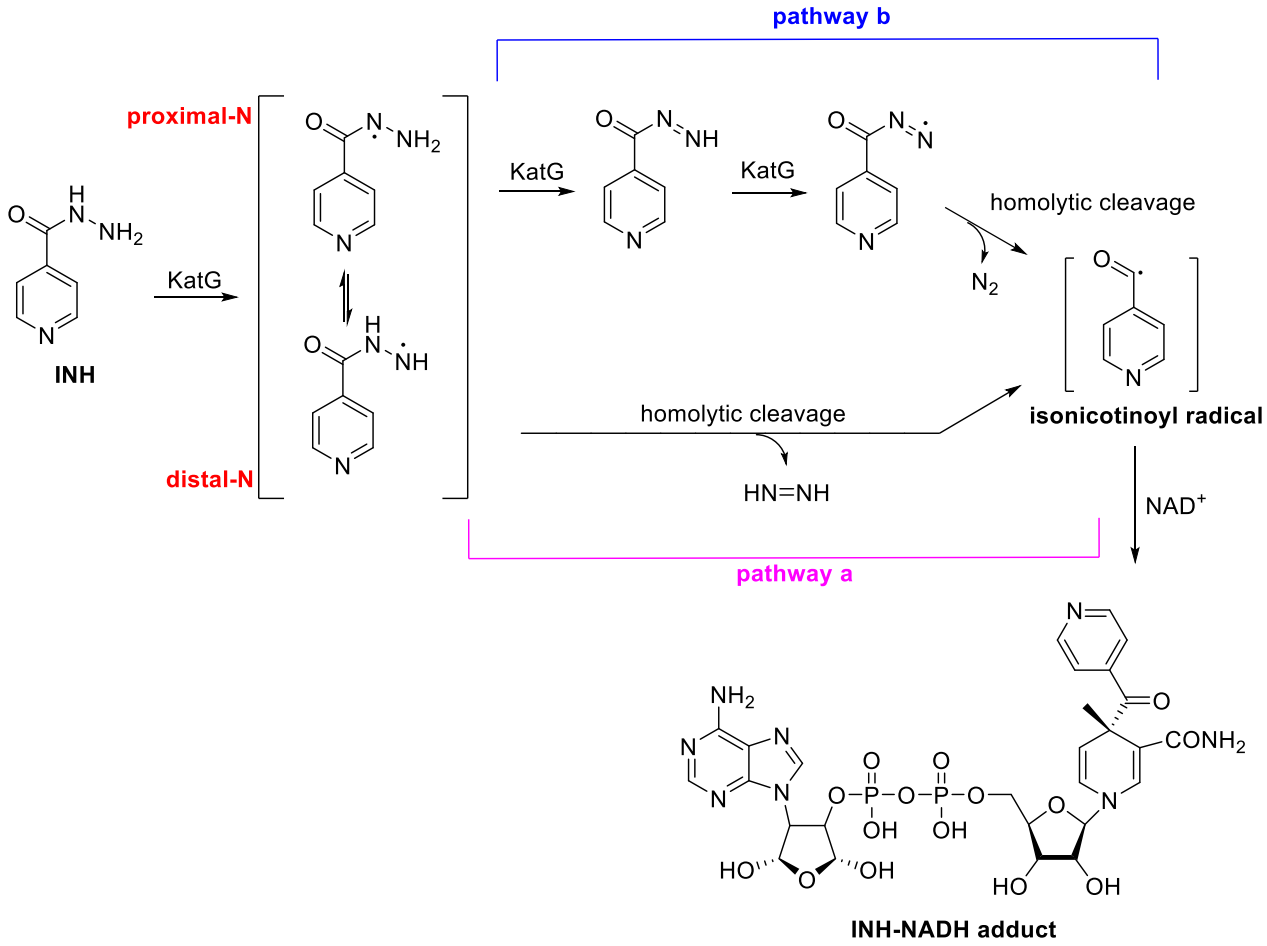

Figure 1.2: Different pathways postulated for the activation of INH by KatG. Two different pathways are described for the formation of the isonicotinoyl radical [74].

The importance of KatG for the activation of INH has been demonstrated by Zhang *et al.* (1993), where the introduction of the KatG gene into INH-resistant strains of *Mtb* reinstates its full susceptibility towards INH [77]. INH is activated via oxidation by KatG, for the formation of an isonicotinoyl acyl radical. This is done either with oxidants such as superoxides and hydrogen

peroxides or without additional oxidants [78-80]. Figure 1.2 depicts the two different mechanistic pathways postulated previously, where the oxidation of INH occurs either on the distal nitrogen, as shown in pathway *a*, or on the proximal nitrogen, as shown in pathway *b* [74]. Nevertheless, recent studies have found that the oxidation occurs on the proximal nitrogen for the formation of a hydrazyl radical, as shown by pathway b in figure 1.2 [81, 82].

The isonicotinoyl acyl radical can form a covalent bond with INH *in-vivo*, generating an INH-NADH adduct. This INH-NADH adduct then binds to and inhibits enoyl ACP reductase (InhA), which in turn, prevents the synthesis of long fatty acid chains. These long fatty acid chains are critical for the formation of the mycolic acids in the cell walls [24, 83, 84]. Eventually, INH prevents the synthesis of cell wall mycolic acid, thereby compromising the integrity of the cell wall [85, 86]. Furthermore, following the activation of INH, the breakdown of INH occurs, producing nitric oxide, providing additional nitrosative stress to *Mtb* [82].

1.2.1.1 Acquiring INH Resistance

Acquisition of INH resistance most commonly occurs with a mutation or inactivation of the KatG gene, preventing the activation of the INH into the isonicotinoyl acyl radical [87]. Other INH-resistant strains have revealed mutations on InhA gene, preventing the binding of the INH-NADH adduct, hence averting the formation of a defective cell wall [88, 89]. Further studies have otherwise found mutations in the KasA, ndh, and AhpC in these resistant strains as well [90]. The most common KatG mutation observed was the single mutation of S315T [91]. With this mutation, *in-vivo* experiments observed a larger than 50-fold increase in the minimal inhibitory concentration (MIC) for INH. Along with the resistance to INH, the $KatG_{S315T}$ loss approximately half of its enzymatic activity [92]. Findings have indicated different KatG mutations for INH resistance, where a small number of INH-resistant strains were even found to have a complete deletion of the katG gene [93].

1.2.1.2 Function of KatG for Mtb

KatG is the only catalase in *Mtb* that can carry out catalase and peroxidase activities [94-96]. As mentioned in section 1.1.4, IFN-γ triggers the production of ROS, which serves as a large obstacle for *Mtb* to survive within the host, hence indicating the importance of catalyzing these reactive species [97, 98]. The importance of the KatG has been demonstrated by the decrease in virulence of INH-resistant strains as compared to the drug susceptible strains [99, 100].

However, one study performed with a mouse model indicated that despite the decrease in enzymatic activity found in $KatG_{S315T}$, *Mtb* with $KatG_{S315T}$ depicts similar virulence to the wild type (WT) *Mtb* [101]. This indicates that even with the loss of activity in KatG, transmission of *Mtb* still occurs, signifying *Mtb* is still functional.

Hence, the question arises on how *Mtb* remains virulent despite the loss of KatG activity? It was discovered by Sherman *et al*. that a compensatory mechanism, the hyperexpression of AhpC that compensates for the loss of KatG activity, comes into play [102]. In addition to the mutation on KatG, further mutations at the promoter region of AhpC have been detected, generating up to 20-times the promoter activity as compared to the WT *Mtb* [102, 103].

AhpC plays a significant role in *Mtb*, which was demonstrated through the overexpression of AhpCs in static cultures, indicating that AhpC expression might be induced under slightly increased hypoxic conditions. In static cultures as well, an increased sensitivity towards organic peroxides was observed for *Mtb* strains with an inactivated AhpC [104, 105]. Additionally, under low oxygen levels, an increase in the expression of AhpC was revealed [106]. These possibly reveal that the overexpression of AhpC could be triggered under specific conditions, signifying the importance of AhpC. Furthermore, the revelation of the retention of the AhpC gene in *Mtb* despite the loss of the oxyR (the major regulator of AhpC), indicates the importance of AhpC [104].

1.2.2 Peroxiredoxins

AhpC is a 195 amino acid protein that belongs to a class of peroxiredoxins (Prxs) [107]. The term peroxiredoxins was coined by Chae *et al*., to define a class of redox-active proteins that are homologous by sequence [108]. Prxs found in bacteria usually provide antioxidant defenses against hydrogen peroxide, peroxynitrite, and a wide range of organic hydroperoxides, relying on their redox-active cysteines for the reduction of peroxides [109, 110].

1.2.2.1 Classification of Prxs

Prxs can be divided into three classes, the typical 2-Cys Prxs, atypical 2-Cys Prxs, and 1-Cys Prxs, depending on the positions and the number of cysteines that are involved in catalysis [111]. All the Prxs begin their catalysis with the reduction of peroxides by one of the redox-active cysteine, known as the peroxidatic cysteine (Cys-S_pH), thereafter, being oxidized to a cysteine

sulfenic acid (Cys-SOH). Here, the three classes of Prxs respond differently to the oxidized Cys-SOH.

The typical 2-Cys Prxs consist of homodimers, where the Cys-S_PH and resolving cysteine (Cys-S_RH), the second cysteine involved in catalysis that resides on the C-terminus, are on different subunits. Cys-S_RH, unlike Cys-S_PH, does not interact with peroxides directly, but instead, it attacks the oxidized Cys-S_POH, resulting in the formation of the disulfide bond. This disulfide bond is then reduced by a cell-specific disulfide oxidoreductase to Cys-S_PH and Cys-S_RH.

An atypical 2-Cys Prxs follows the same mechanism as that of the typical 2-Cys Prxs, with the only exception that an atypical 2-Cys Prxs are functional as a monomer, with the Cys-S_PH and Cys-S_RH on the same polypeptide chain. The 1-Cys Prxs, on the other hand, does not contain any Cys-S_RH. Hence, it was postulated that following the oxidation of Cys-S_PH to Cys-SOH, the reduction is carried out by a thiol-containing electron donor [109].

1.2.2.2 AhpC – A Typical 2-Cys Prxs

AhpC is classified as a typical 2-Cys Prx [107], containing a conserved Cys-S_PH and Cys-S_RH, along with a PXXX(T/S)XXC motif [112]. This class of proteins is known to possess vastly different oligomeric states, the dimer and decamer. The oligomerization of the protein has been found to be sensitive to conditions such as ionic strength, magnesium and calcium concentrations, pH, concentration of proteins, and redox states [109, 113, 114]. Figure 1.3 depicts the catalytic cycle for *Ec*AhpC, a typical 2-Cys Prxs, relating the redox states of AhpC to its oligomeric form [114-116].

The catalytic cycle begins at **I**, where *Ec*AhpC is in its reduced state, possessing both Cys-S_PH and Cys-S_RH at approximately 13 Å away from each other. This is also known as the fully folded (FF) conformation, which provides stability to the oligomer. Hence, under reduced conditions, *Ec*AhpC is found predominantly as a decameric ring. Following this, an attack of the peroxide substrate by Cys-S_PH occurs, resulting in the oxidation of S_PH to a cysteine sulfenic acid (Cys-S_POH), as shown as **II**. Upon oxidation to Cys-S_POH, local unfolding of both the α-helix containing Cys-SOH and C-terminal containing Cys-S_RH occurs. A condensation reaction follows, leading to the disulfide bond formation, as the two cysteines are brought together to only 2 Å apart, as shown in **III**. With the formation of the disulfide bond, the α-helix is trapped

in the locally unfolded (LU) conformation, affecting the stability of the oligomer [109, 113, 117]. Hence, revealing AhpC as a dimer under oxidized conditions.

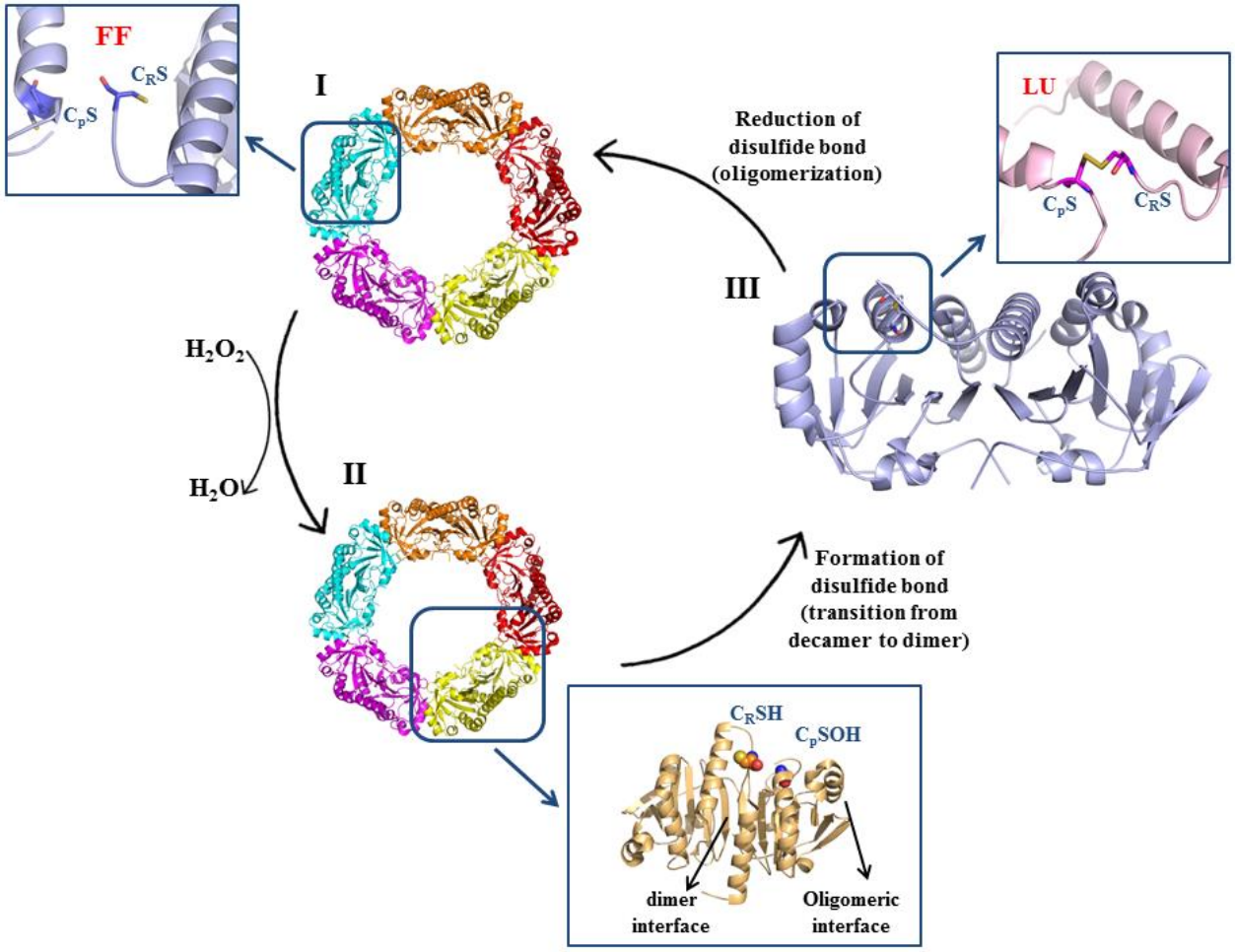

Figure 1.3: Catalytic cycle of *Ec*AhpC. The figure depicts the change in the oligomerization of the protein, in relation to its redox state. **I** Decameric form of *Ec*AhpC with both Cys-S_pH and Cys-S_RH adopting a fully folded (FF) conformation in the reduced AhpC. **II** Upon oxidation by H_2O_2, Cys-S_pH gets oxidized to Cys-S_pOH. **III** The unfolding of the α-helix and C-terminus allows Cys-S_pOH and Cys-S_RH to be near each other, while adopting a locally unfolded (LU) conformation, resulting in the formation of a disulfide bond. However, this destabilizes the oligomeric ring, and results in the presence of a dimer. Upon the reduction of the disulfide bond, both the α-helix and C-terminus returns back to its FF conformation, bringing the protein back to **I.** Reduced *Ec*AhpC (PDB ID: 5B8B) [118], oxidized *Ec*AhpC (PDB ID: 4O5R) [119].

The catalytic cycle is completed when the disulfide bond is reduced by cell-specific disulfide oxidoreductases such as the alkylhydroperoxide reductase subunit F (AhpF) or the thioredoxin system (TrxR, Trx and NAD(P)H) [109, 117]. This results in the generation of free thiol forms of the cysteine residues in preparation for the next catalysis, along with the rearrangement of the α-helix and C-terminal back to its FF conformation, strengthening the oligomerization. Through

these reactions, peroxides are reduced to alcohol and water, protecting the bacteria from harmful ROS.

The oligomer formation is important for its enzymatic activity as shown by studies on the *Salmonella typhimurium* AhpC (*St*AhpC) and *Escherichia coli* AhpC (*Ec*AhpC) [115, 119]. It was revealed by disruption of *St*AhpC's oligomeric ring using site-directed mutagenesis, that the catalytic activity was decreased by 100-fold [115]. During the reduction of peroxides, the LU conformation for the disulfide bond formation is a result of the unwinding of the α-helix containing the Cys-S_pOH. Crystallographic data on *St*AhpC have revealed that the unwound α-helix physically comes into contact with the side chains of L176, L182, and I186 that resides on the C-terminus, forcing the unwinding of the C-terminus [112]. With the unwinding of both the α-helix and C-terminus, the cysteines are brought together for the disulfide bond formation between Cys-S_pH and Cys-S_RH. As the FF α-helix and C-terminus acts as an anchor for the ring formation, the unfolding of the α-helix and C-terminus causes the ring to fall apart into free dimers [109]. Interestingly, although the α-helix forces the unwinding of the C-terminus, the unfolding of the C-terminus could only weaken the α-helix in three ways [112]. Firstly, the unwinding of the C-terminus only prevents a hydrophobic packing between residues L176, L182, and I186 and the first turn of the α-helix that contains the Cys-S_pH, leading to the destabilization of the α-helix [112]. Secondly, as this unfolding of the C-terminus result in the loss of packing for residues L180 and V183 that are on the oligomeric interface, the decameric ring formation is postulated to be weakened, and that in turn affects the α-helix. Lastly, in an indirect manner, residues 137-142 in an FF conformation could interact with the C-terminus of its interacting dimer through residues 163'-166', by forming a short β-sheet. Hence, an unfolding of the C-terminus, which causes a slight displacement of residues 163'-166', would result in a shift in residues 137-142. As E49 forms a hydrogen bond with residue 142, it shifts accordingly as well. This displacement of residues E49 and E138 disturbs the position of R119, a conserved residue, which will be mentioned in section 1.2.2.3 [112], contributing to the weakening of the α-helix.

1.2.2.3 The active site of AhpC

In the FF conformation, surrounding the redox-active cysteine are proline, threonine (or serine), and arginine, which are conserved in all Prxs [120]. Proline restricts the availability for incoming peroxides, hence protecting Cys-S_pH from an over-oxidation, which would result in the formation of a sulfinic acid (Cys-SO_2H), interrupting the catalytic cycle [109, 121].

Nevertheless, bacterial AhpC is shown to be more resistant to over-oxidation, and this occurrence was found more commonly in eukaryotic cells, where they play a role in intracellular H_2O_2 signaling [122, 123].

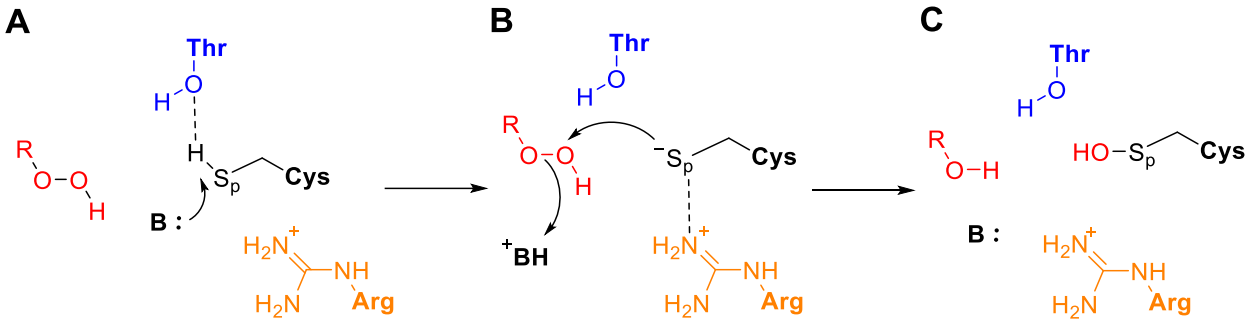

Figure 1.4: Reduction of peroxides in peroxiredoxins. This mechanism was adapted from Flohé, *et al*. [124]. **A** depicts the hydrogen bonding of threonine to Cys-S_pH, allowing the deprotonation by a base. In **B**, with the abstracted proton, arginine assists to stabilize the negatively charged sulfur, while allowing it to reduce the incoming peroxides, generating Cys-SOH and water as shown in **C**.

Threonine (or serine) assists in the protonation of the Cys-S_pH, and at the same time, prepare Cys-S_pH for thiol deprotonation by a catalytic base (Fig. 1.4) [109, 124]. Abstraction of a proton on Cys-S_pH by the base causes the cysteine to become negatively charged. This is stabilized by arginine, thus lowering the pKa of the cysteine to lesser than 6, as compared to a free cysteine with a pKa of approximately 8.5 [109, 122, 125]. Following this, Cys-S_pH can attack peroxides, allowing the reduction of peroxides to water, and itself getting oxidized to Cys-S_pOH [109].

1.2.3 Unique features of *Mt*AhpC

*Mt*AhpC, unlike its bacterial counterparts, is found to possess several unique features, such as the number of cysteine residues, dodecameric ring formation, additional residues at the N-terminus, a cavity within the *Mt*AhpC structure, and the reducing partners of *Mt*AhpC.

1.2.3.1 Number of cysteine residues

Firstly, *Mt*AhpC has three cysteine residues (C61, C174, and C176) rather than two catalytic cysteines, which is commonly found in the case of other bacterial AhpCs. Residue C61 was identified as the Cys-S_pH from mutagenesis studies where a single mutation, *Mt*AhpC$_{C61S}$, was revealed to be inactive [126]. Additional enzymatic assay carried out on *Mt*AhpC$_{C174S}$ and *Mt*AhpC$_{C176S}$ revealed a 10% retention of activity as compared to WT *Mt*AhpC, indicating the importance of both C174 and C176. However, the mechanism involving the three cysteines are baffling as only two cysteines are needed in the catalytic cycle.

Two different mechanisms have been proposed with regards to the involvement of the three cysteine residues (Fig. 1.5). Firstly, site directed mutagenesis studies by Chauhan *et al*. (2002) have led to the hypothesis that C61, after oxidation to SOH, will first form a disulfide bond with C176, which gets replaced by C174 [127]. This was demonstrated by subjecting *Mt*AhpC$_{C61A}$, *Mt*AhpC$_{C174A}$, and *Mt*AhpC$_{C176A}$, on an SDS-PAGE under oxidized conditions, where no disulfide bond was formed with *Mt*AhpC$_{C61A}$. *Mt*AhpC$_{C174A}$ could exist as both a monomer and dimer, and *Mt*AhpC$_{C176A}$ forms only the dimer [127]. Hence, it was hypothesized that a disulfide bond was not possible between C174 and C176 (from the results of *Mt*AhpC$_{C61A}$), while disulfide bond could easily form between C61 and C176, as the results from *Mt*AhpC$_{C174A}$ revealed a pure dimer. Only a portion of *Mt*AhpC$_{C176A}$ could form a disulfide bond between C61 and C174, due to the presence of both the monomer and dimer [127].

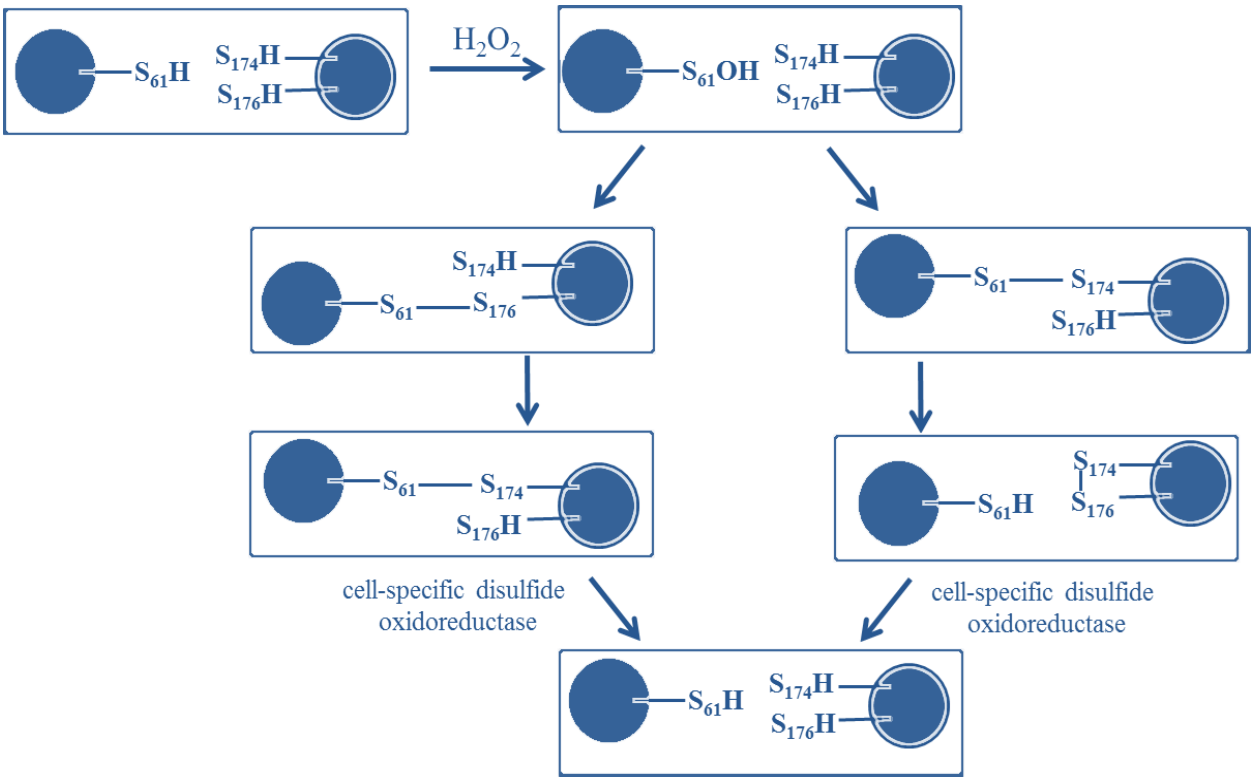

Figure 1.5: Schematic demonstrating the involvement of the three cysteines in the reduction of the disulfide bond. On the left is the mechanism hypothesized by Chauhan *et al*. (2002) while the one on the right was postulated by Guimarães *et al*. (2005).

However, with the crystal structure of *Mt*AhpC$_{C176S}$, it was later proposed by Guimarães *et al*. (2005) that the disulfide bond was first formed between C61 and C174, due to the proximity of the cysteines [107]. Subsequently, an intramolecular disulfide bond forms between C174 and

C176, releasing the α-helix from its unfavorable position. After which, the intramolecular disulfide bond is exposed to subsequent reduction by its cell-specific disulfide reductase.

1.2.3.2 Dodecameric ring formation

Unlike other bacterial AhpCs such as *St*AhpC, *Ampjibacillus xylanus* AhpC (*Ax*AhpC) and *Ec*AhpC, which oligomerize into a 10-mer under reduced conditions [109, 115, 119], *Mt*AhpC forms a 12-mer, as demonstrated in the crystallographic structure of *Mt*AhpC$_{C176S}$ [107] (Fig. 1.6). This dodecameric formation was supported by Wong *et al*. (2017), which highlighted the uniqueness of *Mt*AhpC using electron microscopy (EM) with the projected images of a 12-mer, along with the diameter of approximately 155 Å [128].

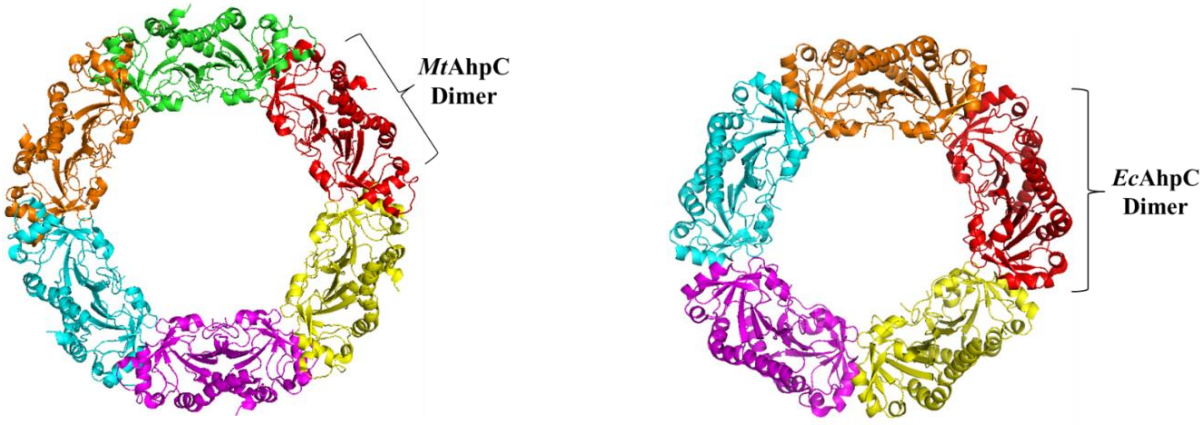

Figure 1.6: Oligomeric ring of *Mt*AhpC and *Ec*AhpC. Ring-shaped 12-mer of *Mt*AhpC$_{C176S}$ (left) (PDB ID: 2BMX) and ring-shaped 10-mer of *Ec*AhpC (right) (PDB ID: 4O5R) [107, 119]. Each oligomeric ring is made up of dimers as indicated.

1.2.3.3 Additional residues in the N-terminus

It was observed through the sequence alignment with other AhpCs proteins, such as *Ec*AhpC and *St*AhpC, that an additional stretch of residues was found in the N-terminus of *Mt*AhpC between residues 23 to 34, conserved only in mycobacterial species (Fig. 1.7) [128]. Deletion mutagenesis studies by Wong *et al*. (2017) demonstrated a loss in oligomerization capabilities of *Mt*AhpC$_{\Delta 23\text{-}34}$. Although residues 23 to 34 do not reside along the dimer-dimer interface to directly inhibit oligomerization, it was hypothesized that the hydrophobic residues along residues 23 to 34 would be required to create an ideal environment for the hydrophobic residues on the dimer-dimer interface. Additionally, *Mt*AhpC$_{\Delta 23\text{-}34}$ was revealed to be enzymatically inactive, supporting the importance of this N-terminal loop in *Mt*AhpC activity.

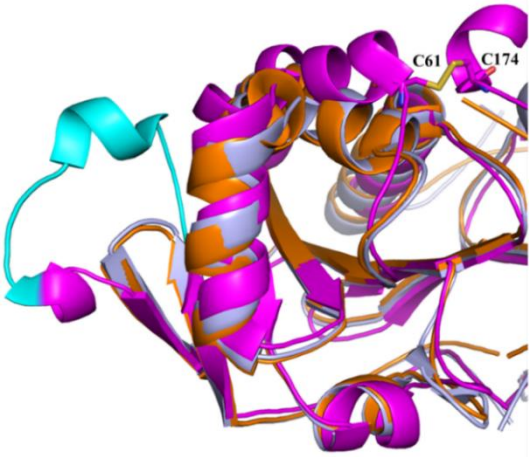

Figure 1.7: Comparison of *Mt*AhpC$_{C176S}$, *Ec*AhpC and *St*AhpC. The crystallographic structure of *Mt*AhpC$_{C176S}$ (pink) (PDB ID: 2BMX) is shown with overlaps of *Ec*AhpC (light blue) (PDB ID: 4O5R) and *St*AhpC (orange) (PDB ID: 1YEP) [107, 115, 119]. The additional stretch of N-terminal residues is highlighted in cyan.

1.2.3.4 Helical displacement of α-helix containing Cys-S_pH

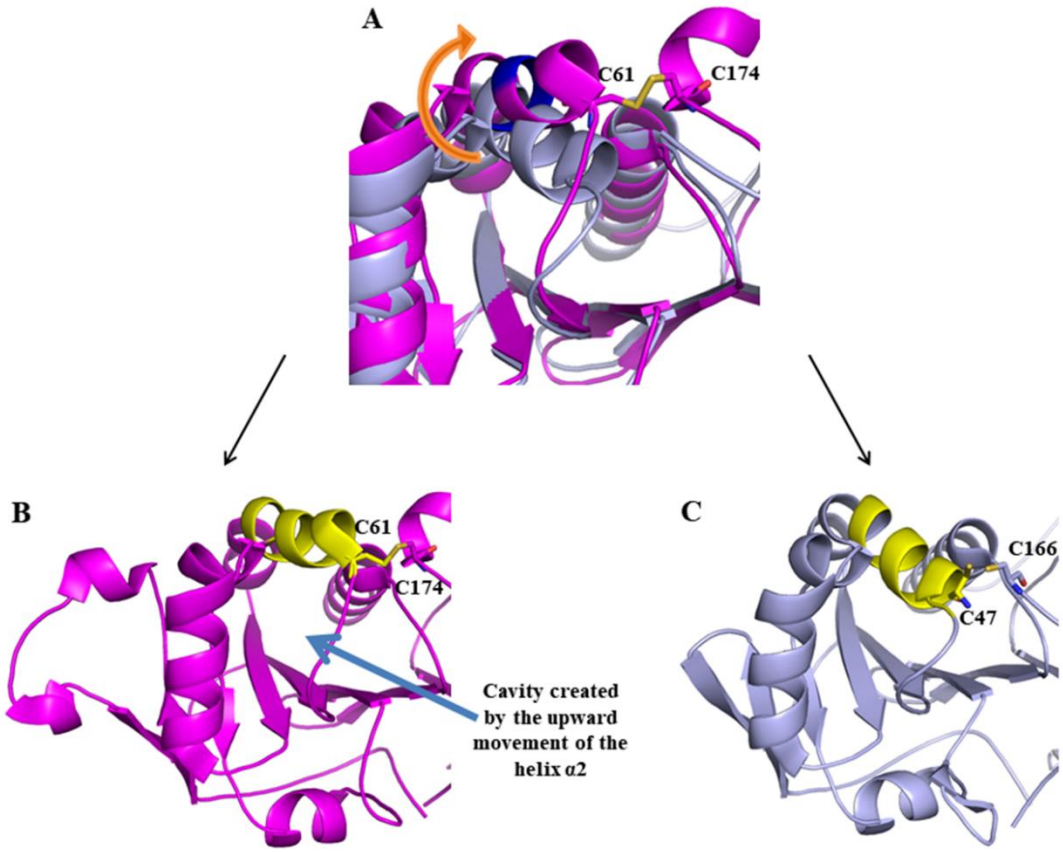

Figure 1.8: Crystallographic structure of *Mt*AhpC$_{C176S}$ reveals a cavity within itself. Crystallographic structure of *Mt*AhpC$_{C176S}$ (pink) (PDB ID: 2BMX) overlap with *Ec*AhpC (light blue) (PDB ID: 4O5R) [107, 119]. **A** As compared to *Ec*AhpC, the *Mt*AhpC α2-helix was observed in an elevated position. The disulfide bond interaction between the dimers can be observed with C61 and C174 (yellow). **B** presents *Mt*AhpC$_{C176S}$ with the α-helix indicated in yellow. A large cavity can be seen here as compared to **C**, where the α-helix (yellow) resides in the cavity.

From the crystal structure of *Mt*AhpC$_{C176S}$, the α-helix containing Cys-S$_p$H was found to be elevated, in contrast to other AhpCs (Fig. 1.8A), creating a cavity within *Mt*AhpC (Fig. 1.8B) [107]. Following this observation, Guimarães *et al*. (2005) postulated that *Mt*AhpC, unlike its bacterial counterparts that utilizing an unwinding mechanism (as described in section 1.2.2.2 for a typical 2-Cys Prxs), possesses a rigid-body movement of the α-helix to bring the catalytic cysteines, C61 and C174, in close proximity for disulfide bond formation [107]. Along with the helical displacement, a cavity in *Mt*AhpC is created.

1.2.3.5 Reducing partners of MtAhpC

Unlike many other AhpCs, such as *Ec*AhpC and *St*AhpC, that are reduced by AhpF, *Mtb* contains AhpD instead, on the gene locus that carries AhpF [119]. Although it was previously mentioned that AhpD is not a compatible reducing partner of AhpC [126], more recent studies have illustrated the interaction between AhpC and AhpD [129, 130]. However, this interaction only occurs with an orchestra of proteins, which includes dihydrolipoamide succinyltransferase (SucB), dihydrolipoamide dehydrogenase (Lpd), along with AhpD (Fig. 1.9).

Additionally, despite prior research indicating the incompatibility of the AhpC with the Trx-system [131], recently published results have debunked the hypothesis. Instead, it was found that TrxR alongside TrxC was able to reduce AhpC (Fig. 1.9) [129, 132].

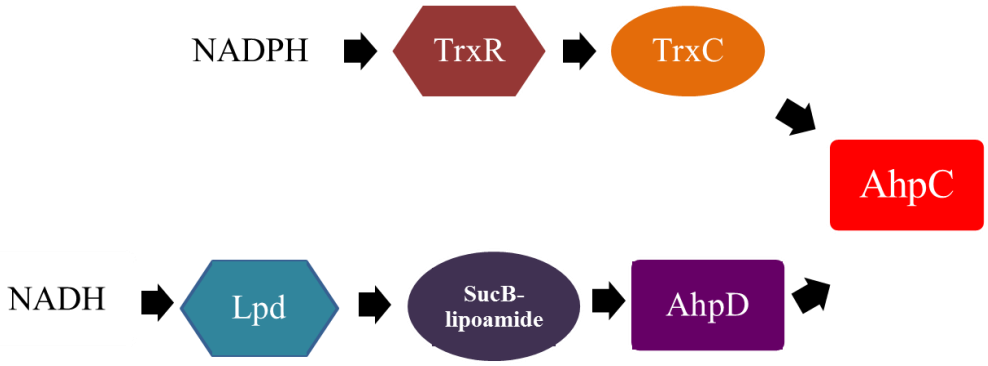

Figure 1.9: Antioxidant process in *Mt*AhpC. *Mt*AhpC can receive its electrons from AhpD, using SucB, Lpd and NADH. Conversely, AhpC can be reduced using the Trx-system, with NADPH as the electron donor.

However, not all the thioredoxins in the Trx-system were able to effectively reduce AhpC. In the study published, it was revealed that TrxA and TrxB are not efficient in reducing AhpC [132]. The efficiency of the reduction of *Mt*AhpC by *Mt*TrxC was supported by an NMR-titration and molecular docking studies by Wong *et al*. (2017) [128]. As *M. bovis* AhpC

(*Mb*AhpC) and *Mb*TrxC share an identical amino acid sequence to *Mt*AhpC and *Mt*TrxC, respectively, the authors utilized *Mb*AhpC and *Mb*TrxC in their assay. The interaction between *Mb*TrxC and *Mb*AhpC was illustrated in a TrxC-AhpC complex model generated with HADDOCK-docking simulation [128].

It was discovered that residues Q76 and V78 on *Mb*TrxC exhibit hydrogen bonding interactions with K70 and T63 on *Mb*AhpC, which resides on the same α-helix that contains the Cys-S_pH. As it was previously postulated that the rigid-body movement of the helix α2 requires only a small rearrangement of F51, F68, and F108, since F68 resides on the same α-helix as K70 and T63, the hydrogen bonding interaction will possibly induce the rearrangement of the phenylalanine, leading to the helical movement [107]. Moreover, as C37 of TrxC is closer to C174 as compared to C61, it coincides with the deduction made by Guimarães, that C176 aids the release of the disulfide bond between C61 and C174, forming an intramolecular disulfide bond, which is then reduced by AhpD or TrxC [107, 128].

Both reducing pathways, the AhpD and TrxC-system, are important for the regeneration of AhpC, as despite AhpD being a more efficient reducing substrate, the concentration of AhpD in *Mtb* was predicted to be much lower than TrxC [105]. All in all, the uniqueness of *Mt*AhpC has illustrated the need for more research studies to be performed on this protein to find practical treatments for INH-resistant TB strains.

1.2.3.6 Exploiting the helical displacement towards drug discovery

In the current study, the hypothesized helical displacement mechanism that results in the cavity within *Mt*AhpC was investigated. As this cavity is unique to *Mt*AhpC, this feature could be exploited for drug discovery as it increases the possibility for drug specificity. It appears fitting to design a molecule that can reside in this cavity, locking *Mt*AhpC in its intermediate form and preventing it from completing the catalytic cycle. This would halt the reduction of peroxides, eventually causing *Mtb* to become susceptible to ROS.

To determine if the cavity would be a good drug target, it would be advantageous to verify the importance of the helix α2 on its enzymatic capabilities. As shown in figure 1.8 (**A**), the residues at the kink of the α-helix that are depicted in blue. These residues are found to be A66, A67, and F68. Using the sequence alignment with several AhpC proteins, conserved G-D-V residues were found for several of the AhpCs, such as *Ec*AhpC and *St*AhpC at residues 66 to 68 (Fig. 1.10). Since these proteins require the unfolding of the α-helix for disulfide bond formation,

mutations carried out to alter the α-helix such that it resembles that observed in *Ec*AhpC and *St*AhpC are hypothesized to impede the rigid body movement of the α-helix. In this study, site-directed mutations were made, and verification of these crucial residues with enzymatic assays and biophysical experiments were carried out to determine its activity.

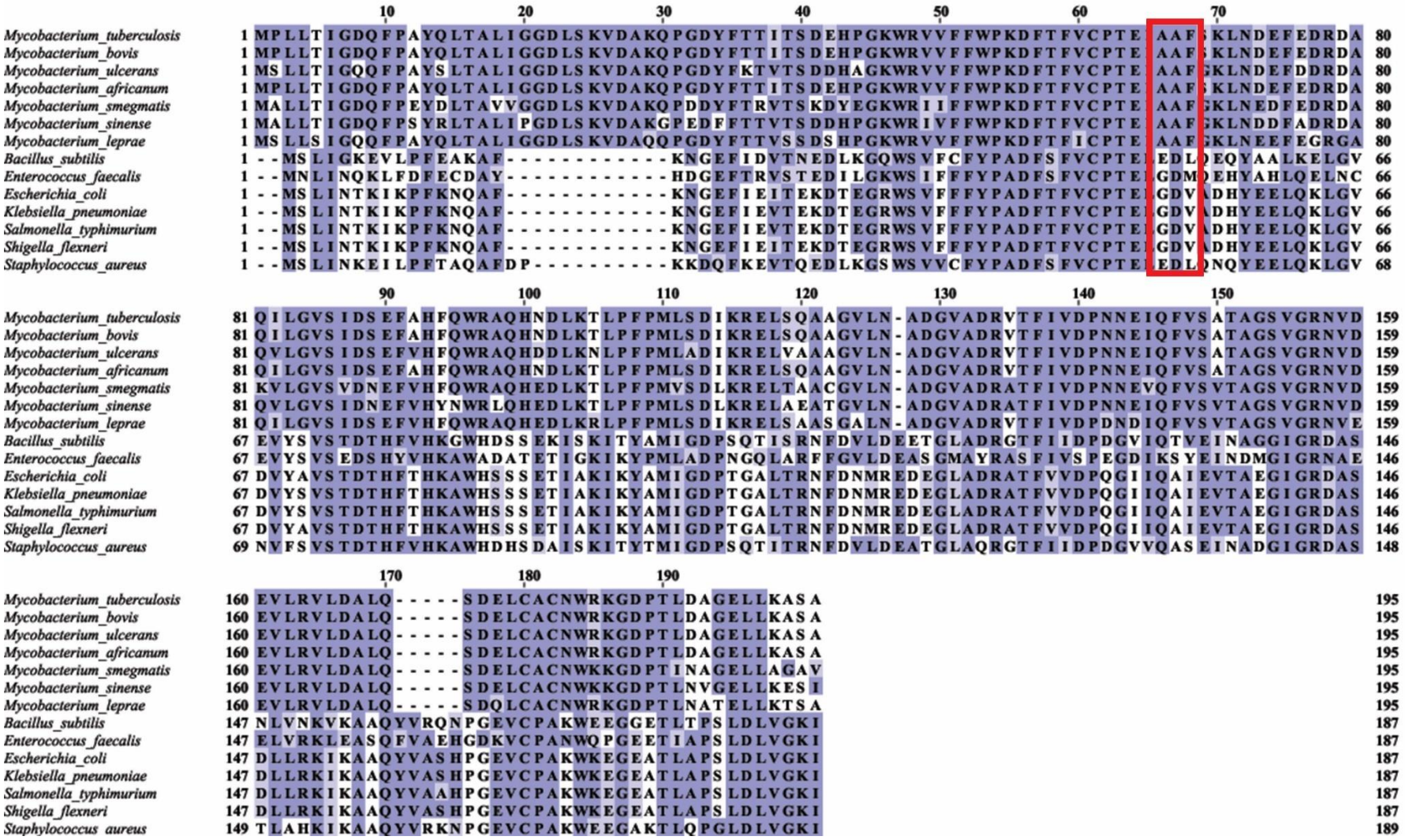

Figure 1.10: Sequence alignment of *Mt*AhpC with other bacterial species performed by ClustalW. Residues 66 to 68 are marked in red. This figure is adapted and modified from Wong *et al.* (2017) [128].

Towards affecting the cytochrome *bcc* complex

1.3 Towards affecting the cytochrome *bcc* complex

1.3.1 Electron transport chain

Adenosine triphosphate (ATP) has been referred to as the energy currency as it stores energy required for most cell functions. ATP can be generated via two methods, by substrate-level phosphorylation or oxidative phosphorylation. With substrate-level phosphorylation, ATP is produced by the breakdown of carbon sources such as glucose, galactose and maltose [133]. In *Mtb*, it was revealed that the ATP produced via substrate-level phosphorylation is insufficient for its survival [134, 135]. Instead, ATP is mostly generated by oxidative phosphorylation through the electron transport chain (ETC), which consists of a series of complexes that initiate a proton motive force (PMF) [136]. The generation of a PMF involves two components, the transmembrane proton gradient and electric potential. Both components are essential for the cell viability, as the collapse of either one component results in cell death [137].

The importance of ATP production through oxidative phosphorylation pathway in *Mtb* was further elevated, following the revelation that the ETC complexes are essential even under hypoxic conditions [137, 138]. Wayne and Hayes (1996) revealed the ability of *Mtb* to transit to a non-replicating state under low-oxygen conditions, simulating the hypoxic conditions of *Mtb* under dormancy [139]. Under these conditions, many functions ceased, such as DNA synthesis and cell division, along with a decrease in net carbon flux [139, 140]. This results in the inactivity or decrease in the activity of many TB drugs acting on these pathways, with a serious consequence of a long-treatment therapy required for TB treatment [139]. The ETC however, was found to be vital, where a higher inactivation of quiescent *Mtb* was revealed when compounds were added to disrupt the PMF [137, 141]. Although a down-regulation of the ETC's main complexes were discovered, it was possibly a reflection of the low level of ATP required during dormancy [137, 138]. These pieces of information strengthen the importance of the oxidation phosphorylation pathway.

The canonical ETC consists of four complexes. Out of which, complex I, III, and IV pump protons across the membrane to generate an electrochemical gradient, exploited by the F-ATP synthase to generate ATP [142, 143]. In *Mtb*, five main differences to the canonical ETC were discovered (Fig. 1.11).

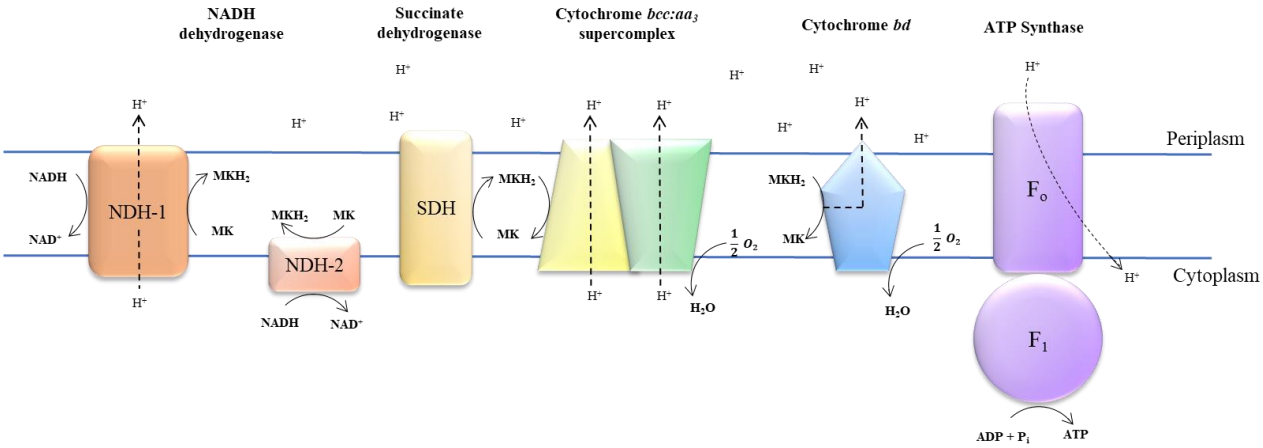

Figure 1.11: The complexes involved in the ETC of *Mtb*. *Mtb* possess two NADH dehydrogenase, NDH-1 and NDH-2, which reduces menaquinone (MK) to menaquinol (MKH_2), depending on the availability of oxygen. NDH-2 is the dominant acceptor of NADH. MK can be reduced alternatively by the succinate dehydrogenase. The electrons from MKH_2 are transferred to cytochrome *bcc*, which passes on the electrons to cytochrome aa_3, to reduce oxygen. *Mtb* possess another terminal oxidase, cytochrome *bd*, which is able to oxidise MKH_2 as well, reducing oxygen to form water.

Firstly, two types of NADH dehydrogenase are found in *Mtb*, namely the type-1 NADH dehydrogenase (NDH-1) and the type-2 NADH dehydrogenase (NDH-2). NADH dehydrogenase is also known as complex I in the ETC. The canonical NADH dehydrogenase accepts electrons from NADH, which are used to reduce ubiquinone, and at the same time, results in a series of conformational change within the protein subunits, allowing proton translocation [143]. NDH-1 is the homologue to the mitochondria complex I, and is encoded by *nuo*ABCDEFGHIJKMN operon. However, it was revealed to be dispensable for growth and persistence [144]. During dormancy, the down-regulation of NDH-1 was found as opposed to the up-regulation of NDH-2 [145]. This was similarly demonstrated when rotenone, an NDH-1 inhibitor, was unable to kill quiescent *Mtb* [137, 139], and further verified through deletion of the *nuo*ABCDEFGHIJKMN operon, which allows the mutant *Mtb* to grow under hypoxic condition similarly to the WT *Mtb* strains [137]. Nevertheless, NDH-1 was found to be important from *in-vivo* experiments, as the *nuo*G gene was revealed to be an anti-apoptosis gene, and the *Mtb* mutant devoid of the *nuo*G subunit was found to have a lowered bacterial virulence in mice [141, 146].

Conversely, NDH-2 was discovered to be the dominant acceptor of NADH, with evidence from THZ, an NDH-2 inhibitor, displaying its ability to kill quiescent *Mtb*, along with a large drop in ATP levels [137, 139]. NDH-2 does not pump protons, and it is present in two copies, *Ndh* and *Ndh*A, with a 67% similarity [147]. To identify the roles of *Ndh* and *Ndh*A, knockout mutants were prepared. Δ*Ndh*Δ*Ndh*A mutants could not be achieved, illuminating the importance

of NDH-2 [148]. Δ*Ndh* mutants demonstrated severe growth deficiencies, while Δ*Ndh*A demonstrated a similar growth rate to the WT *Mtb* strain, indicating the dispensability of *Ndh*A for growth [148]. The essentiality of *Ndh* was further validated in *M. smegmatis*, where the *Ndh* mutant was shown to exhibit growth defects [149, 150]. Additionally, in *M. leprae*, where evolution results in the huge reduction of protein-coding genes, it was believed that only the essential genes are retained. Here, only *ndh* activity was found for the oxidation of NADH [147, 151].

Nevertheless, very recent studies have debunked the essentiality of NDH-2, as the Δ*Ndh*Δ*Ndh*A mutant is able to grow in fatty-acids-free media [152]. Furthermore, a mild decrease of virulence in mice with the Δ*Ndh*Δ*Ndh*A mutant indicates the possibility of switching between the available NADH dehydrogenase. This suggests the need to target both NDH-1 and NDH-2 to fully bring down the activity of the NADH dehydrogenase. As NDH-1 was previously considered to be redundant, no drug discovery towards NDH-1 was attempted [153]. Additionally, as *Ndh* and *Ndh*A are not present in human genomes, it serves as a potential drug target with more drug development efforts towards NDH-2. Example of drugs targeting NDH-2 comprises of phenothiazines antipsychotic drugs such as THZ (as mentioned previously), chlorpromazine, and trifluoperazine [154]. However, due to their low potency and toxicity profile, current efforts are made to improve the phenothiazines for *Mtb* [155, 156]. More recent drug discovery towards NDH-2 have identified quinolinyl pyrimidines through an NDH-2 target screening with a promising MIC_{50} of 0.81 μM [157], and 2-mercapto-quinazolinones, found through whole-cell screening, with an MIC_{50} of 0.6 μM [158].

Secondly, *Mtb* has two succinate dehydrogenase (SDH) enzymes, Sdh-1 and Sdh-2, similar to the canonical SDH, and a fumarate reductase [144]. The canonical SDH, also known as complex II of the ETC, reduces ubiquinone like in NADH dehydrogenase. However, instead of utilizing NADH, it reduces ubiquinone along with the oxidation of succinate to fumarate [159]. In *Mtb*, Sdh-1 is determined to be important during aerobic respiration using a transposon-site hybridization screen [160]. *Mtb* ΔSdh-1 mutant causes an upsurge in oxygen consumption, leading to a decrease in the initial growth of the cells under aerobic conditions, and an increase in cell death during the stationary phase [161]. Additionally, *in-vivo* studies in mice indicate a poorer virulence of the *Mtb* ΔSdh-1 mutant [161]. Sdh-2, on the other hand, was determined to be essential under anaerobic conditions, where it contributes to the membrane potential under

hypoxia [161, 162]. Fumarate reductase catalyzes the opposite reaction, from fumarate to succinate. In organisms such as *Escherichia coli* and *Wolinella succinogenes*, fumarate reductases have demonstrated their ability to act as terminal electron acceptors when a more suitable terminal electron acceptor, such as oxygen, is not present [163, 164]. Coincidentally, upregulation of the fumarate reductase has been found under hypoxic conditions, indicating the importance of the fumarate reductase under anaerobic conditions [165-167].

The SDH is an essential enzyme in the tricarboxylic acid (TCA) cycle, indicating its importance in regulating both the carbon metabolism and the oxidative phosphorylation pathway [168]. Thus, a drug inhibiting the SDH could possibly impact both ATP synthesis pathways. However, with functional redundancy existing between these three enzymes, Sdh-1, Sdh-2, and the fumarate reductase, it suggests that an inhibitor has to target all three enzymes to successfully inhibit *Mtb* [169]. Additionally, with the similarities of this complex in mammalian cells, resistance towards drug discovery with SDH was observed [153, 168, 169]. A current known inhibitor of SDH is 3-nitropropionate, an isoelectronic analog of succinate [170]. Although effective against mycobacterial SDH, it has a high likelihood of inhibiting eukaryotic SDH, rendering it a poor lead compound for drug discovery [141, 171].

Thirdly, a soluble cytochrome *c* (cyt-*c*) was not found in *Mtb*, as observed in a canonical ETC, where the cyt-*c* is able to travel along the membrane freely. This aids in the transfer of electrons from complex III to complex IV. Instead, in *Mtb*, complex III and IV associates to form a supercomplex, allowing the transfer of electrons from cytochrome III to IV easily [72, 73]. This will be discussed further in section 1.3.2.

Fourthly, *Mtb* possesses two main terminal oxidases, transferring the electrons from menaquinol to molecular oxygen, forming water. The first is cytochrome aa_3 (cyt-aa_3), also known as complex IV, and the second is the cytochrome *bd* (cyt-*bd*). Unlike cyt-aa_3, cyt-*bd* is unable to pump protons but instead contributes to the PMF by a transmembrane charge separation [172, 173]. The electron pathway towards cyt-aa_3 is more energetically favourable, and this is supported by deletion mutation studies on the complex IV subunits, which indicates severe growth impairment [174]. Cyt-aa_3 consist of four main subunits, CtaCDEF, with two recently identified subunits, CtaI and CtaJ, observed by Gong *et al*. (2018) [72]. For efficient electron transfer to reduce oxygen, cyt- aa_3 encompasses a Cu_A center to receive electrons from complex III. The electrons are transferred to heme *a*, and ultimately to hemea_3:Cu_B, where it gets transferred onto a bound molecular oxygen [175].

Cyt-*bd* comprises two main subunits, CydA and CydB, along with genetic data demonstrating *Mtb* encoding for CydDC, a putative ABC transporter [176]. CydA is known to possess the quinol binding site (Q-loop), along with the three heme groups, b_{558}, *d*, and b_{595} [177]. The electron transfer within CydA was proposed to occur from the quinol oxidation at the Q-loop, to heme b_{558} [177, 178]. An alternative pathway was additionally identified, known as the cydB pathway. The transfer of electrons was postulated to be carried out via charged or polar amino acids directly towards heme b_{595} and heme *d* [177, 178]. Deletion mutants analysis on *Mtb* CydA unique helical regions by Sviriaeva *et al*. (2020) provided preliminary insights into the essentiality of the Q-loop for cyt-*bd* function and complex assembly [179]. Furthermore, single mutation studies on *Mtb* CydB have identified residue W64 to be critical for Cyt-*bd*'s activity as well as stabilization of the complex [179]. The function of CydDC is unclear in *Mtb*. In *E. coli*, the CydDC is involved in the assembly of the cytochrome *bd*, where even though the polypeptide chain could be synthesized in the absence of CydDC, the heme groups for electron transfer were absent [180, 181].

Cyt-*bd* was found to be dispensable under aerobic conditions with studies from the ΔCydABDC deletion mutant, demonstrating growth and persistence similar to the WT *Mtb* strains [152]. It serves as an alternative pathway as shown in the diminished, but still noticeable, growth of *Mtb* in the absence of cytochrome aa_3, both *in-vitro* and *in-vivo* [152]. The elimination of *Mtb* was only possible with the deletion of both cyt-aa_3 and cyt-*bd*, which was verified when *Mtb* could not be fully eliminated with a complex III inhibitor alone, preventing electron transfer towards cyt-aa_3 [152, 182]. The addition of a cyt-*bd* inhibitor was necessary to enhance the killing of *Mtb*. The potent complex III inhibitor is Telacebec (Q203), which possesses a MIC_{50} value of 2.7 nM in *Mtb* culture broth media [183]. Despite having a high potency at a low concentration, Q203 was unable to initiate killing of *Mtb* even at 200-times the MIC_{50} value, suggesting that although cyt-*bd* alone is unable to sustain growth, it is able to maintain cell viability [184]. Additionally, cyt-*bd* was revealed to be greatly upregulated in the presence of nitric oxide and under hypoxic conditions, indicating its significance under both oxidative stress and hypoxia [136, 145, 185-187]. This was supported by knockout cyt-*bd* studies under microaerophilia, where severe growth impairment were observed [145, 186]. The importance of cyt-*bd* under hypoxia could be attributed to its high oxygen affinity to support its survival under reduced oxygen conditions [188]. This as well represents the importance of cyt-*bd* for *Mtb* to survive in the macrophages where low oxygen tension is prevalent, signifying its importance in

latent TB [144, 189, 190]. The current drug effective against *Mtb* cyt-*bd* is aurachin D, which demonstrated its bactericidal activity in combination with a cyt-*bcc* inhibitor [182].

Lastly, although the F-ATP synthase, complex V, is mostly conserved among all living species, *Mtb*'s F-ATP synthase is found to strongly repress ATP hydrolysis in most mycobacterial species [191, 192]. While ATP hydrolysis was discovered to be important to maintain the PMF in many organisms, poor regulation can lead to cell death due to the depletion of ATP [193]. In many mycobacterial species, however, this repression of the ATP hydrolysis could reflect the adaptation of these organisms to conserve ATP [191].

The *Mtb* F-ATP synthase is encoded by the *atp*BEFHAGDC operon [153], consisting of a membrane embedded F_0 sector and an external F_1 unit, connected by a central and a peripheral stalk (Fig. 1.12) [191, 194]. The F_0 sector comprises of subunits *abb'cc*$_9$ [195], while the water-soluble F_1 unit contains subunits $\alpha_3\beta_3\gamma\delta\varepsilon$ [191]. The central stalk is made up of γ and ε subunits, and the peripheral stalk includes the δ subunit along with subunits *b* and *b'* [196]. The peripheral stalk, originally thought to be rigid, possesses flexibility and was predicted to acquire conformational changes during rotation [197]. Interestingly, in mycobacterial species, the genes encoding the *b*- and δ- subunit (for the peripheral stalk) are fused to form a single gene (*atp*H) [198]. The *δ*- subunit has an additional 111 residues at the N-terminus that aids in the fusion of the *b*- and *δ*- subunits [198, 199]. Additionally, in contrast to the F-ATP synthase in *E. coli*, which contains two *b* subunits, the *Mtb* F-ATP synthase has a smaller *b'* subunit (encoded by *atp*F gene), which lacks the C-terminus from the *b* subunit [198-200].

The F_0 sector, known as the proton-conducting turbine, initiates rotation in the *c*-ring by channeling the protons from the PMF through a proton pathway formed by subunits *a* and *c* [201]. The rotational energy from the *c*-ring is extended to the central stalk [199], resulting in conformational changes in the $\alpha_3\beta_3$ hexamer, the catalytic domain for ATP generation [202]. Conversely, the driving force of ATP hydrolysis in F-ATP synthases is the chemical energy stored in ATP [203]. The breakdown of ATP to ADP and P_i at the $\alpha_3\beta_3$ hexamer initiates the rotation of the central stalk in the opposite direction (counter-clockwise), allowing protons to be pumped across the membrane to maintain the PMF [204]. Studies have demonstrated the ability of the isolated F_1 domain to perform ATP hydrolysis without ATP synthesis capabilities [205].

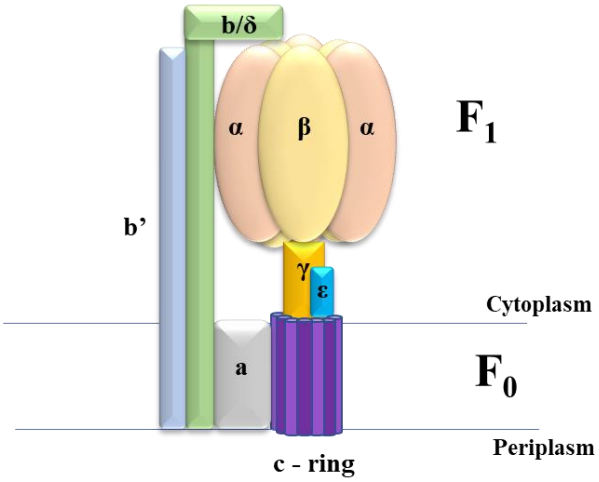

Figure 1.12: Composition of the mycobacterial F-ATP synthase, complex V of the ETC, in *Mtb*. Several unique features are present such as the fusion of the subunit *b* and *δ*, along with a shorter *b'* subunit. The number of *c* subunits to form the *c*-ring is nine and a smaller ε subunit is observed [195, 199].

Mtb F-ATP synthase has several unique structural features that repress ATP hydrolysis. This includes a distinctive loop region in the γ subunit [206, 207]. Deletion studies on this loop region revealed a significant decrease in ATP synthesis, with an increase in ATP hydrolysis. The increase in ATP hydrolysis activity is postulated to result from the loop interacting with the polar residues of the *c*-ring, physically blocking ATP driven proton pumping [206]. Additionally, an extended C-terminal of the subunit α was observed in mycobacterial species [208]. Similarly, the deletion of this unique stretch of amino acid residues results in a drastic decrease in ATP synthesis, with an increase in ATP hydrolysis [208]. The extended C-terminal stretch was found to limit the angular velocity of the power stroke, preventing ATP hydrolysis [208], in agreement with studies from Bogdanović *et al*. (2018) and Kamariah *et al*. (2019), indicating the proximity of the extended C-terminal to the central stalk subunits [199, 209, 210]. *Mtb* F-ATP synthase also possesses a smaller ε subunit that does not reach the catalytic head of the F_1 domain [211]. The repression of the ATP hydrolysis appears to be controlled by the ε subunit as well, where its c-terminal deletion results in an increase in ATP hydrolysis activity [212].

The essentiality of the enzyme has been demonstrated by Sassetti *et al*. (2003) in *Mtb* [134], and by Tran and Cook (2005) in *M. smegmatis*, by generating deletion mutants suggesting that ATP generated via substrate-level phosphorylation is not sufficient to support its growth [135]. Studies carried out under hypoxic conditions revealed a minimum ATP level sustained for survival, as well validating the importance of the ATP synthase [137]. This was further established following the development of an F-ATP synthase inhibitor for *Mtb*, bedaquiline

(BDQ), which causes killing of *Mtb* under both aerobic and hypoxic conditions [213, 214]. BDQ is a highly potent compound that targets both the *c*-ring and ε subunit [195, 211]. However, the emergence of clinical resistance towards BDQ, along with its high cardiotoxicity profile, spurred the discovery of BDQ analogs and other *Mtb* F-ATP synthase inhibitors [215-217]. TBAJ-876, a promising BDQ analog, was identified recently with a lower cardiotoxicity profile and 10 times its potency [218-220]. Drug screening studies against the *Mtb* oxidative phosphorylation pathway have identified squaramides as potent inhibitors [221], while more specific drug screening against the *Mtb* F-ATP synthase allowed the discovery of GaMF1 that binds to the unique loop of the γ subunit [222]. GaMF1 possesses an MIC_{50} value of 11 μM, and is found to increase the potency of BDQ as well [222]. *In-silico* studies on the C-terminal region of the subunit ε have also identified epigallocatechin gallate (EGCG), a catechin found in green tea, as a potential inhibitor [223].

1.3.2 Cytochrome *bcc*

Cytochrome bc_1 (also known as cytochrome *bcc* in *Mtb*), complex III of the ETC, aids in the transfer of electrons from ubiquinol to cytochrome *c*, in turn catalyzing the oxidation and reduction of ubiquinol and cytochrome *c*, respectively. The *Mtb* genome suggests a similar interaction between complex III and IV of the ETC to *M. smegmatis*, where a soluble cytochrome *c* was not found [73, 224]. Instead, a membrane-bound QcrC subunit is discovered in its place, possessing two heme groups, c_{D1} and c_{D2}, instead of the cytochrome *c* and c_1 in the canonical cytochrome bc_1, hence being referred to as cyt-*bcc* in *Mtb* [72, 73]. Along with the lack of a soluble cytochrome *c*, a III-IV supercomplex was found for efficient electron transfer [224-226]. The importance of the cyt-*bcc* complex has been characterized by Matsoso *et al*. (2005), indicating severe growth impairment in the *M. smegmatis* devoid of the cyt-*bcc* complex [174].

The cryo-EM structure of the III-IV supercomplex was recently achieved by Gong *et al*. (2018) and Wiseman *et al*. (2018), revealing the supercomplex possess a linear dimeric arrangement IV_1-III_2-IV_1 (PDB ID: 6ADQ) (Fig. 1.13) [72, 73]. The cyt-*bcc* complex is made up of three subunits, encoded by QcrCAB. QcrA (green), QcrB (blue), and QcrC (magenta) contains the Rieske [2Fe–2S] (FeS) center, hemes b_H and b_L, and hemes c_{D1} and c_{D2}, respectively [72, 73]. The interaction between QcrA and QcrB enforces the dimerization of the complex III, while the

interaction between complex III and IV is supported by phospholipids, such as cardiolipin molecules, found within the groove at the interface of complex III and IV [72, 227].

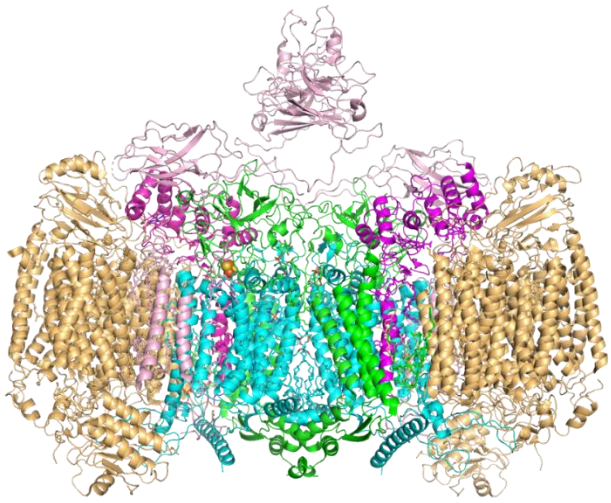

Figure 1.13: Cartoon representation of the *M. smegmatis* III-IV supercomplex. The supercomplex possess a linear dimeric arrangement (PDB ID: 6ADQ) [72]. Complex III is made up 3 subunitss, namely the QcrA (green), QcrB (blue) and QcrC (magenta). Complex IV is represented in light orange while the accessory proteins are represented in light pink.

Three additional proteins were found within the supercomplex [72]. The LpqE, a N-terminal triacylated lipoprotein, the prokaryotic respiratory supercomplex association factor 1 (PRSAF1), and the SodC. LqpE and PRSAF1 has interactions with complex III and IV, providing further stability of the supercomplex [72]. SodC, sitting on top of complex III, was postulated to reduce the ROS formed, as endogenous ROS were found to be largely produced from complex III [72, 73, 228, 229]. The SodC might additionally direct electrons from superoxides back into the ETC [73]. The importance of the SodC was further highlighted from an *Mtb* strain without SodC being highly susceptible to exogenous ROS [230].

The cryo-EM structure of the *M. smegmatis* III-IV supercomplex provides insights into the electron transfer pathway within the cyt-*bcc* (Fig. 1.14) [72]. Menaquinol binds at the Q_o site and transfers its electrons, one to heme b_L, and the other to the [2Fe–2S] center. The electron at heme b_L proceeds towards heme b_H, and finally to the Q_i site where menaquinone is bound and gets reduced to menasemiquinone. A second menaquinol binds at the Q_o site, for a second electron to transfer from heme b_L, to heme b_H, and finally to the bound menasemiquinone, reducing it to menaquinol. This completes the Q-cycle. The other electron at the [2Fe–2S] center continue towards heme C_{D2} and C_{D1}, and finally gets transferred to cyt-aa_3 via the Cu_A center.

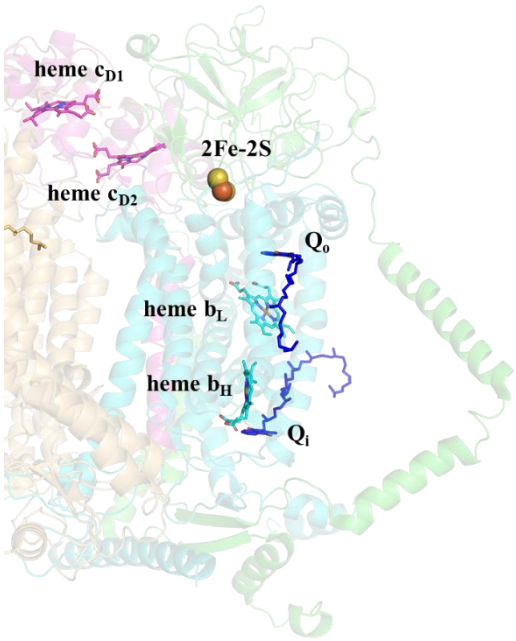

Figure 1.14: Cartoon representation of the prosthetic groups within the *M. smegmatis* III-IV supercomplex. The location of the prosthetic groups involved in electron transfer within cyt-*bcc* complex is as shown (PDB ID: 6ADQ) [72]. QcrA (green) contains the Rieske [2Fe–2S] (FeS) center, QcrB (blue) has heme b_H and b_L along with the Q_o and Qi site indicated in navy, and QcrC (magenta) has the diheme, C_{D1} and C_{D2}.

Strict regulation has to be in place to prevent short-circuiting, where both electrons from the menaquinol at the Q_o site or heme b_L are transferred to the [2Fe–2S] center, bypassing the transfer to heme b_L. This leads to a futile electron transfer and proton release to the periplasm, without contribution to the PMF [231]. Additionally, this results in an accumulation of menasemiquinone at the Q_o site, giving rise to endogenous superoxide formation [232, 233]. In the canonical cyt-bc_1 complex, the regulation was carried out by the displacement of the [2Fe–2S] center, identified in two states [234]. In the b-state, the [2Fe–2S] center is in close proximity to the Q_o site to receive electrons from menaquinol, but unable to pass it on to heme c_{D2}. A displacement of the [2Fe–2S] center then proceeds, shifting into the c_1-state, decreasing the distance between the [2Fe–2S] center and heme c_{D2} for electron transfer. However, this displacement is not favourable, as seen from the cyro-EM structure of the *M. smegmatis* III-IV supercomplex, where the QcrA subunit is held in place by QcrB and QcrC subunit [72].

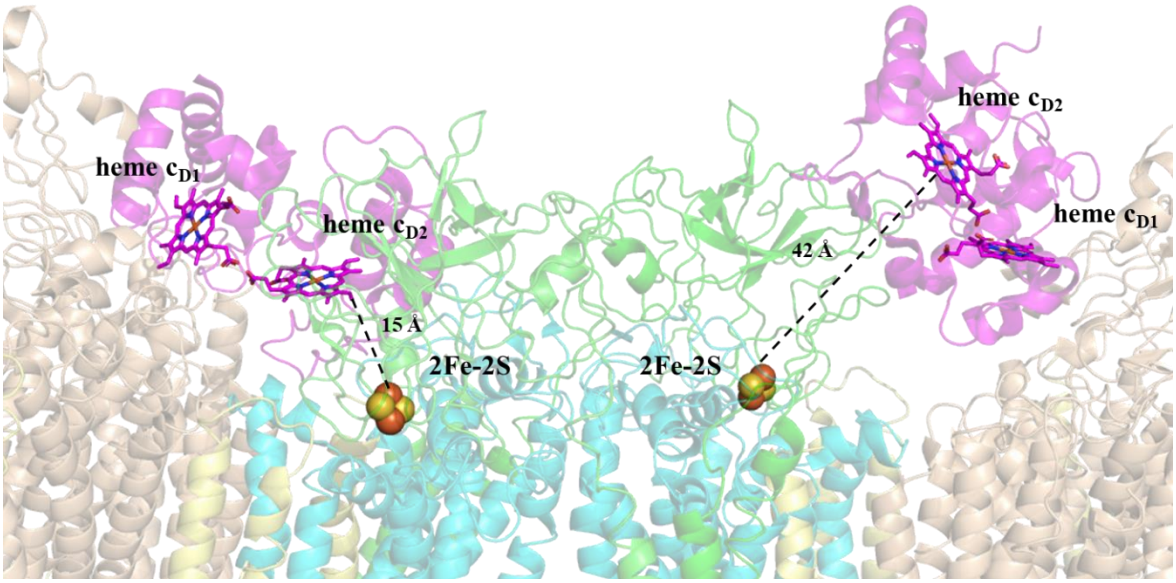

Figure 1.15: Cartoon representation of the *M. smegmatis* III-IV supercomplex, indicating the two configuration of the QcrC subunit. On the left indicates the closed configuration where the [2Fe–2S] center is within 20 Å from heme C_{D2}, allowing electron transfer towards complex IV. On the right shows the open configuration where the distance between the [2Fe–2S] center and heme C_{D2} is 42 Å. This is a possible gating mechanism to prevent short-circuting of the Q-cycle (PDB ID: 6HWH) [73].

Instead, from the cryo-EM structure by Wiseman *et al*. (2018), the authors discovered the QcrC subunit in two different configurations [73] (Fig. 1.15). One such configuration, known as the closed configuration, has the QcrC subunit lying horizontally, resting on both QcrB subunit and cyt-*aa*$_3$ (Fig. 1.15, left). In this position, it places heme C_{D2} in the QcrC subunit at a distance of 15 Å away from the 2Fe–2S center, allowing electron transfer towards cyt-*aa*$_3$. In the open configuration, the QcrC subunit appears to tilt upwards, pivoting itself on cyt-*aa*$_3$ (Fig. 1.15, right). This increases the distancce between QcrC and QcrB subunit, placing the heme C_{D2} 40 Å away from the 2Fe–2S center, preventing electron transfer towards cyt-*aa*$_3$ through heme C_{D2}. This suggested mechanism could regulate the electron transfer towards the 2Fe–2S center and eventually to cyt-*aa*$_3$, funneling the second electron from menaquinol to heme b_L, which is of a lower potential as compared to the 2Fe–2S center.

As mentioned previously, Q203 is a potent inhibitor of cytochrome *bcc* [183]. It binds within the Q_i site of the QcrB subunit, interacting directly with residue T313, possibly preventing menaquinol binding [183, 235]. Positive results in clinical trials indicated the high specificity of Q203 without adverse effects [236]. However, Q203 was found to possess only bacteriostatic activities due to the availability of an alternative terminal oxidase, cyt-*bd*, preventing killing of

Mtb [184]. Q203 becomes bactericidal on the deletion mutants of cyt-*bd*, and was additionally found to be highly bactericidal on mycobacterial species that do not harbour an alternative terminal oxidase such as *M. ulcerans* [237, 238]. Other *in-silico* studies have also identified alternatives potential cyt-*bcc* inhibitors, such as imidazothiazole carboxamides (MIC_{50} < 10 nM) and imidazopyridine ethers (MIC_{50} = 30 nM) [221, 239].

1.3.3 Drug Repurposing

The emergence of MDR-TB and XDR-TB complicated TB treatment due to the ineffectiveness of first-line antibiotics (and fluoroquinolone or second-line antibiotics in the case of XDR-TB), necessitating individualized chemotherapy of up to 18 months, with poor treatment outcomes [240]. Hence, a pressing need for the discovery of new drugs with a novel mechanism of action is essential for TB treatment. However, drug discovery for TB is challenging [241]. Only recently was the emergence of BDQ and delamanid, obtaining FDA approval in 2012 and 2013, respectively [213, 242], along with Q203, which has recently received positive results from the Phase II clinical trials [236]. Despite the effectiveness of BDQ and delamanid, a startling rate of resistance shortly after its launch was observed, especially for BDQ [33, 34, 243]. Currently, cautious use of BDQ and delamanid is in play due to the possibility of cardiotoxicity [244, 245].

With the difficulty and lengthy time required for drug discovery, drug repurposing is a strategy employed to limit risks, reduce development time, and lower development costs [246]. Examples of drug repurposing for TB include chloroquine initially indicated for malaria, and clofazimine, originally for leprosy, and currently used against MDR-TB [247]. Here, we look at an antimalarial compound, SCR0911, as it was found to be active against cytochrome bc_1 of *Plasmodium falciparum*, binding at the Q_i site [248]. Additionally, structural scaffolds of SCR0911 were determined to be cytochrome *bd* inhibitors of *Mtb* [249]. In this study, the possibility of SCR0911 binding to *cyt-bcc* and *cyt-bd* in *M. smegmatis* and *M. bovis* bacillus Calmette–Guérin (BCG) was examined, to provide hints on its inhibition in *Mtb*. Computational studies with a homology model of *Mtb cyt-bcc* will be carried out for this purpose. With a known synthesis scheme of SCR0911, antimicrobial susceptibility testing can be implemented immediately after organic synthesis. Following the results from the compounds efficiency, further computational studies can be carried out to obtain lead analogs to be synthesized, and thus allowing a structure-activity relationship (SAR) investigation [248, 250, 251].

1.3.4 An antimalarial compound, SCR0911

The structure of SCR0911 has been designed by Charoensutthivarakul *et al*. (2015), modified from the lead compounds obtained from a high-throughput screen (HTS) by Biagini G. A. (2012) [248, 252]. It was proposed that 4-(1H)-pyridones, such as SCR0911, binds to the Q_i site in the cytochrome bc_1 [253]. Furthermore, Charoensutthivarakul *et al*. have prepared a homology model of cytochrome bc_1 of *Plasmodium falciparum*, with the docking of the analog of SCR0911 [248]. The analog of SCR0911 was similar to SCR0911, except that the (trifluoromethoxy)benzene group is on para position (Fig. 1.16).

SCR0911	Analog of SCR0911 in homology model
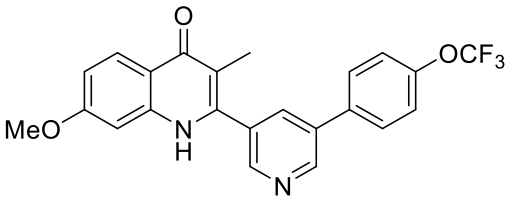	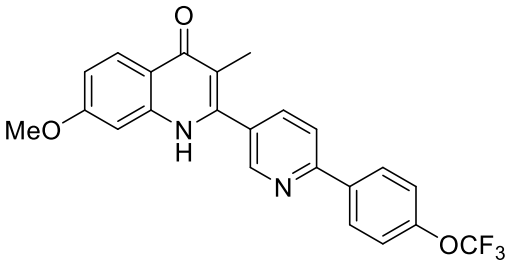

Figure 1.16: Chemical structure of SCR0911 and its analog. The analog of SCR0911 was subjected to docking in the homology model of cytochrome bc_1 of *P. falciparum* [248].

The docking study reports the binding of the SCR0911 analog to the Q_i site, which further substantiates the ability of SCR0911 to bind to the Q_i site. They discovered that quinolones have several important interactions, namely the hydrogen bonding between D218 and the NH group, along with another hydrogen bonding between S196 and the carbonyl group. The hydrophobic residues around the quinolone functional group were found to be L214, I22, F210, and W26, while the pyridyl group was interacting with F30 and H12. These functional groups were revealed to be conserved in both the cytochrome *b* of bovine and *P. falciparum*, as shown in the sequence alignment in figure 1.17, except for L214, F30 and H12, which are Y224, S35 and A17, respectively.

A crystal structure of bovine cytochrome bc_1 was published later on [254]. SCR0911 was reported to bind in the Q_i site, with hydrogen bonding to residues such as H201 and S35. These residues in *P. falciparum* was determined to be H192 and F30, respectively, in contrast to the prediction in the homology model of *P. falciparum* by Charoensutthivarakul *et al.* [248]. Other hydrophobic interactions around SCR0911 are G38, I39, and A232. In *P. falciparum* these residues were found to be G33, I34, and F222. Interestingly, despite the similar binding site of SCR0911 in *P. falciparum* and bovine, SCR0911 was revealed to have an IC_{50} of 12 nM in *P.*

falciparum, but only a 19% inhibition of the bovine heart bc_1 at 100 nM. [248]. This could be due to a different binding orientation of SCR0911.

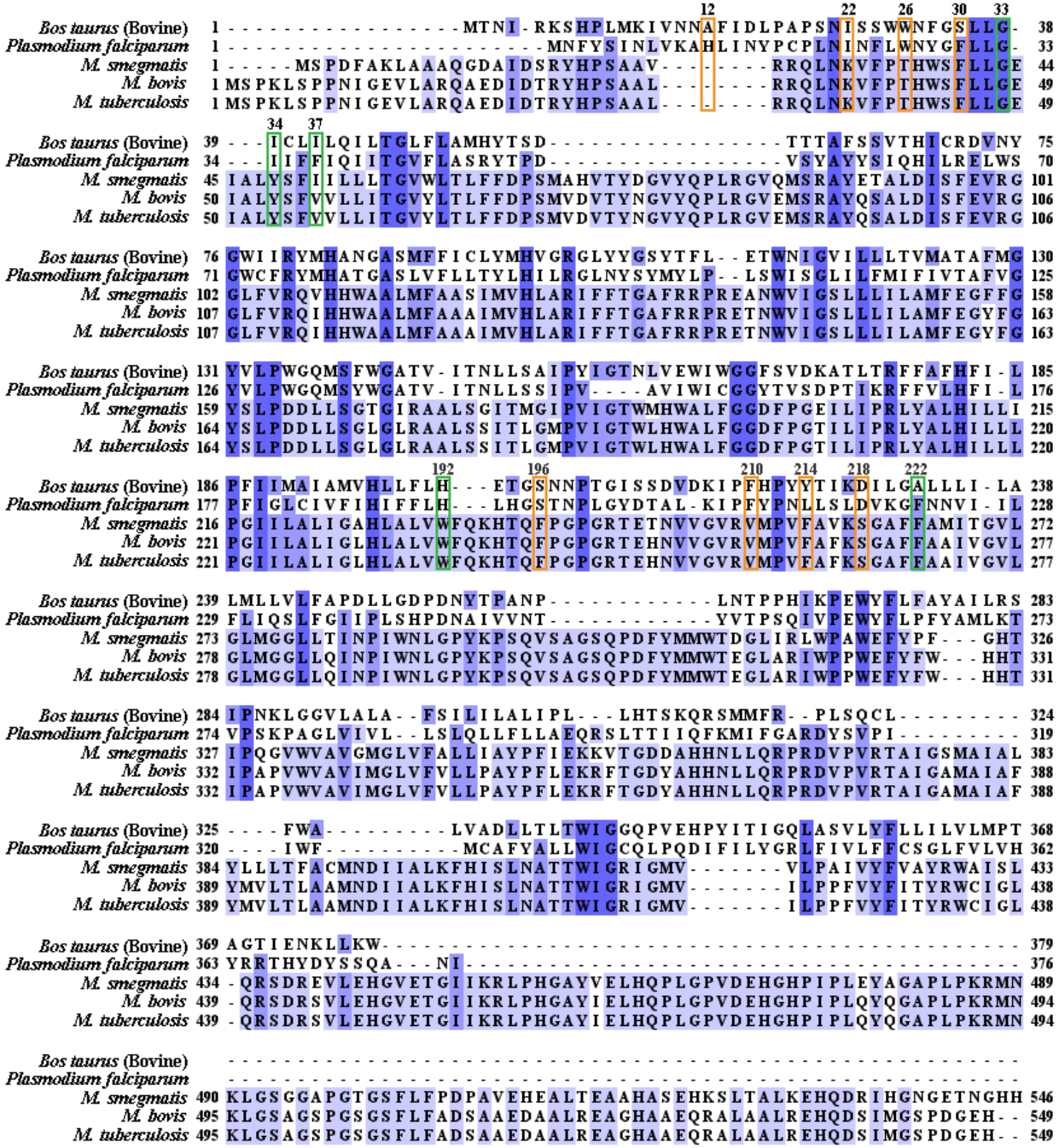

Figure 1.17: Sequence alignment of the cytochrome *b* of bovine, *P. falciparum*, *M. smegmatis*, *M. bovis*, and *Mtb*. The orange boxes indicate the residues that are significant in the *P. falciparum* homology model with the binding of the analog of SCR0911. The green boxes indicate the residues that are significant in the bovine crystal structure with the binding of SCR0911. The numbers on the boxes refers to the residue number with respect to *P. falciparum.*

As human and bovine cytochrome *b* are determined to have an approximately 80% conservation, a low inhibition of the bovine heart bc_1 could possibly translate to a lower

possibility of being toxic to humans [254]. In addition, from the sequence alignment in figure 1.17, the hydrophobic interactions found in the crystal structure of bovine cytochrome bc_1 as I39 and A232 (I34 and F222 in *P. falciparum*), are not conserved in human cytochrome bc_1, and were revealed to be A38 and L222, respectively. This could further indicate a decreased likelihood of mitochondrial toxicity in humans.

Furthermore, although the indicated residues in both the homology model of *P. falciparum* and the crystal structure of bovine cytochome *b* were shown to be mostly conserved from the sequence alignment, these residues are not conserved in the mycobacterial species, except for residue G38 in the crystal structure. Hence, it will be interesting to carry out a docking study on SCR0911 on *Mtb* cytochrome bc_1, to firstly determine if it is able to bind in the Q_i site, and to later study its ability in inhibiting the cytochrome *bcc* in mycobacterial species. In this report, the synthesis of SCR0911 was carried out for *in-vivo* and *in-vitro* testing on *M. smegmatis* and *M. bovis*. *M. smegmatis* and *M. bovis*, a fast grower and a slow grower, respectively, possess a high sequence identity towards *Mtb* (*M. smegmatis* ~75%, *M. bovis* ~ 99%), providing more valuable insights into *Mtb* as a target of SCR0911.

Aims and objectives of reseach

1.4 Goals of this thesis

*Mt*AhpC plays an important role in antioxidant defense. Previous research has shown that, especially in INH-resistant *Mtb*, ROS reduction is carried out mainly by *Mtb Mt*AhpC [102-106]. Numerous studies on AhpCs of other organisms have revealed the mechanism of AhpC to reduce peroxides [115, 119, 255, 256]. The crystal structure of the *Mt*AhpC$_{C176S}$ mutant, along with EM data on *Mt*AhpC, and deletion mutagenesis studies, have outlined several unique features of the enzyme [107, 128]. One such unique feature of *Mt*AhpC is the presence of a cavity within the protein, not found in its bacterial counterparts [107]. This cavity was postulated to be a result of a helical displacement. To gain mechanistic and strucutral insights into the hypothesized helical movement, WT *M. bovis* AhpC (*Mb*AhpC) was utilized as it shares the same amino acid composition as *Mt*AhpC. Firstly (i) site-directed mutagenesis was performed to identify critical residues, before (ii) determining the enzymatic activity of the recombinant proteins in reducing peroxides, and (iii) gaining structural information on the mutants to understand the effect of the mutations through x-ray crystallography.

Mycobacterial cytochrome *bcc*, complex III of the electron transport chain (ETC), has an essential role within the pathogen, to provide the PMF for ATP synthesis [72, 73]. During the transfer of electrons within its complex, it indirectly encourages the formation of endogenous ROS [70, 72, 73]. The significance of the complex and its relation to ROS generation intrigues us to investigate further. Cytochrome *bcc* was determined to be an attractive drug target, as can be seen from several nonselective inhibitors, the antimalarial drug, atovaquone, and Q203 that target the *Mtb* enzyme [183, 248]. It was found to be important for *Mtb* as it has been revealed that mutations on cytochrome *bcc* significantly affects the growth rate of *Mtb* [174]. A drug repurposing approach was envisioned for cytochrome *bcc*, by utilizing an antimalaria compound. The lead compound will be subjected to (i) ligand-protein docking, (ii) antimicrobial susceptibility testing, and (iii) on-target activity assay on *M. smegmatis* and *M. bovis*. In improving the lead compound for anti-tuberculosis activity, (iv) computational studies, (v) synthesis of analogs, and (vi) on-target activity assay in lead optimization will be carried out.

Materials and Methods

2. Materials and methods

2.1 Materials

2.1.1 Chemicals

All the chemicals used for the study were of at least analytical grade. Chemicals were purchased from the following companies:

Buffers and salts	Sigma-Aldrich (St. Louis, MO, USA)
	USB (Sampscott, MA)
	Fluka (Sigma, Buchs Germany)
	Roth (Karlsruhe, Germany)
	Serva (Heidelberg, Germany)
Chemicals (organic synthesis)	Sigma-Aldrich (St. Louis, MO, USA)
	TCI (Tokyo, Japan)
	Alfa Aesar (Massachusetts, USA)
	Strem Chemicals (Massachusetts, USA)
DTT	Sigma-Aldrich (St. Louis, MO, USA)
Pefabloc^{SC}	BIOMOL (Hamburg, Germany)
Agarose, SDS, glycine, APS etc.	Bio-Rad (Hercules, CA, USA)
Antibiotics	Calbiochem, Sigma, Gibco
IPTG	Gold Bio (St. Louis, MO, USA)
SF6847	Alexis Corporation (Lausen, Switzerland)

2.1.2 Molecular biology materials

Primers	IDT (Singapore)
Pfu DNA polymerase	Thermo Scientific (Waltham, MA, USA)
KAPA HIFI DNA polymerase	Kapa Biosystem (Massachusetts, USA)
BamHI, NdeI, XhoI	Fermentas (Glen Burnie, MD, USA)
T4 DNA ligase	Promega (Wisconsin, USA)
PreScission^{TM} Protease	GE Healthcare (Uppsala, Sweden)
QIAprep® Spin Miniprep Kit	QIAGEN (Hilden, Germany)
NucleoBond® AX Midiprep Kit	MACHEREY-NAGEL (Düren, Germany)

QIAquick® Gel Extraction Kit	QIAGEN (Hilden, Germany)
QIAquick® PCR Purification Kit	QIAGEN (Hilden, Germany)
E. coli plasmid propagation strain	DH5α
E. coli protein production strain	BL21(DE3)

2.1.3 Chromatography

2.1.3.1 Affinity chromatography

Ni-NTA	Sigma-Aldrich (St. Louis, MO, USA)

2.1.3.2 Size exclusion chromatography and anion exchange chromatography

Superdex 75 10/300 GL	GE Healthcare (Uppsala, Sweden)
HiLoad 16/600 Superdex 75 pg	GE Healthcare (Uppsala, Sweden)
Superdex 200 10/300 GL	GE Healthcare (Uppsala, Sweden)
Superdex 200 Increase 10/300 GL	GE Healthcare (Uppsala, Sweden)
Mono Q 10/100 GL	GE Healthcare (Uppsala, Sweden)

2.1.3.3 Instruments and Accessories

ÄKTA FPLC	GE Healthcare (Uppsala, Sweden)
ÄKTA Pure	GE Healthcare (Uppsala, Sweden)
Syringe, needles, and accessories	BD Biosciences
Minisart® Filters (0.45 μm)	Sartorius Stedim Biotech (Göttingen, Germany)

2.1.3.4 Protein Concentration Estimation

BioSpec-Nano micro-volume spectrophotometer	Shimadzu Corporation (Kyoto, Japan)
Pierce™ BCA Protein Assay Kit	Pierce (Rockford, IL, USA)
Amicon Ultra (10, 30, 50 kDa)	Millipore (Co-cork, Ireland)
Vivacon 500 (10, 50 kDa)	Sartorius Stedim Biotech (Göttingen, Germany)

2.1.4 Other instruments

Biometra T personal PCR thermocycler	Biometra (Göttingen, Germany)
Biometra T gradient PCR thermocycler	Biometra (Göttingen, Germany)
Sonoplus HD2200 ultrasonicator	Bandelin (Berlin, Germany)
Micropulser Electroporator	Bio-Rad (Hercules, CA, USA)
Ultraspec 2100Pro Spectrophotometer	GE Healthcare (Uppsala, Sweden)
MetalJet-NANOSTAR	Bruker AXS (Karlsruhe, Germany)
Infinite Pro 200 Plate Reader	Tecan (Männedorf, Switzerland)
Cary Eclipse Fluorescence Spectrophotometer	Varian Inc (California, USA)
Ultrospec 2100 Pro UV–visible Absorption Spectroscopy	Amersham Biosciences (New Jersey, USA)
SX20 Stop-flow Spectrometer	Applied Photophysics (Surrey, UK)
Ultrasonic Homogenizer	Bandelin (Berlin, Germany)
Microfluidizer LM20	Analytik (Cambridge, UK)

2.1.5 Biological assay test kits and accessories

PeroxiDetect™ Kit	Sigma-Aldrich (St. Louis, MO, USA)
BacTiter-Glo™ Microbial Cell Viability Assay kit	Promega (Wisconsin, USA)
CellTiter-Glo® Luminescent Cell Viability Assay kit	Promega (Wisconsin, USA)
BD GasPak™ EZ anaerobic jar	BD (New Jersey, USA)
GasPak™ EZ anaerobe paper sachet	BD (New Jersey, USA)
BD BBL™ dry anaerobic indicator strips	BD (New Jersey, USA)
96-well flat-bottom Costar™ cell culture plates	Corning (New York, USA)
white flat-bottomed 96-well microtiter plates	Corning (New York, USA)

2.1.6 Computer software

Serial Cloner v2.6.1	© Franck Perez (SerialBasics)
PyMOL v1.8	Schrödinger, LLC (Portland, Oregon, USA)
OriginPro 9	OriginLab (Northampton, MA, USA)

Coot	Emsley and Cowtan, 2004 [257]
HKL2000 package	Otwinowski and Minor, 1997 [258]
Refmac5 (CCP4 package)	Murshudov *et al*., 1997 [259]
PROCHECK	Laskowski *et al*., 1993 [260]
Ramachandran plot	Ramachandran *et al*., 1963 [261]
UCSF Chimera	Pettersen *et al*., 2004 [262]
PHENIX	Adams *et al*., 2010 [263]
GraphPad Prism 7.00	GraphPad Software (California, USA)
Ligplot+	Laskowski and Swindells, 2011 [264]
GOLD 5.6.3	Jones *et al*., 1997 [265]
PHASER	McCoy *et al*., 2007 [266]
AutoDock 4.2	Morris *et al*., 2009 [267]

2.2 Methods

2.2.1 Site Directed Mutagenesis

To identify critical residues involved in the redox oligomerization and the enzymatic activity of the protein, site directed mutagenesis was carried out, following the steps as shown below.

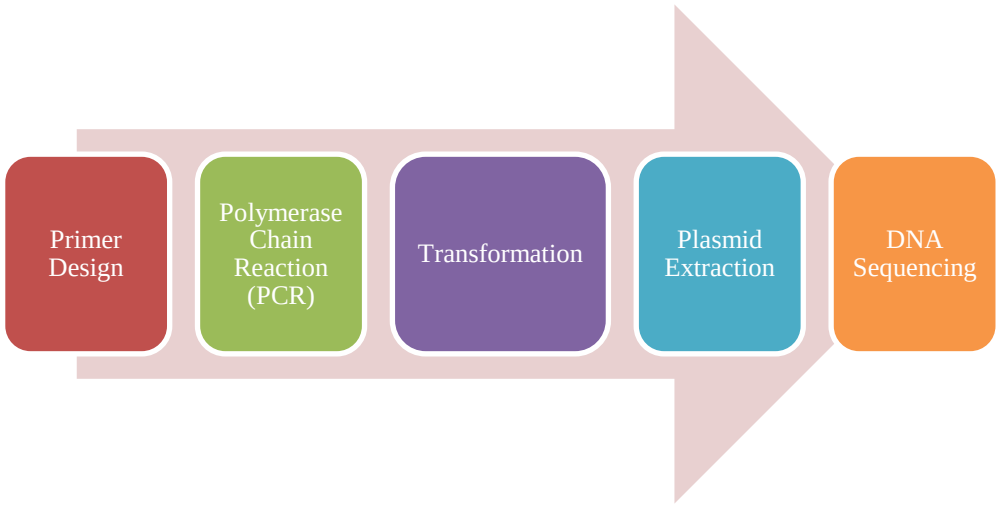

Figure 2.1: Steps taken for site-directed mutagenesis.

2.2.1.1 Primer Design

Based on the sequence alignment, the following mutations were made as shown in table 2.1.

Amino Acid	A (66)	A (67)	F (68)	A (92)	C (176)
DNA	GCG	GCG	TTC	GCG	TGC

Mutated Amino Acid	G (66)	D (67)	V (68)	R (92)	S (176)
DNA	GGA	GAT	GTA	CGG	AGC

Table 2.1: Mutations in amino acids prepared for site-directed mutagenesis.

The first three constructs made were *Mb*AhpC$_{A66G/A67D/F68V}$, *Mb*AhpC$_{A67D/F68V}$, and *Mb*AhpC$_{A7D}$ using the In-Fusion site directed mutagenesis [268], which requires an addition of at least 15 base pairs (bp) overlap on the primers, excluding the mutated regions (table 2.2). The primers were ordered from IDT (Integrated DNA Technologies, USA).

Primer Sequence		
***Mb*AhpC$_{A66G/A67D/F68V}$**	Forward	5'-AGA TCG GAG ATG TAA GCA AGC TCA ATG ACG AGT TC-3'
	Reverse	5'- GCT TAC ATC TCC GAT CTC GGT AGG GCA CAC G-3'
***Mb*AhpC$_{A67D/F68V}$**	Forward	5'-ATC GCG GAT GTA AGC AAG CTC AAT GAC GAG TTC-3'
	Reverse	5'-TTG CTT ACA TCC GCG ATC TCG GTA GGG CA-3'
***Mb*AhpC$_{A67D}$**	Forward	5'-GCG GAT TTC AGC AAG CTC AAT GAC GAG T-3'
	Reverse	5'-GAA ATC CGC GAT CTC GGT AGG GCA-3'

Table 2.2: Primers designed for site-directed mutagenesis for *Mb*AhpC$_{A66G/A67D/F68V}$, *Mb*AhpC$_{A67D/F68V}$, and *Mb*AhpC$_{A7D}$.

Following that, two additional constructs were prepared: *Mb*AhpC$_{F68V}$ and *Mb*AhpC$_{A92R}$. The primer sequence order is shown in table 2.3.

Primer Sequence		
***Mb*AhpC$_{F68V}$**	Forward	5'-GCG GTA AGC AAG CTC AAT GAC GAG TTC G-3'
	Reverse	5'-TGC TTA CCG CCG CGA TCT CGG TAG-3'
***Mb*AhpC$_{A92R}$**	Forward	5'-TTC CGG CAT TTC CAG TGG CGT GCA C-3'
	Reverse	5'-AAT GCC GGA ATT CGC TGT CAA TCG AAA CC-3'

Table 2.3: Primers designed for site-directed mutagenesis for *Mb*AhpC$_{F68V}$ and *Mb*AhpC$_{A92R}$.

For crystallization of the mutant proteins, an additional cysteine mutant was incorporated to prepare the following mutants: *Mb*AhpC$_{A7D/C176S}$ and *Mb*AhpC$_{F68V/C176S}$. These constructs were prepared using the *Mb*AhpC$_{A7D}$ and *Mb*AhpC$_{F68V}$ as the template DNA, with the primer encoding the mutation for C176S (table 2.4).

Primer Sequence		
***Mb*AhpC$_{C176S}$**	Forward	5'-CGC AAG CAA CTG GCG CAA GG-3'
	Reverse	5'- TTG CTT GCG CAC AGC TCG TC-3'

Table 2.4: Primers designed for site-directed mutagenesis for *Mb*AhpC$_{A7D/C176S}$, *Mb*AhpC$_{F68V/C176S}$, and *Mb*AhpC$_{A92R/C176S}$.

2.2.1.2 Polymerase Chain Reaction (PCR)

The pET-9d plasmid containing full-length *Mb*AhpC (pET-9d-*Mb*AhpC) and Histidine$_6$-tag was generously provided by Mr. Arvind Kumar from Professor Gerhard Grüber's laboratory (SBS, NTU) [128].

Component	Final conc.	Vol. of component for 50 µl of reaction mixture (µl)
Water, nuclease-free	-	34.5
5x HiFi GC buffer	1x	10
10 mM dNTP mix	0.2 mM of each	1.0
Forward primer (100 µM)	2 µM	1.0
Reverse primer (100 µM)	2 µM	1.0
Template DNA	10 ng	1.0
KAPA HiFi DNA polymerase	6 U	1.5

Table 2.5: Components for PCR reaction.

The PCR reaction was set up on ice, with the components listed in table 2.5. GC-buffer was used for all reactions, except in the preparation of the *Mb*AhpC$_{A92R}$. In *Mb*AhpC$_{A92R}$ the GC-buffer did not yield successful PCR products. Hence, HF-buffer was used instead. KAPA HiFi DNA polymerase was added as the last component. The mixture was immediately placed in the PCR thermocycler that was preheated to 95 °C. The programme was set as shown in table 2.6.

No.	Step	Cycles	Temp.	Time
I	Initial Denaturation	1	98 °C	2 min
II	1. Denaturation	20	98 °C	20 s
III	2. Primer annealing	20	Varying temperatures	15 s
IV	3. Primer extension	20	72 °C	3 min
V	Final extension	1	72 °C	7 min

Table 2.6: PCR thermocycler programme for *Mb*AhpC constructs.

For optimization, four or five gradient primer annealing temperatures were set on the PCR thermocycler as shown in table 2.7.

Constructs	Annealing Temperatures
***Mb*AhpC$_{A66G/A67D/F68V}$**	66, 67.3, 68.6, 70, 71.3 °C
***Mb*AhpC$_{A67D/F68V}$**	50, 54, 61.2, 65.9 °C
***Mb*AhpC$_{A67D}$** ***Mb*AhpC$_{F68V}$**	54.7, 60.9, 65.2, 70.6 °C
***Mb*AhpC$_{A92R}$**	50, 54, 61.2, 65.9, 70 °C
***Mb*AhpC$_{A67D/C176S}$** ***Mb*AhpC$_{F68V/C176S}$**	58.8, 61.2, 63.6, 65.9°C

Table 2.7: Gradient PCR annealing temperatures.

The PCR thermocycler was set to remain at 4 °C after the final extension until the PCR products are removed. To determine the presence and purity of the gene products, 5 µl of each PCR reaction mixture from the different primer annealing temperatures were subjected to analysis with a 1.5% agarose gel, running at 100 V. The fragment size was confirmed using the standard GeneRuler 1 kb ladder (ThermoScientific). Following this, the gene product would then be subjected to further treatment before transformation into *E. coli* cells.

2.2.1.1 DpnI treatment and DNA precipitation

To remove the methylated template DNA, DpnI treatment was carried out. The components were added as shown in table 2.8. The sample was incubated at 37 °C for 1 hour, and thereafter, subjected to heat at 80 °C for 20 minutes to inactivate the enzyme. Subsequently, the sample was cooled to room temperature before DNA precipitation. The latter was carried out to facilitate desalting and concentration of the DpnI treated product. 10 µl of the DpnI treated product was added to 90 µl of filtered and distilled water. 1 ml of 100% butanol was then added to the sample before subjecting to centrifugation at 13,000 rpm for 5 minutes. The supernatant was discarded thereafter. Subsequently, 200 µl of 70% ethanol was added to remove excess butanol. The mixture was centrifuged again at 13,000 rpm for 5 minutes, and the supernatant was discarded.

The pellet was left under the biosafety cabinet to air dry any remaining ethanol present. Following which, 6 µl of sterile water was added to the precipitated DNA and left on ice before transformation.

Component	Final conc.	Vol. of component for 50 µl of reaction mixture
Water, nuclease-free	-	34.0
10x CutSmart buffer	1 x	5.0
DpnI (NEB)	0.2 mM of each	1.0
PCR product	-	10.0

Table 2.8: Components for DpnI reaction.

2.2.2 Transformation into *E. coli* DH5α cells

The electrocompetent *E. coli* DH5α cell strain was thawed on ice for 5 minutes before addition to the precipitated DNA. A Micropulser Electroporator (Bio-Rad, USA) at 2,500 V was used to transform the precipitated DNA into electrocompetent *E. coli* DH5α cell strain. 1 ml of LB (Luria-Bertani) media was added to collect the electroporated cells, and the transformed cells were incubated at 37 °C, 180 rpm for 1 hour. 150 µl of the cell suspension was plated onto an LB plate supplemented with kanamycin antibiotics (30 µg/ml) and left to incubate at 37 °C overnight.

2.2.3 Plasmid Extraction

Five different colonies from the agar plates were inoculated into 5 ml of LB media, supplemented with kanamycin antibiotics (30 µg/ml) and subsequently, incubated at 37 °C, 180 rpm, overnight. After overnight incubation, 2 ml of each of the cell suspensions were obtained, and the cells were subjected to centrifuge at 13,000 rpm for 5 minutes. Plasmid extraction and isolation were carried out on the pellet, following the protocol provided by QIAGEN Mini-Prep Kit (QIAGEN, Germany). The sequences of the selected plasmid were confirmed by DNA sequencing (1st Base, Singapore).

2.2.4 Transformation into *E. coli* BL21(DE3) expression cell strain

After analyzing the DNA sequence, transformation of the isolated DNA plasmid was carried out. Electrocompetent *E. coli* BL21(DE3) cell strain was thawed on ice for 5 minutes. 1 µl of the DNA plasmid was added to the *E. coli* BL21(DE3) cells and transformation of the precipitated

DNA was performed with the Micropulser Electroporator (Bio-Rad, USA) at 2,500 V. 1 ml of LB media was then added to collect the electroporated cells and the transformed cells were incubated at 37 °C, 180 rpm for 1 hour. 150 µl of the cell suspension were plated onto a LB plate supplemented with kanamycin antibiotics (30 µg/ml) and incubated at 37 °C overnight.

2.2.5 Protein Purification

Following fresh transformation of pET-9d-*Mb*AhpC mutants into *E. coli* BL21(DE3) cells as mentioned in section 2.2.4, the cells were first cultured in an overnight culture, containing 30 ml LB medium with kanamycin antibiotics (30 µg/ml). The OD_{600} was measured, and the overnight culture was added to a large volume of LB medium with kanamycin antibiotics (30 µg/ml), with a starting OD_{600} = 0.1. Once the OD_{600} reaches approximately 0.6, the cells were then induced with 1 mM isopropyl β-d-1-thiogalactopyranoside (IPTG) and incubated at 20 °C, 180 rpm overnight. The cells were harvested at 4 °C, 6,500 g for 12 minutes, using Beckman Coulter Avanti J-26XP Centrifuge (Beckman Coulter, USA) and JLA-9.1000 rotor. To ensure the purity of the proteins, all proteins were purified in a two-step purification method. The first, involves affinity chromatography. As His_6-tag was cloned into the recombinant proteins, Ni-NTA (nickel-nitrolotriacetic acid) affinity chromatography was used for purification of these proteins. After affinity chromatography, the second step of purification utilizes size exclusion chromatography (SEC).

2.2.5.1 Purification of $MbAhpC_{A66G/A67D/F68V}$, $MbAhpC_{A67D/F68V}$, $MbAhpC_{A67D}$, $MbAhpC_{F68V}$ and $MbAhpC_{A92R}$ in oxidized conditions

2 g of cells were re-suspended in 30 ml of buffer A (50 mM Tris/HCl, pH 7.5, 200 mM NaCl). 2 mM Pefabloc^{SC} was also added prior to sonication to initiate cell lysis. Sonication was performed three times with one-minute interval each time, with the sonicator tip, KE76, at 25% power. The cell suspension was then centrifuged at 12,000 g for 25 minutes at 4 °C with an Eppendorf 5810R Centrifuge (Eppendorf, Germany). Subsequently, the supernatant was filtered with a 0.4 µm filter and incubated for 1 hour with 1 ml of Ni-NTA agarose beads on a spinning wheel at 4 °C. Elution was performed with the imidazole-gradient as shown in table 2.9. Ethylenediaminetetraacetic acid (EDTA) was added in the elution vials to remove the presence of any free nickel ions. 12 µl of protein sample at each elution was analyzed with a 17% SDS-PAGE gel to identify the fractions at which the proteins elute out. The fractions containing the eluted proteins were then pooled and concentrated with Centricon (10 kDa molecular mass cut

off; Millipore, Ireland) spin concentrators, and thereafter, subjected to SEC (Superdex 200 Increase 10/300 GL; GE Healthcare, Sweden) which was pre-equilibrated with buffer A. The purity of the protein eluted was analyzed with a 17% SDS-PAGE gel, by the method of Laemmli [269].

	Volume [ml]	Imidazole conc. [mM]	Buffer A [µl]	2 M Imidazole [µl]	500 mM EDTA [µl]
1	15	20	14,850	150	-
2	2	50	1,950	50	40
3	2	100	1,900	100	40
4	2	125	1,875	125	40
5	2	250	1,750	250	40
6	2	300	1,700	300	40
7	2	400	1,600	400	40
8	2	600	1,400	600	40

Table 2.9: Elution profile of Ni-NTA in oxidized conditions.

2.2.5.2 Purification of MbAhpC$_{A66G/A67D/F68V}$, MbAhpC$_{A67D/F68V}$, MbAhpC$_{A67D}$, MbAhpC$_{F68V}$ and MbAhpC$_{A92R}$ in reduced conditions

A similar procedure for the purification of proteins in the reduced conditions is utilized, except with an addition of 0.8 mM dithiothreitol (DTT) in the elution of proteins in affinity chromatography. The components of the elution buffers are shown in table 2.10.

	Volume [ml]	Imidazole conc. [mM]	Buffer A [µl]	2 M Imidazole [µl]	1.25 M DTT [µl]	500 mM EDTA [µl]
1	15	20	14,840.4	150	9.6	-
2	2	50	1,948.72	50	1.28	40
3	2	100	1,898.72	100	1.28	40
4	2	125	1,873.72	125	1.28	40
5	2	250	1,748.72	250	1.28	40
6	2	300	1,698.72	300	1.28	40
7	2	400	1,598.72	400	1.28	40
8	2	600	1,398.72	600	1.28	40

Table 2.10: Elution profile of Ni-NTA in reduced conditions.

2.2.5.3 Purification of MbAhpC$_{A67D}$, MbAhpC$_{F68V}$, MbAhpC$_{A67D/C176S}$ and MbAhpC$_{F68V/C176S}$

Purification for protein crystallization was performed in the absence of reducing agents, following the procedures in section 2.2.5.1. However, as the presence of salt in the buffer promotes solubility, buffer B (20 mM Tris/HCl, pH 7.5) was utilized instead during SEC.

2.2.5.4 Purification of MbAhpC$_{A67D/C176S}$ with anion exchange chromatography

Purification of *Mb*AhpC$_{A67D/C176S}$ was carried out with a three-step purification method, to further increase the purity of the proteins for crystallization. The protocol for purification follows that as mentioned in section 2.2.5.1, with an additional an anion exchange chromatography (Mono Q 10/100 GL; GE Healthcare, Sweden) before SEC. The anion exchange chromatography uses a salt gradient for protein elution, with buffer B (20 mM Tris/HCl, pH 7.5) as a start buffer and buffer C (buffer B with 1 M NaCl) as an elution buffer. The column was set to run at 5% of buffer B prior to injection, and following injection of sample, the column was set to reach 100% of buffer B in 15 column volumes. The eluted proteins were then concentrated with Centricon (10 kDa molecular mass cut off; Millipore, Ireland) spin concentrators, and thereafter, subjected to SEC (Superdex 200 Increase 10/300 GL; GE Healthcare, Sweden) which was pre-equilibrated with buffer B.

2.2.5.5 Purification of MbTrxC and *MbTrxR*

Purification of *Mb*TrxC and *Mb*TrxR was carried out in accordance with Section 2.2.5.1. However, the proteins were concentrated using Centricon (3 kDa cut-off, Millipore, Ireland) spin concentrators and subjected to a SEC (Superdex 75 10/300 GL; GE Healthcare, Sweden) column instead.

2.2.6 Dynamic Light Scattering (DLS)

Malvern Zetasizer Nano ZS spectrophotometer (Malvern, UK) was employed for the DLS data measurements. 30 µl of the purified recombinant proteins were added into a low-volume quartz batch cuvette (ZEN2112), and data collections were performed at 25 °C, with a 60 s equilibration time and at 173° backscattering. The analysis of the scattering intensities was carried out with the in-built Zetasizer software v7.01 to calculate the hydrodynamic diameter (D_H), size and volume distribution of the protein samples.

2.2.7 Enzymatic Assay

Peroxidase-dependent activity of the two purified *Mb*AhpC mutant proteins were measured by coupling its activity with NADPH ($\varepsilon 280 = 6220 M^{-1}S^{-1}$), thioredoxin reductase (*Mb*TrxR) and thioredoxin (*Mb*TrxC), using a SX20 Stop-flow spectrometer (Applied Photophysics, UK). Two reaction mixtures were set up. The first contained 50 mM Hepes Buffer, 100 mM ammonium

sulfate, 1.0 mM EDTA, 0.5 μM *Mb*TrxR, 4 μM *Mb*TrxC, and 6 μM *Mb*AhpC. The second reaction mixture contains 0.05 mM H_2O_2. The two reaction mixtures were applied to the stopped-flow spectrophometer SX20, to obtain the time-resolved data at 25 °C (Fig. 4.3). The decrease in NADPH-absorbance at 340 nm for 120 s was recorded. Herein, the decrease in NADPH-absorbance is proportional to the activity of the proteins. The experiment has been carried out on three replicates and the error bars represent the standard deviations.

2.2.8 Enzyme kinetics analysis

To obtain the full Michaelis-Menten plot of the proteins, a full enzymatic kinetics assay was performed. All conditions were kept identical as mentioned in section 2.2.7. However, instead of only utilizing 0.05 mM H_2O_2, varying concentrations of H_2O_2 from 250 nM to 100 μM was utilized. The rate of reaction was plotted against the concentration of substrate using Origin Pro 9 (OriginLab, USA), yielding the Michaelis-constant (K_m) and turnover number (k_{cat}), which provides information on the enzymatic activity of the mutants. The experiment has been carried out on three replicates and the error bars represent the standard deviations.

2.2.9 Ferrous Oxidation-Xylenol Orange (FOX) Assay

FOX reagent was prepared by mixing ferrous ammonium sulfate reagent and aqueous peroxide color reagent in the ratio of 1:100 (PeroxiDetect™ Kit; Sigma Aldrich, United States). A series of known concentrations of H_2O_2 was prepared and 10 μl of the H_2O_2 solution was added to 200 μl of the FOX reagent. The overall mixture was vortexed and incubated for 30 minutes. Subsequently, the absorbance of the H_2O_2 complex was measured at 560 nm. A standard curve was then plotted using these results. A control was prepared with the addition of 100 μM DTT and 100 μM H_2O_2. 10 μl of the solution was added to 200 μl of the FOX reagent at specific intervals. The overall mixture was vortexed and incubated for 30 minutes. Subsequently, the absorbance was also measured at 560 nm. The values were then plotted to obtain the peroxide concentration versus time.

The enzymatic assay then proceeded with the addition of 5 μM of the protein of interest, along with 100 μM DTT and 100 μM of H_2O_2. In an identical manner following the protocol for the control, the decline in absorbance was measured. The values were then plotted to obtain the peroxide concentration versus time. The experiment has been carried out on three replicates and the error bars represent the standard deviations.

2.2.10 Crystallization of *Mb*AhpC$_{A67D}$, *Mb*AhpC$_{F68V}$, *Mb*AhpC$_{A67D/C176S}$ and *Mb*AhpC$_{F68V/C176S}$

To gain structural insights into the *Mb*AhpC mutants, the purified recombinant proteins were concentrated to various concentrations using a Centricon (10 kDa molecular mass cut-off; Millipore, Ireland) spin concentrators. *Mb*AhpC$_{A67D}$ was concentrated to 4 mg/ml, 7.5 mg/ml and 12 mg/ml. *Mb*AhpC$_{F68V}$ was concentrated to 3 mg/ml, 7 mg/ml and 16 mg/ml, *Mb*AhpC$_{A92R-1}$ was concentrated to 3 mg/ml and *Mb*AhpC$_{A92R-2}$ was concentrated to 5 mg/ml, 10 mg/ml and 19 mg/ml. Proteins with the cysteine mutations such as *Mb*AhpC$_{A67D/C176S}$ was concentrated to 3 mg/ml, 7 mg/ml, 14 mg/ml and 22 mg/ml, *Mb*AhpC$_{F68V/C176S}$ was concentrated to 7 mg/ml, 15 mg/ml, 22 mg/ml and 37 mg/ml whereas *Mb*AhpC$_{A92R/C176S}$ was concentrated to 3.3 mg/ml, 6 mg/ml, 13 mg/ml and 16 mg/ml.

Crystal drops were set-up using vapour diffusion in the conditions originally published, with 0.1 M sodium citrate, 16% ammonium sulfate, at pH 6.0 [107]. Further optimizations were carried out by systemically varying the concentration of ammonium sulfate, pH, protein concentration, and overlaying with paraffin/silicon oil. As the results yielded were not optimal for crystal growth and diffraction, further screening was performed with Additive Screen (Hampton Research, United States), and crystal screening using Hampton screen I, Hampton screen II and Wizard screen II. Cryo-protectant solution was optimized by varying the percentages of glycerol. The final optimized crystals were quickly dipped in cryo-protectant solution and were flash frozen in liquid nitrogen at 100 K. Optimized crystals were tested in-house at 100 K on a Rigaku RAXIS IV image plate detector with a Rigaku RA-Micro 7 HFM rotating copper anode generator (Rigaku/MSC).

As the crystals obtained were not diffracting sufficiently, purification of *Mb*AhpC$_{A67D/C176S}$ with an additional anion exchange chromatography was carried out, as mentioned in section 2.2.5.4. *Mb*AhpC$_{A67D/C176S}$ was concentrated to 4 mg/ml and 8 mg/ml and crystal drops were set-up using vapour diffusion with the conditions of 0.1 M sodium citrate, 16% ammonium sulfate, at pH 6.4. Further optimizations were carried out by systemically varying the concentration of ammonium sulfate, pH, protein concentration, and overlaying with paraffin/silicon oil. As the results yield promising crystals, drops were set up with varying concentration of proteins and with drop variation of protein: reservoir (1:1, 1.5:1, 2:1, 2.5:1 and 3:1) to obtain larger crystals. Cryo-protectant solution was optimized by varying the percentages of glycerol. The final

optimized crystals were quickly dipped in cryo-protectant solution containing 30% glycerol and were flash frozen in liquid nitrogen at 100 K.

2.2.11 Data collection and structure determination

A single wavelength dataset was collected at 100 K, beamline 13B1 of the National Synchrotron Radiation Research Center (NSRRC, Hsinchu, Taiwan) using an ADSC Quantum 315 CCD detector by remote control. The diffraction data were indexed, integrated and scaled using HKL2000 suite [258]. Oxidized *Mb*AhpC$_{A67D/C176S}$ crystals belong to the hexagonal space group P622 with the unit cell parameters, $a = b = 137.55$ Å, $c = 96.842$ Å and $\alpha = \beta = 90°$, $\gamma = 120°$. The asymmetric unit contains two molecules with the solvent content of about 60%. The crystallographic structure of oxidized *Mt*AhpC$_{C176S}$ (PDB ID: 2BMX) [107] was used as a model for molecular replacement by the program PHASER [266]. PHENIX [263] was used for the refinement and a reference model (PDB: 2BMX), was employed to improve the quality of the structure during refinement [107]. The model building was performed with Coot [257] and the figures were generated using PyMOL [270].

2.2.12 Homology modelling of *Mtb* cyt-*bcc*

The *Mtb* cyt-*bcc*-model was generated using homology modelling within the SWISS-MODEL server [271]. The program accepts the target amino acid sequence and searches for evolutionary related protein structures against the template library SMTL using BLAST [272] and HHblits [273]. The templates were then ranked based on global model quality estimate (GMQE) and quaternary structure quality estimate (QSQE). Finally, the 3D model of the *Mtb* cyt-*bcc* was generated with the *M. smegmatis* EM structure (PDB ID: 6ADQ; [11]) as a template and using ProMod3 modelling engine that first transfers conserved atom coordinates defined by the target-template alignment [72]. Afterwards, insertions/deletions were constructed using loop modelling. The heme groups were manually modelled into the *Mtb* complex, the individual subunits were assembled to generate a monomer, and a dimer model was created based on the *M. smegmatis* EM structure (PDB ID: 6ADQ).

2.2.13 Docking studies of SCR0911 with *Mtb* cyt-*bcc*

Docking studies were carried out for SCR0911 with the homology model of *Mtb* cyt-*bcc*. The three-dimensional structure of SCR0911 was retrieved from the crystal structure of bovine

cytochrome bc_1 complex (PDB ID: 5OKD) [254]. The SCR0911 was docked into the model of *Mtb* cyt-*bcc* -using AutoDock 4.2 [267]. Autodock is a computational docking program which is based on the Lamarckian Genetic Algorithm search method and an empirical free energy scoring function. The free-energy scoring function is based on a linear regression analysis, the AMBER force field, and a larger set of diverse protein-ligand complexes with known inhibition constants. The program consists of two parts, AutoDock for docking of the ligand to a set of grids describing the target protein; and AutoGrid for pre-calculating these grids. The 100 protein-ligand complex models scored based on the weighted sum of steric interactions, hydrophobic interaction, and hydrogen bonding were analyzed. The complex configurations were then clustered based on the results by conformational similarity, visualizing conformations, visualizing interactions between ligands and proteins, and visualizing the affinity potentials created by AutoGrid. The best model with the highest score from each cluster was selected for further analysis. The model was visualized using PyMOL [270], and the interactions profile was represented using LIGPLOT [274].

2.2.14 Minimum inhibitory concentration determination

The growth inhibition dose-response assay was carried out using the broth microdilution method, as described previously [275, 276]. Briefly, clear 96-well flat-bottom Costar cell culture plates (Corning, US) were filled with 100 µl of complete 7H9 medium supplemented with albumin–dextrose–catalase (ADC), without glycerol, in each well. Each compound was added to the first well in each row to create two times the desired highest final concentration. Subsequently, a 10-point 2-fold serial dilution was carried out starting from the first well in each row. *M. bovis* BCG, *M. smegmatis* mc^2155- and the isogenic *M. smegmatis* strain ZCW111 Δ*bcc* mutant (kindly provided by Professor Gregory M. Cook, Department of Microbiology and Immunology, School of Biomedical Sciences, University of Otago, Dunedin 9054, New Zealand [277]) used for the assays were grown to mid-log phase in complete 7H9 medium. The cells were washed with glycerol-free 7H9 media and subsequently diluted to an OD_{600} of 0.1 and 0.01, respectively. 100 µl of the diluted culture was added to each well to create a final OD_{600} of 0.05 and 0.005 for *M. smegmatis* and *M. bovis* BCG respectively, in all wells. For *M. smegmatis* strains, the plates were incubated at 37 °C on an orbital shaker set at 180 rpm for 24 hours. For *M. bovis* BCG strains, the plates were incubated at 37 °C without shaking for 7 days. At the end of the incubation period, the culture in all wells was manually resuspended, and the OD_{600} was

read using an Infinite Pro 200 plate reader (Tecan, Switzerland). The MIC_{50} reported represents the concentration that inhibits 50% of growth compared to the untreated culture. The experiment has been carried out on two biological replicates and the error bars represent the standard deviations.

2.2.15 Intracellular ATP synthesis assay

The intracellular ATP synthesis assay was carried out using the broth microdilution method as described previously, using the BacTiter-Glo™ Microbial Cell Viability Assay kit (Promega, US) to quantify the intracellular ATP [275, 276, 278]. Clear 96-well flat-bottom Costar cell culture plates (Corning, US) were filled with 100 µl of complete 7H9 medium supplemented with albumin−dextrose−catalase (ADC), in each well. Each compound was added to the first well in each row to create two times the desired highest final concentration. Subsequently, a 10-point 2-fold serial dilution was carried out starting from the first well in each row. *M. bovis* BCG stains were grown in complete 7H9 medium to mid-log phase and subsequently diluted to an OD_{600} of 0.1. 100 µl of the diluted culture was added to each well to create a final OD_{600} of 0.05 in all wells. The plates were incubated at 37 °C on an orbital shaker set at 110 rpm for 24 hours. 50 µl of samples (total culture) were mixed with an equal volume of freshly prepared BacTiter-Glo™ reagent in white flat bottomed 96 well plates (Corning) and lysis was carried out for 10 min at room temperature with shaking at an amplitude of 3 mm inside the TECAN Infinite Pro 200 plate reader. Emitted luminescence was displayed as relative light units (RLU). The experiment has been carried out on two biological replicates and the error bars represent the standard deviations.

2.2.16 Production of *M. smegmatis* inverted membrane vesicles (IMVs)

IMVs were prepared as previously described by Hotra *et al*. (2016) [206]. In essence, cells of the WT *M. smegmatis mc² 155*- and the *M. smegmatis* Δ*bcc* mutant strain, deficient of the gene encoding the mycobacterial cytochrome *bcc* complex were grown to mid-log phase in LB media supplemented with Tween 80 (0.05%) by shaking at 37 °C and 180 rpm. The cells were lysed on ice by sonication with an ultrasonic homogenizer (Bandelin, Berlin, Germany, KE76 tip) for 3 × 1 min in buffer A (50 mM MOPS/NaOH, pH 7.5, 2 mM $MgCl_2$) with EDTA-free protease inhibitor cocktail (one tablet per 20 ml buffer, Roche) and 1.2 mg/ml lysozyme. The suspension was left to stir for 45 minutes at room temperature before adding 300 µl of 1 M $MgCl_2$ and 50 µl

DNase I and the stirring was continued for another 15 minutes. Bacteria were broken by 3 passages through an ice-cooled microfluidizer LM20 (Analytik, Cambridge, UK) at 15,000 psi. The suspension containing lysed cells was centrifuged at 4,200 g at 4 °C for 20 minutes. The supernatant containing the membrane fraction was further subjected to ultracentrifugation at 45,000 g at 4 °C for 1 hour. The supernatant was discarded, and the precipitated membrane fraction was suspended in membrane preparation buffer containing 15% glycerol, frozen and stored at -80 °C. The concentrations of the proteins in the vesicles were determined by the bicinchoninic acid assay (BCA; Pierce, Rockford, IL, USA).

2.2.17 Production of *M. smegmatis* inside-out plasma membrane vesicles (PMVs)

PMVs were prepared following the procedures of Kamariah *et al*. (2019) [199]. Cells of the WT *M. smegmatis mc² 155*- and the *M. smegmatis* Δ*bcc* mutant strain, were grown to mid-log phase in LB media supplemented with Tween 80 (0.05%) by shaking at 37 °C and 180 rpm. The cells were lysed on ice by sonication with an ultrasonic homogenizer (Bandelin, Berlin, Germany, KE76 tip) for 3 × 1 min in buffer B (50 mM MOPS/NaOH, pH 7.5, 2 mM $MgCl_2$, 2 mM Pefabloc^{SC}, and 50 µl/100 ml of DNase). After sonication, bacteria were broken by three passages through ice-cooled microfluidizer LM20 (Analytik, Cambridge, UK) at 15,000 psi. The cell lysate was then centrifuged at 15,000 × g for 20 min at 4 °C (Eppendorf, Hamburg, Germany) to remove cell debris and non-lysed cells. The resulting supernatant was subjected to an ultracentrifugation step at 27,000 × g for 40 min at 4 °C. The supernatant was collected and centrifuged at 160,000 × g for 60 min at 4 °C as described by Kamariah *et al.*, 2019 [199]. The pellet, containing the inside-out PMVs, was resolved in buffer A containing 15% glycerol, liquid-nitrogen frozen and stored at -80 °C. The protein concentration within the vesicles were determined by the bicinchoninic acid assay (BCA; Pierce, Rockford, IL, USA).

2.2.18 ATP synthesis assay using IMVs

The ATP synthesis assay was quantified with the CellTiter-Glo® Luminescent Cell Viability Assay kit (Promega, US) [206]. ATP synthesis measurement was carried out on white flat-bottomed 96-well microtiter plates (Corning, US). 2.5 µl of compounds at varying concentration was spotted on the individual wells. This was followed by the addition of 25 µl of PMVs or IMVs (5 µg/ml) and 25 µl of assay buffer (50 mm MOPS, pH 7.5, 10 mM $MgCl_2$), containing 10 µM ADP, 250 µM Pi and 1 mM NADH. The plates were incubated at room temperature for 30

minutes before the addition of 25 µl of CellTiter-Glo® reagent. The plates were incubated for another 10 min in the dark at room temperature. The luminescence was measured by a TECAN Infinite Pro 200 plate reader. The experiment has been carried out on two biological replicates and the error bars represent the standard deviations.

2.2.19 Oxygen consumption assay

Oxygen comsumption assay was carried out using methylene blue as previously described by Li *et al.*, 2017 [279]. 1-fold, 2.5-fold, 5-fold and 10 fold MIC_{50} of SCR0911 were added into 2 ml of mid-log phase *M. smegmatis* culture, subjected to pre-incubation at 37 °C, 1 h, at 160 rpm. THZ (80 µM) was used as a control. Methylene blue (0.001%) was subsequently added. the tubes were transferred to the pre-treated anaerobic jar (BD GasPak™ EZ, US) with GasPak™ EZ anaerobe paper sachet (BD, US) and monitored by BD BBL™ dry anaerobic indicator strips. The tubes were incubated at 37 °C for 12 h. The percentage of methylene blue decolourization in the samples was determined using the methylene blue absorbance readings and the equation below as described previously by Benetoli *et al*., where A_o represents the absorbance of the 7H9 sample, while A_s represents the absorbance of the sample of interest [280]. The experiment has been carried out on two biological replicates and the error bars represent the standard deviations.

$$D\% = \frac{A_o - A_s}{A_o} \times 100$$

2.2.20 Assay for ATP-driven proton translocation

ATP-driven proton translocation of plasma membrane vesicles of *M. smegmatis* were measured on the basis of a decrease in ACMA fluorescence using a Cary Eclipse fluorescence spectrophotometer (Varian Inc., Palo Alto, CA) as described previously [192]. IMVs or PMVs (0.18 mg/ml) were pre-incubated at 37 °C in 10 mM HEPES/KOH (pH 7.5), 100 mM KCl, 5 mM $MgCl_2$ containing 2 µM ACMA, 50 µM ADP and 5 mM Pi. A baseline was obtained by monitoring for 2 min. The reaction was started by adding 0.5 mM NADH as an electron donor. After approximately another 2 minutes when the florescence intensity was quenched completely, 15 µM of the test compound was added. The addition of 2 µM of the uncoupler SF6847 (Alexis Corporation, Lausen, Switzerland) was added after another 2 minutes, for the proton gradient to collapsed completely. The excitation and emission wavelengths were 410 and 480 nm, respectively. The experiment has been carried out on three biological replicates.

2.2.21 Spectral analysis with sodium dithionite

PMVs were analyzed with an Amersham Biosciences Ultrospec 2100 pro UV–visible absorption spectroscopy (New Jersey, US) by recording spectra from 420 nm to 650 nm. PMVs (2 mg/ml) were first spiked with potassium ferricynaide (100 μM) to obtain a defined oxidized state. After collecting the oxidized spectrum, sodium dithionite (100 mM) was added, to generate the reduced spectrum. The difference spectra of the reduced minus the oxidized forms were then computed.

2.2.22 Spectral analysis with NADH as an electron donor

PMVs were analyzed with an Amersham Biosciences Ultrospec 2100 pro UV–visible absorption spectroscopy (New Jersey, US) by recording spectra from 420 nm to 650 nm. PMVs (2 mg/ml) were first spiked with potassium ferricynaide (100 μM) to obtain a defined oxidized state. After collecting the oxidized spectrum, NADH (2 mM) was added reduce complex I and the respective cytochrome oxidase complexes within the PMVs. The UV-spectra were recorded immediately after addition of NADH (0 min) and after 3 minutes, confirming that the PMVs are functional in electron transfer. The difference spectra of the reduced minus the oxidized forms were then computed. To study the effect of compounds, the respective compounds were added after the addition of the oxidant and before the addition of the electron donor NADH.

2.2.23 Docking studies of SCR0911 analogs with *Mtb* cyt-*bcc*

Docking studies were carried out for SCR0911 and its analogs with the homology model of *Mtb* cyt-*bcc* prepared by Dr. Malathy Sony Subramanian Manimekalai [277]. The three-dimensional structure of SCR0911 was prepared using chemdraw and energy minimization was carried out using chem3D, MM2 energy minimization. The ligand was docked into model of *Mtb* cyt-*bcc* using GOLD 5.6.3 with default settings, with residue Y53-OH as a reference atom for the binding site [265]. The model was visualized using PyMOL [270], and the interactions profile was represented using LIGPLOT [274].

2.2.24 Synthesis of SCR0911 and its analogs

2.2.24.1 Synthesis of SCR0911

4,4,5,5-Tetramethyl-2-(4-(trifluoromethoxy)phenyl)-1,3,2-dioxaborolane (2)[281]

A mixture of bis(pinacolato)diboron (0.658 g, 2.59 mmol), 1-bromo-4-(trifluoromethoxy)benzene (0.500 g, 2.07 mmol), potassium acetate (0.311 g, 3.17 mmol) and Pd(dppf)Cl_2 in tetrahydrofuran (THF) (5 ml) was heated at reflux overnight under nitrogen before cooling to room temperature. Ethyl acetate (15 ml) was added, and the mixture was filtered through a pad of Celite (R). The filtrate was washed with water (10 ml x 2) and concentrated in *vacuo*. The residue was purified by flash chromatography (10 – 25% ethyl acetate:hexane) to afford the title compound as a colourless solid (0.39 g, 1.35 mmol, 65%). δ_H (400 MHz, $CDCl_3$) 7.84 (d, *J* = 8.6 Hz, 2H), 7.20 (d, *J* = 8.7 Hz, 2H), 1.34 (s, 12H) ppm [282].

5-Bromo-*N*-methoxy-*N*-methylnicotinamide (9)[283]

4- (Dimethylamino)pyridine (DMAP) (0.242 g, 1.98 mmol) and *N*-(3-dimethylaminopropyl)-*N*'-ethylcarbodiimide hydrochloride (EDCI) (2.85 g, 14.9 mmol) were added to a solution of 5-bromonicotinic acid (2 g, 9.90 mmol) and *N, O*-dimethylhydroxylamine hydrochloride (1.45 g, 14.9 mol) in dichloromethane (36 ml). The mixture was placed under nitrogen and triethylamine (2.0 ml, 14.8 mmol) was added dropwise. The mixture was stirred overnight at room temperature. Water (50 ml) was added, followed by extraction with dichloromethane (3 x 30 ml). The combined organic layers were washed with brine (50 ml), dried over anhydrous Na_2SO_4 and concentrated in *vacuo*. The residue was purified by flash chromatography (50% ethyl acetate: hexane) to afford the title compound as a yellow solid (2.10 g, 8.55 mmol, 86%). δ_H (400 MHz, $CDCl_3$) 8.87 (d, J = 1.8 Hz, 1H), 8.75 (d, J = 2.3 Hz, 1H) 8.18 (t, J = 2.0 Hz, 1H), 3.57 (s, 3H), 3.38 (s, 3H) ppm [284].

1-(5-Bromopyridin-3-yl)propan-1-one (3)[285]

Ethyl magnesium bromide (34.2 mmol, 4.0 eq) was added dropwise to a solution of amide **9** (2.11 g, 8.61 mmol) in THF (85 ml) under nitrogen at 0 °C. The solution was stirred for 30 minutes at 0 °C, then quenched with saturated NH_4Cl (50 ml) before extraction with diethyl ether (3 x 50 ml). The combined organic layers were washed with brine (50 ml), dried over $MgSO_4$ and concentrated in *vacuo*. The residue was purified by flash chromatography (50% ethyl acetate: hexane) to afford the title compound as a yellow solid (0.655 g, 3.06 mmol, 36%). δ_H

(400 MHz, $CDCl_3$) 9.07 (d, J = 1.7 Hz, 1H), 8.84 (d, J = 2.1 Hz, 1H), 8.40 – 8.33 (m, 1H), 3.01 (q, J = 7.2 Hz, 2H), 1.25 (t, J = 7.2 Hz, 3H) ppm; δ_C (400 MHz, $CDCl_3$) 197.74, 153.98, 147.09, 137.43, 132.90, 120.92, 32.08, 7.46 ppm; IR (CH_2Cl_2) 1697.04 cm^{-1}; MS (ESI) 213.99 $[M+H]^+$; HRMS (Q-Tof) calcd for C_8H_8BrNO: 213.9868; found: 213.9858 $[M+H]^+$.

1-(5-(4-(Trifluoromethoxy)phenyl)pyridin-3-yl)propan-1-one (1)[248]

Compound **2** (0.321 g, 1.12 mmol) was added to a stirred solution of compound **3** (0.218 g, 1.02 mmol), $Pd(dppf)Cl_2$ (0.059 g, 0.081 mmol) and potassium carbonate (0.463 g, 3.37 mmol) in THF: H_2O (16 ml: 6.4 ml) under nitrogen. The mixture was heated at reflux overnight before cooling to room temperature. Water (10 ml) was added, and the organic layer was extracted with ethyl acetate (3 x 15 ml). The combined organic layers were washed with brine, dried over $MgSO_4$ and concentrated in *vacuo*. The residue was purified by flash chromatography (30% ethyl acetate: hexane) to afford the title compound as a yellow solid (0.284 g, 0.96 mmol, 47%). δ_H (400 MHz, $CDCl_3$) 9.16 (d, *J* = 2.0 Hz, 1H), 8.98 (d, *J* = 2.3 Hz, 1H), 8.40 (t, *J* = 2.2 Hz, 1H), 7.67 – 7.62 (m, 2H), 7.36 (d, *J* = 7.9 Hz, 2H), 3.09 (q, *J* = 7.2 Hz, 2H), 1.29 (t, *J* = 7.2 Hz, 3H) ppm [248].

2-Iodo-5-methoxyaniline (11)[286]

N-Iodosuccinimide (0.995 g, 4.06 mmol) was added to a solution of 3-methoxyaniline (0.46 ml, 4.06 mmol) in dichloromethane (100 ml) and acetic acid (0.25 ml, 4.25 mmol). The mixture was stirred overnight at room temperature. Aqueous $NaHCO_3$ (100 ml) was added, and the organic layer was extracted with ethyl acetate (3 x 40 ml). The combined organic layers were washed with brine, dried over $MgSO_4$ and concentrated in *vacuo*. The residue was purified by flash chromatography (ethyl acetate: hexane) to afford the title compound as a brown oil (0.530 g, 2.13 mmol, 52%). δ_H (400 MHz, $CDCl_3$) 7.48 (d, J = 8.7 Hz, 1H), 6.33 (d, J = 2.8 Hz, 1H), 6.14 (dd, J = 8.7, 2.8 Hz, 1H), 4.07 (s, 2H), 3.74 (s, 3H) ppm [286].

Methyl 2-amino-4-methoxybenzoate (12)[287]

A solution of compound **11** (0.123 g, 0.440 mmol), and $Pd(dppf)Cl_2$ (0.0129 g, 0.0176 mmol) in methanol (2 ml) was placed under an atmosphere of carbon monoxide (balloon). Triethylamine (0.06 ml, 0.474 mmol) was added to the reaction mixture and carbon monoxide was bubbled through the mixture for 30 seconds. The mixture was heated at reflux overnight. Ethyl acetate (10 ml) was added and the mixture was filtered through a pad of Celite(R), before

concentration in *vacuo*. The residue was purified by flash chromatography (10 – 25% ethyl acetate:hexane) to afford the title compound as a brown solid (0.07 g, 0.384 mmol, 87%). δ_H (400 MHz, $CDCl_3$) 7.78 (d, J = 9.0 Hz, 1H), 6.23 (dd, J = 8.9, 2.5 Hz, 1H), 6.11 (d, J = 2.5 Hz, 1H), 5.78 (s, 2H), 3.83 (s, 3H), 3.79 (s, 3H) ppm [288].

2-Amino-4-methoxybenzoic acid (6)[289]

Lithium hydroxide (0.032 g, 0.77 mmol) was added to a solution of compound **12** (0.070 g, 0.38 mmol) in THF:H_2O (1 ml :1ml). The mixture was heated at reflux for 5 hours. The mixture was allowed to cool to room temperature and the aqueous layer was collected. 2 M HCl was added dropwise until the pH reached to 3. The aqueous solution was extracted with EtOAc (3 x 10 ml) before concentrating in *vacuo* to afford a white solid (0.057 g, 0.343 mmol, 89%). δ_H (400 MHz, $(CD_3)_2SO$) 7.60 (d, *J* = 8.9 Hz, 1H), 6.22 (d, *J* = 2.5 Hz, 1H), 6.09 (dd, *J* = 8.9, 2.5 Hz, 1H), 3.71 (s, 3H) ppm [290].

2-(4,4-Dimethyl-4,5-dihydrooxazol-2-yl)-5-methoxyaniline (4)[291]

Triphenylphosphine (0.474 g, 1.81 mmol), triethylamine (0.25 ml, 1.81 mmol), CBr_4 (0.599 g, 1.81 mmol), aromatic acid **6** (0.100 g, 0.602 mmol), and 2-amino-2-methylpropan-1-ol (0.07 ml, 0.704 mmol) in toluene (3 ml) was stirred under nitrogen for 20 minutes at room temperature before being heated at 90 °C overnight. The solvent was evaporated under reduced pressure, and the residue was diluted with diethyl ether and filtered. The residual solid was washed with ether three times. The filtrate was concentrated in *vacuo* and purified by flash chromatography (5% - 20% ethyl acetate:hexane) to afford the title compound as a white solid (0.0256 g, 0.116 mmol, 19%). δ_H (400 MHz, $CDCl_3$) δ 7.59 (d, J = 8.8 Hz, 1H), 6.24 (dd, J = 8.8, 2.5 Hz, 1H), 6.17 (d, J = 2.2 Hz, 1H), 6.13 (s, 2H), 3.96 (s, 2H), 3.78 (s, 3H), 1.35 (s, 6H) ppm [248].

7-methoxy-3-methyl-2-(5-(4-(trifluoromethoxy)phenyl)pyridin-3-yl)quinolin-4(1H)-one (SCR0911)[248]

Trifluoromethane sulfonic acid (0.006 ml, 0.067 mmol) was added to a solution of oxazoline **1** (0.0806 g, 0.366 mmol) and ketone **4** (0.983, 0.33 mmol) in dry *n*-butanol (5.5 ml). The mixture was heated at reflux for 24 hours. Saturated sodium carbonate solution (10 ml) was added. The aqueous solution was extracted with ethyl acetate (3 x 15 ml) and combined organic layers were washed with brine (50 ml), dried over $MgSO_4$ and concentrated in *vacuo*. The residue was purified by flash chromatography (5 – 20% ethyl acetate: hexane) to afford the title

compound as a brown solid (0.062 g, 0.155 mmol, 42%). δH (400 MHz, DMSO) 11.58 (s, 1H), 9.09 (d, J = 2.0 Hz, 1H), 8.79 (d, J = 1.8 Hz, 1H), 8.34 (t, J = 1.9 Hz, 1H), 8.04 (d, J = 8.9 Hz, 1H), 8.00 (d, J = 8.8 Hz, 2H), 7.54 (d, J = 8.5 Hz, 2H), 6.97 (d, J = 1.9 Hz, 1H), 6.93 (dd, J = 8.9, 2.3 Hz, 1H), 3.84 (s, 3H), 1.93 (s, 3H) ppm; HRMS (Q-Tof) calcd for $C_{23}H_{17}F_3N_2O_3$: 427.1270; found: 427.1288 $[M+H]^+$ [248].

2.2.24.2 Synthesis of SCR0911-A1

5-bromonicotinaldehyde (A1-1)[292]

Lithium aluminum hydride (0.406 g, 10.7 mmol) was added portionwise to a stirred solution of Weinreb amide **9** (2.184 g, 8.9 mmol) in THF (27 mL) at -78 °C, over 15 minutes. The reaction temperature was increased to -40 °C after lithium aluminum hydride was fully added. After 4 hours, saturated ammonium chloride (30 ml) was added slowly, followed by an extraction with ethyl acetate (3 x 30 ml). The combined organic layers were dried over anhydrous Na_2SO_4 and concentrated in *vacuo*. The residue was purified by flash chromatography (10% ethyl acetate: hexane) to afford the title compound as a white solid (1.45 g, 7.81 mmol, 88%). δ_H (400 MHz, $CDCl_3$) 10.08 (s, 1H), 8.99 (d, J = 1.8 Hz, 1H), 8.91 (d, J = 2.3 Hz, 1H), 8.31 (t, J = 2.1 Hz, 1H) [293].

3-bromo-5-ethynylpyridine (A1-2)[294]

Diethyl (3-diazo-2-oxopropyl)phosphonate (1.26 g, 5.70 mmol) was added to a solution of potassium carbonate (2.15 g, 15.5 mmol) and aldehyde **A1-1** (0.96 g, 5.18 mmol) in dry methanol (15 ml). The mixture was stirred overnight at room temperature. Diethyl ether (15 ml) was added, followed by washing with sodium bicarbonate (15 ml). The organic layer was dried over anhydrous Na_2SO_4 and concentrated in *vacuo*. The residue was purified by flash chromatography spiked with triethylamine (10% ethyl acetate: hexane) to afford the title compound as a white solid (0.66 g, 3.62 mmol, 70%). δ_H (400 MHz, $CDCl_3$) 8.63 (dd, J = 6.4, 2.0 Hz, 2H), 7.92 (t, J = 2.0 Hz, 1H), 3.27 (s, 1H) [295].

2-(5-bromopyridin-3-yl)-7-methoxyquinolin-4(1H)-one (A1-3)[296]

2-Iodo-5-methoxyaniline **11** (0.137 g, 0.549 mmol), 3-bromo-5-ethynylpyridine **A1-2** (0.200g, 1.099 mmol), 1,8-Diazabicyclo(5.4.0)undec-7-ene (DBU) (4.01 µl, 0.028 mmol) and Pd(dppf)Cl_2 (0.020 g, 0.028 mmol) were added in triethylamine (3ml). Carbon monoxide was added at 100 psi and the reaction was stirred for 7 days at 75 °C. The reaction was diluted in

CH_2Cl_2 and extrated with CH_2Cl_2 (3 x 15 ml). The combined organic layers were washed with ammonium chloride and dried ovver Na_2SO_4. The residue was purified by flash chromatography (ethyl acetate: hexane) to afford the title compound as a brown oil (0.091 g, 0.275 mmol, 50%). δ_H (400 MHz, $CDCl_3$) 8.73 (s, 1H), 8.57 (d, J = 1.9 Hz, 1H), 7.95 (s, 1H), 7.68 (d, J = 8.6 Hz, 1H), 7.01 (s, 1H), 6.60 (s, 1H), 6.56 (dd, J = 8.6, 2.0 Hz, 1H), 6.50 (d, J = 2.0 Hz, 1H), 3.89 (s, 3H). MS (ESI) 331.05 $[M+H]^+$; HRMS (Q-Tof) calcd for $C_{15}H_{11}BrN_2O_2$: 331.0082; found: 331.0076 $[M+H]^+$.

Results

Part 1

Mutations on the Cys-S_pH containing α-helix reveals critical residues for catalysis

3. Results

3.1 Mutations on the Cys-S_pH containing α-helix reveals critical residues for catalysis

3.1.1 Site-directed mutagenesis of *Mb*AhpC$_{A66G/A67D/F68V}$, *Mb*AhpC$_{A67D/F68V}$ and *Mb*AhpC$_{A67D}$

To understand the importance of the α-helix containing the Cys-S_pH, site-directed mutagenesis to prepare a triple mutation *Mb*AhpC$_{A66G/A67D/F68V}$, a double mutation *Mb*AhpC$_{A67D/F68V}$, and a single mutation *Mb*AhpC$_{A67D}$ were performed. As the pET-9d plasmid containing full-length *Mb*AhpC (pET-9d-*Mb*AhpC) and Histidine$_6$-tag was available, primers were designed for whole plasmid mutagenesis, allowing the mutated plasmid to be obtained within a day [268]. Both the forward and reverse primers were designed according to the In-Fusion site directed mutagenesis methods [268], containing at least a 15 bp overlap, excluding the mutated regions, for the primers to bind and to remain annealed sufficiently for primer extension. Several annealing temperatures were applied using a Biometra T gradient PCR thermocycler (Biometra, Germany). The PCR was first carried out for *Mb*AhpC$_{A66G/A67D/F68V}$, and *Mb*AhpC$_{A67D/F68V}$ (Fig. 3.1A and B), indicating the presence of the amplified gene products at higher annealing temperatures above 60 °C. This led to the PCR of *Mb*AhpC$_{A67D}$ at the three annealing temperature, 60.9 °C, 65.2 °C, and 70.6 °C (Fig. 3.1C). PCR products for *Mb*AhpC$_{A66G/A67D/F68V}$, *Mb*AhpC$_{A67D/F68V}$ and *Mb*AhpC$_{A67D}$ were obtained from reactions at annealing temperatures of 71.3 °C, 65.9 °C, and70.6 °C, respectively.

As the template DNA was amplified by *E. coli*, the template DNA is naturally methylated, while the mutated plasmid that was synthesized through *in-vitro* means is unmethylated. A restriction enzyme, DpnI, specific to methylated DNA was employed to remove the template DNA, prior to DNA precipitation for transformation into *E. coli* DH5α cells for plasmid amplification. Plating of the cell suspension on an LB plate supplemented with kanamycin antibiotics yielded single colonies. Cells from single colonies were inoculated into LB media, supplemented with kanamycin antibiotics, for plasmid extraction. The sequences of the selected plasmid were confirmed by DNA sequencing (1st Base, Singapore).

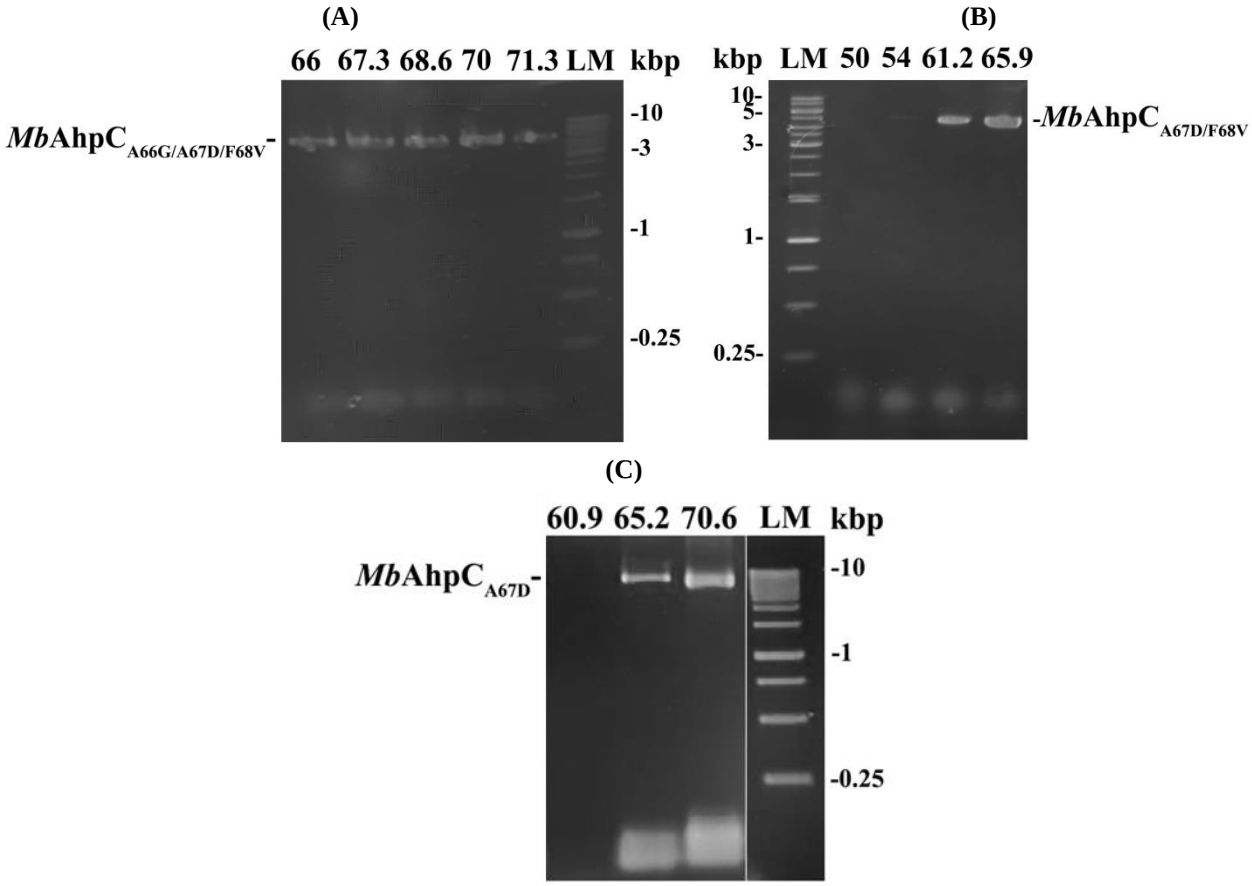

Figure 3.1: PCR amplification results. The numbers above represent the different annealing temperatures (°C) chosen. (A) PCR results from *Mb*AhpC$_{A66G/A67D/F68V}$. Clear bands were observed at all annealing temperatures. (B) PCR results from *Mb*AhpC$_{A67D/F68V}$. Clear bands were observed at only two annealing temperatures. (C) PCR results from *Mb*AhpC$_{A67D}$. Clear bands were observed at two out of three chosen annealing temperatures. As the agarose gel was ran alongside other samples, a gap was shown between the samples and the LM; [LM (ladder marker)].

3.1.2 Purification of *Mb*AhpC and its mutants

Previous research has validated the redox sensitivity of *Mt*AhpC, resulting in the protein oligomerization under reduced conditions and de-stabilization of the oligomer into a dimer under oxidized conditions [128]. To confirm this phenomenon, purification of WT *Mb*AhpC was carried out, following a two-step purification method. The first involves Ni-NTA affinity chromatography, with increasing concentrations of imidazole for competitive elution of the protein. The Ni-NTA elution profile analyzed on a 17% SDS gel revealed that *Mb*AhpC eluted mainly at 100-, 125- and 250 mM imidazole fractions in both the presence and absence of the reducing agent, DTT (Fig. 3.2). The three fractions were pooled together and concentrated before subjecting to SEC.

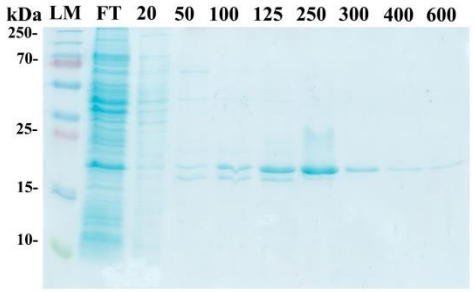

Figure 3.2: 17% SDS-PAGE gel of Ni-NTA fractions of *Mb*AhpC under oxidized conditions. The numbers indicate the imidazole concentration (mM) and a significant yield of *Mb*AhpC was present in 100 mM to 250 mM imidazole fractions; [FT (flow through), LM (ladder marker)]

Purification of WT *Mb*AhpC through SEC in the absence and presence of DTT indicated that the protein eluted at 16 ml and 12 ml, respectively (Fig. 3.3), signifying the redox sensitivity of *Mb*AhpC. The elution at 16 ml reveals the dimeric form, which possibly oligomerizes into a dodecameric ring under reduced conditions, resulting in the elution at 12 ml [128]. To gain preliminary understandings on the redox sensitivity of *Mb*AhpC$_{A66G/A67D/F68V}$, *Mb*AhpC$_{A67D/F68V}$, and *Mb*AhpC$_{A67D}$, purification of the mutants in the presence and absence of DTT were performed.

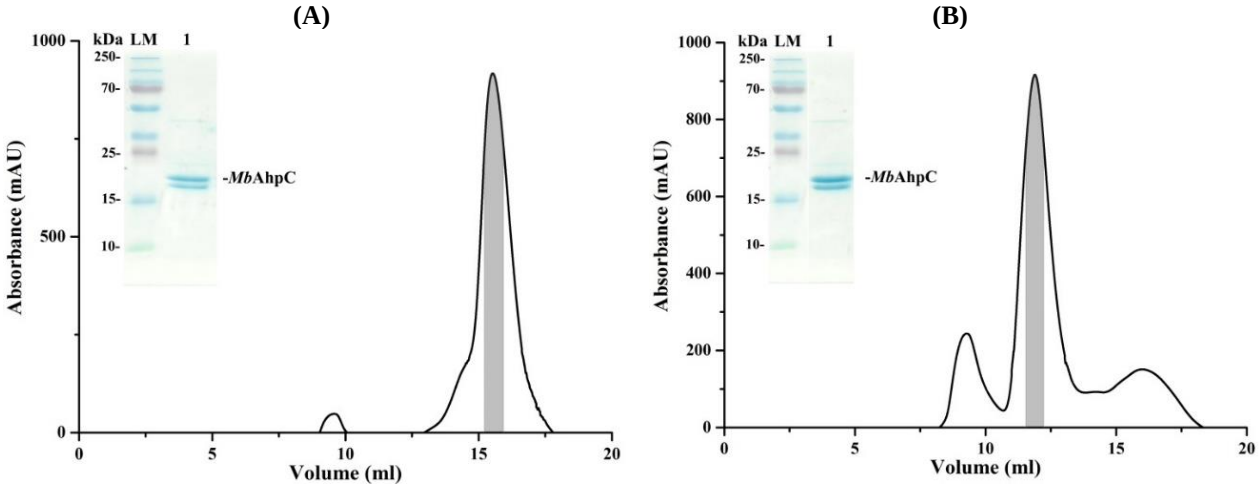

Figure 3.3: Size exclusion chromatography results for the purification of WT *Mb*AhpC. The purification of WT *Mb*AhpC (A) in the presence and (B) absence of reducing agent, DTT are as shown. The grey border indicates the purified proteins kept and used for analysis. The purity of the protein was confirmed on a 17% SDS-PAGE gel [297]. The two bands on the SDS-PAGE gel are a typical profile of the recombinant protein in a semi-denaturing SDS-page as described by Wong *et al*. [128].

The Ni-NTA elution profile analyzed on a 17% SDS-PAGE gel revealed that all the three mutants eluted at 100-, 125- and 250 mM imidazole fractions in the presence and absence of the reducing agent (Fig. 3.4). The three fractions were pooled together and concentrated before

subjecting to SEC. Interestingly, the SEC elution profile revealed the elution of *Mb*AhpC$_{A66G/A67D/F68V}$, *Mb*AhpC$_{A67D/F68V}$, and *Mb*AhpC$_{A67D}$ at 16 ml, regardless of the addition of a reducing agent (Fig. 3.5D-F). This is similar to the WT *Mb*AhpC SEC elution profile in the absence of DTT.

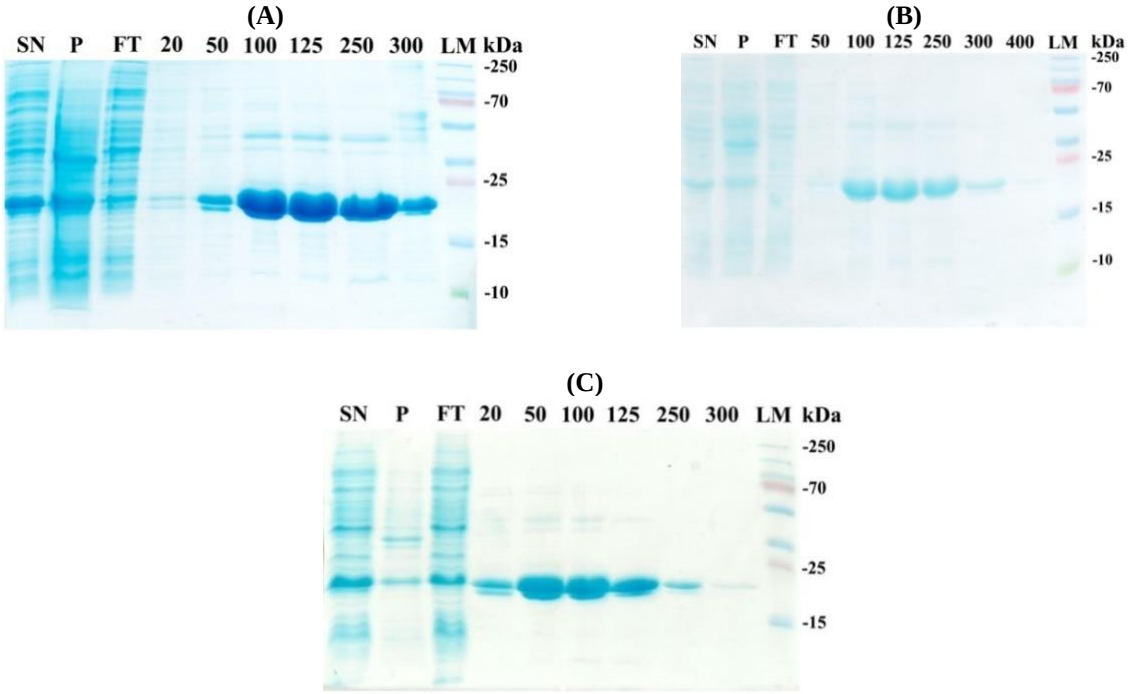

Figure 3.4: 17% SDS-PAGE gel of Ni-NTA fractions of the *Mb*AhpC mutants. (A) *Mb*AhpC$_{A66G/A67D/F68V,}$ (B) *Mb*AhpC$_{A67D/F68V}$, and (C) *Mb*AhpC$_{A67D}$ in the absence of DTT are shown [SN (supernatant), P (pellet), FT (flow through), LM (ladder marker)]. The numbers indicate the imidazole concentration (mM) and the fractions at 100 mM to 250 mM imidazole fractions were used for further purification steps.

To confirm this observation, the top 20% of the eluted proteins purified with and without reducing agents, as highlighted in grey, were collected and subjected to DLS analysis (Fig. 3.5A-C). From the DLS studies, a hydrodynamic diameter of 8.3 ± 2.7 nm and 7.2 ± 1.8 nm was calculated for the oxidized and reduced form of *Mb*AhpC$_{A66G/A67D/F68V}$, respectively (Fig. 3.6A). This is in contrast to the hydrodynamic diameter of WT *Mb*AhpC, revealing the presence of a dimer in oxidized conditions (6.85 ± 2.59 nm) and a dodecamer formation under reduced conditions (12.08 ± 2.98 nm) [128]. Similarly, *Mb*AhpC$_{A67D/F68V}$ confirmed the presence of a dimer with its hydrodynamic diameter of 7.3 ± 1.7 nm and 6.5 ± 1.6 nm under oxidized and reduced conditions, respectively (Fig. 3.6B). The DLS result for *Mb*AhpC$_{A67D}$ was similarly at 8.1 ± 2.0 nm and 8.6 ± 2.0 nm under oxidized and reduced conditions, respectively (Fig. 3.6C).

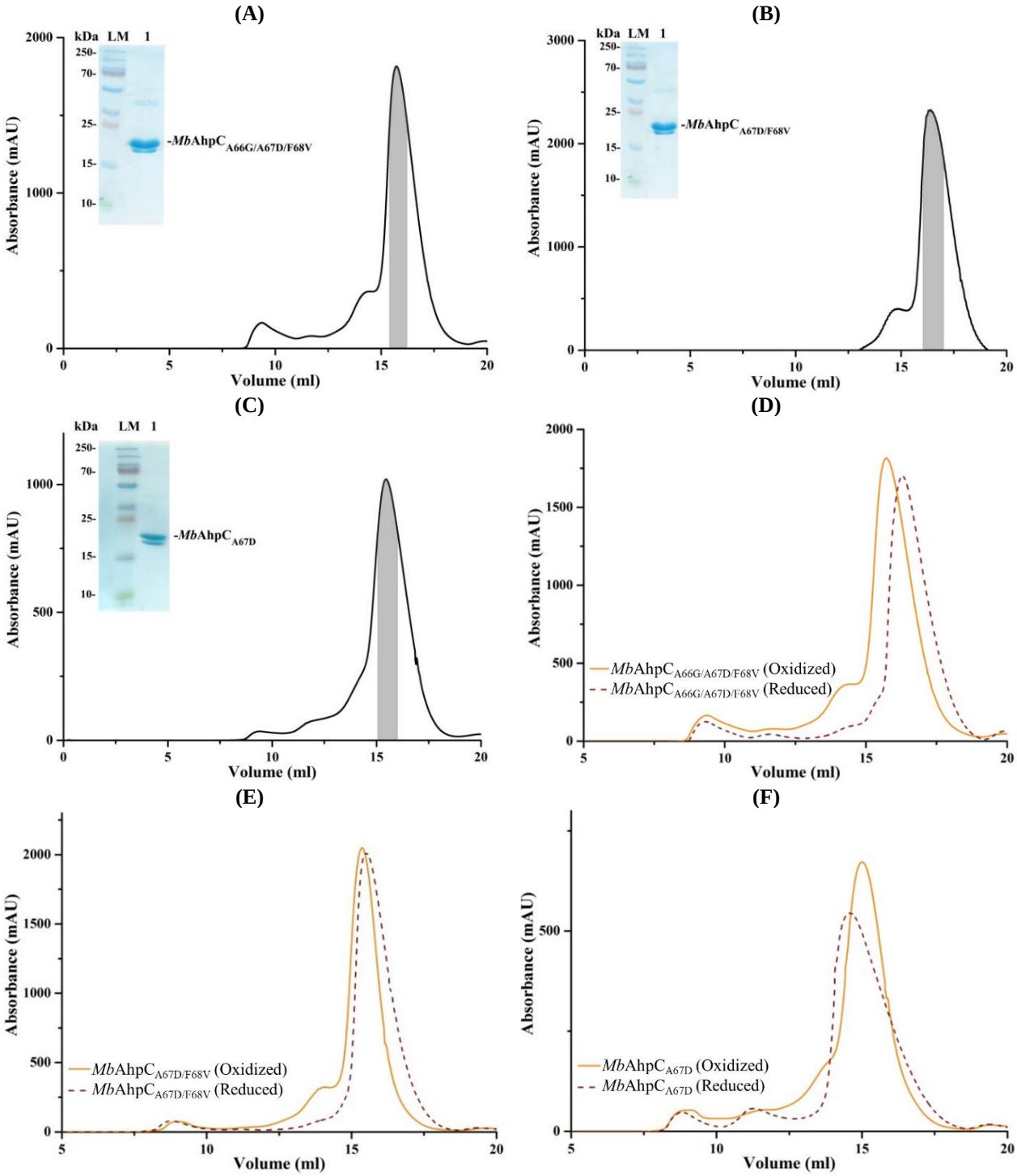

Figure 3.5: Size exclusion chromatogram of *Mb*AhpC$_{A66G/A67D/F68V}$, *Mb*AhpC$_{A67D/F68V}$, and *Mb*AhpC$_{A67D}$. SEC elution profile for the purification under oxidized conditions shows that (A) *Mb*AhpC$_{A66G/A67D/F68V}$, (B) *Mb*AhpC$_{A67D/F68V}$, and (C) *Mb*AhpC$_{A67D}$ eluted at approximately 16 ml. The grey border indicates the purified proteins kept and used for analysis. The purity of the protein was confirmed on a 17% SDS-PAGE gel (inset). The comparison of the elution profile under oxidized (orange) and reduced (brown dotted) conditions for (D) *Mb*AhpC$_{A66G/A67D/F68V}$, (E) *Mb*AhpC$_{A67D/F68V}$, and (F) *Mb*AhpC$_{A67D}$ indicates the elution at 16 ml under both conditions [297].

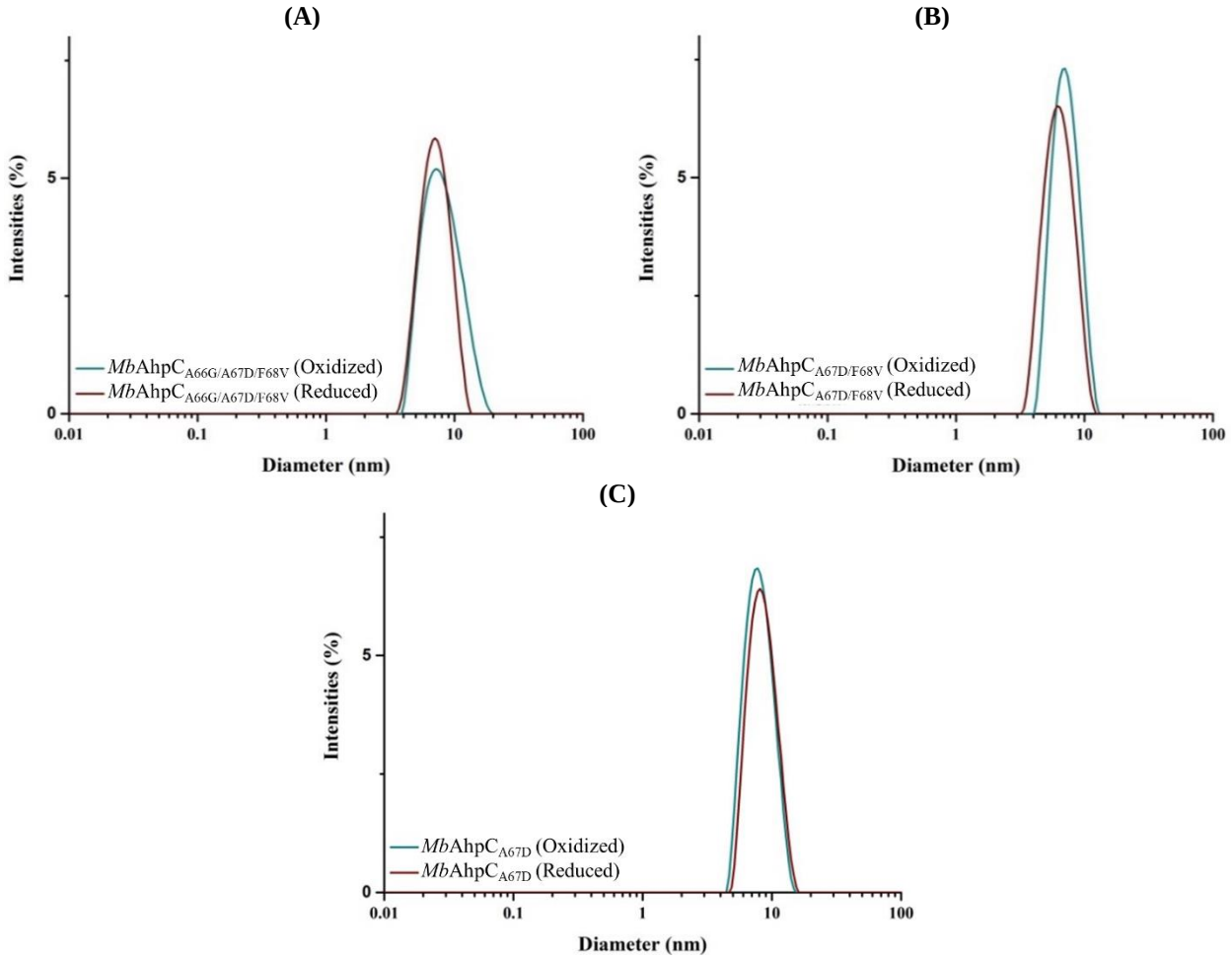

Figure 3.6: DLS results for *Mb*AhpC$_{A66G/A67D/F68V}$, *Mb*AhpC$_{A67D/F68V}$, and *Mb*AhpC$_{A67D}$. The DLS analysis for (A) *Mb*AhpC$_{A66G/A67D/F68V}$, (B) *Mb*AhpC$_{A67D/F68V}$, and (C) *Mb*AhpC$_{A67D}$ confirmed the hydrodynamic diameter of approximately 7 nm for both oxidized and reduced recombinant proteins [297].

The three recombinant mutants (*Mb*AhpC$_{A66G/A67D/F68V}$, *Mb*AhpC$_{A67D/F68V}$, *Mb*AhpC$_{A67D}$) have displayed an inability to form oligomers in dodecamer form under both oxidized and reduced conditions, possibly demonstrating the importance of the A67 residue, as all the mutants contain the A67D mutation. Additionally, the lack of oligomerization might suggest the loss of the redox sensitivity of the three mutants generated. In other bacterial AhpC, upon reduction, the Cys-S_pH-containing helix starts shifting towards its FF conformation, acting as a keystone for the oligomeric ring formation [112]. Hence, the mutations on the helix could breakdown this synchronization for oligomerization. To determine if the mutants are still enzymatically active, peroxide-dependent assays were performed to investigate if the recombinant proteins can reduce peroxides.

3.1.3 Enzymatic Activity of *Mb*AhpC$_{A66G/A67D/F68V}$, *Mb*AhpC$_{A67D/F68V}$ and *Mb*AhpC$_{A67D}$

An enzymatic assay was carried out with stopped-flow spectroscopy using the thioredoxin system, where *Mb*AhpC can be reduced by *Mb*TrxC, which is in turn, reduced by *Mb*TrxR. *Mb*TrxR then obtains its electrons from NADPH (see Fig. 1.9) [128, 129]. This allows the activity of *Mb*AhpC to be observed from the absorbance of NADPH over 120 s. The decrease in the absorbance of NADPH would be directly proportional to the ability of the recombinant proteins to reduce peroxides. As shown in figure 3.7, the triple and double mutants have a negligible decline of the NADPH absorbance at 340 nm, as it lies very closely to the control. However, the single mutant possesses a substantial decline, retaining 64% of its activity, as compared to WT *Mb*AhpC.

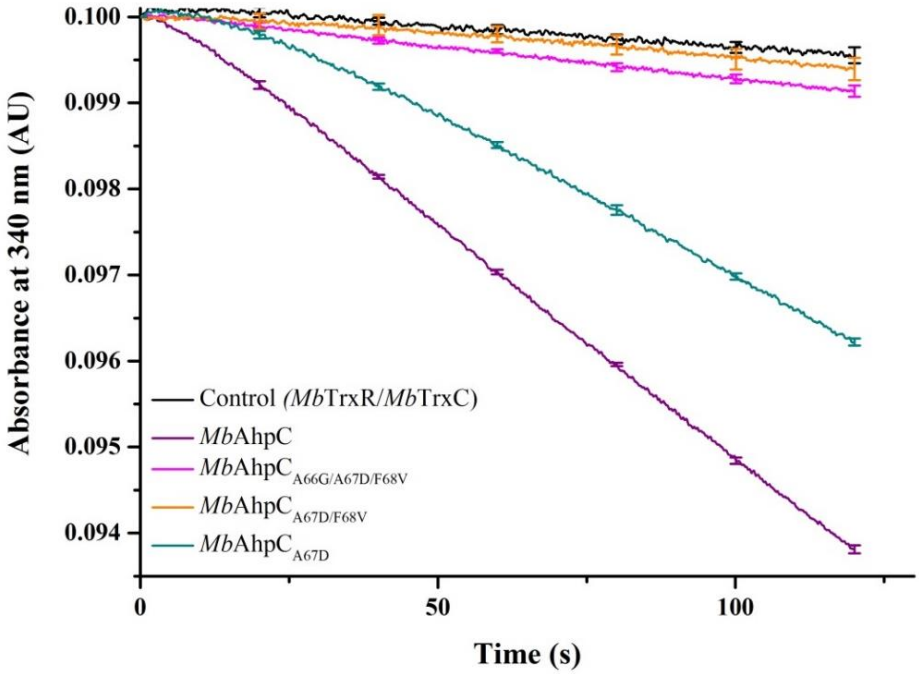

Figure 3.7: Analysis of the enzymatic activity of WT and the mutants of *Mb*AhpC. The black line represents the control whereby no enzymes were added, while the violet line represents the absorbance of WT *Mb*AhpC. Both the triple mutant (pink) and double mutant (orange) have a decline in absorbance similar to the control. A significant decline in absorbance was found in the single mutant (cyan).

Along with the loss of dodecameric ring formation in the presence of reducing agent, a loss in the catalytic ability of the mutants, especially in the cases of *Mb*AhpC$_{A66G/A67D/F68V}$ and *Mb*AhpC$_{A67D/F68V}$, were observed. As the single mutant retained 64% of its activity, it indicates that the transfer of electrons from TrxC towards AhpC is still favourable, allowing disulfide bond formation. To ensure that the neglegible enzymatic activity is not due to the incompatibility

of the Trx-system, ferrous oxidation-xylenol orange (FOX) assay was carried out. Herein, DTT was utilized as the general reducing agent for *Mb*AhpC and its mutants.

3.1.4 FOX Assay

The FOX assay utilizes a reagent containing Fe (II) and xylenol orange. In the presence of H_2O_2, Fe (II) becomes oxidized to Fe (III), which is able to react with xylenol orange, forming a coloured adduct that absorbs light at 560 nm. To assess the ability of the protein to reduce H_2O_2, each reaction mixture contains a fixed amount of protein and DTT as a general reductant. A fixed amount of H_2O_2 was added at the start of each reaction. The remaining amount of H_2O_2 left after the reduction by the recombinant proteins could be identified with the FOX reagent. This allows the measurement of H_2O_2 directly, where the protein/substrate solution was added into the FOX reagent at specific intervals.

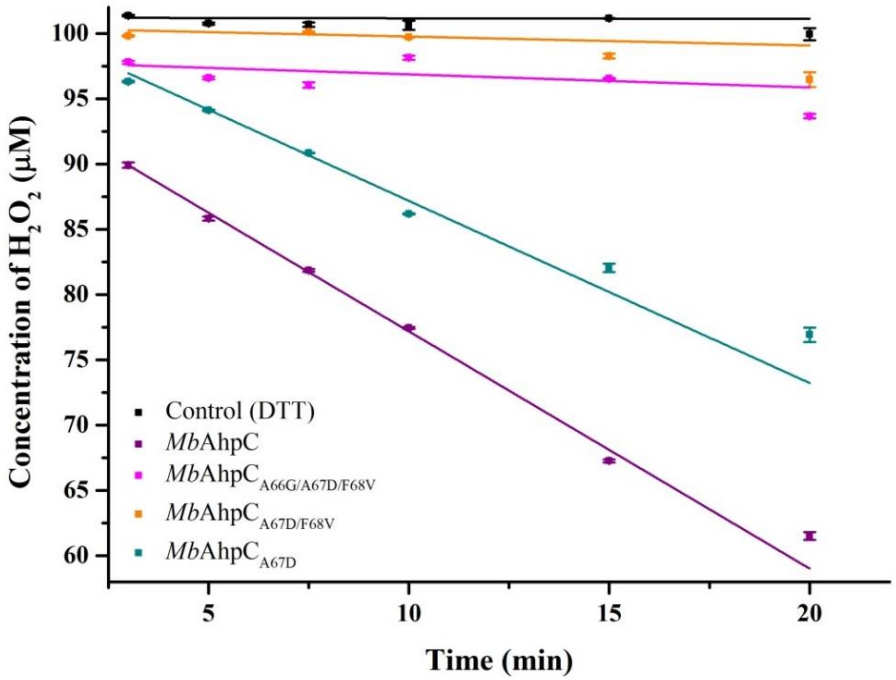

Figure 3.8: FOX assay results of WT and the mutants of *Mb*AhpC. The black line represents the control whereby no enzymes were added, while the violet line represents the absorbance of WT *Mb*AhpC. Both the triple mutant (pink) and double mutant (orange) have a decline in absorbance similar to the control. A significant decline in absorbance was found in the single mutant (cyan).

The activity of the recombinant mutants from the FOX assay resembles that of the stopped-flow spectroscopy (Fig. 3.8). Both the triple and double mutant possesses activity that runs closely to the control, while the single mutant has reduced activity, retaining approximately 67% of WT *Mb*AhpC's activity. These results suggest that the mutations have rendered the protein to be less active due to at the binding of peroxides at the active site. As compared to *Mb*AhpC$_{A67D}$,

*Mb*AhpC$_{A67D/F68V}$ and *Mb*AhpC$_{A66G/A67D/F68V}$ revealed negligible activity in the peroxide-dependent assay and the FOX assay, demonstrating F68 to be a critical residue, causing the inactivity of the protein. To confirm this hypothesis, the single mutant, *Mb*AhpC$_{F68V}$, was generated, which will be described in chapter 3.2 in depth.

3.1.5 Enzyme kinetics of *Mb*AhpC$_{A67D}$

To characterize the effect of the alanine to aspartate substitution in mutant *Mb*AhpC$_{A67D}$ in the peroxidase activity, the catalytic turnover number (K_{cat}) and the Michaelis-Menten constant (K_m) for its binding with H_2O_2 were determined. The enzymatic characterization of WT *Mb*AhpC has been previously characterized by Ms. Chui Fann Wong from Professor Grüber's laboratory (SBS, NTU) [298].

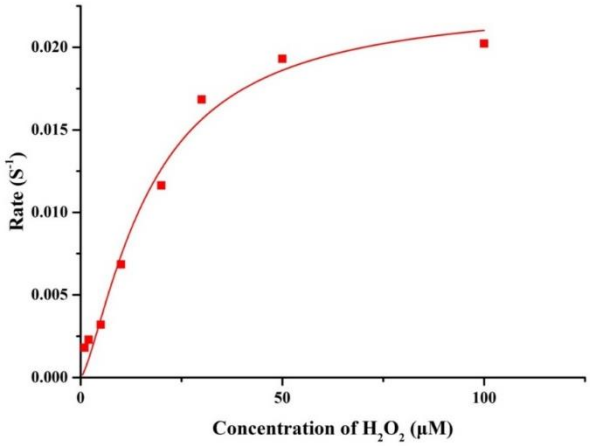

Figure 3.9: Enzymatic kinetics of *Mb*AhpC$_{A67D}$. Michaelis-Menten plot of *Mb*AhpC$_{A67D}$ reveal a K_{cat} of 0.023 ± 0.002 (s^{-1}) and a K_M of 17.19 ± 3.6 μM [297].

	K_{cat} ± SD (s^{-1})	K_M ± SD (μM)	K_{cat}/K_M ($M^{-1}s^{-1}$)
***Mb*AhpC$_{A67D}$**	0.023 ± 0.002	17.19 ± 3.6	1.33 x 10^3
***Mb*AhpC**	0.021 ± 0.001	2.57 ± 0.36	8.17 x 10^3

Table 3.1: Enzyme kinetics parameters for WT *Mb*AhpC and *Mb*AhpC$_{A67D}$.

The K_{cat} was similar for both the WT *Mb*AhpC (0.021 ± 0.001 s^{-1}) and the single mutant, *Mb*AhpC$_{A67D}$ (0.023 ± 0.002 s^{-1}) (Fig. 3.9), indicating that despite the mutation, the ability of the protein to reduce H_2O_2 per unit time remains the same. On the other hand, the K_m of *Mb*AhpC$_{A67D}$ was approximately 7-fold higher than that of the WT *Mb*AhpC. Hence, the catalytic efficiency (k_{cat}/K_m (H_2O_2)) of *Mb*AhpC$_{A67D}$ is 1.33 x 10^3 M^{-1} s^{-1}, significantly lower than

WT *Mb*AhpC (8.17×10^3 M^{-1} s^{-1}), possibly indicating an unsuitable binding site for the peroxides, that can be overcome by providing more substrates.

Results

Part 2

Single mutation on the Cys-S_pH containing α-helix of MbAhpC causes loss in enzymatic activity

3.2 Single mutation on the Cys-S_pH containing α-helix of *Mb*AhpC causes loss in enzymatic activity

3.2.1 Site-directed mutagenesis of *Mb*AhpC$_{F68V}$

As both *Mb*AhpC$_{A67D/F68V}$ and *Mb*AhpC$_{A66G/A67D/F68V}$, revealed no significant activity in the peroxide-dependent assay and FOX assay, and both contain the mutation of F68V, the single F68V mutant, was prepared to validate if this phenylalanine residue is critical for its activity. Similar to the preparation of *Mb*AhpC$_{A67D}$, site-directed mutagenesis to prepare *Mb*AhpC$_{F68V}$ was performed at annealing temperatures of 60.9 °C, 65.2 °C, and 70.6 °C, as PCR reactions for *Mb*AhpC$_{A67D/F68V}$ and *Mb*AhpC$_{A66G/A67D/F68V}$ indicated the presence of amplified gene products at higher annealing temperatures above 60 °C (Fig. 3.1). The amplified gene products are shown in figure 3.10, and the PCR product was obtained from the reaction at 70.6 °C. DpnI treatment to remove the methylated template DNA was carried out, prior to transformation into *E. coli* DH5α cells for plasmid amplification. Plating of the cell suspension on an LB plate supplemented with kanamycin antibiotics yielded single colonies. Cells from single colonies were inoculated into LB media, supplemented with kanamycin antibiotics, for plasmid extraction. The sequences of the selected plasmid were confirmed by DNA sequencing (1st Base, Singapore).

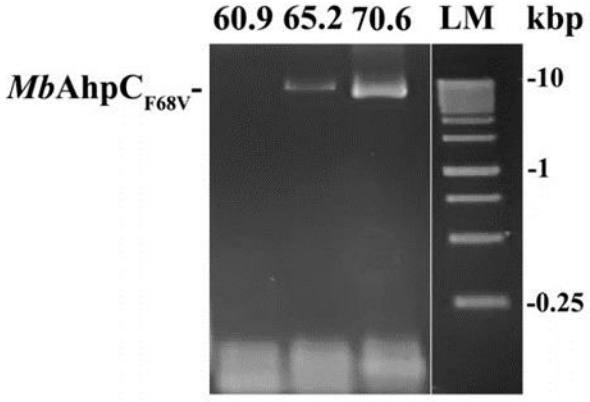

Figure 3.10: PCR amplification results from *Mb*AhpC$_{F68V}$. The numbers above represent the different annealing temperature (°C) chosen. Clear bands were observed at two out of three chosen annealing temperatures. As the agarose gel was ran alongside other samples, a gap was shown between the samples and the LM; [LM (ladder marker)].

3.2.2 Protein Purification of *Mb*AhpC$_{F68V}$

As shown on the SDS-PAGE in figure 3.11, *Mb*AhpC$_{F68V}$ eluted in 100-, 125- and 250 mM imidazole fractions in the absence and presence of DTT. The fractions were pooled together and concentrated before subjecting to SEC to obtain a pure and homogeneous protein. The SEC

elution profile revealed no significant difference for both *Mb*AhpC$_{F68V}$ purified in the absence (Fig. 3.12A, orange) and in the presence (Fig. 3.12A, brown dotted) of DTT, which eluted at approximately 16 ml, reflecting the presence of a dimer.

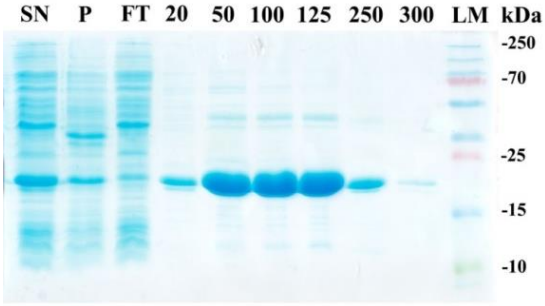

Figure 3.11: Protein purification of *Mb*AhpC$_{F68V}$. SDS-PAGE gel of Ni-NTA chromatography in oxidized conditions show elution at 100-, 125- and 250 mM imidazole fractions.

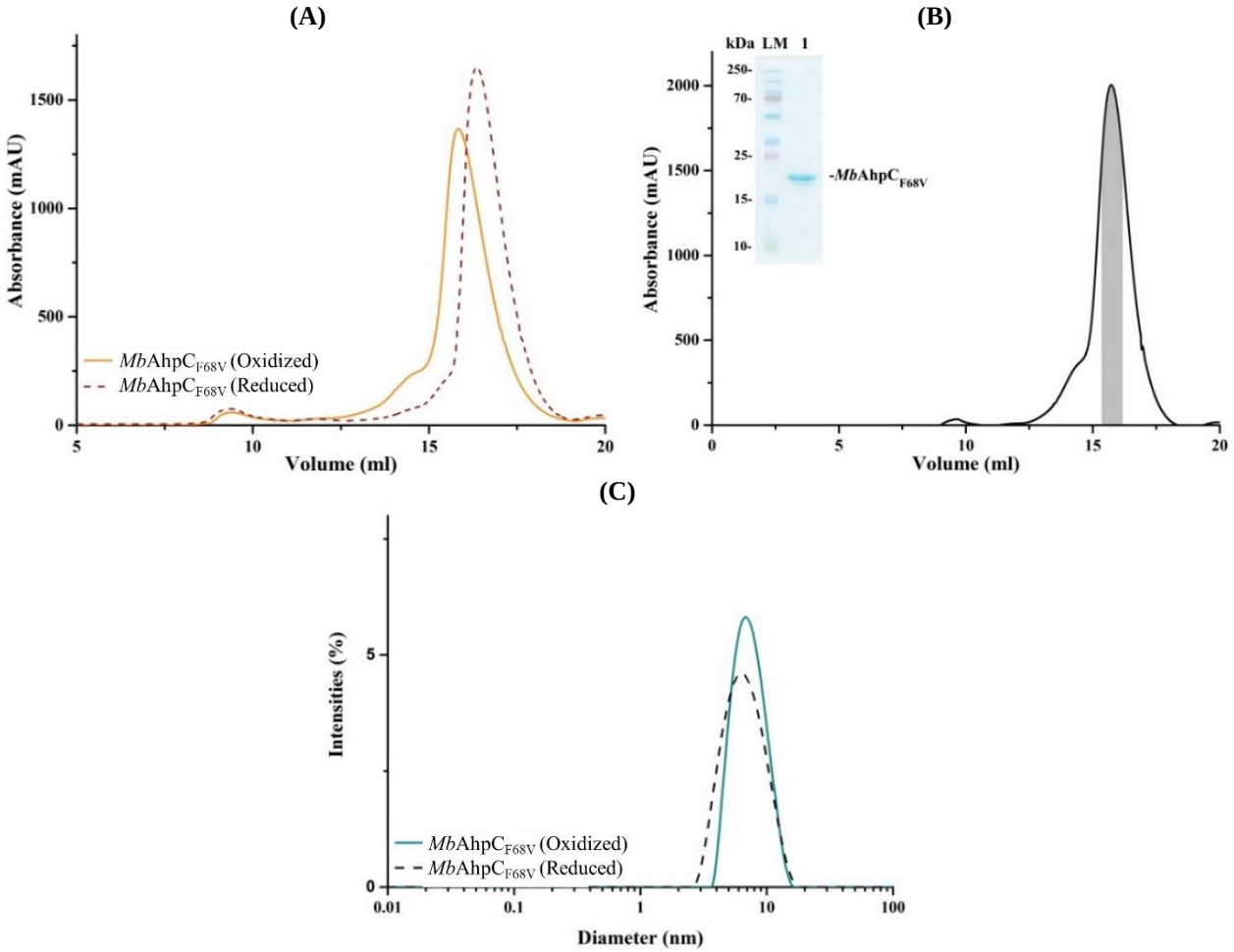

Figure 3.12: SEC and DLS results for *Mb*AhpC$_{F68V}$. (A) Comparison of the elution profile under oxidized (orange) and reduced (brown dotted) conditions. (B) SEC elution profile for the purification under oxidized conditions showed that *Mb*AhpC$_{F68V}$ eluted at approximately 16 ml. The grey border indicates the purified proteins kept and used for analysis. The purity of the protein was confirmed on a 17% SDS-PAGE gel (inset). (C) DLS analysis confirmed a hydrodynamic diameter of approximately 7 nm for both oxidized and reduced recombinant proteins [297].

To further confirm the presence of a dimer, *Mb*AhpC$_{F68V}$ for DLS analysis were obtained from only the top 20% of the eluted proteins from SEC, under both conditions, as highlighted in grey (Fig. 3.12B). The DLS data confirmed the presence of a dimer with a hydrodynamic diameter of 7.5 ± 2.2 nm and 7.0 ± 2.2 nm in the presence and absence of DTT, respectively (Fig. 3.12C).

3.2.3 Enzymatic Assay for single mutants

To study the effect of the single mutation, an enzymatic assay was carried out with stopped-flow spectroscopy, using the Trx-system, where *Mb*AhpC can be reduced by *Mb*TrxC [129]. In a similar fashion, the activity of *Mb*AhpC$_{F68V}$ can be observed from the absorbance of NADPH over 120 s (Fig. 3.13). As *Mb*AhpC$_{F68V}$ has a negligible decline of the NADPH absorbance at 340 nm, it can be inferred that this mutation has effectively hampered the ability of the recombinant protein to carry out electron transfer in this catalytic cycle, and subsequently, disrupting its ability to reduce peroxides.

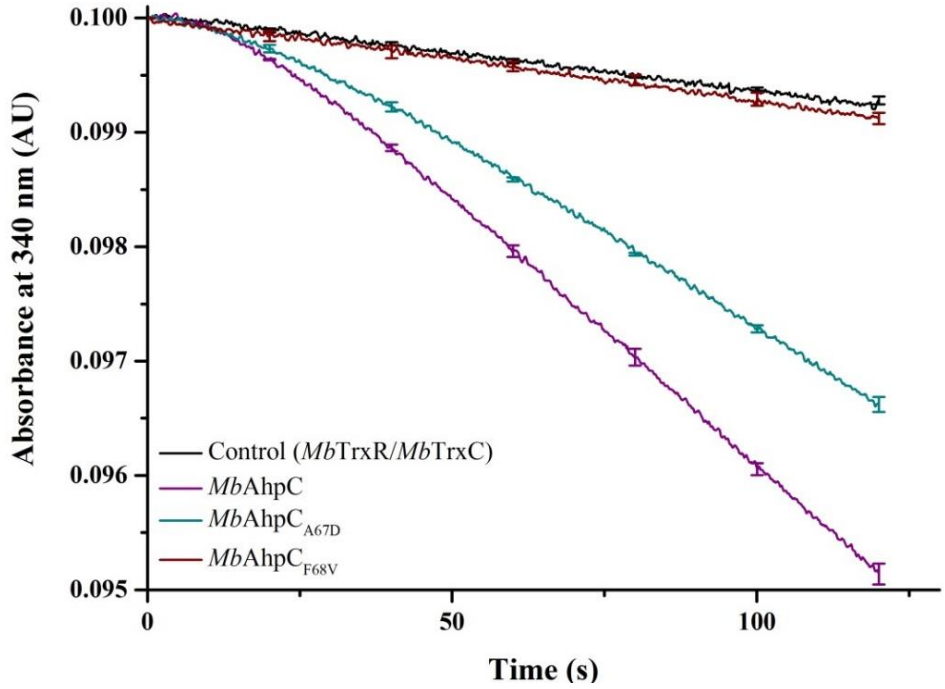

Figure 3.13: Analysis of the enzymatic activity of the recombinant proteins. The black line represents the control whereby no enzymes were added, while the violet line represents the absorbance of WT *Mb*AhpC. *Mb*AhpC$_{F68V}$ (brown) have a decline in absorbance similar to the control. *Mb*AhpC$_{A67D}$ have a significant decline in activity, however, is not as much as WT *Mb*AhpC [297].

3.2.4 FOX Assay with *Mb*AhpC$_{F68V}$

The FOX assay results support the loss of activity with the single mutation, indicating there is a negligible activity for the *Mb*AhpC$_{F68V}$. The decline in the concentration of H_2O_2 in the presence of *Mb*AhpC$_{F68V}$ (as shown in pink) demonstrated no significant difference as compared to the control (Fig. 3.14). WT *Mb*AhpC, as represented in purple, shows a substantial decrease in the concentration of H_2O_2. These results are similar to the enzymatic assay using the Trx-system (Fig. 3.13).

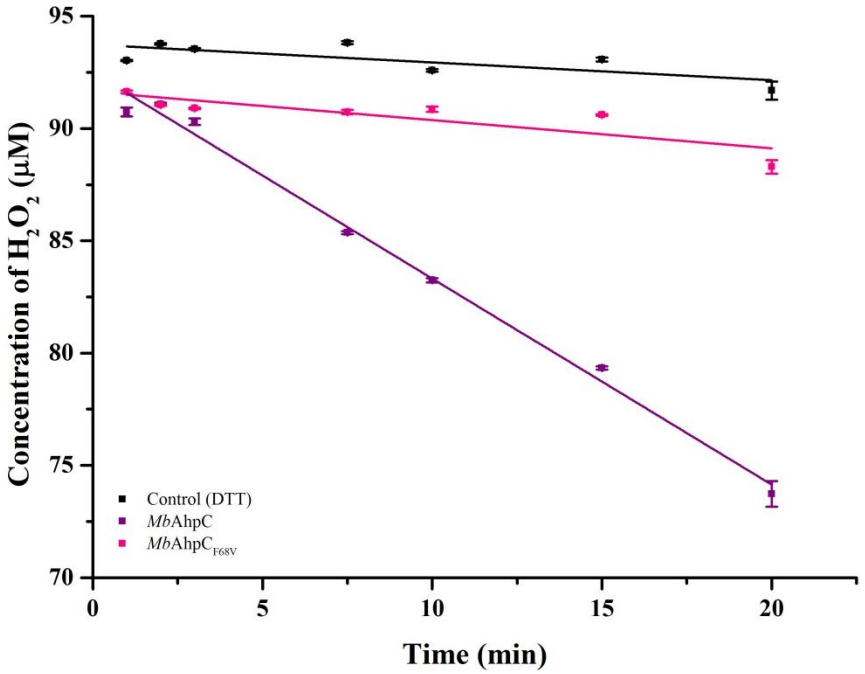

Figure 3.14: FOX assay results of WT *Mb*AhpC and *Mb*AhpC$_{F68V}$. The black line represents the control whereby no enzymes were added, while the violet line represents the absorbance of WT *Mb*AhpC. *Mb*AhpC$_{F68V}$ (pink) have a decline in absorbance similar to the control [297].

The mutation from phenylalanine to valine have inflicted detrimental consequences to the catalytic activity and the dodecameric formation of *Mb*AhpC, revealing the importance of the phenylanaline residue for catalytic activities. The mutation could have prevented the helical displacement of the Cys-S_pH containing helix for disulfide bond formation, preventing efficient electron transfer from DTT or *Mb*TrxC, towards *Mb*AhpC and H_2O_2. It can be inferred that the mutation to valine is the residue that results in the loss of activity for *Mb*AhpC$_{A67D/F68V}$ and *Mb*AhpC$_{A66G/A67D/F68V}$ (Fig. 3.8).

Results

Part 3

Atomic understanding of MbAhpC$_{A67D/C176S}$ to gain strucural insights into the effect of A67D mutation

3.3 Atomic understanding of *Mb*AhpC$_{A67D/C176S}$ to gain strucural insights into the effect of A67D mutation

Efforts in different laboratories to crystalize WT *Mb*AhpC failed [107, 128]. The crystal structure of *Mt*AhpC$_{C176S}$ has allowed the observation of the Cys-S$_p$H containing helix at an elevated position, with a cavity within its structure [107]. Here, crystallization was performed to achieve atomic understanding into the effect of mutagenesis.

3.3.1 Crystallization of *Mb*AhpC$_{A67D}$ and *Mb*AhpC$_{F68V}$

Crystallization was performed on the single mutants, *Mb*AhpC$_{A67D}$ and *Mb*AhpC$_{F68V}$, with the conditions used for crystallization of *Mt*AhpC$_{C176S}$ as published [107]. Numerous optimizations were carried out, such as varying protein concentrations, salt concentration, and the ratio of the drop is to reservoir volume. However, all of them resulted in precipitation. Previously, it has been shown that *Mt*AhpC$_{C176S}$ crystals with good diffraction properties have been grown [107]. In an attempt to crystalize the mutants, molecular cloning was carried out to construct the double mutants, *Mb*AhpC$_{A67D/C176S}$ and *Mb*AhpC$_{F68V/C176S}$, incorporating the C176S mutation.

3.3.2 Site-directed mutagenesis to prepare *Mb*AhpC$_{A67D/C176S}$ and *Mb*AhpC$_{F68V/C176S}$

PCR reactions examined on the agarose gel indicated the presence of bands at approximately 5 kbp at all annealing temperatures for *Mb*AhpC$_{A67D/C176S}$ (Fig. 3.15). For *Mb*AhpC$_{F68V/C176S}$, PCR products were generated at an annealing temperature of 63.6 °C.

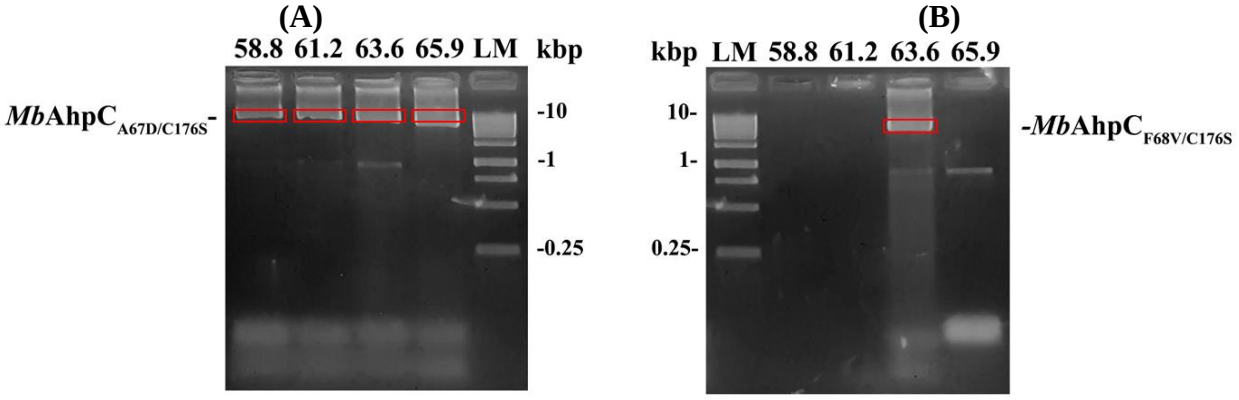

Figure 3.15: PCR amplification results for insertion of the C176S mutation. The agarose gel for (A) *Mb*AhpC$_{A67D/C176S}$ and (B) *Mb*AhpC$_{F68V/C176S}$ are as shown. The numbers above represent the annealing temperature chosen. The presence of the plasmid was indicated in the red frame; [LM (ladder marker)].

The PCR products from 65.9 °C and 63.6 °C for *Mb*AhpC$_{A67D/C176S}$ and *Mb*AhpC$_{F68V/C176S}$, respectively, were then subjected to DpnI treatment. Plasmid amplification was performed with

E. coli DH5α cells, followed by plasmid extraction. The sequences of the selected plasmid were confirmed by DNA sequencing (1st Base, Singapore).

3.3.3 Protein Purification of *Mb*AhpC$_{A67D/C176S}$ and *Mb*AhpC$_{F68V/C176S}$

*Mb*AhpC$_{A67D/C176S}$ and *Mb*AhpC$_{F68V/C176S}$ were generated and purified based on a two-step purification method. The Ni-NTA elution profile analyzed on a 17% SDS PAGE revealed that all the three mutants eluted at 100-, 125- and 250 mM imidazole fractions in the absence of DTT (Fig. 3.16). The three fractions were pooled together and concentrated before subjecting to SEC, utilizing a buffer without NaCl, as the presence of salt interferes with crystallization. Interestingly, without the presence of salt, the SEC elution profile reveals the elution of *Mb*AhpC$_{A67D/C176S}$ and *Mb*AhpC$_{F68V/C176S}$ at approximately 14 ml instead of 16 ml. This indicates that the salt prevents oligomerization of the protein. The top 20% of the eluted proteins, as highlighted in grey in figure 3.16, were utilized for crystallization.

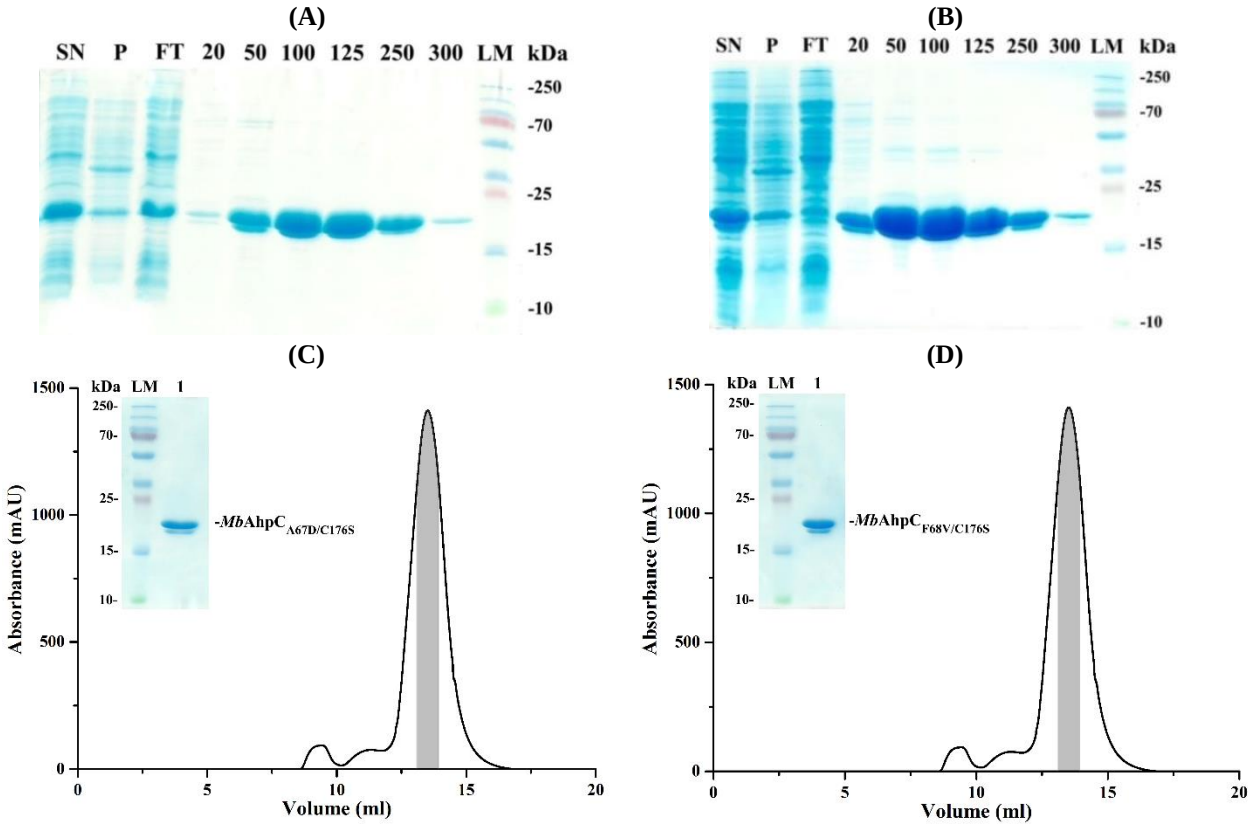

Figure 3.16: SDS-PAGE gel of Ni-NTA fractions and SEC chromatograph of *Mb*AhpC$_{A67D/C176S}$ and *Mb*AhpC$_{F68V/C176S}$. The SDS-PAGE gel of Ni-NTA fractions (A) *Mb*AhpC$_{A67D/C176S}$ and (B) *Mb*AhpC$_{F68V/C176S}$; [SN (supernatant), P (pellet), F (flow through), LM (ladder marker)], and SEC chromatograph of (C) *Mb*AhpC$_{A67D/C176S}$, and (D) *Mb*AhpC$_{F68V/C176S}$ under oxidized conditions.

3.3.4 Crystallization of *Mb*AhpC$_{F68V/C176S}$

*Mb*AhpC$_{F68V/C176S}$ was purified, and drops were first set up with the conditions as published for *Mt*AhpC$_{C176S}$ (0.1 M sodium citrate, 16% ammonium sulfate, pH 6.0 at 18^{o}C) [107] with variations in the protein concentration and protein: reservoir ratio, using the hanging drop method. However, most conditions resulted in precipitation. Further optimization was carried out, with adjustment of the salt concentration, optimization of the pH, along with further drop size variation. Nevertheless, most drops prepared for *Mb*AhC$_{F68V/C176S}$ did not indicate any improvement (Fig. 3.17). Sitting drop, temperature change, and overlaying with oil were also attempted, with no avail.

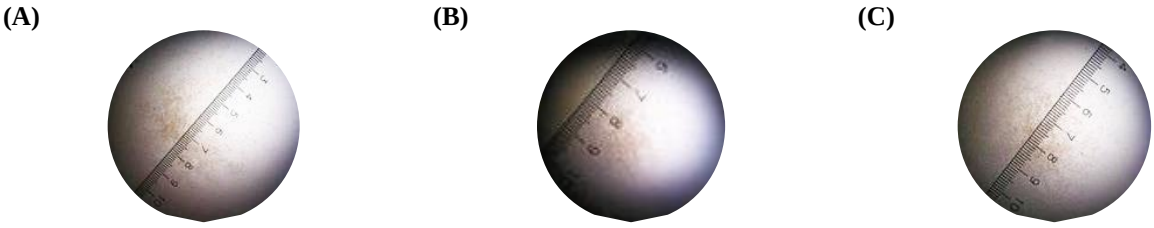

Figure 3.17: Crystallization of *Mb*AhpC$_{F68V/C176S}$. The drops are set using the hanging drop method, with 350 µl of mother liquor (0.1 M sodium citrate and 16% ammonium sulfate), at a ratio of protion to mother liquor at 1 µl : 1 µl, and a protein concentration of 8 mg/ml. The drops here show the results after pH variations, including pH values of (A) 5.4, (B) 6.0 and (C) at 6.4.

3.3.5 Crystallization of *Mb*AhpC$_{A67D/C176S}$

*Mb*AhpC$_{A67D/C176S}$ was purified, and drops were first set up with the conditions as published for *Mt*AhpC$_{C176S}$ [107]. The optimization process of the crystals is displayed in figure 3.18. Different protein concentrations and drop variations were carried out initially, yielding small plate-like crystals at protein concentration of 3 mg/ml and a drop variation of 1:1 (protein : reservior) (**B**). Optimizations with varying sodium citrate concentrations, ammonium sulfate concentrations, and pH were performed, revealing that thicker and larger (approximately 1 mm) were obtained at pH 6.4 with 0.1 M sodium citrate and 16% ammonium sulfate (**G**). Crystals were picked and soaked in cryoprotectant before flash freezing with liquid nitrogen to 100 K in liquid nitrogen for in-house x-ray diffraction. However, the crystals were unable to diffract.

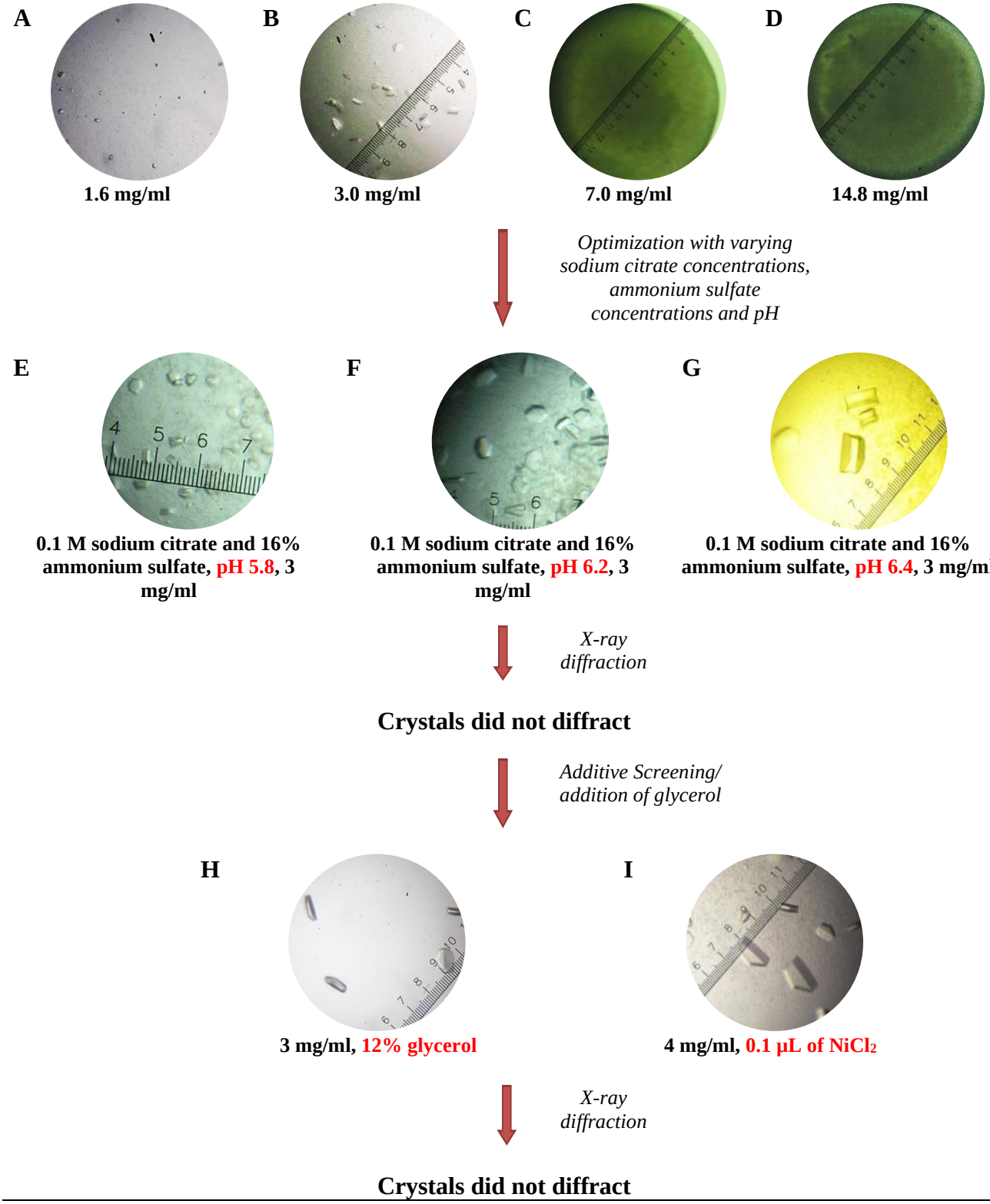

Figure 3.18: Flowchart representing initial steps taken to crystallize *Mb*AhpC$_{A67D/C176S}$. Initial conditions used were 0.1 M sodium citrate, 16% ammonium sulfate at pH 6.0.

Further optimizations were carried out, with the addition of glycerol and additive screening, each time using a variation of protein concentration. Nevertheless, despite the concentration of glycerol used, the best crystals were observed with the addition of 12% glycerol, which were small and flat. With the addictive screening, the addition of nickel (II) chloride yielded crystals of approximately 1 mm in size. However, in-house x-ray diffraction revealed the crystals obtained were unable to diffract. Hence, as previous SDS-page gel of *Mb*AhpC$_{A67D/C176S}$ from SEC indicated slight impurities after the purification, a three-step purification was attempted to obtain a purer form of the protein.

3.3.6 Protein Purification of *Mb*AhpC$_{A67D/C176S}$ with three-step purification

*Mb*AhpC$_{A67D/C176S}$ was purified with the inclusion of an anion exchange chromatography. The proteins eluted similarly at 100-, 125- and 250 mM imidazole fractions in the Ni-NTA step, and the three fractions were pooled together before subjecting to the anion exchange column. The protein eluted at approximately 51 ml at 36% of elution buffer, 360mM NaCl, and the fractions collected were analyzed on a 17% SDS-PAGE (Fig. 3.19). The SDS-PAGE revealed the presence of proteins, where a clean band was observed between fractions 1 to 7. The two smaller peaks that elute at approximately 56 ml and 60 ml were collected and analyzed on a 17% SDS-PAGE as fractions 8 and 9. As these fractions contain impurities of a lower molecular weight, fraction 1 to 7 were subjected to SEC. The top 50% of the proteins were collected and concentrated before subjecting to SEC.

The SEC elution profile reveals that the protein elutes at 14 ml, indicating that the absence of salt promotes oligomerization. The chromatogram obtained after anion exchange chromatography indicated the presence of only one fraction (Fig. 3.20) as compared to the previous SEC obtained directly after the affinity chromatography (Fig 3.16). The purity of the protein was confirmed on a 17% SDS-PAGE. The top 20% of the eluted proteins, as highlighted in grey in figure 3.20, was utilized for crystallization.

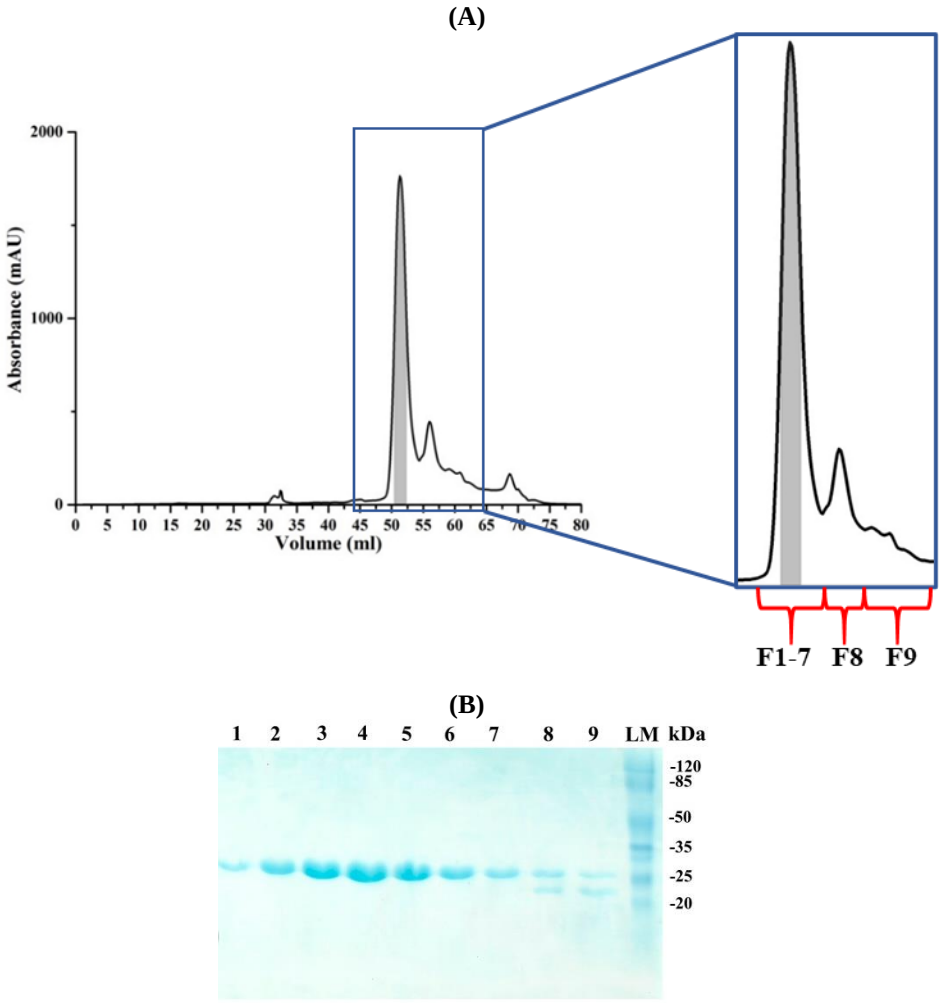

Figure 3.19: Anion exchange chromatography elution profile of *Mb*AhpC$_{A67D/C176S}$. (A) Elution profile for the purification in the absence of DTT. The grey border indicates the purified proteins collected for injection into the SEC. The fractions collected (F1-9) were indicated in the chromatogram. These fractions were analyzed on a 17% SDS-PAGE shown in (B), revealing the higher purity of proteins obtained after the anion exchange chromatography.

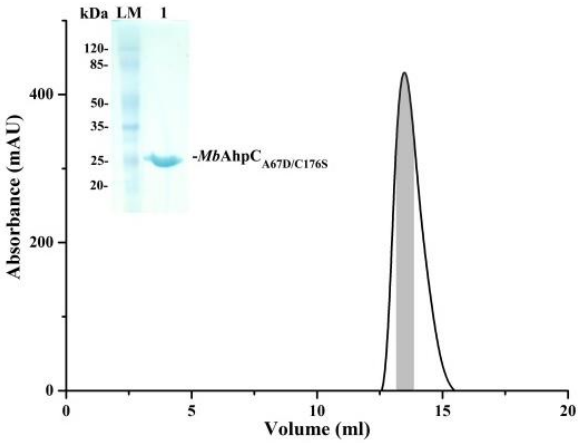

Figure 3.20: SEC elution profile of *Mb*AhpC$_{A67D/C176S}$. The purification was carried out under oxidized conditions (20 mM Tris/HCl, pH 7.5). The grey border indicates the purified proteins kept and used for analysis. The purity of the protein was confirmed on a 17% SDS-PAGE gel (inset).

3.3.7 Structural insights into *Mb*AhpC$_{A67D/C176S}$ with crystallization

The crystal drops were set-up using vapour diffusion with 0.1 M sodium citrate, 16% ammonium sulfate, at pH 6.4, as larger crystals were obtained in this condition previously.

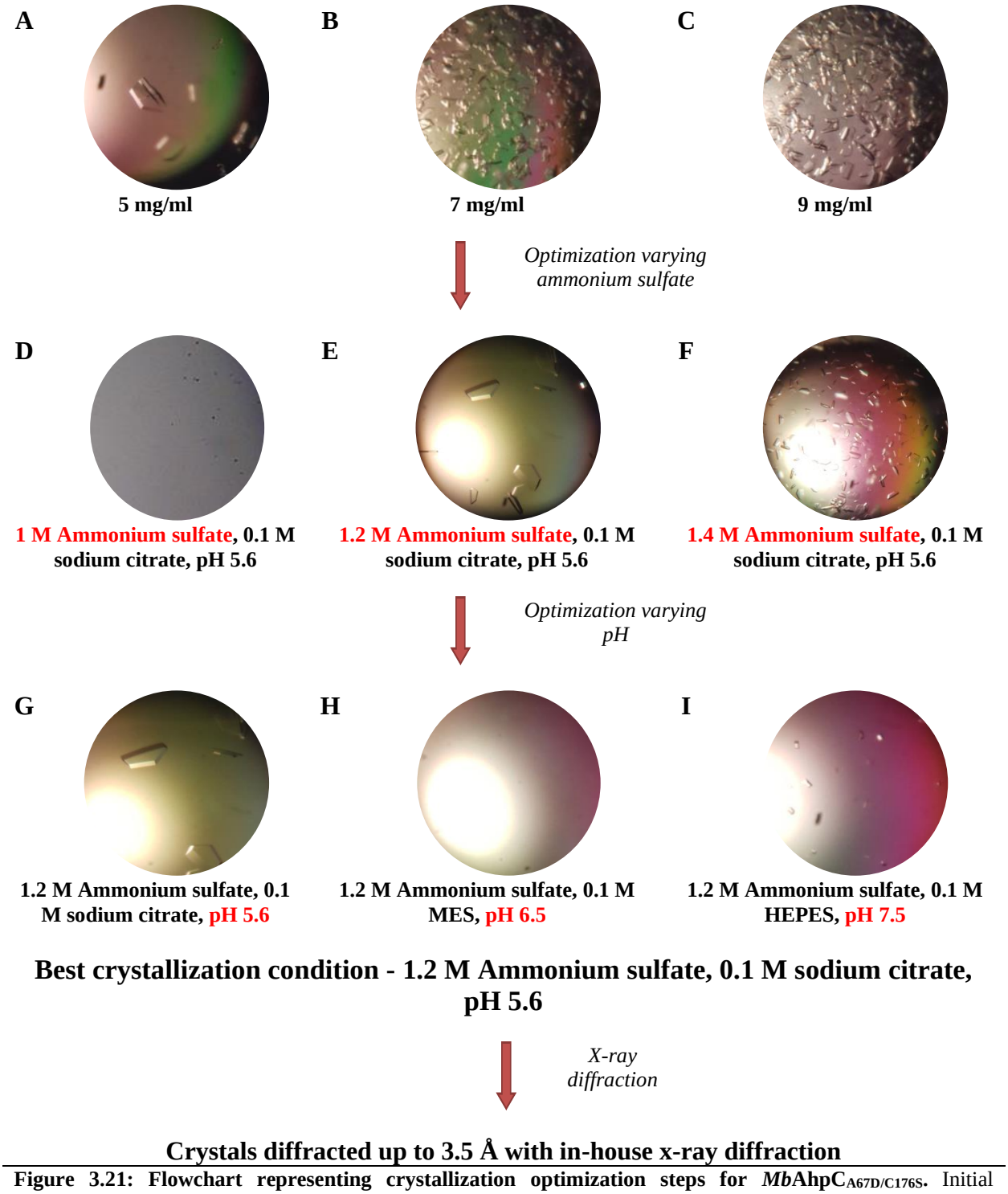

Figure 3.21: Flowchart representing crystallization optimization steps for *Mb*AhpC$_{A67D/C176S}$. Initial condition used were 0.1 M sodium citrate, 16% ammonium sulfate at pH 6.0.

Protein concentration variation indicated crystals obtained at 5 mg/ml **A** (Fig. 3.21). However, these crystals were not of sufficient thickness, and higher protein concentrations (7 mg/ml **B** and 9 mg/ml **C**) resulted in much smaller and plate-like crystals. Hence, optimization was carried out sequentially by varying the concentration of ammonium sulfate and the pH. A range of buffers was prepared, with concentrations of ammonium sulfate varying from 1 M to 1.4 M, and pH ranging from 5.6 to 10.4. Different buffers were tested with a concentration of 0.1 M. *Mb*AhpC$_{A67D/C176S}$ of 5 mg/ml, 7 mg/ml, and 9 mg/ml were set up at all conditions. At 1 M ammonium sulfate concentration, clear drops were present despite different protein concentrations or pH (not shown). A higher concentration of salt was necessary for crystal formation. However, at a high pH along with 1.2 M or 1.4 M of ammonium sulfate concentrations, formation of very small needle-like crystals was observed (not shown).

The best crystals were found under the condition of 1.2 M Ammonium sulfate, 0.1 M sodium citrate, pH 5.6 **E**. The crystals were approximately 1 mm in size and are slightly thicker than those found previously. These crystals were soaked in cryoprotectant and flash frozen to 100 K in liquid nitrogen before sending for in-house x-ray diffraction. The crystals were found to diffract up to 3.5 Å. Nevertheless, despite various data processing methods, the R_{work} and R_{free} values, which assesses the quality of the crystal model, could not be improved. This indicates a discrepancy between the crystal model and the experimental data, which reflected on the quality of the crystals.

Best crystallization condition - 1.2 M Ammonium sulfate, 0.1 M sodium citrate, pH 5.6

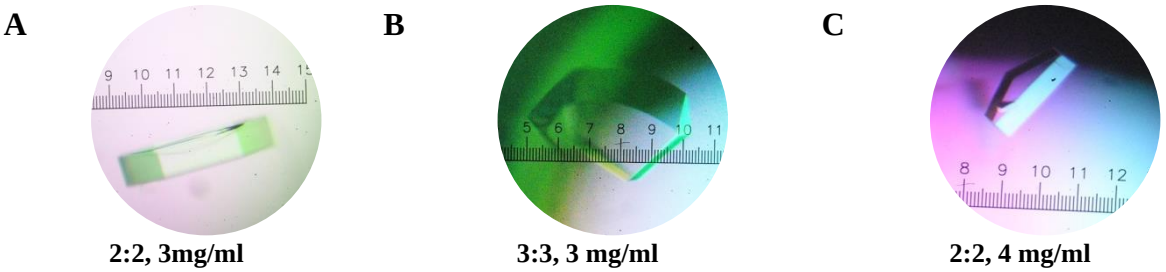

Figure 3.22: Visual representation of *Mb*AhpC$_{A67D/C176S}$ crystals obtained with a larger drop size. Ratios represents amount of drop:reservior.

In the hope of increasing the size of the crystal, further optimizations such as varying drop to reservoir ratios, attempting sitting drop, overlaying with oil, increasing drop size, or decreasing reservoir volume, were performed to reduce the diffusion rate. The best crystals were obtained

with a larger drop size, with crystal size of up to 4 mm and approximately 1 mm thickness (**A, B, C**) (Fig. 3.22).

The synchrotron dataset was collected and analyzed with the guidance of Dr. N. Kamariah from Professor G. Grüber's laboratory. The crystals were soaked in cryoprotectant solution containing 30% glycerol and flash frozen to 100 K in liquid nitrogen. Single wavelength datasets were remotely collected at 100 K on beamline 13B1 at the National Synchrotron Radiation Research Center (NSRRC, Hsinchu, Taiwan) (Fig. 3.23). Data were collected as a series of 0.5^{o} oscillation images with 7 s exposure time, covering a crystal rotation range of 240^{o}, at a detector distance of 400 mm. All diffraction data were indexed, integrated, and scaled using the HKL2000 suite of programs.

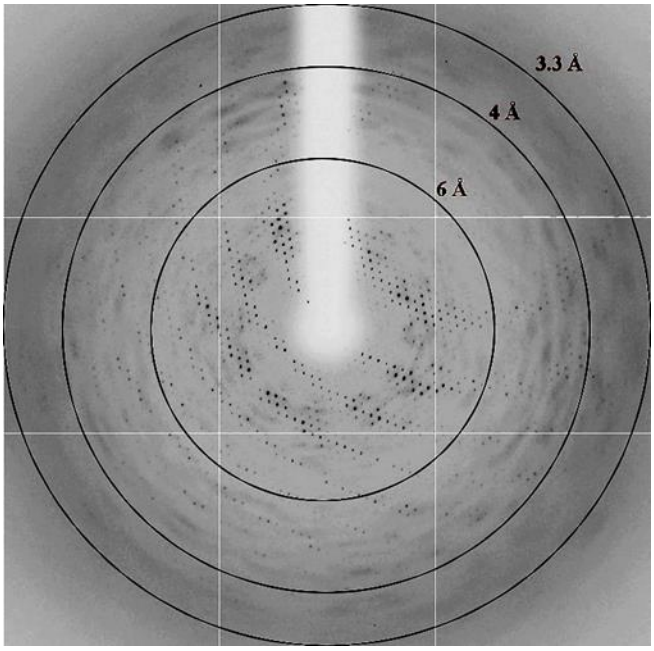

Figure 3.23: Diffraction pattern obtained from the NSRRC of *Mt*AhpC$_{A67D/C176S}$.

The crystallographic structure of oxidized *Mt*AhpC$_{C176S}$ (PDB ID: 2BMX) [107] was used as a model for molecular replacement by the program PHASER [266], and PHENIX [263] was used for the refinement and validation of the structure. The summary of data collection and refinement parameters is shown in table 3.2. The $CC_{1/2}$ was found to be 89.6% for the highest resolution shell and 97.9% for the entire data set, supporting the resolution cutoff at 3.3 Å [299]. The Matthews coefficient [300] confirmed the presence of two molecules in the asymmetric unit with a corresponding solvent of 59.9%. The statistics presented in table 3.2 indicates that the diffraction data were of reasonable quality.

Data Collection Statistics	
Temperature (K)	100
Wavelength (Å)	1.00
Resolution Range (Å)	30-3.3
Crystal system	Hexagonal
Space group	P622
Unit Cell parameters (Å)	a=b=137.55, c= 96.842 $\alpha = \beta = 90^{\circ}, \gamma = 120^{\circ}$
Total number of reflections	101079
Unique reflections	8,566
R_{merge}[b](%)	6.2 (42.9)
Completeness (%)	98 (88.1)
Average I/**σ** (I)	28.3 (1.9)
No of molecules in asymmetric unit	2
CC*	99.5 (97.2)
$CC_{1/2}$	97.9 (89.6)
Redundancy	11.8 (4.0)
R factor (%)	30.95
R free (%)	34.44
Number of amino acid residues	349
Ramachandran Most favoured (%)	95.65
Ramachandran Outliers (%)	0.0
Clash score	9.25
Molprobity score	2.19

Table 3.2: Summary of crystallographic data collection for *Mb*AhpC$_{A67D/C176S}$. Values in parentheses represent the corresponding values of the highest resolution shell (3.42 – 3.30 Å)

3.3.8 Crystal structure of *Mt*AhpC$_{A67D/C176S}$

The crystal structure of *Mb*AhpC$_{A67D/C176S}$ at 3.3 Å resolution contains two molecules (Chain A – Chain B) in each asymmetric unit, forming a dimer (Fig. 3.24A). Chain A and chain B consists of 170 and 179 residues, respectively. The backbone of the crystal structure was well resolved, except for residues 17, 18, 21, 26, 34, 60, 113 on chain A and residues 17, 18, 89, 98 on chain B, which are poorly defined. In the crystal, *Mb*AhpC$_{A67D/C176S}$ associates to form a dodecameric ring, like the case of *Mb*AhpC$_{C176S}$ (Fig. 3.24B). Nevertheless, the formation of the dodecameric ring could be due to the crystal packing force, as both the DLS and SEC results shown in section 3.1.2 have demonstrated the incapability of *Mb*AhpC$_{A67D}$ to form a dodecamer even under reduced conditions. Additionally, the purification of *Mb*AhpC$_{A67D/C176S}$ in the absence of salt promoted oligomerization as observed from the SEC purification at 14 ml (Fig. 3.20).

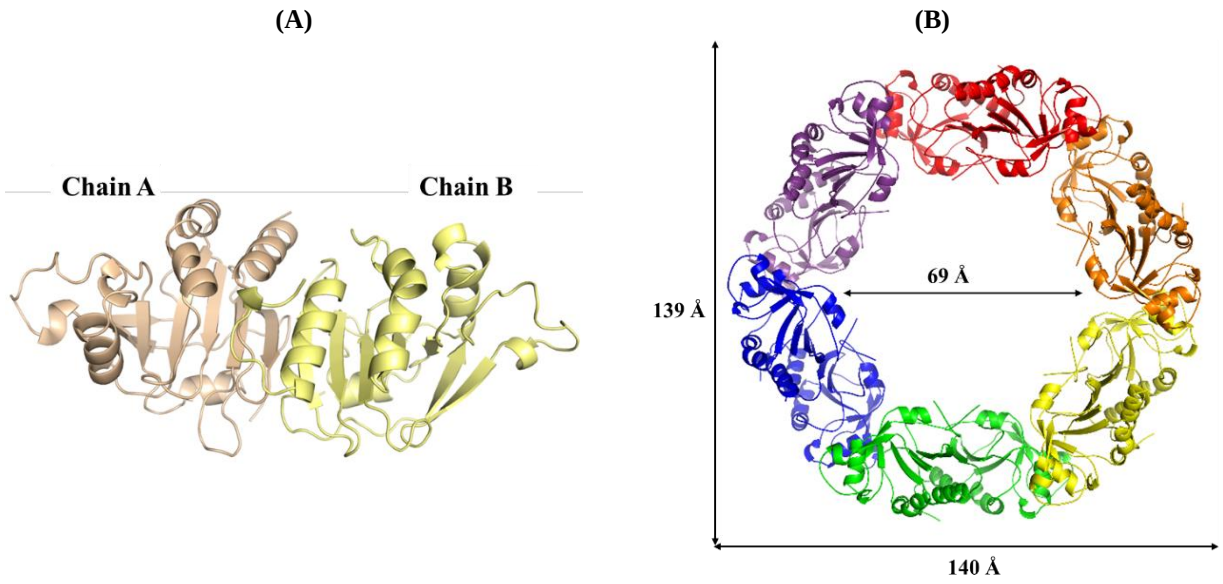

Figure 3.24: Crystal structure of *Mt*AhpC$_{A67D/C176S}$. (A) Representation of one asymmetric unit of *Mt*AhpC$_{A67D/C176S}$, consisting of two molecules (A-B), forming a dimer. (B) Dodecameric ring formation with an outer diameter of approximately 140 Å and inner diameter of approximately 70 Å [297].

From the electron density map, a lack of electron density was found for the disulfide bonding between C61 (of chain A) and C174 (of chain B) (Fig. 3.25). The distance of the backbone between C61 and C174 is 5.3 Å in *Mb*AhpC$_{A67D/C176S}$ (shown in red), in comparison to 5.7 Å in the *Mt*AhpC$_{C176S}$ structure (shown in green) (Fig. 3.25), demonstrating that the cysteine residues are in close proximity for disulfide bond formation. Hence, the lack of electron density for the disulfide bond might be due to radiation damage, as disulfide bonds are usually the most susceptible to radiation damage, where the disulfide bonds stretch before breaking apart [301].

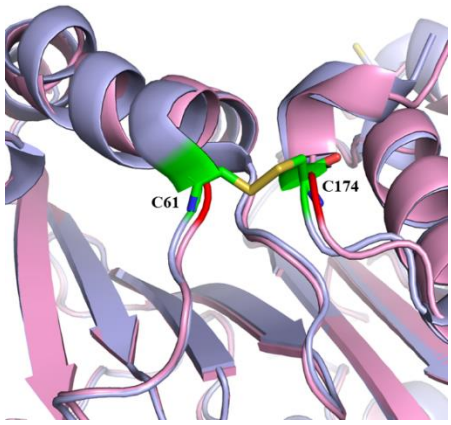

Figure 3.25: Comparison of *Mt*AhpC$_{C176S}$ and *Mb*AhpC$_{A67D/C176S}$. An overlap of *Mt*AhpC$_{C176S}$ (PDB ID: 2BMX) [107] (blue) on *Mb*AhpC$_{A67D/C176S}$ structure (pink). C61 of chain A and C174 of chain B for *Mt*AhpC$_{C176S}$ were shown in green for *Mt*AhpC$_{C176S}$ while C61 and C174 were indicated in red for MbAhpC$_{A67D/C176S}$ [297].

3.3.8.1 Helical displacement of Cys-S_pH containing helix

Similar to the crystal structure of *Mt*AhpC$_{C176S}$ (PDB: 2BMX), the Cys-S_pH containing helix was demonstrated to adopt an elevated position (Fig. 3.26), indicating *Mt*AhpC$_{A67D/C176S}$ was crystallized in the oxidized state. This contrasts with the oxidized *St*AhpC (PDB ID: 1YEX) which can be observed in figure 3.26. The Cys-S_pH containing helix of *St*AhpC is lowered, in comparison to *Mt*AhpC$_{A67D/C176S}$. Further analysis revealed the effect of the A67D mutation on the helix itself, where the flexibility of the helix is likely impacted, especially in chain B of the crystal structure (figure 3.27B). The Cys-S_pH containing loop prior to the A67D mutation demonstrated a significant structural change, indicating the effect of the mutation on the structure and flexibility of this helix and loop. Figure 3.27C includes the electron density map for the Cys-S_pH containing helix of chain B.

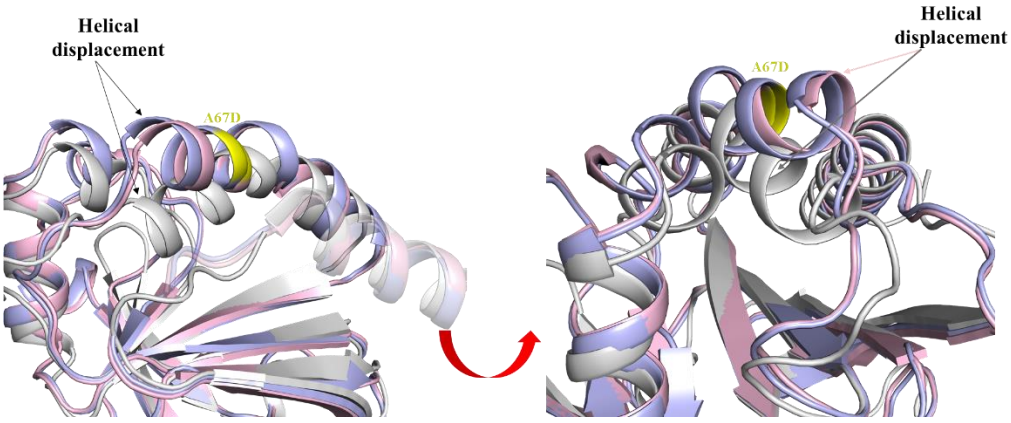

Figure 3.26: Comparison of *Mt*AhpC$_{C176S}$, *Mb*AhpC$_{A67D/C176S}$ and *St*AhpC. Cartoon representation of *Mb*AhpC-$_{A67D/C176S}$ (pink), *Mt*AhpC$_{C176S}$ (blue) (PDB ID: 2BMX) [107] and *St*AhpC (grey) (PDB ID: 1YEX) [115]. *Mb*AhpC-$_{A67D/C176S}$ and *Mt*AhpC$_{C176S}$ were observed to have the helix containing the catalytic cysteine at an elevated position, in contrast to the oxidized *St*AhpC.

Chain B of *Mb*AhpC$_{A67D/C176S}$ appears to possess an unwinding mechanism, resembling that of *St*AhpC. During oxidation of the *St*AhpC, unwinding of the α-helix that contains the Cys-S_PH occurs, positioning the Cys-S_PH and Cys-S_RH at a much closer distance for the disulfide bond formation to occur [255]. This unwinding, which is shown in Chain B, could reflect that the protein is trapped in an intermediate conformation, and could signify the effect of the A67D mutation, causing an increase in flexibility. From figure 3.27B, a shift in the position of the Cys-S_PH that occurs along with the unwinding mechanism can be observed, possibly bringing the Cys-S_PH closer to the Cys-S_RH. However, as chain A consists of only the first 170 residues, the interacting Cys-S_RH at residue 174 could not be observed.

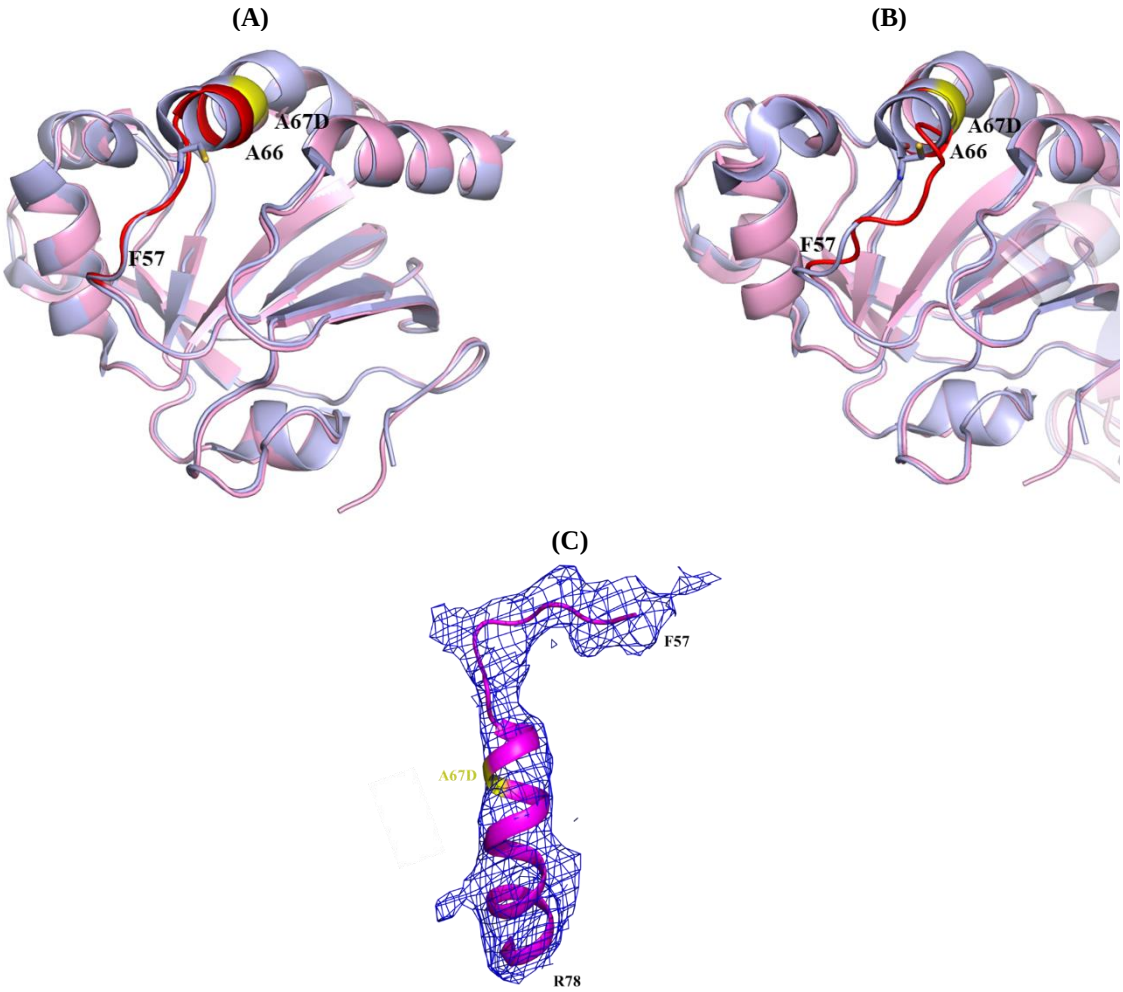

Figure 3.27: Crystallographic structure of *Mb*AhpC$_{A67D/C176S}$ reveals a shift on the α-helix. (A) An overlap of *Mt*AhpC$_{C176S}$ (PDB ID: 2BMX) (blue) on *Mb*AhpC$_{A67D/C176S}$ structure (pink) of chain A, indicating no significant difference in the Cys-S_pH containing helix. (B) In contrast to the Cys-S_pH containing helix on chain A, chain B have a shorter helix, resembling an unwinding mechanism that is found in *St*AhpC. The unwinding of this helix is marked in red. (C) The electron density map ($2F_o$-F_C) for *Mb*AhpC$_{A67D/C176S}$ chain B [297].

3.3.8.2 Disruption of the oligomerization

Analysis into the dimer-dimer interface revealed an alteration in the loop near the oligomeric interface, as highlighted in magenta (Fig. 3.28). The loop was slightly more inwards in *Mb*AhpC$_{A67D/C176S}$ as compared to *Mb*AhpC$_{C176S}$, possibly preventing the hydrophobic interaction at the interface. Additionally, residue F57 is directly involved in the hydrophobic interaction on the oligomeric interface, and a shifting of these residues could result in the loss of oligomerization (Fig. 3.30). This supports the SEC and DLS analysis, where *Mb*AhpC$_{A67D}$ is present as a dimer even under reduced conditions.

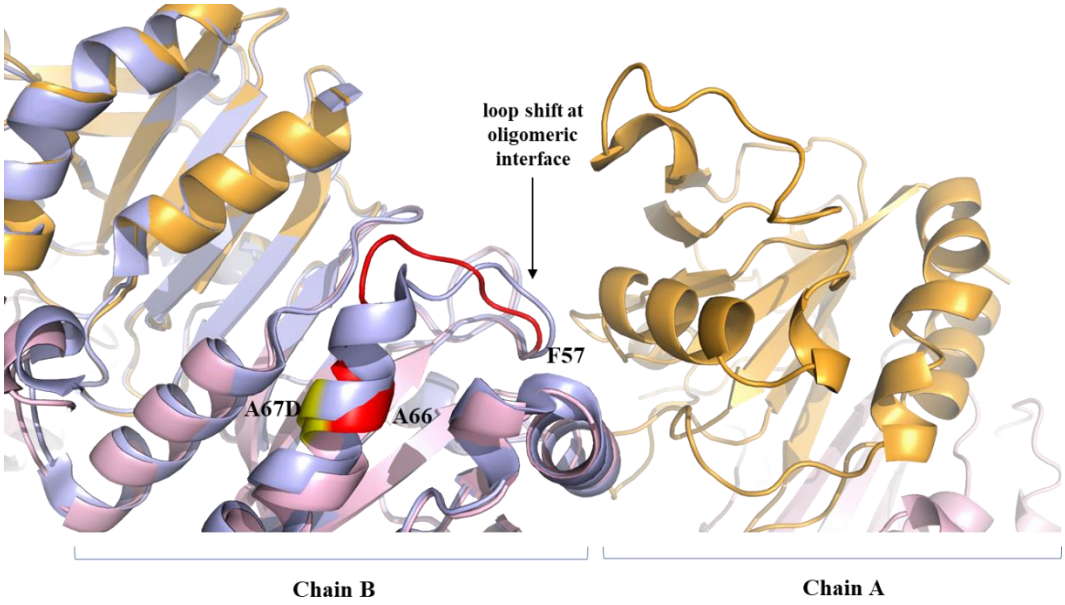

Figure 3.28: Dodecameric structure of *Mb*AhpC$_{A67D/C176S}$ with an overlap of *Mt*AhpC$_{C176S}$. An overlap of *Mb*AhpC$_{A67D/C176S}$ (brown – chain A, pink – chain B) with MtAhpC$_{C176S}$ (blue) reveals the loop (red) is away from the oligomeric interface for dimer-dimer interaction [297].

Results

Part 4

Residue A92 is important for oligomeric formation and activity

3.4 Residue A92 is important for oligomeric formation and activity

3.4.1 Site-directed mutagenesis for *Mb*AhpC$_{A92R}$

Previous mutagenesis studies carried out on *St*AhpC have indicated the importance of the decameric ring formation to reduce peroxides at its full potential [115]. Various factors could affect the ability of AhpC to form the decameric ring. In *Ec*AhpC, the truncated C-terminal mutants were found to inhibit decameric ring formation, while in *Mb*AhpC, deletion of N-terminal residues (23-34) revealed the presence of a dimer even under reduced conditions [128, 255]. Parsonage *et al*. (2005) have demonstrated a disruption of the oligomeric ring, along with an impairment in its catalytic efficiency, by preparing a single mutation, T77, which resides at the oligomeric interface [115]. Here, a mutation on the oligomeric interface was prepared to study the importance of the oligomerization in the case of *Mt*AhpC. Analysis of the *Mt*AhpC$_{C176S}$ and *St*AhpC crystal structure was performed, which led to the identification of the residue that coincides with T77, as A92 (Fig. 3.29).

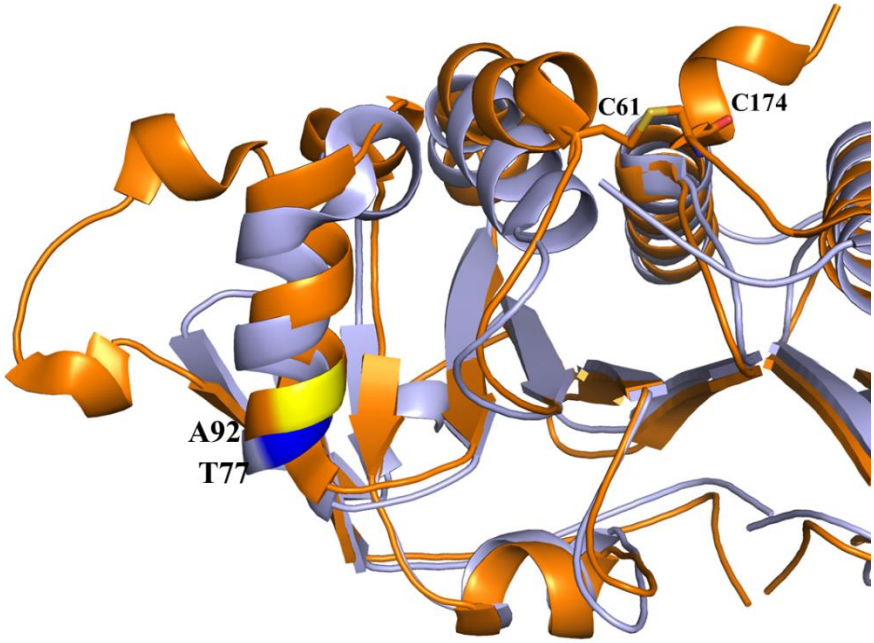

Figure 3.29: Comparison of *Mt*AhpC$_{C176S}$ and *St*AhpC. Crystallographic structure of *Mt*AhpC$_{C176S}$ (orange) (PDB ID: 2bmx) with overlaps from *St*AhpC (pink) (PDB ID: 1yep) [107, 115]. Cyan indicates T77 on *St*AhpC while yellow indicates the residue on *Mt*AhpC$_{C176S}$ that overlaps T77. This residue is A92.

As the oligomeric-building interface relies on its hydrophobic interaction for the formation of the dodecamer ring (Fig. 3.30), a mutation from alanine to arginine was carried out to insert a charged, and a much larger residue. This serves to disrupt the formation of the oligomeric ring, and at the same time, conserve the active site.

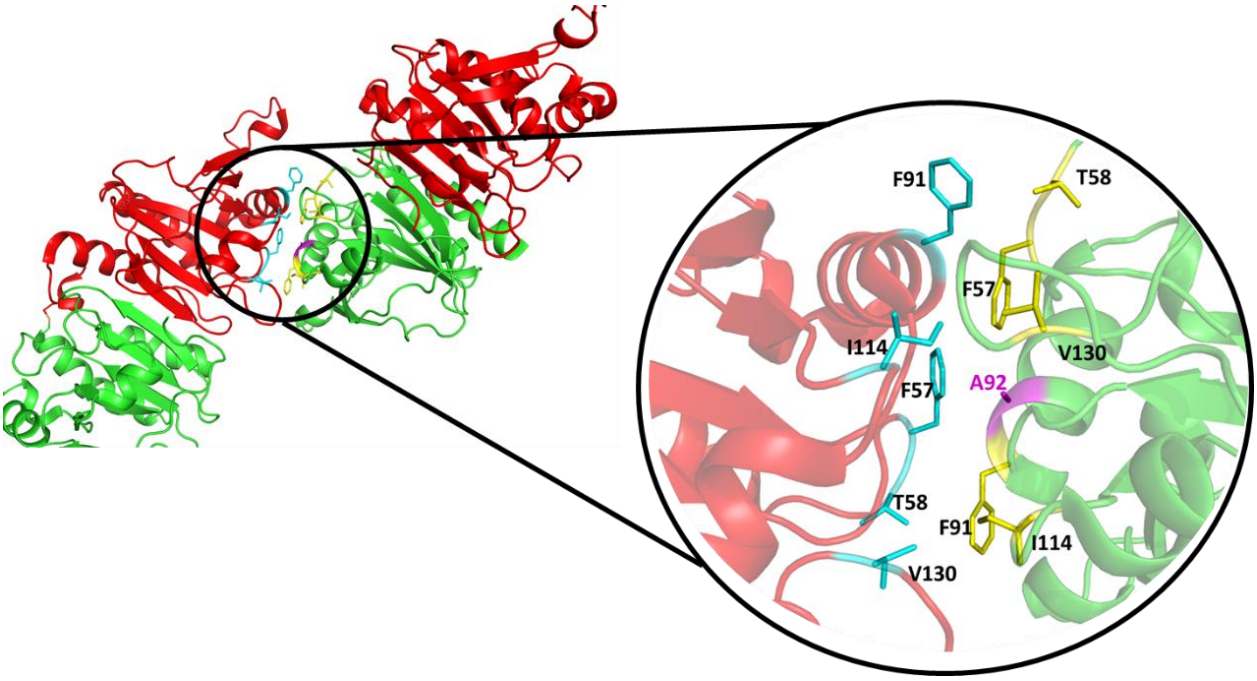

Figure 3.30: Cartoon representation of *Mt*AhpC$_{C176S}$ crystallographic structure. The hydrophobic interaction that helps to stabilize the oligomeric interface was as shown. Green and red indicates the different monomer and the blue and yellow side chains depict the interactions between the monomers (PDB ID: 2BMX) [107].

The first PCR was unsuccessful as no bands were observed at approximately 5 kbp from the agarose gel electrophoresis, despite employing a range of annealing temperatures (not shown). The PCR reaction was repeated, with an alteration in the choice of buffer. Initially, GC buffer was utilized due to the high GC content of the template DNA. As this was not successful, HF buffer was used instead, as it has a lower error rate (4.4×10^{-7}) as compared to GC buffer (9.5×10^{-7}) [302]. The utilization of the HF buffer was successful, as the agarose gel electrophoresis revealed clear bands at approximately 5 kbp, at annealing temperatures of 70 ^{o}C for *Mb*AhpC$_{A92R}$ (Fig. 3.31).

Prior to DNA sequencing (1st Base, Singapore), DpnI treatment was carried out to remove the methylated template DNA. The plasmid was then transformed into *E. coli* DH5α cells for plasmid amplification, followed by plasmid extraction.

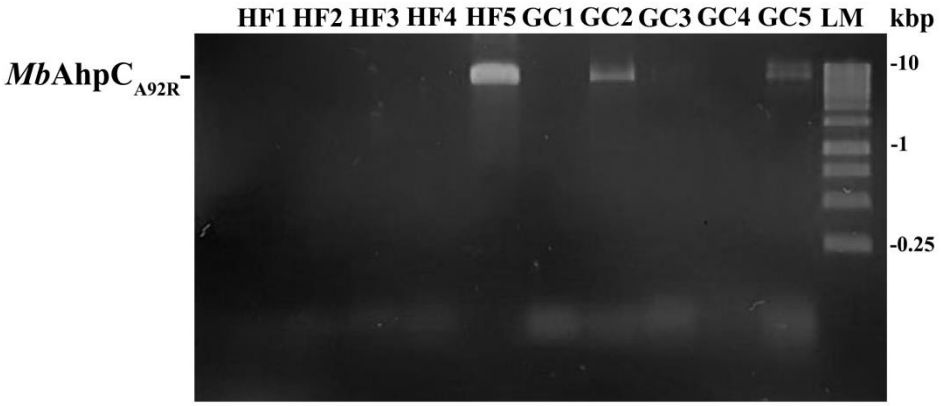

Figure 3.31: PCR amplification results of *Mb*AhpC$_{A92R}$. HF represents the use of HF buffer while GC represents the use of GC buffer. The numbers 1, 2, 3, 4 and 5 represents temperatures of 50, 54, 61.2, 65.9, 70 °C, respectively; [LM (ladder marker)].

3.4.2 Protein production and purification of *Mb*AhpC$_{A92R}$

Once the DNA sequence of the *Mb*AhpC$_{A92R}$ plasmid was confirmed, the plasmid was transformed into *E. coli* BL21(DE3) expression cell strain for protein expression. A two-step protein purification was implemented, with the first step involving Ni-NTA affinity chromatography, with increasing concentrations of imidazole for competitive elution of the protein. The Ni-NTA elution profile analyzed on a 17% SDS gel revealed that *Mb*AhpC eluted mainly at 100-, 125- and 250 mM imidazole fractions in both the presence and absence of the reducing agent, DTT (Fig. 3.32). The three fractions were pooled together and concentrated before subjecting to SEC.

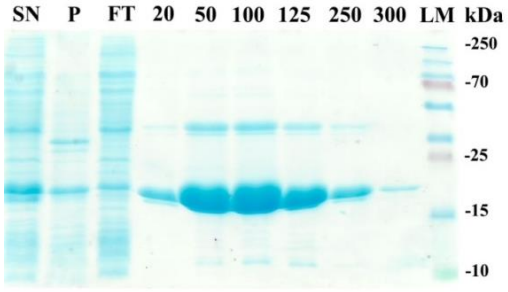

Figure 3.32: Protein purification of *Mb*AhpC$_{A92R}$. SDS-PAGE gel of Ni-NTA chromatography in oxidized conditions show elution at 100-, 125- and 250 mM imidazole fractions.

Interestingly, under oxidized conditions, *Mb*AhpC$_{A92R}$ eluted as two peaks, with the first peak of *Mb*AhpC$_{A92R}$ (*Mb*AhpC$_{A92R-1}$) at approximately 14.8 ml, and the second peak of *Mb*AhpC$_{A92R}$ (*Mb*AhpC$_{A92R-2}$) eluting at approximately 16 ml (Fig. 3.33A). For comparison, an overlap with the elution profile of the oxidized WT *Mb*AhpC (red dotted line) was included, indicating the

similarity of the WT *Mb*AhpC's elution profile to *Mb*AhpC$_{A92R-2}$ (Fig. 3.33A). These results revealed that *Mb*AhpC$_{A92R-1}$ possesses a larger oligomeric form, as compared to *Mb*AhpC$_{A92R-2}$ which most likely elutes as a dimer. On the other hand, the mutant *Mb*AhpC$_{A92R}$ eluted as a single peak at approximately 16 ml in the presence of DTT, indicating the presence of a dimeric form (Fig. 3.33C).

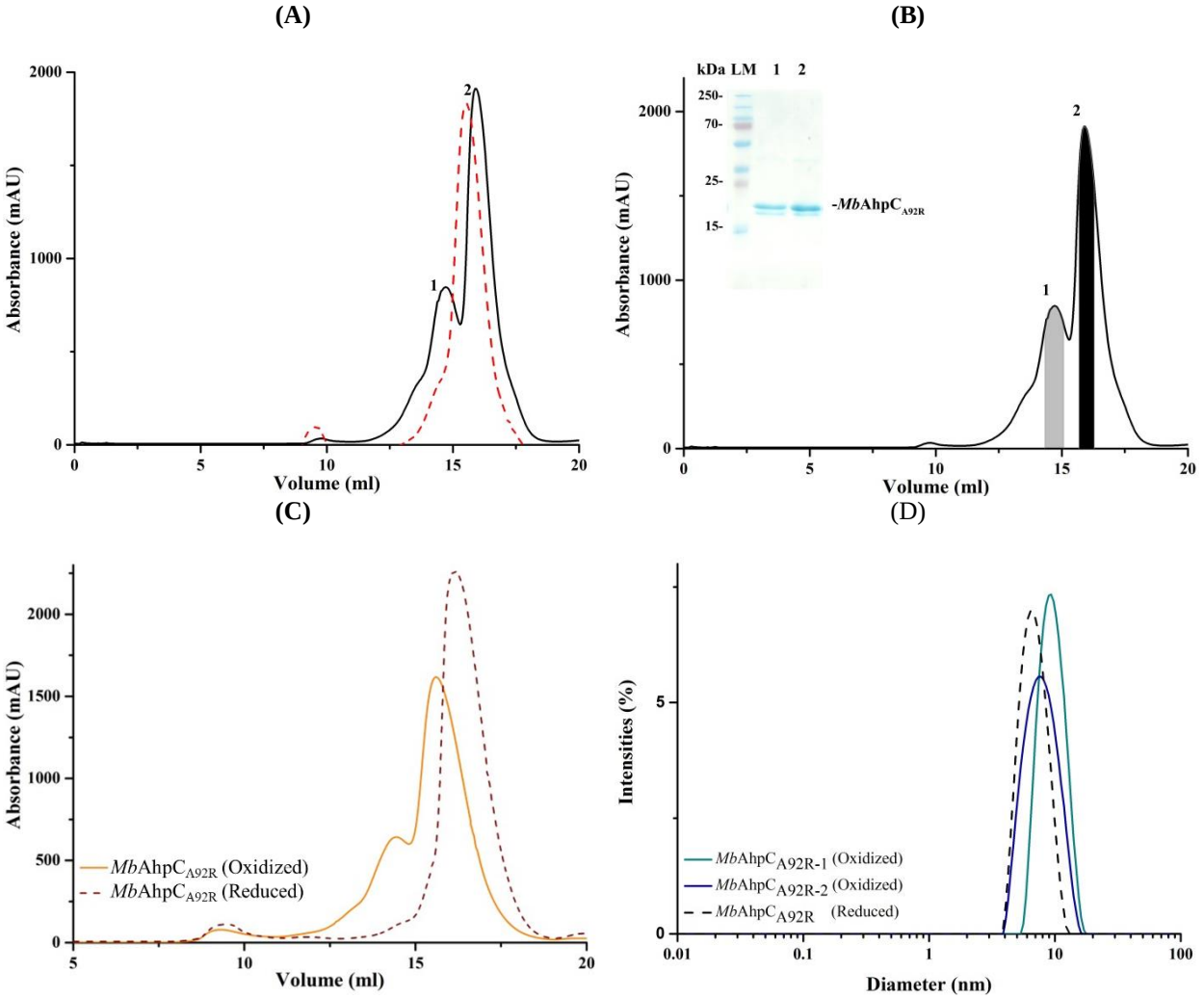

Figure 3.33: SEC and DLS results for *Mb*AhpC$_{A92R}$. (A) SEC elution profile for the purification under oxidized conditions showed that *Mb*AhpC$_{A92R}$ eluted at approximately 14.8 ml and 16 ml. The WT *Mb*AhpC elution profile is included as a red dotted line. (B) SEC elution profile under oxidized conditions. The grey border indicates the purified proteins kept and used for analysis. The purity of the protein was confirmed on a 17% SDS-PAGE gel (inset). (C) Comparison of the elution profile under oxidized (orange) and reduced (brown dotted) conditions. (D) DLS profile signifying a hydrodynamic diameter of approximately 7 nm for both peak 2 oxidized and reduced *Mb*AhpC$_{A92R}$. Peak 1 oxidized fraction has a hydrodynamic diameter of approximately 9.7 nm.

To confirm the analysis observed in SEC, the top 20% of the eluted proteins were utilized for DLS (Fig. 3.33B). Comparing the results of the protein obtained under oxidized conditions, *Mb*AhpC$_{A92R-2}$ has a hydrodynamic diameter of 8.0 ± 2.3 nm, while *Mb*AhpC$_{A92R-1}$ was revealed

to be slightly larger, as reflected by a hydrodynamic diameter of 9.7 ± 2.2 nm (Fig. 3.33D). Furthermore, the reduced *Mb*AhpC$_{A92R}$ has a hydrodynamic diameter of 6.9 ± 1.7 nm. These results demonstrate that both *Mb*AhpC$_{A92R-2}$ and reduced *Mb*AhpC$_{A92R}$ eluted as a dimer instead of a dodecamer like the WT enzyme.

3.4.3 Enzymatic Assay for *Mb*AhpC$_{A92R}$

To study the effect of the mutagenesis, an enzymatic assay was carried out. Interestingly, *Mb*AhpC$_{A92R-1}$ and *Mb*AhpC$_{A92R-2}$ presented varying activities (Fig. 3.34). *Mb*AhpC$_{A92R-1}$ possesses approximately 61% of the WT *Mb*AhpC's activity, while *Mb*AhpC$_{A92R-2}$, the dimer, retains approximately 82% of WT *Mb*AhpC's activity. This initial result supports the importance of oligomerization of the proteins, as revealed from the SEC and DLS data, that *Mb*AhpC$_{A92R-1}$ formed a larger oligomer. As such, a full enzymatic kinetic analysis was carried out for both *Mb*AhpC$_{A92R-1}$ and *Mb*AhpC$_{A92R-2}$ to gain more insights into the activity of the recombinant proteins.

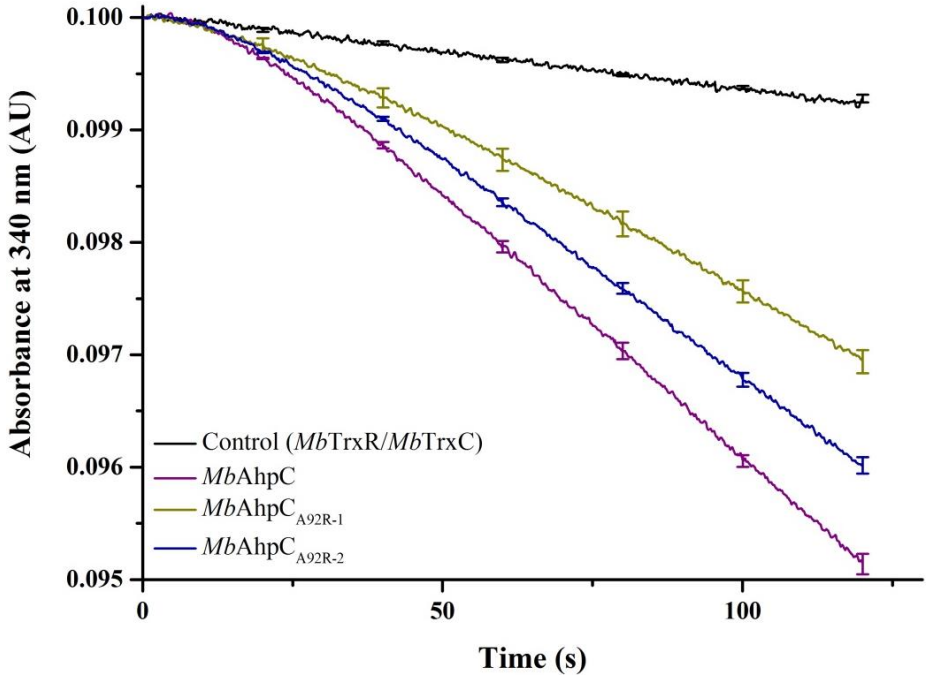

Figure 3.34: Analysis of the enzymatic activity of the recombinant proteins. The black line represents the control whereby no enzymes were added, while the violet line represents the absorbance of WT *Mb*AhpC. *Mb*AhpC$_{A92R-1}$ (yellow) and *Mb*AhpC$_{A92R-2}$ (blue) both have a significant decline in absorbance.

3.4.4 Enzyme kinetics analysis of *Mb*AhpC$_{A92R-1}$ and *Mb*AhpC$_{A92R-2}$

A small decrease in the K_{cat} value was observed for both *Mb*AhpC$_{A92R-1}$ and *Mb*AhpC$_{A92R-2}$ when compared to WT *Mb*AhpC, underlining that the number of catalytic cycles that each active

site undergoes per unit time decreases slightly (Fig. 3.35). The K_m, on the other hand, demonstrated a significant increase in both *Mb*AhpC$_{A92R-1}$ and *Mb*AhpC$_{A92R-2}$ proteins.

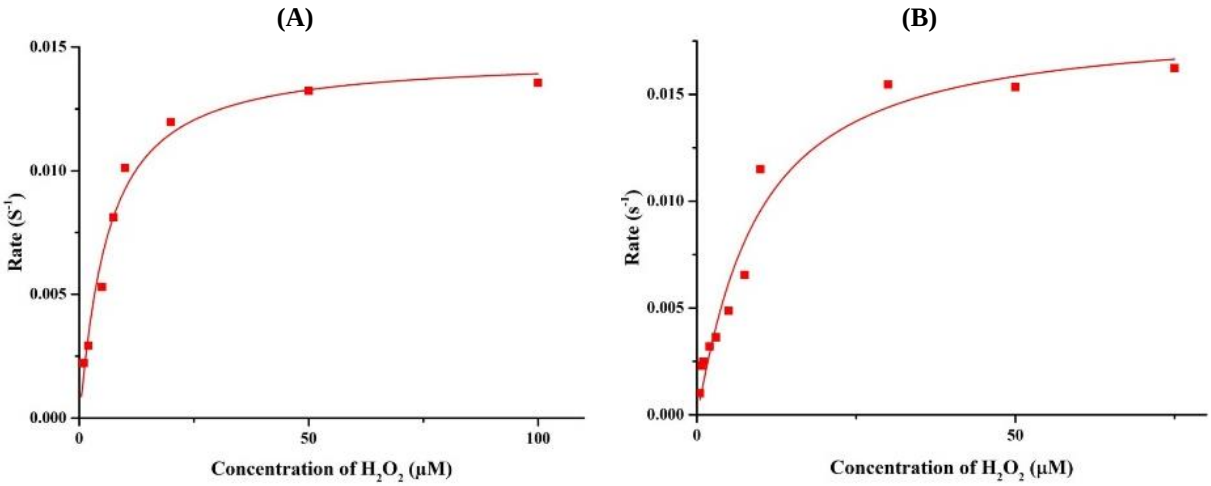

Figure 3.35: Enzyme kinetics of *Mb*AhpC$_{A92R}$. Michaelis-Menten plot of (A) *Mb*AhpC$_{A92R-1}$ and (B) *Mb*AhpC$_{A92R-2}$. Both plot illustrated the best fit line of the experimental data. However, the graph depiceted a lower K_M in the formor as compred to the latter.

	K_{cat} ± SD (s^{-1})	K_M± SD (μM)	K_{cat}/K_M ($M^{-1}s^{-1}$)
***Mb*AhpC$_{A92R-1}$**	0.015 ± 0.001	6.03 ± 1.21	2.42 x 10^3
***Mb*AhpC$_{A92R-2}$**	0.018 ± 0.002	9.19 ± 2.92	1.99 x 10^3
***Mb*AhpC**	0.021 ± 0.001	2.57 ± 0.36	8.17 x 10^3

Table 3.3: Enzyme kinetics parameters for WT *Mb*AhpC, *Mb*AhpC$_{A92R-1}$, and *Mb*AhpC$_{A92R-2}$.

The K_{cat} values were similar for *Mb*AhpC$_{A92R-1}$ and *Mb*AhpC$_{A92R-2,}$ while the increase in K_m was less significant in the case of *Mb*AhpC$_{A92R-1}$. This indicates the binding pocket of the *Mb*AhpC$_{A92R-1}$ is more favourable for the reduction of the peroxides, as compared to *Mb*AhpC$_{A92R-2}$. The similar K_{cat} values suggest the ability of the enzymes to adopt an active site, similar to that of the WT *Mb*AhpC, at higher substrate concentrations. The results could have highlighted the importance of the oligomerization in *Mb*AhpC, where a partial oligomerization in *Mb*AhpC$_{A92R-1}$ retains a binding pocket that is more favorable for the reduction of peroxides.

Discussion

4. Discussion

4.1 Enzymatic and Structural Insights into the *Mt*AhpC

4.1.1 Correlation between oligomerization and enzymatic activity of the AhpC mutants

AhpCs are redox sensitive and undergo the change from oligomeric rings to dimers as it gets oxidized. The SEC data and DLS analysis revealed that the mutants, *Mb*AhpC$_{A66G/A67D/F68V}$, *Mb*AhpC$_{A67D/F68V}$, and *Mb*AhpC$_{A67D}$, were unable to oligomerize into a dodecameric ring in the presence of DTT. As both *Mb*AhpC$_{A66G/A67D/F68V}$ and *Mb*AhpC$_{A67D/F68V}$ revealed a complete loss of enzymatic activity, it led to the construction of the single mutant, *Mb*AhpC$_{F68V}$. The enzymatic results from the single mutant *Mb*AhpC$_{A67D}$, showed its ability to reduce peroxides. This possibly suggests its ability to form a disulfide bond, indicating the probable movement of the α-helix for coordination between the cysteines.

The enzyme kinetics results showed a major impact on the catalytic efficiency of *Mb*AhpC$_{A67D}$ on the K_m rather than the K_{cat} was observed. The loss of electron transfer could be attributed to the incapability to oligomerize, in agreement to the study by Parsonage *et al*. (2005) [115], where a single mutation on the oligomeric interface of *St*AhpC disrupts the decameric ring. The enzymatic assay carried out on these mutants demonstrates a much more affected K_m than K_{cat} as well, reflecting that the binding pocket in the dimeric form could be less favourable for the binding of peroxides, resulting in a lower K_m, that could be overcome by an increase in substrate concentration [115]. Similarly, the effect of the *Mb*AhpC$_{A67D}$ could affect mainly the oligomerization of the protein, causing this decrease in catalytic efficiency. The enzyme kinetics results were compared with *Mb*AhpC$_{A92R}$, the mutation on the oligomeric interface, and will be discussed later.

4.1.2 A conceptual model for understanding *Mb*AhpC$_{A67D}$

The crystallization results have revealed an alteration of the Cys-S_pH containing helix with A67D mutation along with the loop preceding the helix, demonstrating the impact of a single mutation on the structure and flexibility of the helix. This, in turn, affected the position of the peroxidatic cysteine, as well as the loop at the dimer-dimer interface, possibly resulting in the loss of dodecameric ring formation.

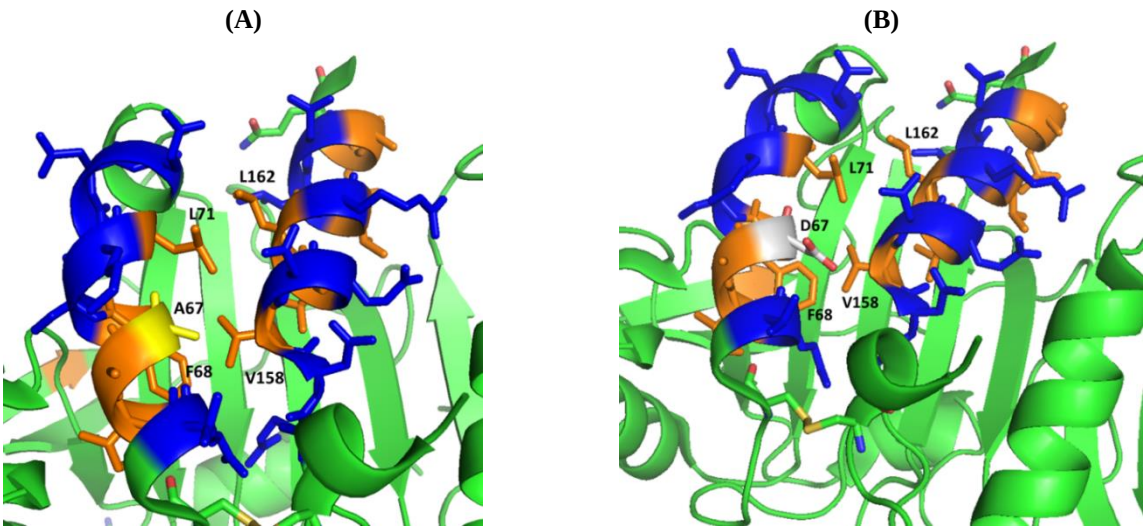

Figure 4.1: Cartoon representation of *Mt*AhpC$_{C176S}$ crystallographic structure. (A) The hydrophobic environment of the A67 residue was shown. (B) Mutagenesis of A67D was carried out on the structure to postulate the effect of the mutation on the hydrophobic region. Despite aspartic acid being a larger residue than alanine, it does not result in a steric hindrance as the nearest residue is approximately 5 Å away. The hydrophobic residues are shown in orange while the hydrophilic resides are displayed in blue (PDB ID: 2BMX) [107].

Figure 4.1A illustrates the hydrophobic alanine residue residing in a hydrophobic environment, surrounded by residues F68, L71, V158, and L162. Thus, a mutation to a charged and hydrophilic residue, such as aspartic acid, would possibly disrupt the movement of the α-helix, in turn affecting the catalytic site. As shown in figure 4.1B, it depicts aspartic acid being a much larger residue, lying at approximately 5 Å to the nearest hydrophobic residue. The distance is too much to cause steric hindrance. Hence, the mutation might not completely prevent the movement of the helix α2 but results in a decrease in activity.

4.1.3 Understanding the effect of the F68 mutation

The FOX assay experiments have provided valuable insights on the mechanism of action for the F68V mutation. As DTT is a chemical reductant used in the FOX assay, it can reduce the disulfide bonds without a specific conformation. Unlike in the case of TrxC reduction. Here, it can be inferred that the loss of activity is a result of the peroxide binding pocket of *Mb*AhpC. The loss of oligomerization and negligible enzymatic activity strongly supports the importance of F68. It was suggested that the movement of the Cys-S_pH containing helix was carried out with a small rearrangement of the three phenylalanine side chains, F51, F68 and F108 [107]. As shown in figure 4.2A, the three phenylalanine side chains appear to be near each other, allowing a coordinated movement for the rigid-body movement of the helix to occur. This is especially the case in the reduced *Mb*AhpC. The reduced model of *Mt*AhpC$_{C176S}$ was prepared using iTasser

with *St*AhpC$_{T43S}$ as a template (Fig. 4.2B), as the *St*AhpC$_{T43S}$ crystallographic structure was obtained under reduced conditions. The model obtained will simulate the Cys-S_pH containing helix in a downwards orientation, where the three phenylalanine side chains are at a close distance of 2.8 Å.

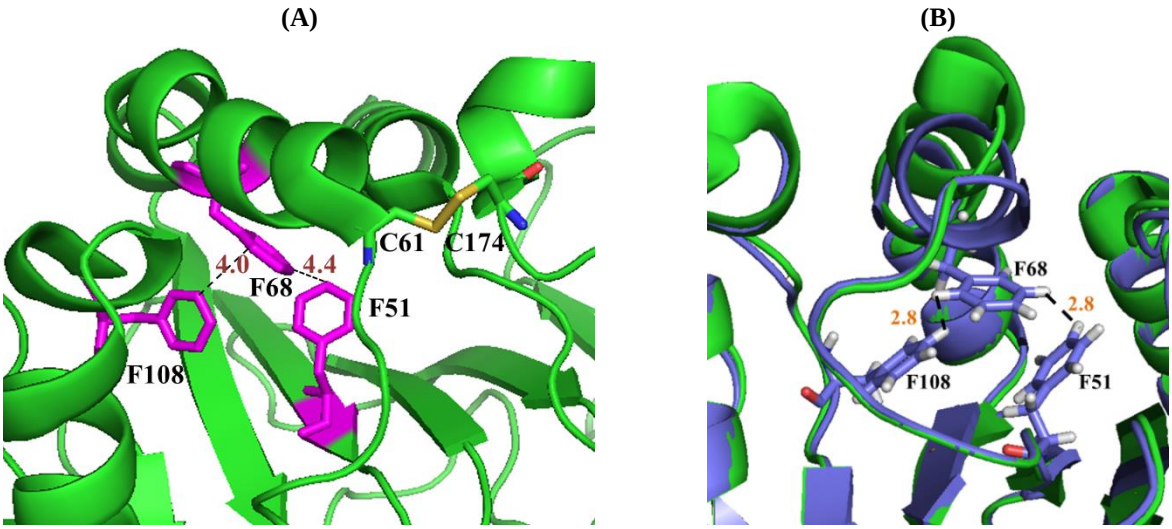

Figure 4.2: Oxidized and reduced structure of *Mt*AhpC$_{C176S}$. (A) Cartoon representation of *Mt*AhpC$_{C176S}$ crystallographic structure (green) (PDB ID: 2BMX) [107] and (B) *Mt*AhpC$_{C176S}$ model (blue) generated from iTasser, with *St*AhpC$_{T43V}$ as a template to gain insights into the reduced structure of *Mt*AhpC [303-305]. Both structures show the three phenylalanine side chains required for the rigid-body movement of the helix α3.

Previous research has proposed that the three phenylalanine side chains rearrangement will allow the peroxidatic cysteine to be within H-bonding distance of R133. This allows the guanidinium groups of both R133 and R156 to interact with E64. Figure 4.3A reflects the position of these residues under oxidized conditions, where they are not in close contact [107]. Using the iTasser model of the reduced *Mt*AhpC$_{C176S}$, residues E64, R133 and R156 appear in close proximity, where the sulfur from C61 can form a hydrogen bond with R133 at approximately 2.5 Å away. R133 and R156 could additionally form a salt bridge with E64 at approximately 3.0 Å distance. This creates an active site for the reduction of the peroxides to occur, where particularly, R133 is able to form a hydrogen bond with both the peroxide oxygen as well as the thiolate from the cysteine residue [120].

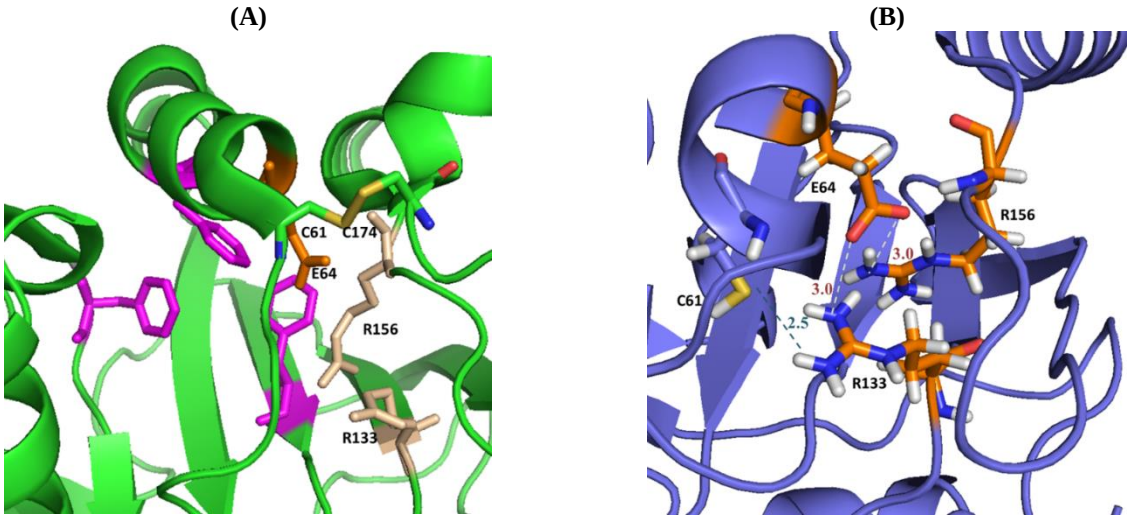

Figure 4.3: Oxidized and reduced structure of *Mt*AhpC$_{C176S}$ highlighting residues at active site. (A) Cartoon representation of *Mt*AhpC$_{C176S}$ (PDB ID:2bmx) [107]. The critical residues E64, R133 and R156 involved in the reduction of peroxides are as shown. (B) Cartoon representation of *Mt*AhpC$_{C176S}$ model generated from iTasser, with *St*AhpC$_{T43V}$ as a template to gain insights into the reduced structure of *Mt*AhpC [303-305]. The E64, R133 and R156 would be postulated to be in close proximity in reduced *Mt*AhpC$_{C176S}$.

This study supports the hypothesis that the rearrangement of the three phenylalanine side chains is the driving force for the rigid-body movement of the α-helix. Following the reduction of the peroxides, the rearrangement of the three phenylalanine side chains occurs, allowing the upward movement of the α-helix for the formation of the disulfide bond.

4.1.4 Comparing the enzyme kinetics data of *Mb*AhpC$_{A67D}$ and *Mb*AhpC$_{A92R-2}$

*Mb*AhpC$_{A92R}$ upon purification from SEC was found to elute as two different fractions. *Mb*AhpC$_{A92R-1}$ has a larger oligomeric state under oxidized conditions, while *Mb*AhpC$_{A92R-2}$ elutes as a dimer. Previous studies have shown that a high concentration of AhpC could force the oligomeric ring formation even under oxidized conditions [113]. This mutation could have caused an increased sensitivity of *Mb*AhpC to oligomerize even at a lower concentration. However, the full dodecamiric ring was not formed, which might be due to the mutation at the oligomeric interface.

The results of *Mb*AhpC$_{A67D}$ was compared to *Mb*AhpC$_{A92R-2}$ as it forms a dimer, possibly indicating the loss of activity solely due to the lack of oligomerization, as the disulfide bonds at the active sites were not affected. Comparing the catalytic efficiency of *Mb*AhpC$_{A67D}$ (1.33×10^3 M^{-1} s^{-1}) to *Mb*AhpC$_{A92R-2}$ (1.99×10^3 M^{-1} s^{-1}), *Mb*AhpC$_{A92R-2}$ was found to be a more efficient enzyme. Hence, it can be ascertained that the *Mb*AhpC$_{A67D}$ mutation not only affects the

oligomeric interface, but also plays a role in affecting the helical region, resulting in a decrease in the ability of peroxides reduction, arising in a lower catalytic efficiency.

4.1.5 Proposed explanation for understanding *Mb*AhpC$_{A92R}$ enzymatic activity

The oligomeric interface consists of hydrophobic residues, as shown in figure 4.4, which include residues F57, T58, F91, I116, and V130. With the mutation of alanine to arginine, it adds a much larger and charged molecule into the oligomeric interface, increasing steric hindrance, which could explain the loss in the formation of an oligomeric ring. Similar to the case of *St*AhpC, the oligomeric ring was found to be inessential for the reduction of peroxides, but contributes to the full potential of the enzyme [115].

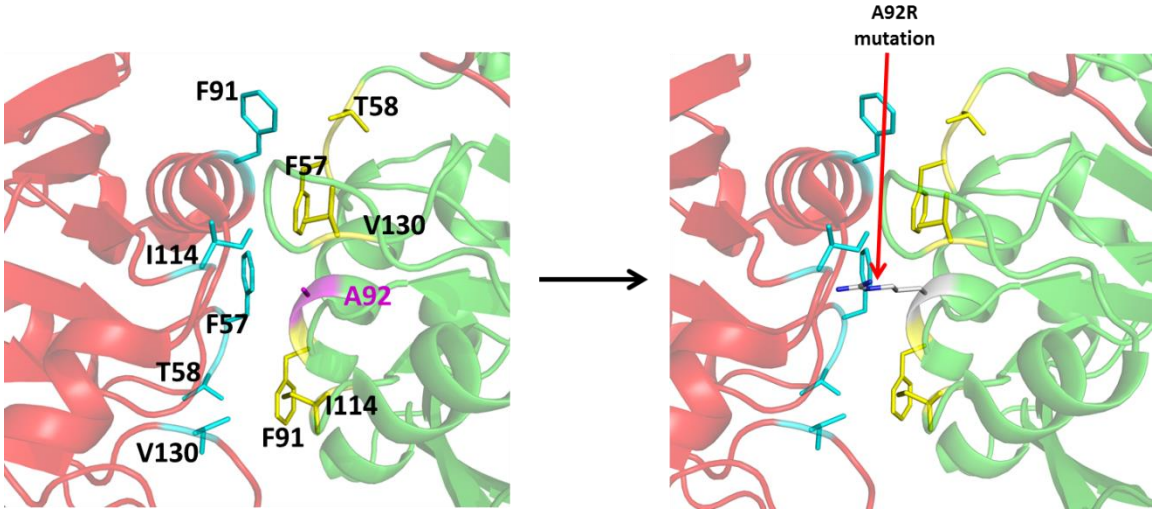

Figure 4.4: Cartoon representation of *Mt*AhpC$_{C176S}$ crystallographic structure at oligomeric interface. The hydrophobic interaction that helps to stabilize the oligomeric interface was as shown. Green and red indicates the different monomer and the blue and yellow side chains depict the interactions between the monomers. The mutation of alanine to arginine has resulted in steric hindrance (PDB ID: 2BMX) [107].

Furthermore, comparing *Mb*AhpC$_{A92R-1}$, that has a higher oligomeric form, and *Mb*AhpC$_{A92R-2}$, that forms a dimer under oxidized conditions, it further implies the importance of the concerted rearrangement between the active sites that occur alongside oligomerization, as the ability to oligomerize in the case of *Mb*AhpC$_{A92R-1}$ shows a higher catalytic efficiency as compared to *Mb*AhpC$_{A92R-2}$. These results suggest the importance of the dodecameric ring formation, for the protein to exhibit its full potential in reducing peroxides.

Results

Part 5

Docking of SCR0911 to Mtb cyt-bcc complex and synthesis of SCR0911

5. Results

5.1 Docking of SCR0911 to *Mtb* cyt-*bcc* complex and synthesis of SCR0911

5.1.1 Docking of SCR0911 with *Mtb* cyt-*bcc* complex

To understand the potential binding site of SCR0911 in the *Mtb* cyt-*bcc* complex, docking studies of SCR0911 in the homology model of *Mtb* cyt-*bcc* complex were carried out by Dr. Malathy Sony from Professor G. Grüber's laboratory [277]. As the structure of *Mtb* cyt-*bcc* complex is not available, the homology model was also prepared by Dr. Malathy Sony, with the SWISS-MODEL server [271], using the *M. smegmatis* EM structure (PDB ID: 6ADQ) as a template [72]. With the high sequence identity of the cyt-*bcc* complex between *Mtb* and *M. smegmatis*, a homology model was prepared with good confidence. The docking of SCR0911 was carried out using AutoDock 4.2 [267]. Four binding sites were discovered from the docking studies, with populations of 33%, 21%, 13%, and 8%. Multiple binding sites are probable, as menaquinol has a total of five binding sites in *M. smegmatis* cyt-*bcc* complex [72].

The binding site with the largest population has SCR0911 on both subunits QcrB and QcrC (Fig. 5.1A). The stabilization of SCR0911 within this binding pocket is mainly contributed by QcrB through hydrophobic interactions, with residues M390 and F308 interacting with the methoxy group of SCR0911. The pyridine ring and trifluoromethoxyphenyl group are stabilized by residues M126, and residues L349 and I386, respectively. As the quinolone group extends into the QcrC subunit, hydrophobic interactions with residue M259 was observed, along with a π-π interaction with residue W262. Figure 5.1B illustrates the position of SCR0911, close to the Q_o-site, being 3.6 Å away from residue F308. Furthermore, SCR0911 was found to be in a menaquinone binding site [72]. Although the purpose of menaquinone binding at that region has yet to be elucidated, this could indicate the importance of this binding site in addition to its proximity to the Q_o-site. SCR0911 binding in this region could possibly disrupt the electron transfer through the cytochrome *b*, leading to an inactivation of the enzyme.

The 2nd binding site with a population of 21% has SCR0911 interacting with subunits QcrA, QcrB, and QcrC (Fig. 5.2). However, SCR0911 was revealed to be 17.5 Å from heme b_L, 29.6 Å from heme b_H, and 17.2 Å away from heme c_{D2}. It is also a distance from the Q_i-site and Q_o-site, with SCR0911 being 21.0 Å and 25.6 Å, respectively, resulting in the difficulty to determine the significance of the binding site with the current knowledge of the cyt-*bcc* complex.

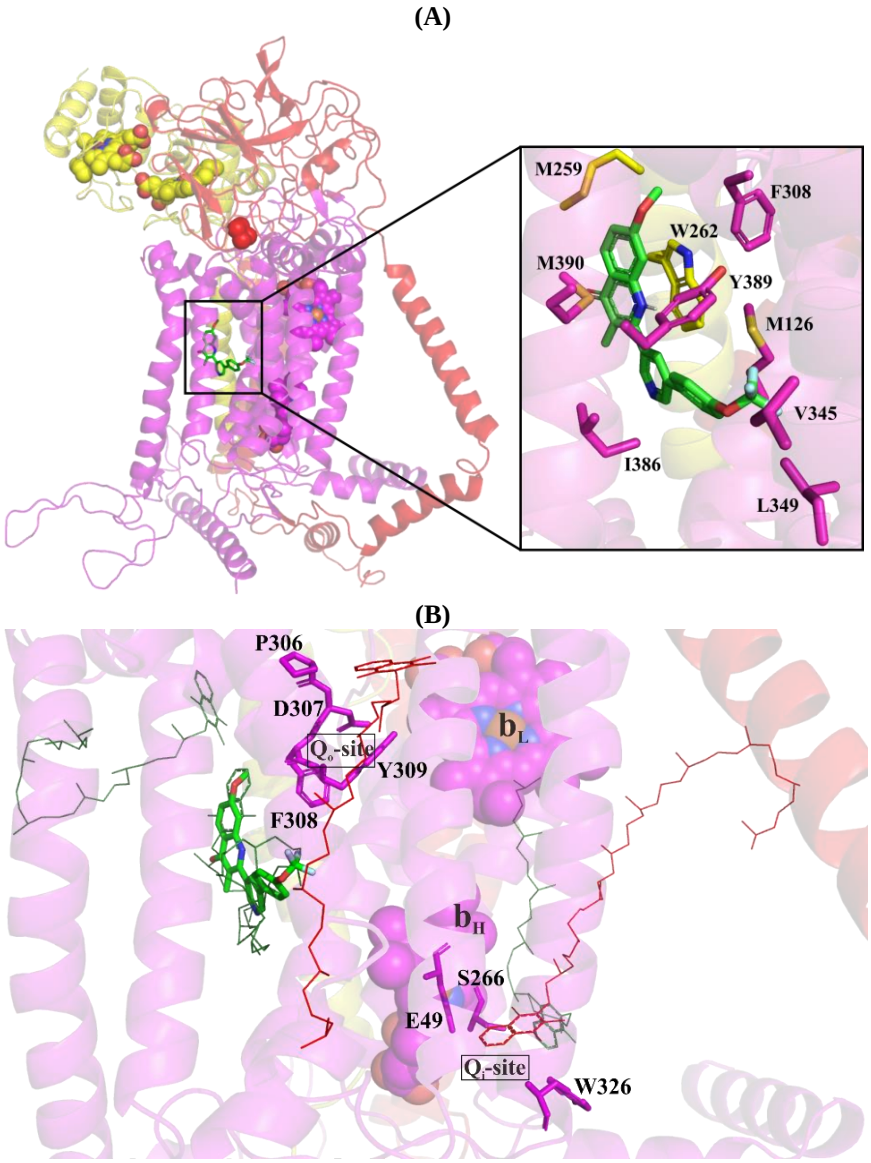

Figure 5.1: Cartoon representation of the first binding model (33% population) of SCR0911 into the *Mtb* cyt-*bcc* complex. (A) QcrA, QcrB and QcrC are represented in red, magenta and yellow respectively. The heme groups are represented as spheres while the 2Fe-2S cluster is shown as red spheres. SCR0911 is shown as green sticks. (B) A closed-up illustration of SCR0911 within the *Mtb* cyt-*bcc* complex to demonstrate the proximity of SCR0911 to the Q_o site, Q_i site, and the heme groups. SCR0911 is found in one of the menaquinone binding sites. Figures adapted from Chong *et al*. (2020) [277].

The 3rd binding site from the docking studies has a population of 13%. It mainly interacts with subunits QcrA and QcrB. However, similar to the 2nd binding site of SCR0911, SCR0911 was docked in a region that is a distance from the heme groups and the Q-sites. It is closest to the iron-sulfur (2Fe-2S) cluster at 10.9 Å.

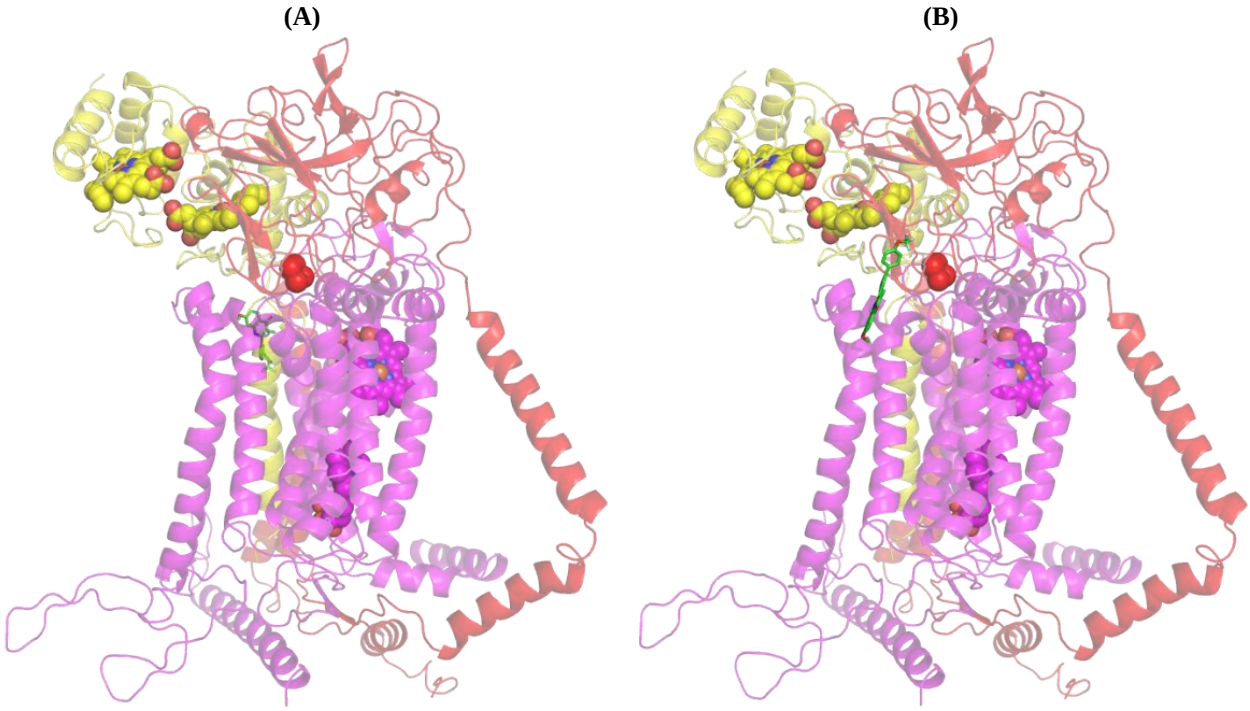

Figure 5.2: Cartoon representation of the second and third binding model of SCR0911 into the *Mtb* cyt-*bcc* complex. (A) represents the second binding model (21% population) and (B) represents the third binding model (13% population) of SCR0911 into the *Mtb* cyt-*bcc* complex. QcrA, QcrB and QcrC are represented in red, magenta and yellow respectively. The heme groups are represented as spheres while the 2Fe-2S cluster is shown as red spheres. SCR0911 is shown as green sticks. Figures adapted from Chong *et al*. (2020) [277].

The 4th binding site, despite having the lowest population at 8%, binds to a functionally important region, as it binds in the Q_i-site, and is 3.2 Å away from heme b_H (Fig. 5.3A). SCR0911 lies within subunit QcrB, and is stabilized by hydrophobic interactions, such as residues L52, H240, and F45 interacting with its methoxy group, and residues L31, L35, and Q34 surrounding the trifluoromethoxyphenyl group. Additionally, hydrogen bonding interaction between the oxygen atom of the quinolone to residue Y53, and a face-to-face π-interaction of residue W236 and the trifluoromethoxyphenyl group were found. SCR0911 in this region could potentially prevent menaquinone binding, as well as the electron transfer, leading to an inactivation of the enzyme (Fig. 5.3B). In addition, the crystal structure of bovine cyt-bc_1 complex with SCR0911 has demonstrated the Q_i-site as the primary binding pocket as well (section 1.3.4) [254].

An overlap of the crystal bovine cyt-bc_1 complex and the 4th docking model with SCR0911 demonstrates the binding in the same site, albeit the different orientation of SCR0911 (Fig. 5.3C). The different orientation could be a result of the structural difference between the two complexes, especially at the N-terminal helices. The helix containing residue W236 of the Q_i-site was observed to be slightly more inward, which could have led to the placement of the 2nd helix

from the N-terminus tilting more downwards, creating a larger cavity for a different binding configuration.

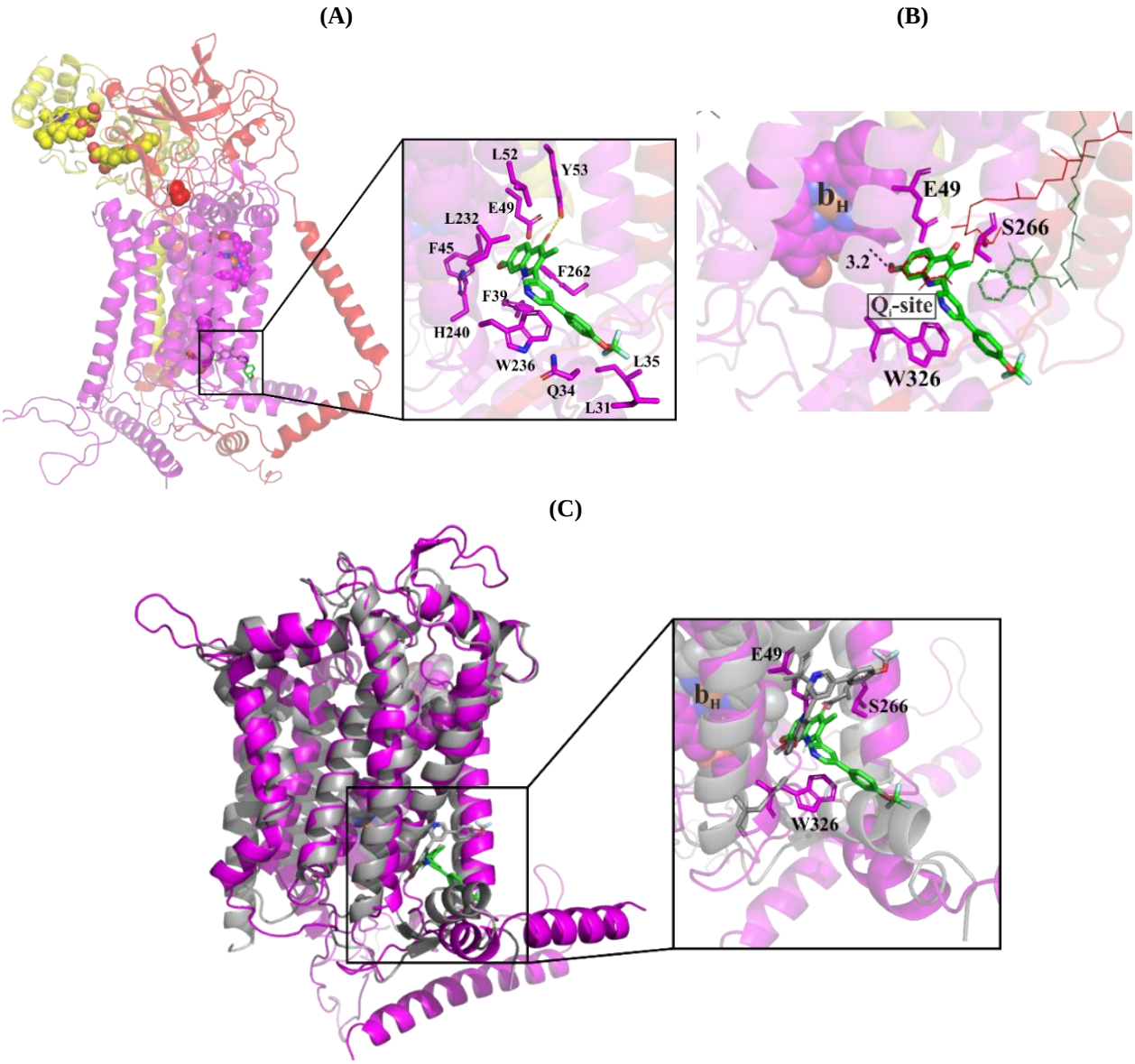

Figure 5.3: Cartoon representation of the fourth binding model (8% population) of SCR0911 into the *Mtb* cyt-*bcc* complex. (A) QcrA, QcrB and QcrC are represented in red, magenta and yellow respectively. The heme groups are represented as spheres while the 2Fe-2S cluster is shown as red spheres. SCR0911 is shown as green sticks. (B) A closed-up illustration of SCR0911 within the *Mtb* cyt-*bcc* complex to demonstrate the proximity of SCR0911 to the Q_o site, Q_i-site, and the heme groups. SCR0911 is found to bind within the Q_i-site. (C) An overlap of subunit QcrB of the cyt-*bcc* complex from *Mtb* (magenta) and bovine (grey) (PDB ID: 5OKD) [254]. SCR0911 from the docked model with *Mtb* cyt-*bcc* complex is represented in green, while SCR0911 co-crystallized with the bovine cyt-bc_1 complex is shown in grey. Despite binding in the same position in both complex, a different orientation was observed. Figures adapted from Chong *et al.* (2020) [277].

5.1.2 Synthesis of SCR0911

Following the docking results of SCR0911 into the *Mtb* cyt-*bcc* model, the total synthesis of SCR0911 was carried out to perform antimicrobial activity testings, by *in-vivo* and *in-vitro* assays. The synthesis by Charoensutthivarakul *et al*. (2015) is shown in figure 5.4 [248].

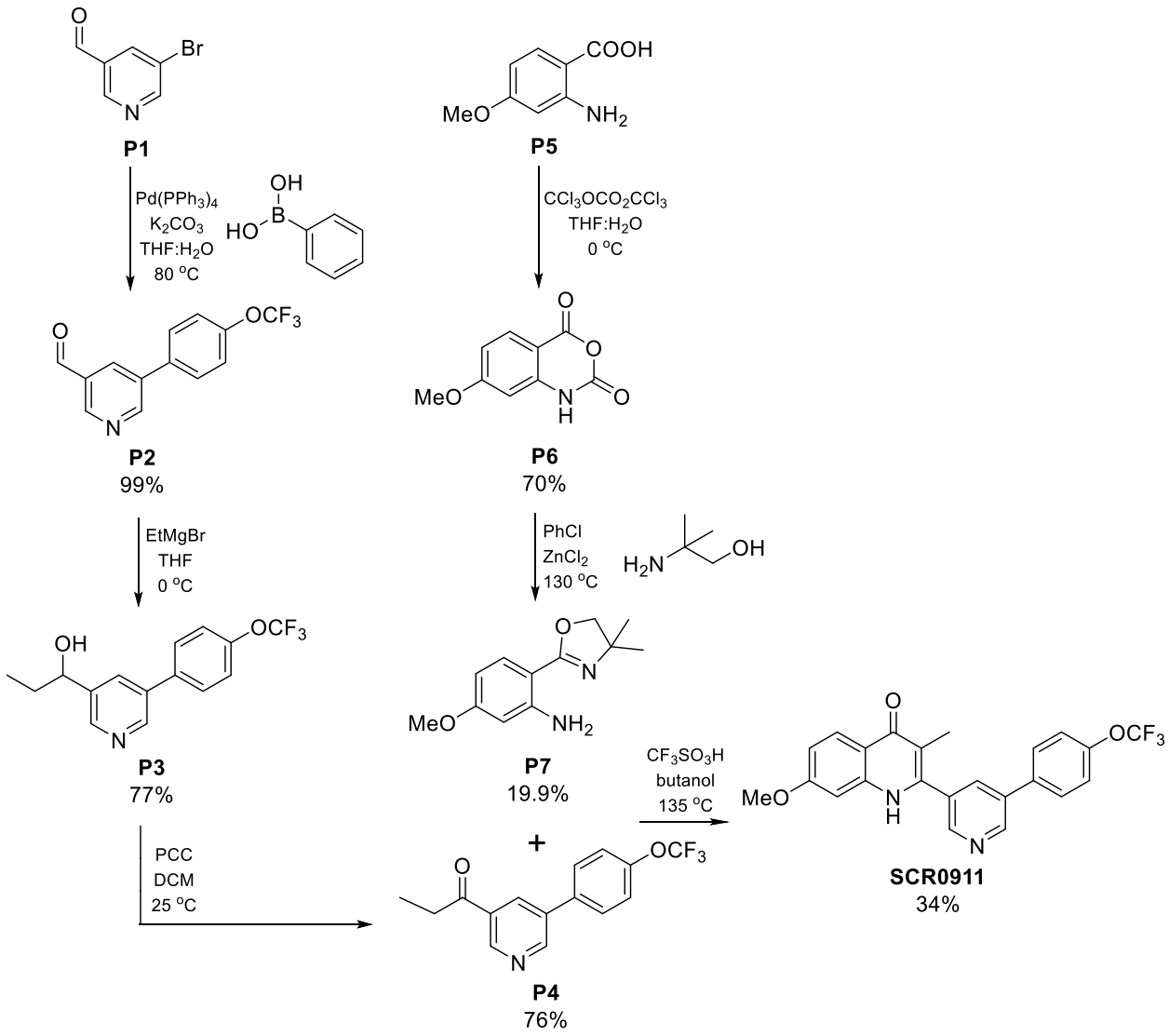

Figure 5.4: Synthetic scheme for the synthesis of SCR0911 by Charoensutthivarakul *et al*. (2015) [248].

Due to the availability of the compounds, an alternative route was applied, with the retrosynthetic scheme as described in figure 5.5. The main difference is the synthesis of the aryl ketone **3**, which can undergo a Suzuki reaction with boronic ester **2** to synthesize aryl ketone **1**. Aryl ketone **3** could be synthesized via a Grignard reaction on a Weinreb amide, avoiding the use of pyridinium chlorochromate (PCC) due to its toxicity.

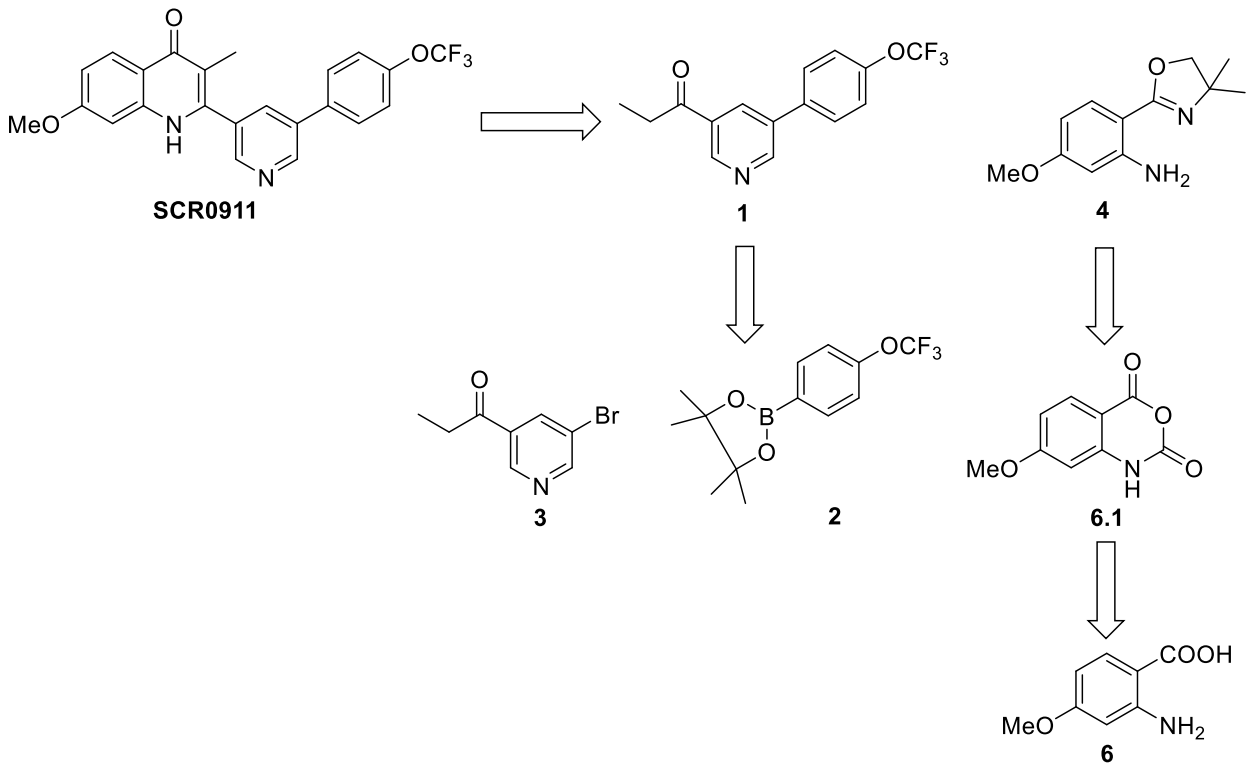

Figure 5.5: Retrosynthetic scheme for the synthesis of SCR0911.

5.1.2.1 Synthesis of boronic ester 2

Boronic ester **2** was synthesized via a one-step reaction, with the addition of *bis*-(pinacolato)diboron by the Miyaura borylation reaction to provide the boronic ester in 65% yield (Fig. 5.6) [281]. The identity of the boronic ester was confirmed by ^{1}H nuclear magnetic resonance (NMR) spectroscopy, with a distinctive singlet at 1.34 ppm with an integration of 12 H (Appendix A), allowing the Suzuki cross-coupling of boronic ester **2** with the aryl ketone **3**.

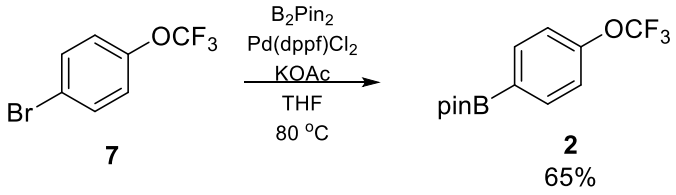

Figure 5.6: Synthesis of boronic ester 2.

5.1.2.2 Synthesis of aryl ketone 3

The synthesis of the aryl ketone **3** can be prepared from 5-bromonicotinic acid **8** as a starting material, through the conversion of the carboxylic acid to a ketone group, using Weinreb amide as an intermediate. The synthesis of Weinreb amide utilizes an addition of a base and activating agents, N-(3-Dimethylaminopropyl)-N'-ethylcarbodiimide hydrochloride (EDCI) and 4-

Dimethylaminopyridine (DMAP). The reaction proceeded in good yield of 86%, affording the amide **9**, as confirmed by ^{1}H NMR spectroscopy with two singlets at 3.38 and 3.57 ppm indicating the presence of the two methyl groups (Fig. 5.7) (Appendix B) [283]. Grignard reaction was employed, following the formation of the Weinreb amide. Activated magnesium was first added to bromoethane in tetrahydrofuran (THF) to be stirred at 40°C for 1 hr, for the preparation of the Grignard reagent [306]. The solution prepared was directly added to the solution of the amide in THF, stirred at 0°C, affording the aryl ketone **3** with a yield of 36% [285]. The low yield could be due to a side reaction between the ethyl magnesium bromide and the bromoaryl, instead of the reaction on the Weinreb amide. ^{1}H NMR spectroscopy confirmed the addition of the ethyl group with a triplet at 1.25 ppm and quartet at 3.01 ppm (Appendix C). This procedure allows regioselectively of the Grignard reaction, while eliminating the use of PCC in the original synthesis scheme, which is carcinogenic.

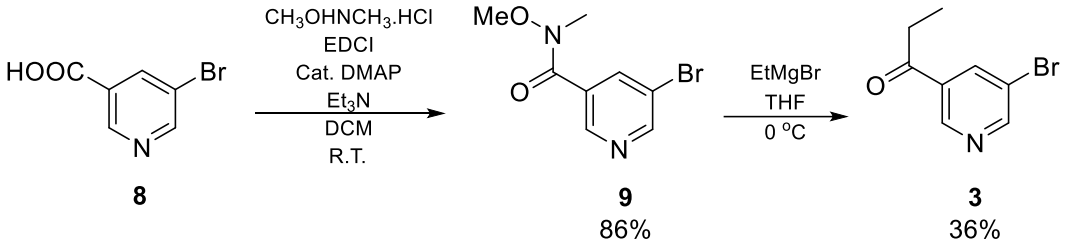

Figure 5.7: Synthesis of compound 3 via the synthesis of a Weinreb amide followed by a Grignard reaction.

5.1.2.3 Suzuki cross-coupling of boronic ester 2 and aryl ketone 3

The biaryl compound **1** can be obtained through the Suzuki cross-coupling between an organoboron **2** and an organic halide **3**, with an addition of a palladium catalyst and a base.

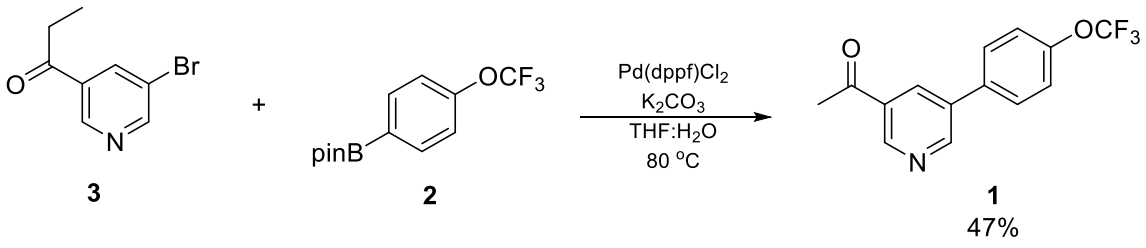

Figure 5.8: Suzuki coupling of boronic acid 2 and organic halide 3.

The reaction was initially carried out following the procedures from Charoensutthivarul *et al*. [8], using $Pd(PPh_3)_4$, tetrakis(triphenylphosphine)palladium(0). However, the reaction failed to proceed, and decomposition of the starting materials were observed. Hence, $Pd(dppf)Cl_2$,

[1,1'Bis(diphenylphosphino)ferrocene]dichloropalladium(II) was utilized instead [307]. ^{1}H NMR spectroscopy confirmed the reaction progressed smoothly, revealing the presence of the 7 aromatic hydrogens, along with a triplet and quartet at 3.09 and 1.29 ppm, respectively (Appendix D). Biaryl compound **1** was achieved with a yield of 47% (Fig. 5.8) [248].

5.1.2.4 Iodination of m-anisidine

m-Anisidine **10** was the starting material for the preparation of the oxazole **4**. Iodination of the ortho-position of the aromatic ring to the amine was envisioned, for the conversion to the carboxylic acid **6**, as described in the retrosynthetic scheme (Fig. 5.5) [308]. However, iodination of *m*-anisidine was tedious due to the poor selectivity of the product ortho to the amino group, resulting in the synthesis of the ortho-, para- and disubstituted product. Several methods have been attempted, as shown in figure 5.9.

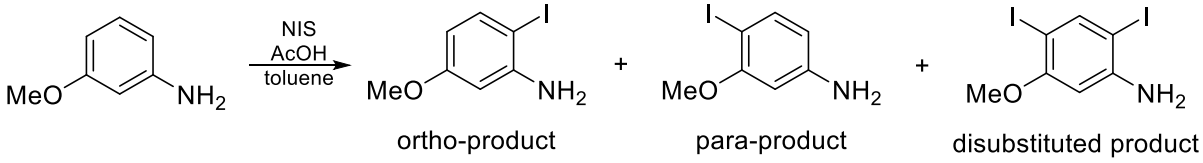

Figure 5.9: Iodination of *m*-anisidine.

Initial attempts involve the use of iodine and silver acetate to promote salt formation, preventing the formation of hydrogen iodide that could dissociate the iodine from the aromatic ring [309]. However, the yield for the ortho product was only 4%, with 35% being the para product. A second attempt was carried out using iodine monochloride and sodium acetate with acetic acid as the solvent, providing a yield of 20% [310]. The third attempt utilizes *n*-iodosuccinimide (NIS) in the presence of acetic acid, as it was postulated that the addition of acetic acid allows the formation of an acetic hypoiodous anhydride, which can coordinate with the amine, and thus brings the iodine to the ortho-position (Fig. 5.10) [286]. The procedure was modified slightly to utilize toluene instead of benzene due to the toxicity of benzene. However, the yield obtained was only 21%, due to the presence of the para- and disubstituted products.

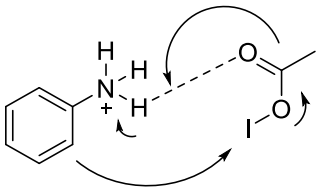

Figure 5.10: Proposed mechanism of the acetic hypoiodous anhydride for selective addition of the ortho-product [286].

When the reaction was scaled up, the yield obtained decrease significantly to 7%. Measures were taken to improve the yield of the iodination from *m*-anisidine by increasing the solvent volume and altering the solvent. Doubling the amount of solvent increased the yield to 13%, which could be due to less di-substituted products being formed. Finally, while keeping the solvent volume constant, different solvents such as dichloromethane (DCM) and acetonitrile were utilized. With the use of DCM, the yield increased substantially from 13% to 52%. The identity of the ortho-iodinated product was confirmed by comparison of the ^{1}H NMR spectrum from the previous synthesis by Shen *et al*. (2012), with the aromatic hydrogens at 7.48, 6.33, and 6.14 ppm, with a singlet at 3.74 ppm representing the methyl group (Appendix E) [286].

5.1.2.5 Carbonylation to synthesize compound 6

Following the synthesis of iodoarene **11**, carbonylation with carbon monoxide was carried out to obtain the carboxylic acid, benzoic acid **6**. The initial procedure incorporates Pd(dppf)Cl_2, CO, and a base, with THF and water as the solvent, to synthesize the carboxylic acid directly. However, this method was unsuccessful, and the product could not be isolated. Thus, a different solvent, methanol, was used to generate an ester **12** instead of a carboxylic acid directly. The ^{1}H NMR spectrum confirmed the identity of ester **12** with two downfield singlets at 3.79 and 3.83 ppm, representing the two methyl groups (Appendix F). The carboxylic acid can be generated via acid hydrolysis with lithium hydroxide (LiOH) to obtain benzoic acid **6** (Fig. 5.11). The ^{1}H NMR spectrum indicated the aromatic hydrogens at 7.60, 6.22, and 6.09 ppm, with the methyl group at 3.71 ppm (Appendix G). Both the carbonylation and hydrolysis provide good yield of 87% and 89%, respectively.

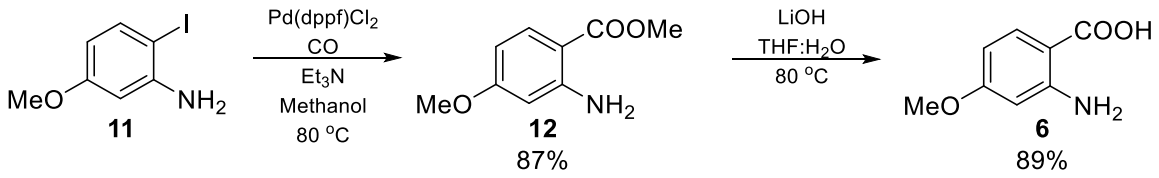

Figure 5.11: Synthesis of compound 6 through the formation of an ester by carbonylation followed by hydrolysis.

5.1.2.6 Synthesis of Isatoic anhydride 6.1

The isatoic anhydride **6.1** was synthesized by including triphosgene, following the procedures by Charoensutthivarakul *et al*. (2015) [248], with a yield of 72% (Fig. 5.12).

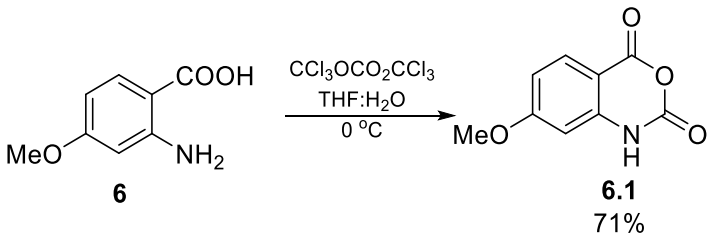

Figure 5.12: Synthesis of the isatoic anhydride 5.

5.1.2.7 Preparation of Oxazoline 4

Oxazoline **4** was initially prepared following the procedures from Charoensutthivarakul *et al*. (2015), with the addition of anhydrous zinc chloride and amino alcohol [248].

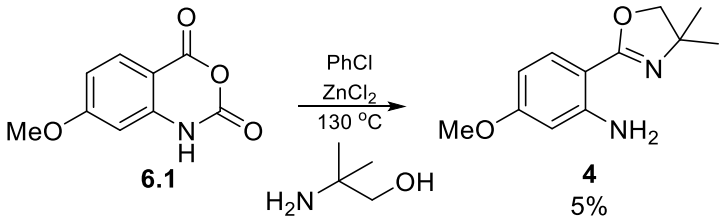

Figure 5.13: Synthesis of the oxazoline 4.

Initial attempts were unsuccessful, as the anhydrous zinc chloride might be insufficiently anhydrous due to the hygroscopic nature of zinc chloride. The experiment was repeated by heating the zinc chloride under vacuum for 3 hours in advance, in an attempt to remove the moisture. The experiment was successful, with a low yield of 5% (Fig. 5.13). In the search for an alternative method for the synthesis of the oxazoline **4**, a one-pot reaction, according to Jiang *et al*. (2013), was attempted [291]. This reaction allows the direct addition of the amino alcohol to the benzoic acid **6**, eliminating one reaction step (Fig. 5.14). Furthermore, the use of triphosgene, a hazardous compound, was eliminated. The synthesis of oxazoline **4** was confirmed by ^{1}H NMR spectroscopy, with a singlet at 1.35 ppm representing two of the methyl groups, with a downfield singlet at 3.78 ppm, signifying the methyl ester, with a yield of 19% (Appendix H).

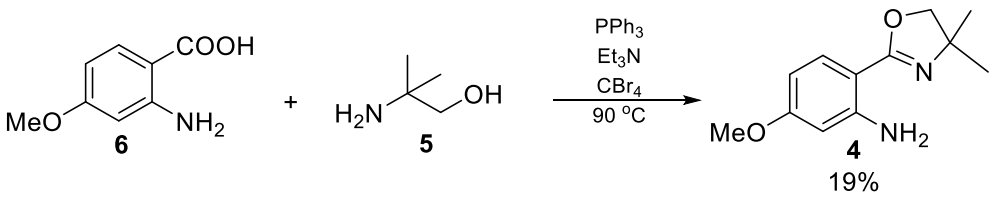

Figure 5.14: Alternative route for tbe synthesis of the oxazoline 4.

5.1.2.8 Modified synthesis route for SCR0911

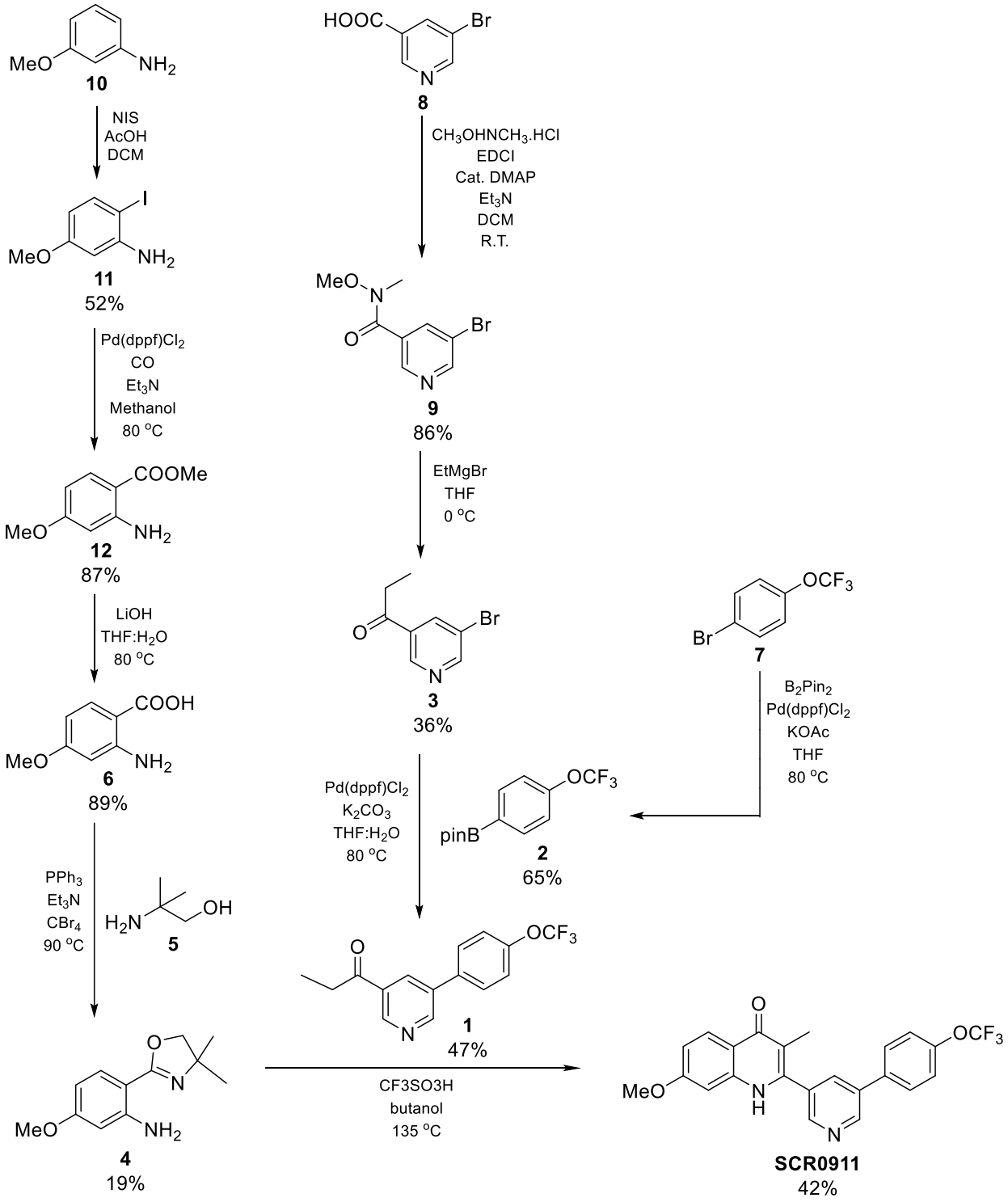

Figure 5.15: Synthetic scheme for the preparation of SCR0911.

The synthesis of SCR0911 can be achieved following the procedures by Charoensutthivarakul *et al*. (2015) by combining the biaryl compound **1** and oxazole **4** (Fig. 5.15) [248]. SCR0911 was

obtained with a 42% yield, similar to that as reported by Charoensutthivarakul *et al*. (2015) [248] (Appendix I). The final synthesis scheme for SCR0911 is shown in figure 5.15.

5.1.3 Understanding the inhibitory effect of SCR0911 in the ETC

5.1.3.1 Growth inhibitory assay with SCR0911

A growth inhibitory assay was carried out on both *M. smegmatis* and *M. bovis* BCG strains by assessing its minimum inhibitory concentration (MIC), to gain a preliminary indication on the effectiveness of SCR0911 on *Mtb*. The mycobacterial F-ATP synthase inhibitor, BDQ, was used as a control, and the MIC_{50} of BDQ obtained for both *M. smegmatis* and *M. bovis* BCG were found to be similar to that of published data, at 17 ± 2.3 nM and 188 ± 14 nM, respectively [184, 311]. The MIC_{50} of SCR0911 was determined to be 272 ± 41 µM and 107 ± 5.8 µM for *M. smegmatis* and *M. bovis* BCG, respectively (Fig. 5.16).

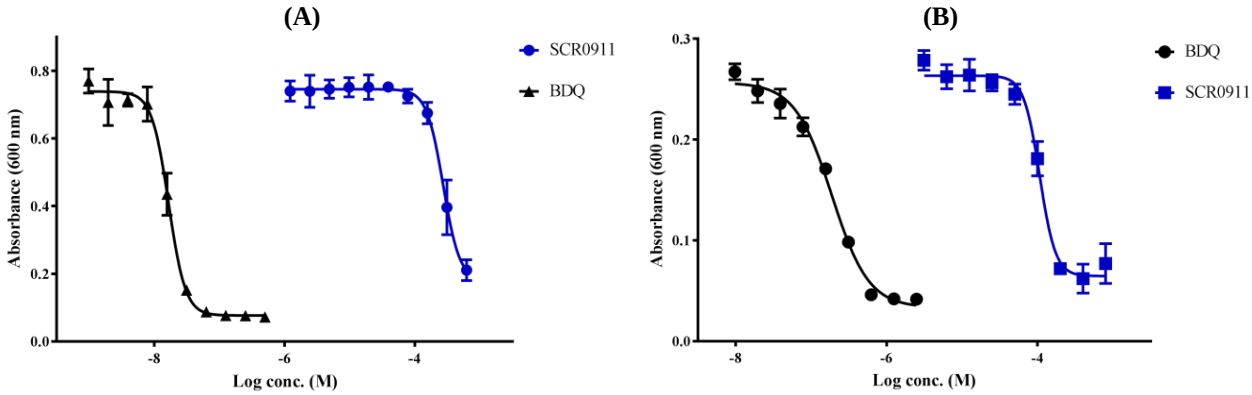

Figure 5.16: Growth inhibiton assay with SCR0911. MIC_{50} assay of BDQ (black) and SCR0911 (blue) against (A) *M. smegmatis* and (B) BCG. The MIC_{50} of BDQ was 17 nM and 188 nM for *M. smegmatis* and BCG respectively, while the MIC_{50} for SCR0911 was 272 µM and 107 µM respectively. Figures adapted from Chong *et al*. (2020) [277]. Error bars represent the standard deviations. The experiment has been carried out on two biological replicates.

To further determine if SCR0911 is active against the cyt-*bcc* complex as hypothesized, the *M. smegmatis* Δ*bcc* mutant strain (section 2.2.14) was employed (Fig. 5.17). If the mode of action of SCR0911 involves the inhibition of the cyt-*bcc* complex, it would be ineffective against the *M. smegmatis* Δ*bcc* mutant. BDQ was used as a negative control. An MIC_{50} of 16 ± 1.9 nM was obtained for BDQ, similar to the WT *M. smegmatis* strain. SCR0911, similar to Q203, a known cyt-*bcc* complex inhibitor, was unable to inhibit cell growth at the highest concentration tested at 800 µM. From the results, it appears that SCR0911 does inhibit the cyt-*bcc* complex.

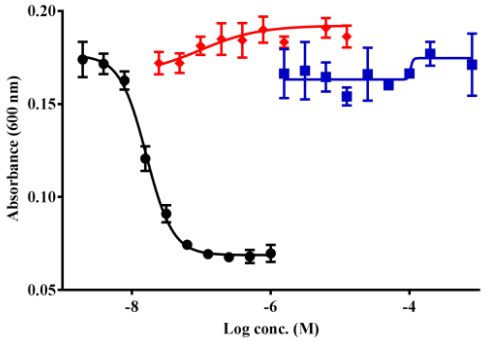

Figure 5.17: Growth inhibiton assay of *M. smegmatis* Δ*bcc* mutant with SCR0911. MIC_{50} assay of BDQ (black), Q203 (red) and SCR0911 (blue) against *M. smegmatis* Δ*bcc* mutant. The MIC_{50} of BDQ was 16 nM, while Q203 and SCR0911 are unable to inhibit the cell growth. Figures adapted from Chong *et al*. (2020) [277]. Error bars represent the standard deviations. The experiment has been carried out on two biological replicates.

5.1.3.2 Intracellular ATP synthesis assay

To determine if the growth inhibition effect by SCR0911 is due to the inhibition of the oxidative phosphorylation pathway, an intracellular ATP systhesis assay was carried out using *M. bovis* BCG (Fig. 5.18). Similar to published data in *Mtb* H37Rv, the IC_{50} of Q203 and BDQ was determined to be 0.5 ± 0.03 nM and 29 ± 2.7 nM, respectively [183]. Here, SCR0911 has demonstrated its ability in disrupting the ATP synthesis, with an IC_{50} of 50 ± 6.7 μM. However, as intracellular ATP synthesis assay allows the measurement of ATP synthesis within the cell, which, other than ATP synthesis from the electron transport chain, includes the disruption from the cell activities, such as the various metabolic pathways, further *in-vitro* analysis was carried out, to gain further understanding on the effect of SCR0911.

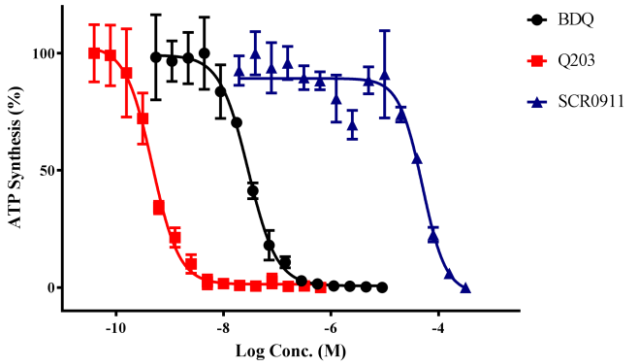

Figure 5.18: Intracellular ATP synthesis assay. BDQ (black), Q203 (red) and SCR0911 (blue) reveals an IC_{50} of 29, 0.5, and 50 μM, respectively in *M. bovis* BCG. Figure adapted from Chong *et al*. (2020) [277]. Error bars represent the standard deviations. The experiment has been carried out on two biological replicates.

5.1.3.3 ATP synthesis assay with inverted membrane vesicles (IMVs)

Here, an ATP synthesis assay with IMVs of both *M. smegmatis* and *M. bovis* BCG were carried out, to measure the ATP synthesis from the activity of the electron transport chain itself.

An electron donor, NADH, was added, and the IC_{50} obtained from the IMVs of *M. smegmatis* and *M. bovis* BCG were found to be 7.6 ± 0.4 and 6.9 ± 1.4 μM, respectively (Fig. 5.19). The IC_{50} indicates the ability of SCR0911 in inhibiting the oxidative phosphorylation pathway, in turn preventing ATP synthesis. It is interesting to note the large difference in the intracellular ATP synthesis data (50 ± 6.7 μM) and the ATP synthesis assay on the IMVs (6.9 ± 1.4 μM). This might be comparable to the cases of BDQ and Q203, where an increase in respiration was observed following the inhibition of the F-ATP synthase and the cyt-*bcc* complex, which could possibly impact the metabolism pathway [312].

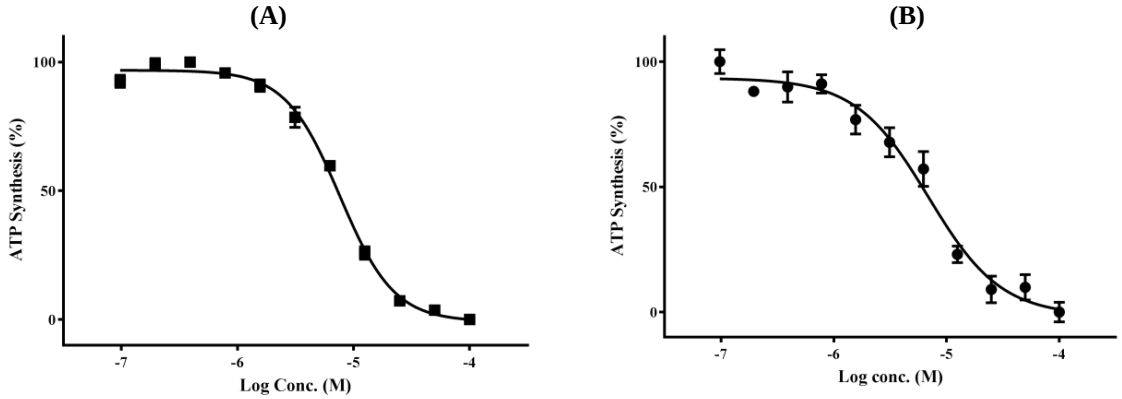

Figure 5.19: ATP synthesis assay with IMVs. (A) *M. smegmatis* and (B) *M. bovis* BCG, reflects an IC_{50} of 7.6 μM and 6.9 μM, respectively. Figures adapted from Chong *et al*. (2020) [277]. Error bars represent the standard deviations. The experiment has been carried out on two biological replicates.

To further understand the effect of SCR0911, ATP synthesis assay was carried out with an alternative electron donor, succinate, instead of NADH. Succinate will be oxidized directly by complex II (succinate-dehydrogenase), bypassing complex I (NADH-dehydrogenase), in turn allowing the characterization of the ATP synthesis activity without the involvement of the NADH-dehydrogenase. In addition, for this assay, a purer form of *M. smegmatis* IMVs was utilized, the inside-out plasma membrane vesicles (PMVs), that involves two additional ultracentrifugation steps. Q203 was employed as a positive control in this assay as it is a cyt-*bcc* complex inhibitor.

The PMVs of *M. smegmatis* were first utilized in the presence of NADH as a control (Fig. 5.20). NADH donates an electron to the NADH-dehydrogenase, thus initiating the cascade of electron transfer to the terminal oxidase, and finally, allowing the proton gradient generated to produce ATP. From the results, SCR0911 demonstrated its ability in inhibiting the ATP synthesis, with an IC_{50} of 3.8 ± 0.3 μM, similar to the ATP synthesis assay using IMVs. In

comparison, Q203 displayed an IC_{50} of 1.1 ± 0.8 nM, which was comparable to values determined in Kalia, *et al*., 2017 [184] (Fig. 5.20A).

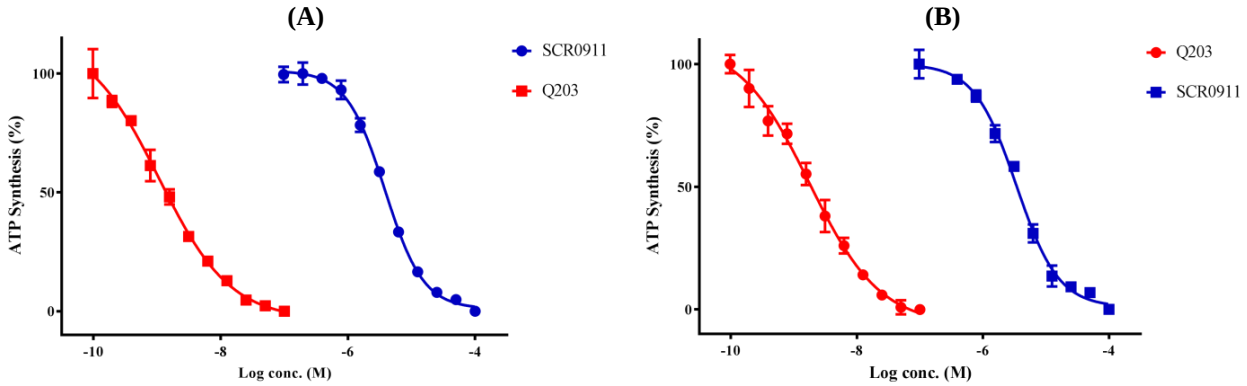

Figure 5.20: ATP synthesis assay with PMVs of *M. smegmatis*. (A) NADH and (B) succinate are utilized as electron donors. IC_{50} of Q203 (*red*) and SCR0911 (*blue*) were found to be 1.1 nM and 3.8 µM, respectively when utilizing NADH. In the presence of succinate, the IC_{50} of Q203 (*red*) and SCR0911 (*blue*) 2.0 nM and 3.4 µM, respectively. Figures adapted from Chong *et al*. (2020) [277]. Error bars represent the standard deviations. The experiment has been carried out on two biological replicates.

Next, the ATP synthesis assay was carried out with succinate instead of NADH (Fig. 5.20B). The IC_{50} for both Q203 and SCR0911 were 2.0 ± 0.1 nM and 3.4 ± 0.8 µM, respectively, similar to using NADH as an electron donor. As succinate is taken up directly by the succinate-dehydrogenase, it is possible to exclude the binding of the compound to NADH-dehydrogenase, with the similar IC_{50} values from both assays.

5.1.3.4 Determination of oxygen respiration inhibition of SCR0911

To ascertain if SCR0911 contributes to the inhibition of oxygen consumption, SCR0911 was subjected to an assay with methylene blue as an oxygen probe. In the presence of oxygen, methylene blue becomes oxidized, and a blue solution becomes prevalent. This could be observed in figure 5.21A, where the 7H9 media turned blue with the addition of methylene blue. However, in the presence of actively respiring *M. smegmatis* cells, in the drug-free (DF) cell culture tube, oxygen is being consumed, and the methylene blue solution remains colourless. THZ was added as a positive control, as it is known to inhibit respiration [166]. A blue solution was observed in the cell culture tube with the addition of THZ. With this, SCR0911 was subjected to the assay, and at 2.5× MIC_{50}, a blue solution was detected, indicating the effect of SCR0911 on the respiratory cytochrome oxidases. The decolourization percentage calculated for SCR0911 2.5× MIC_{50} was found to be 0% (Fig. 5.21B). The blue solution persists at 5× MIC_{50} and 10× MIC_{50} of SCR0911, although the decolourization percentage values calculated could

have been affected by the solubility of SCR0911 at these higher concentrations during the absorbance measurement.

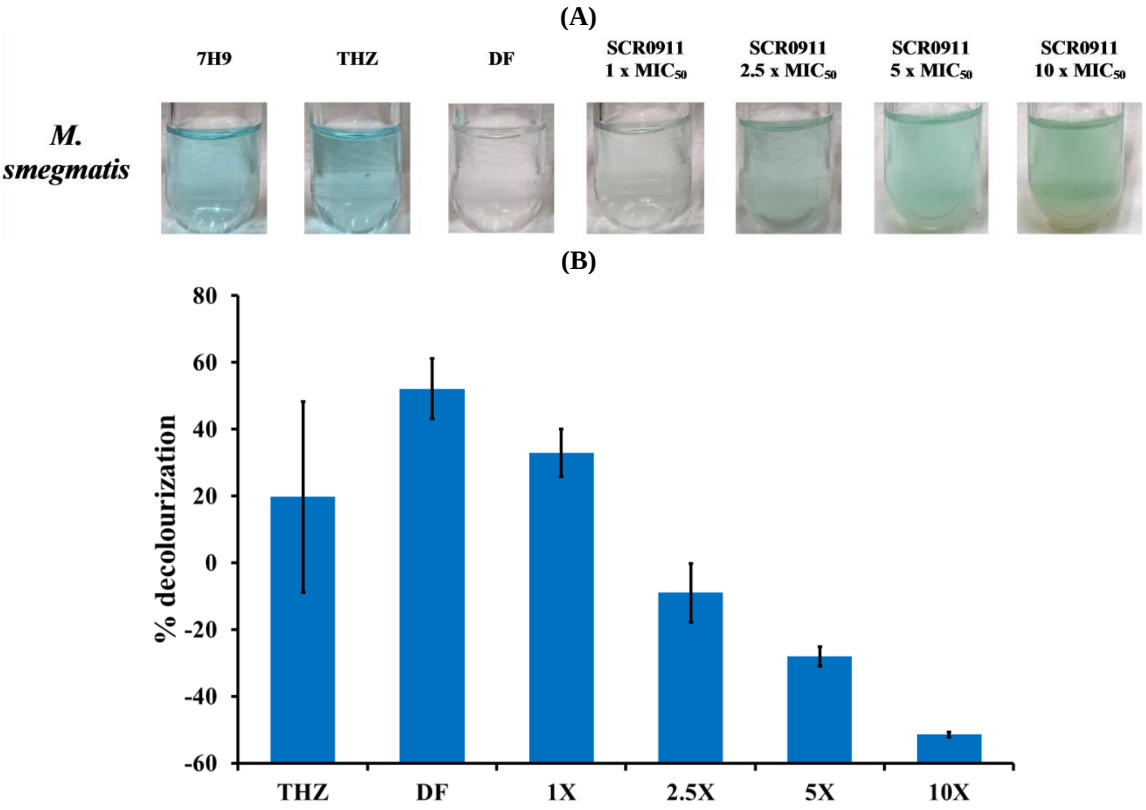

Figure 5.21: Methylene blue assay with WT *M. smegmatis*, in the presence of SCR0911. The 7H9 sample served as a blank, while the drug-free (DF) sample contains untreated *M. smegmatis*.THZ served as a positive control. (A) Visual representation of the tubes at the various conditions are presented. (B) Bar chart of percent decolorization at the various conditions. Figures adapted from Chong *et al*. (2020) [277]. Error bars represent the standard deviations. The experiment has been carried out on two biological replicates.

5.1.3.5 ATP-driven proton translocation

BDQ was found to be an uncoupler as well [313]. To have a greater understanding on the effect of SCR0911 on the proton gradient, an ATP-driven proton translocation assay was carried out. At the start of the experiment, ACMA was added to the plasma membranes, and the fluorescence intensity was observed. With the addition of NADH, electron transfer begins, and the proton gradient was established, causing the quenching of the fluorescence dye. When SCR0911 was added, very minimal reversal of the fluorescence intensity was observed (Fig. 5.22). The proton gradient only collapsed with the addition of the known uncoupler, SF6847, indicating that SCR0911 does not possess any uncoupling activity.

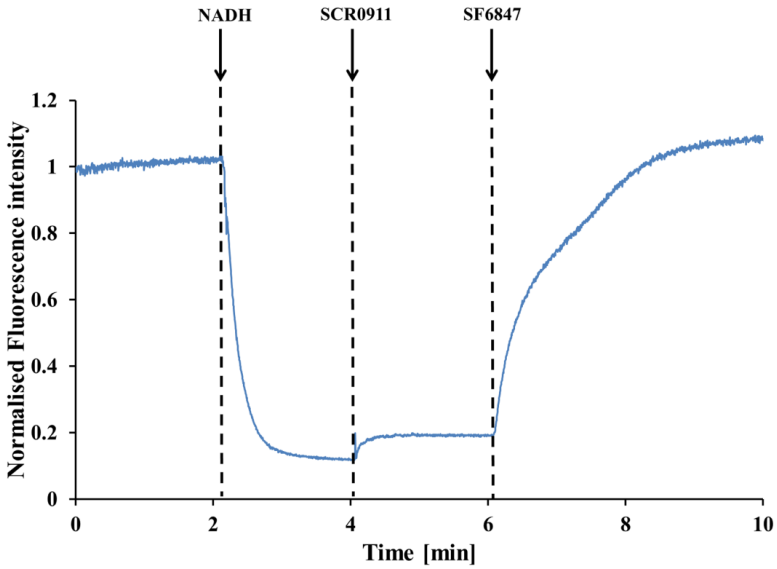

Figure 5.22: ATP-driven proton translocation assay on WT *M. smegmatis* PMVs, with NADH as the substrate. No uncoupling activity were observed at 15 µM of SCR0911 added. Figures adapted from Chong *et al*. (2020) [277]. The experiment has been carried out on three biological replicates.

5.1.4 Spectral analysis with PMVs in identifying cytochrome inhibitors

5.1.4.1 Spectral analysis with PMVs of WT M. smegmatis and Δbcc M. smegmatis

The electron transport chain within *Mtb* contains the supercomplex, cytochrome *bcc-aa*$_3$, and cytochrome *bd*. These cytochromes carry an iron atom within their heme groups that shuttles between Fe^{3+} to Fe^{2+}. Spectral analysis is a distinctive method to determine the presence of the cytochromes. The differential spectra of the PMVs produce a fingerprint of the cytochromes as these heme groups can absorb at specific wavelengths. Previous methods use sodium dithionite as a reductant that reduces the cytochromes directly (Fe^{3+} to Fe^{2+}), allowing the characterization of the specific cytochromes due to their absorption at specific wavelengths [72, 186, 224, 314].

Figure 5.23 illustrates the comparison of the differential spectrum of WT *M. smegmatis* (*black*) and Δ*bcc* of *M. smegmatis* (*green*) in the presence of sodium dithionite. The different strains revealed several distinctive bands. Considering the spectrum for WT *M. smegmatis*, the γ bands at 432 nm and 443 nm were observed. These correspond to heme *b* and heme *a* respectively, relating to the cytochrome *bcc-aa*$_3$. The prominent β-band and α-band at 523 nm and 552 nm, respectively, correlate to cytochrome *c*, while the α-band at 563 nm relates to that of cytochrome *b*. A peak at 600 nm indicates the presence of heme *a*.

Δ*bcc M. smegmatis* (*green*), on the other hand, has a γ-band at 428 nm that relates to heme *b*, of the cytochrome *bd*. The β-band and α-band were found at 529 nm and 557 nm, respectively,

corresponding to heme *b* of the cytochrome *bd*, while the characteristic α band at 600 nm and 630 nm correlates to heme *a* of cytochrome aa_3 and heme *d* of cytochrome *bd*, respectively [172, 315].

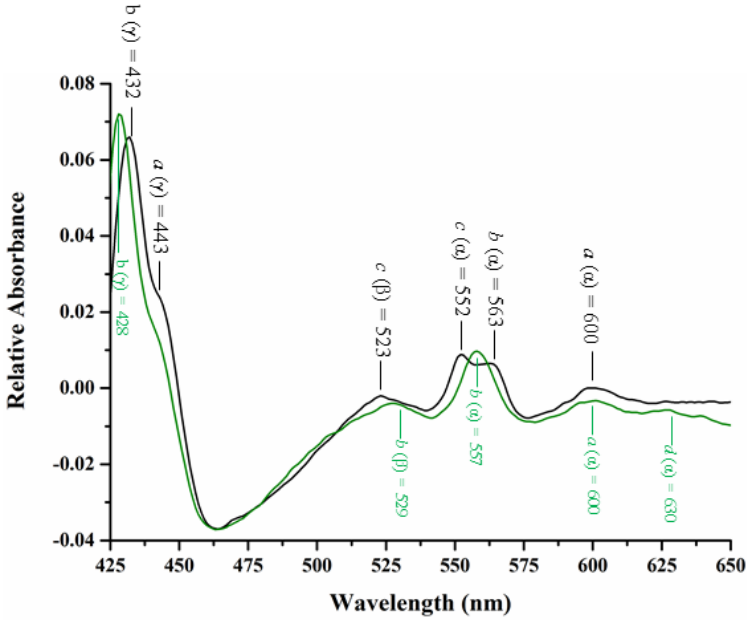

Figure 5.23: Spectral analysis of the PMVs of *M. smegmatis* with sodium dithionite. The spectrum of WT *M. smegmatis* (*black*) and Δ*bcc M. smegmatis* (*green*) are as shown. The peaks corresponding to the heme groups are indicated in the graphs.

In the WT *M. smegmatis* strains, a band corresponding to heme *d* of cytochrome *bd* was not observed. This was observed only in the Δ*bcc M. smegmatis* strains, which could be an overexpression of cytochrome *bd* to compensate for the lack of its main electron acceptor from menaquinol, the cytochrome *bcc*.

5.1.4.2 Spectral Analysis with PMVs of WT M. smegmatis using NADH as an electron donor

Next, sodium dithionite was replaced with NADH. Unlike sodium dithionite that reduces the iron in the cytochrome directly, NADH initiates the transfer of electrons through the complexes in the ETC. This ultimately permits the analysis of the electron transfer within the ETC, providing insights into the reduction of the complexes, especially with cytochrome *bcc-aa₃* and cytochrome *bd*. As time is required for the NADH reduction of the cytochromes completely, the spectrum was recorded when NADH was initially added and mixed (as indicated with 0 minutes), and again after 3 minutes. The absolute spectrum of WT *M. smegmatis* and Δ*bcc M. smegmatis* with NADH is shown in figure 5.24, where the spectrum at 0 minutes was deducted from the 3 minutes spectrum.

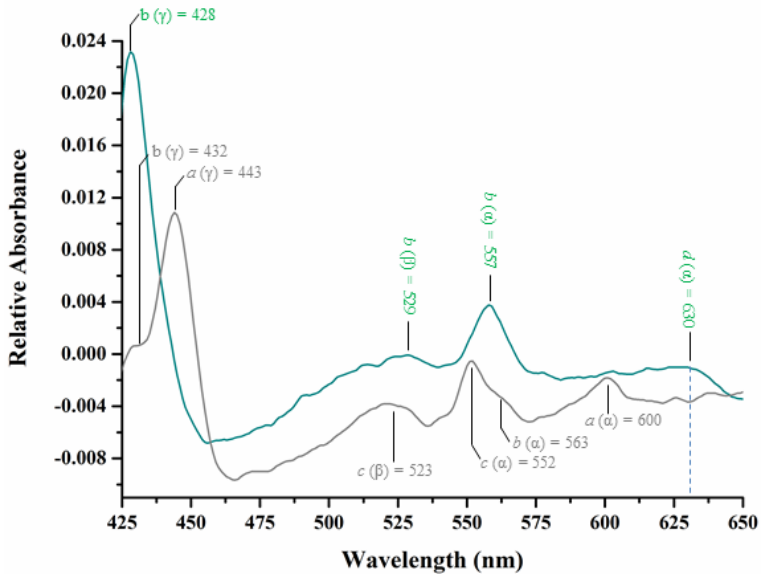

Figure 5.24: Absolute spectrum of the PMVs of WT and *Δbcc M. smegmatis* after 3 minutes. The peaks corresponding to the heme groups are indicated in the graphs. Due to the different pathways of electron transfer in the WT (*grey*) and Δ*bcc* strains (*green*), different heme groups are being reduced by NADH.

The bands for WT *M. smegmatis* was found to be at an identical wavelength to that of the sodium dithionite experiment, corresponding to that of cytochrome *bcc-aa*$_3$. Δ*bcc M. smegmatis* on the other hand, possess a similar spectrum as the sodium dithionite spectra analysis, except with the α-band at 600 nm which corresponds to cytochrome *aa*$_3$ were not observed. Hence, in the absence of cytochrome *bcc*, the electrons transfer towards cytochrome *aa*$_3$ could be impeded, preventing the reduction of cytochrome *aa*$_3$. This data demonstrates the comparison of WT and Δ*bcc M. smegmatis* strains, providing an alternative to study the cytochrome *bd*. DMSO was added in a control experiment, to ascertain that the bands are not affected by the presence of DMSO. With these findings, Q203 that inhibits cytochrome *bcc* was added (Fig. 5.25).

From figure 5.25, it can be observed that with the addition of Q203, the integrity of most of the peaks was compromised. As Q203 is an inhibitor of cytochrome *bcc* the binding to cytochrome *bcc* could prevent the transfer of electrons towards cytochrome *aa*$_3$ resulting in a spectrum that does not show any reduced cytochromes.

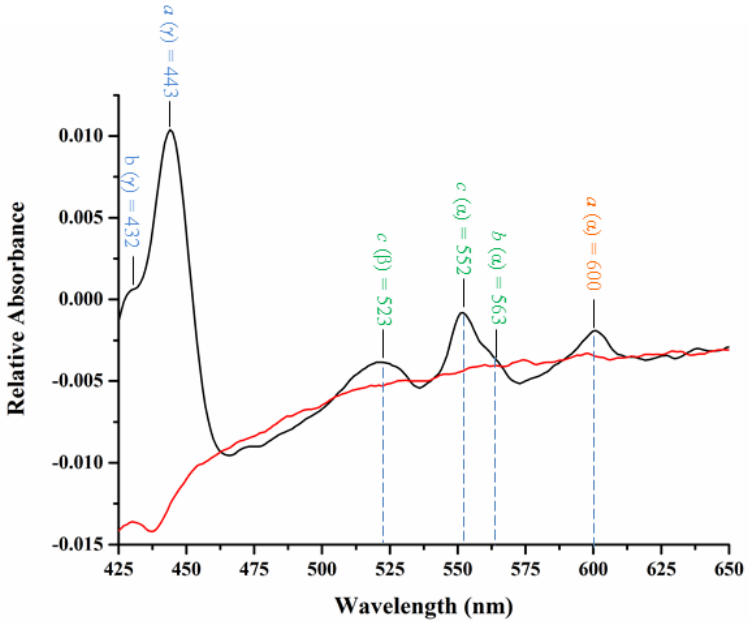

Figure 5.25: Absolute spectra of the PMVs of WT *M. smegmatis* in the presence of Q203. The peaks corresponding to the heme groups are indicated in the graphs. With the addition of Q203 7.5 µM (*red*), the bands were mostly compromised, as compared to the drug-free spectrum (*black*).

After confirming the efficiency of this method to analyze the cytochrome inhibitors with Q203, SCR0911 was tested, as shown in figure 5.26. However, the bands in the spectrum with the addition of SCR0911 appears similarly to that of the drug-free spectrum.

This could reflect on the mechanism of action of SCR0911, as compared to Q203. The binding site of Q203 was found to be the Q_0-site, where menaquinol binding takes place, passing electrons to heme b_L and 2Fe-2S cluster [72, 183]. Eventually, the electrons are transferred to menaquinone (at the Q_i-site) and to the cytochrome aa_3 complex. Hence, Q203 binding would directly impede the electron transfer process. In the case of SCR0911, the most important binding site indicated from the SCR0911 docking is at the Q_i-site. This binding site would not impede the transfer of electrons from menaquinol at the Q_o site towards the cytochrome aa_3 complex, which could explain the reduction of the heme groups. Nevertheless, analysis of SCR0911 with the Δ*bcc M. smegmatis* strains was carried out to gain further insights on the effect of SCR0911 in the Δ*bcc M. smegmatis* strains.

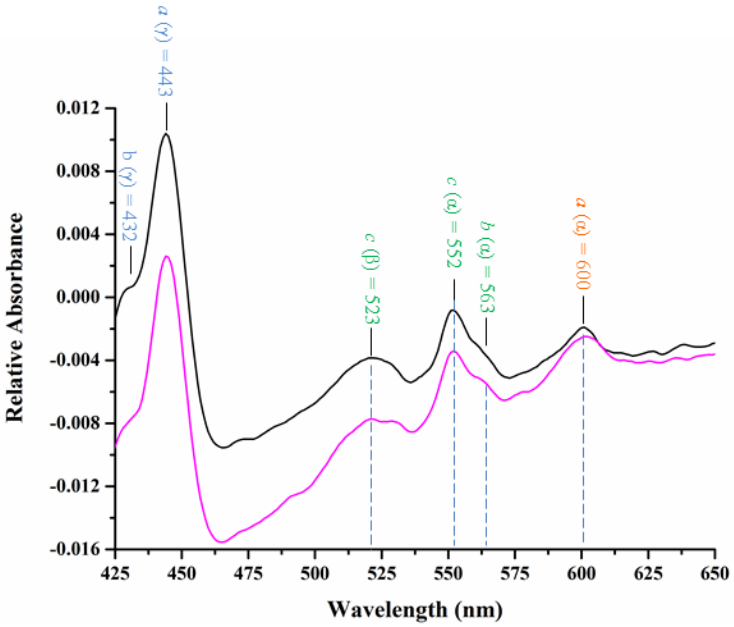

Figure 5.26: Absolute spectra of the PMVs of WT *M. smegmatis* in the presence of SCR0911. The peaks corresponding to the heme groups are indicated in the graphs. With the addition of SCR0911 50 μM (*pink*), the bands were not compromised, with bands appearing at similar wavelengths to the drug-free spectrum (*black)*.

5.1.4.3 Spectral Analysis with PMVs of Δbcc M. smegmatis using NADH as an electron donor

The same set of experiments was carried out on the PMVs of Δ*bcc M. smegmatis*. The addition of Q203 results in bands similar to the drug-free spectrum, indicating that Q203 does not inhibit the reduction of cytochrome *bd* (Fig. 5.27).

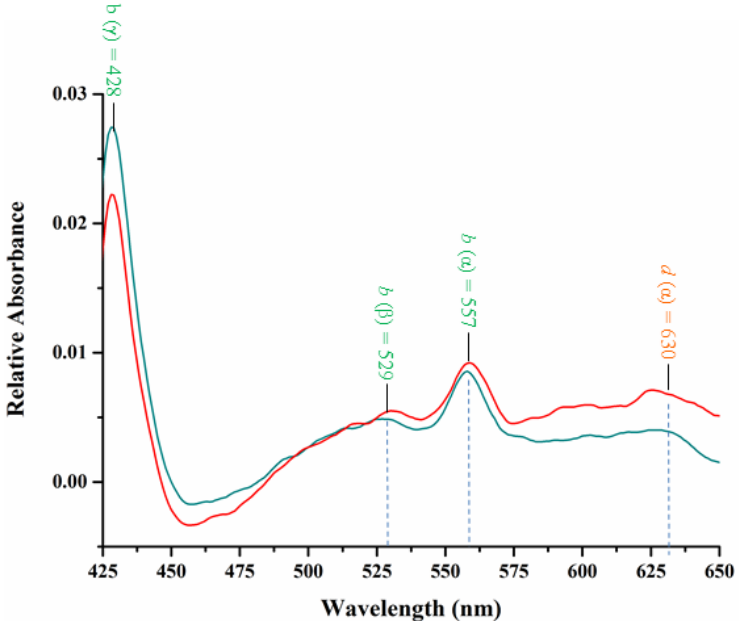

Figure 5.27: Absolute spectra of the PMVs of Δ*bcc M. smegmatis* in the presence of Q203. The peaks corresponding to the heme groups are indicated in the graphs. With the addition of Q203 10 μM (*red*), the bands were not compromised, with bands appearing at similar wavelengths to the drug-free spectrum (*green*).

Likewise, the experiment was repeated for SCR0911 with the PMVs of Δ*bcc M. smegmatis*, as shown in figure 5.28. Similar to the results from Q203, the bands appear at identical wavelengths to that from the drug-free spectrum.

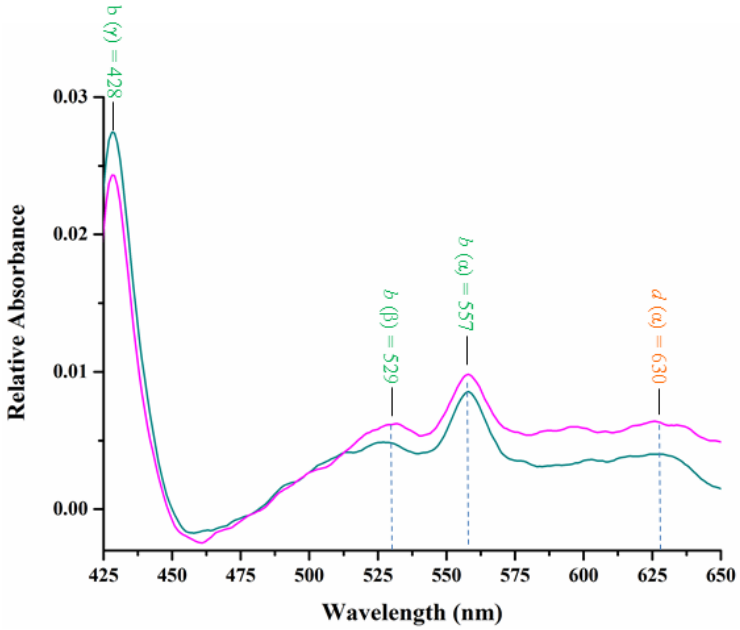

Figure 5.28: Absolute spectra of the PMVs of Δ*bcc M. smegmatis* in the presence of SCR0911. The peaks corresponding to the heme groups are indicated in the graphs. With the addition of SCR0911 50 µM (*pink*), the bands appear similar to the drug-free spectrum (*green*) with only slight differences.

Here, a novel spectral analysis experiment has shown the effectiveness in determining the target of cytochrome inhibitors. In addition, when comparing the spectra of sodium dithionite reduced and NADH reduced spectra of Δ*bcc M. smegmatis*, it is fascinating to note that bands at 443 nm and 600 nm, which correspond to cytochrome aa_3, were not observed in the NADH reduced spectrum unlike in the sodium dithionite reduced. This portrays that with the knockout cytochrome *bcc*, electrons are unable to be transferred to cytochrome aa_3, even though it is present, and cytochrome *bd* takes over as an alternative pathway.

Results

Part 6

Designing analogs of SCR0911

5.2 Designing analogs of SCR0911

5.2.1 Docking studies using GOLD software

To improve the activity of SCR0911 (Fig. 5.29), analogs were prepared, based on the 4th binding site obtained from the docking studies, as it was revealed to be the most functionally relevant. Analogs were designed with the intention to interact with residues such as E49 and H240 (Fig. 5.3A). Besides being specific and conserved only in mycobacterial species, these residues were found to be in proximity in the docking model, with hydrophobic interactions to SCR0911. More importantly, these residues could form hydrogen bonding which may well increase the binding efficiency of SCR0911. Hence, analogs designed for this intention are outlined in the table 5.1.

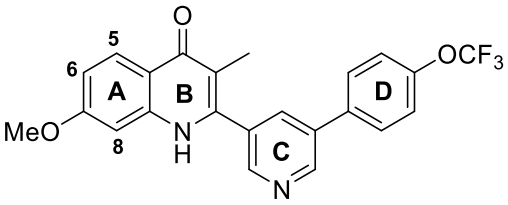

Figure 5.29: Chemical structure of SCR0911.

No.	Analogs	Explanation
1	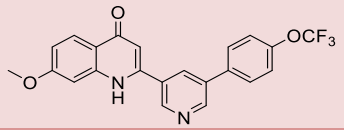	Removal of methyl group on ring B to understand the importance of this methyl group.
2	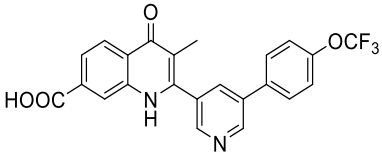	Altering OMe on ring A to COOH, to allow a H-bonding with residue H240. The oxygen on OMe is currently approximately 4.4 Å away from H240.
3	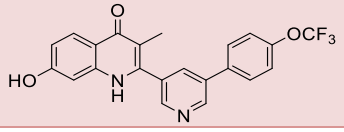	To determine the importance of the OMe group on ring A.
4	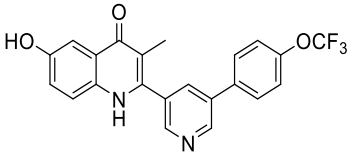	Alter the position of OH on ring A, to be much closer to residue E49. E49 is currently 2.7 Å away from the carbon containing the OH on analog 3. With the addition of OH, it could be much closer to initiate a hydrogen bonding.
5	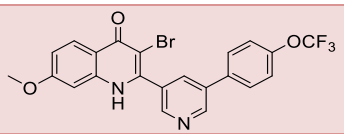	Addition of a halogen in place of the methyl group

Table 5.1: First stage of analogs designed for SCR0911

Docking studies were carried out on these analogs to assess their interaction profile. SCR0911 was first docked in the homology model of *Mtb* cyt-*bcc* prepared by Dr. Sony from Professor G.

Grüber's laboratory using GOLD to set a standard for the docking of the analogs [277]. The resulting ligand interaction profile was compared to the previously docked complex carried out by Dr. Sony, using AutoDock 4.2 [277]. With the same ligand interaction profile obtained, docking of the analogs was proceeded with the same settings in GOLD. The docking results of the analogs are shown in table 5.2.

Analog 1 has the methyl group on ring B removed to determine the importance of the methyl group (Fig. 5.29). Interestingly, with this alteration, the analog was found to have different interactions from SCR0911, with the analog has the quinolone moiety of the analog facing an opposite direction from SCR0911.

For analog 2, a carboxylic acid was intended to be added in place of OMe on ring A (Fig. 5.29), as the COOH group allows an extension, in hope to interact with residue H240. The docking studies in table 5.2 indicated the ability of the added carboxylic acid to interact with E49. However, with the alteration of the group, the analog lies differently in the protein, thus, it does not form a hydrogen bonding with H240 as predicted initially. Instead, an additional interaction between the pyridine moiety and S266 was found.

To further understand the importance of the OMe group on ring A, an additional docking study was carried out, with an alteration of OMe to alcohol. Analog 3 was found to have a very similar conformation to SCR0911. With a similar ligand interaction profile, it indicates that the added OH group does not allow any additional hydrogen bonding.

Analog 4 was designed with OH at position 6 instead of position 7 in analog 3 (Fig. 5.29). This was intended to allow an additional hydrogen bonding with E49, as the carbon 6 is at a distance of 2.7 Å away from residue E49. As expected, analog 4 has a very similar conformation and interaction profile to SCR0911, with the addition of an H-bonding with E49. This could allow a stronger interaction with the protein.

Analog 5 has a bromide group on ring B, in place of the methyl group (Fig. 5.29). As bromine has a similar size to a methyl group, a greater understanding on the importance of the methyl group can be achieved when comparing to SCR0911 and analog 1. Additionally, a bromide group could act as a Lewis acid, allowing an additional interaction with a Lewis base within the protein. The docking results in table 5.2, unexpectedly has s similar interaction profile to analog 1, instead of SCR0911. The synthesis of these analogs will provide valuable insights into the SAR.

<table>
<tr><th>Analog</th><th>Interaction</th><th colspan="2">Explanation</th></tr>
<tr><td rowspan="2">1
 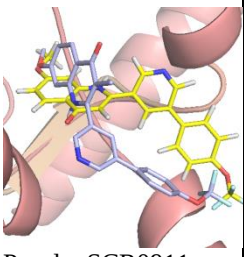
Purple: SCR0911
Yellow: Analog
ChemPLP 65.5660</td><td rowspan="2"> 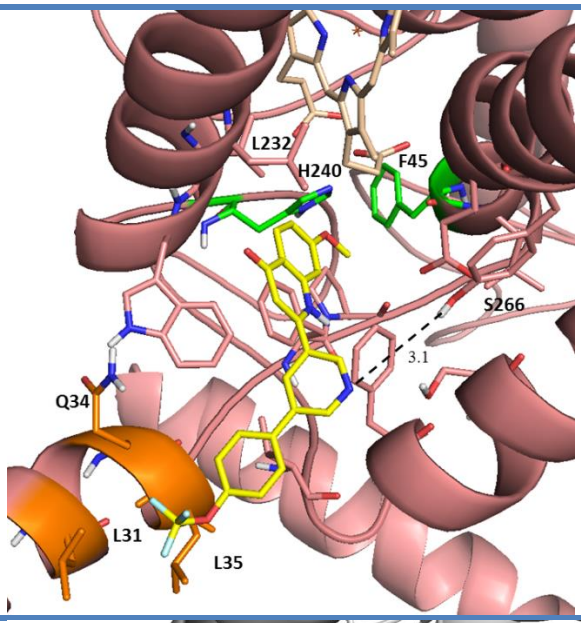
</td><td>Similar interactions</td><td>New interactions</td></tr>
<tr><td>L31, Q34 and L35 (stabilizing the OCF_3 phenyl group)
F45 and H240 (stabilizing the quinolone moiety)</td><td>S266 (H bonding)
L232 (stabilizing the quinolone moiety)</td></tr>
<tr><td colspan="3">Conformers generated from GOLD have oxygen of the quinolone moiety of the analog facing an opposite direction from SCR0911 Methyl group on the quinolone might be important.</td></tr>
<tr><td rowspan="2">2
 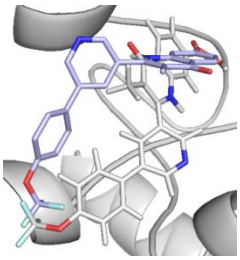
Purple: SCR0911
White: Analog
ChemPLP 61.8579</td><td rowspan="2"> 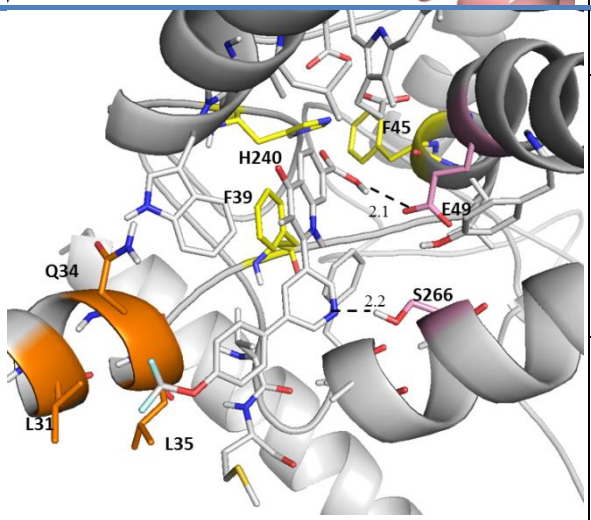
</td><td>Similar interactions</td><td>New interactions</td></tr>
<tr><td>L31, Q34 and L35 (stabilize OCF_3 phenyl group)
F31, F45 and H240 (stabilize quinolone)</td><td>S266 and E49 in pink (H bonding)</td></tr>
<tr><td colspan="3">Conformers generated have oxygen of quinolone moiety facing opposite from SCR0911, indicating COOH might have directed the compound to sit differently.</td></tr>
<tr><td rowspan="2">3
 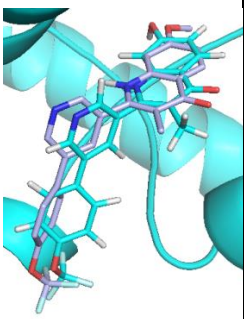
Purple: SCR0911
Blue: Analog
ChemPLP 59.5594</td><td rowspan="2"> 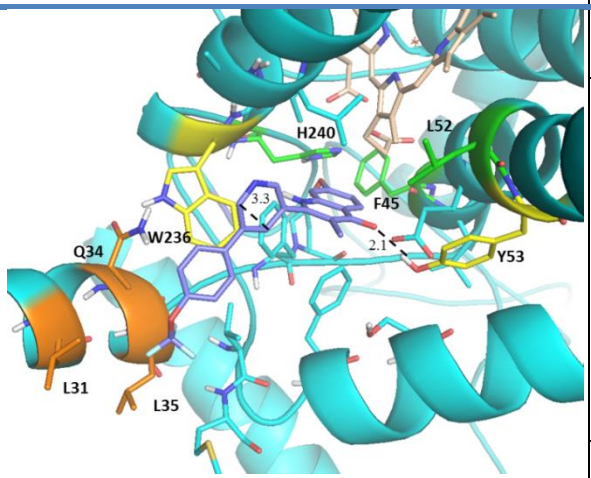
</td><td>Similar interactions</td><td>New interactions</td></tr>
<tr><td>Y53 and W236 (H bonding, pi interaction)
L31, Q34 and L35 (stabilize OCF_3 phenyl group)
F31, F45 and H240 (stabilize quinolone)</td><td>OH does not form any interaction</td></tr>
<tr><td colspan="3">Very similar conformation to SCR0911.</td></tr>
</table>

<table>
<tr>
<td>4
 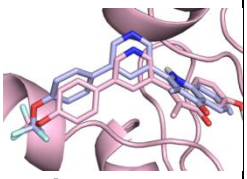
Purple: SCR0911
Blue: Analog
ChemPLP 61.4655</td>
<td> 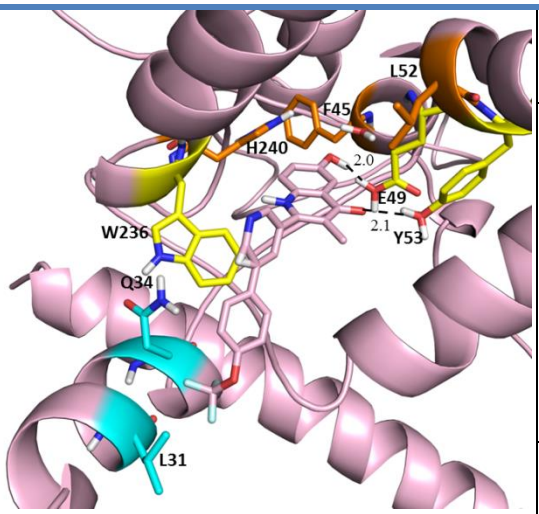
</td>
<td>Similar interactions to SCR0911</td>
<td>New interactions</td>
</tr>
<tr>
<td></td>
<td></td>
<td>Y53 and W236 (H bonding, pi interaction)
L31 and Q34 (stabilize OCF_3 phenyl group)
F31, F45 and H240 (stabilize quinolone)</td>
<td>E49 (H bonding)</td>
</tr>
<tr>
<td></td>
<td></td>
<td colspan="2">Analog appears to have similar interactions as SCR0911, except with the addition of a OH bonding with E49.</td>
</tr>
<tr>
<td>5
 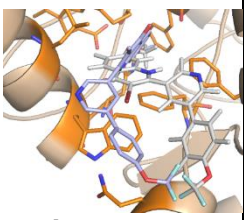
Purple: SCR0911
White: Analog
ChemPLP 64.9811</td>
<td> 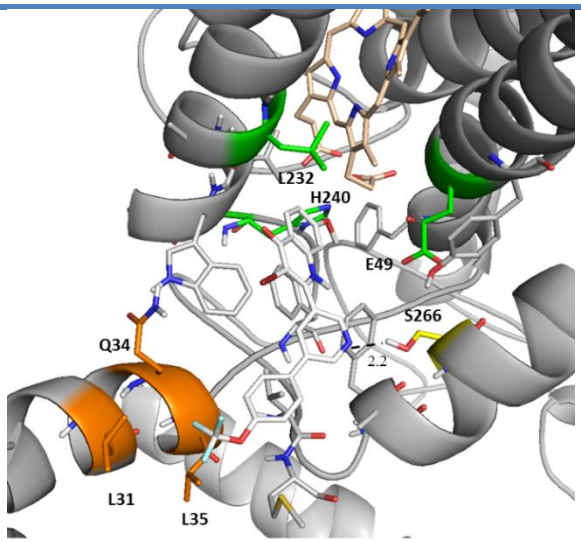
</td>
<td>Similar interactions to SCR0911</td>
<td>New interactions</td>
</tr>
<tr>
<td></td>
<td></td>
<td>L31, Q34 and L35 in orange (stabilizing the OCF_3 phenyl group)
H240 in green (stabilizing the quinolone moiety)</td>
<td>S266 (H bonding)</td>
</tr>
<tr>
<td></td>
<td></td>
<td colspan="2">Similar to analog 1</td>
</tr>
</table>

Table 5.2: Docking results of the analogs. Figures on the 1st column compares the docking position of SCR0911 (purple) with its respective analog, while figures on the 2nd column reveals its interacting residues. The 3rd column lists out the residues that are similar to SCR0911, and the new interactions found from the analog. Analog 1, with a removal of methyl group, initiates a change in the binding interaction with the protein. Analog 2 was found to have a different conformation from SCR0911 with a slight change to COOH on ring A, similar to analog 1. Analog 3 on the other hand, was found to be very similar to SCR0911 with no additional interactions. Analog 4, although very similar to the interactions of SCR0911, has an additional H-bonding. Analog 5, with an addition of a bromine on ring B has a similar interaction with analog 1.

5.2.2 Synthetic scheme for the 1st Analog of SCR0911

The first analog to be prepared was analog 1, SCR0911-A1 (Table 5.1), to gain an understanding on the importance of the methyl group on ring B (Fig. 5.29). Synthesizing SCR0911-A1 has its advantages, due to a shorter synthesis route (Fig 5.30), and the ease of adding a halogen in the same position for future SAR analysis.

The synthesis of SCR0911 involves the preparation of 1-(5-bromopyridin-3-yl)propan-1-one **3** from the commercially available 5-bromonicotinic acid **8** via a Weinreb amide **9** (Fig. 5.15). This was followed by a Suzuki cross-coupling with the organoboron **2**, prepared from 1-bromo-4-(trifluoromethoxy)benzene **7**, to generate rings C and D of SCR0911. Rings A and B were prepared from the commercially available *m*-anisidine **10**, to include a carboxylic acid at an ortho-position to the amide. The carboxylic acid with the amino alcohol permits the formation of the oxazoline **4**, which was eventually combined with rings C and D to synthesis SCR0911.

The proposed synthesis of SCR0911-A1 was shorter, due to the incorporation of a tandem carbonylative-Sonogashira and a 6-endo-aza-Michael addition reaction (Fig. 5.30). Furthermore, instead of preparing 2-amino-4-methoxybenzoic acid **6** from *m*-anisidine **10**, which requires 3 synthesis steps, 2-iodo-5-methoxyaniline **11** was utilized, which can be prepared in one synthesis step from *m*-anisidine, allowing a shorter synthesis route.

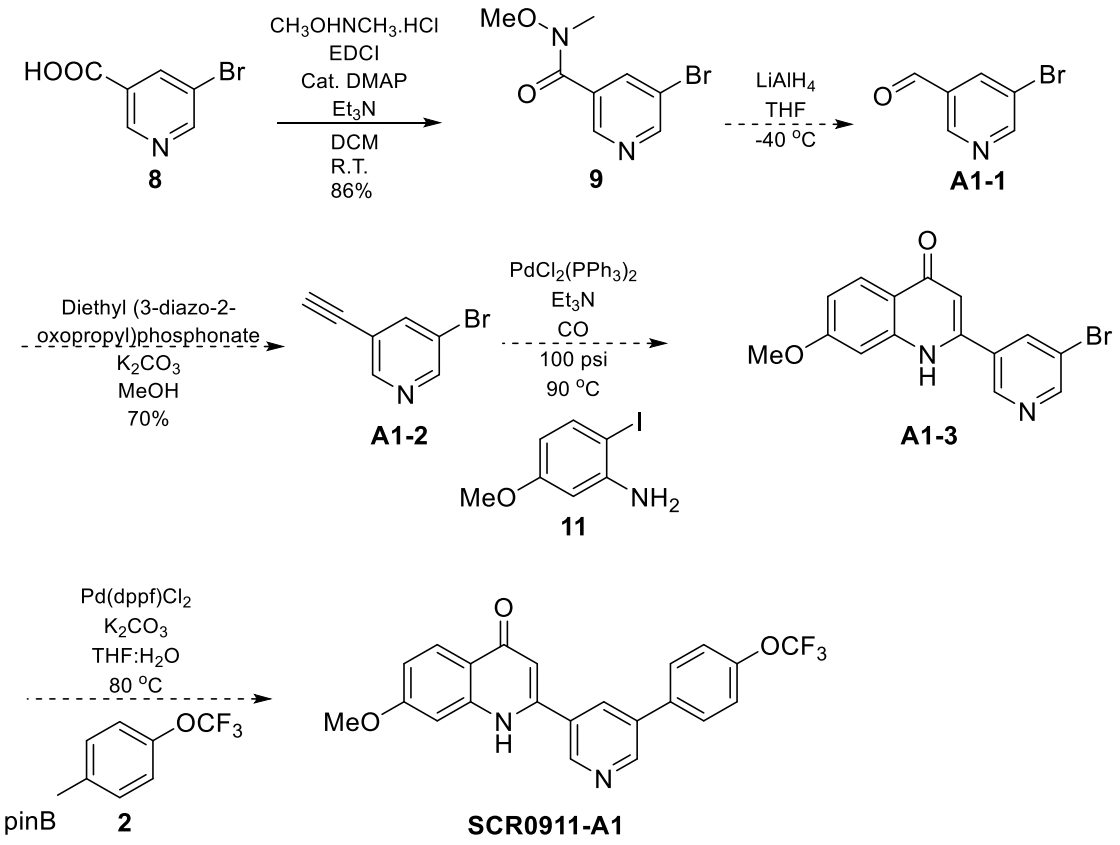

Figure 5.30: Synthesis route for SCR0911-A1. The carbonylative-Sonogashira completes the synthesis of SCR0911-A1 more efficiently as compared to SCR0911.

5.2.3 Synthesis of SCR0911-A1

5.2.3.1 Preparation of Weinreb amide 9

The synthesis route for SCR0911-A1 involves the synthesis of a Weinreb amide, with the addition of a base and activating agents, N-(3-dimethylaminopropyl)-N'-ethylcarbodiimide hydrochloride (EDCI) and 4-dimethylaminopyridine (DMAP) in good yield of 86%, affording the amide [283]. This has been carried out previously in the synthesis of SCR0911.

5.2.3.2 Synthesis of aldehyde A1-1

The synthesis of the aldehyde was obtained via the reduction of the Weinreb amide using lithium aluminium hydride, by following the procedure of Howard *et al*. [292]. 2 equivalents of $LiAlH_4$ was used initially, however the reaction was not completed overnight, and the starting material was still present from thin layer chromatography (TLC) analysis. An additional 2 equivalents of $LiAlH_4$ was added and left over another two days. Although more starting material was used up, the reaction was still not fully completed. A work up with water resulted in a 30% yield (Table 5.3, expt 1).

Expt.	Eq. of $LiAlH_4$	Temperature	Solvent	Reaction time	Workup	Yield
1	4	-78 °C	THF	3 days	Water	30%
2	8	-78 °C	Diethyl ether	1 day	Water	2%
3	1.2 (portionwise)	-78 °C	THF	3 days	1 M HCl	36%
4	1.2 (portionwise)	-78 °C	THF	3 days	Sat. NH_4Cl	50%
5	1.2 (portionwise)	-40 °C	THF	4 hours	1 M HCl	55%
6	1.2 (portionwise)	-40 °C	THF	4 hours	Sat. NH_4Cl	88%

Table 5.3: Conditions towards the optimization for the synthesis of the aldehyde 3.

A change in solvent to diethyl ether was attempted, with four equivalents of $LiAlH_4$ and a work up with water. The reaction was not completed after 24 hours, and an additional four equivalents of $LiAlH_4$ was added. However, starting materials were still present the following day, and a workup with water was carried out, resulting in a 2% yield (Table 5.3, expt 2).

Two different workup methods were attempted, with an acidic workup using 1 M hydrochloric acid, and a basic workup with saturated ammonium chloride. The reaction proceeded with the addition of $LiALH_4$ portionwise, to a total of 1.2 equivalents. After 3 days, TLC analysis indicated a small amount of the starting material present. The acidic workup resulted in a 36% yield, while the basic workup resulted in a 50% yield (Table 5.3, expt 3 and 4).

Finally, the reaction was carried out at -40 °C instead of -78 °C due to the lengthy reaction time of three days. At -40 °C, the reaction completed in 4 hours. Moreover, contrary to quenching the reaction with 1 M hydrochloric acid, that results in a yield of 55%, the reaction was quenched with saturated ammonium chloride. The yield was greatly improved to 88%, as the product could have been lost in the aqueous layer as a salt due to its basicity, when hydrochloric acid was added (Table 5.3, expt 5 and 6). The synthesis of aldehyde A1-1 was confirmed via ^1H NMR spectroscopy with a distinctive aldehyde singlet at 10.08 ppm (Appendix J).

5.2.3.3 Formulation of alkyne A1-2

A one-pot reaction for the synthesis of an alkyne from an aldehyde was utilized, using diethyl (3-diazo-2-oxopropyl)phosphonate, a similar compound to the Bestmann-Ohira reagent, dimethyl (3-diazo-2-oxopropyl)phosphonate (Fig. 5.31) [294]. Initially, a very low yield was obtained following silica gel flash chromatography. Due to the basicity of the alkyne **A1-2**, the silica gel flash chromatography was spiked with triethylamine to obtain a good yield of 70%. ^1H NMR spectroscopy revealed the presence of the alkyne, with the aromatic hydrogens at 8.63 and 7.92 ppm, with the alkyne hydrogen at 3.27 ppm. Rotary evaporation has to be carried out carefully to prevent loss of products.

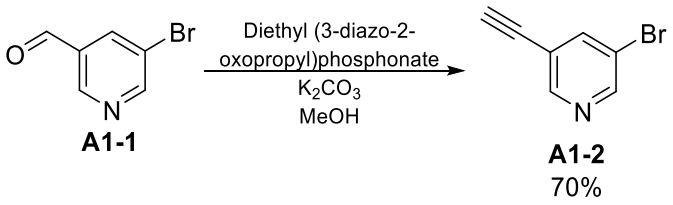

Figure 5.31: Synthesis of alkyne A1-2.

5.2.3.4 Synthesis of quinolone A1-3 via carbonylative-Sonogashira reaction

To synthesize the quinolone **A1-3**, a carbonylative-Sonogashira reaction under high carbon monoxide pressure was attempted on alkyne **A1-2** and iodinated aniline **11.** Iodinated aniline **11** was prepared after previous optimization from the synthesis of SCR0911, with a yield of 52%.

Synthesis of quinolone **A1-3** was carried out with the procedures from Torii *et al*., using triethylamine instead, at a carbon monoxide pressure of 100 psi (Table 5.4, expt 1) [296]. The reaction was first carried out at 120°C, which resulted in decomposition of the starting materials.

	Catalyst	**Temp.**	**Time (days)**	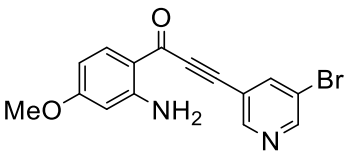 **A1-4**	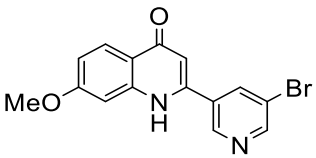 **A1-3**
1	$PdCl_2(PPh_3)_2$	120 °C	1	-	-
2	$Mo(CO)_6/PdCl_2$	95 °C	1	-	-
3	$PdCl_2(PPh_3)_2$	75 °C	7	30%	8%
4	$Pd(dppf)Cl_2$	75 °C	7	95%	-
5	$PdCl_2(PPh_3)_2$/ XPhos	75 °C	7	Quantitative	-
6	$PdCl_2(PPh_3)_2$/ XPhos	85 °C	3	Quantitative	-
7	$Pd(dppf)Cl_2$/DBU	75 °C	7	-	50%

Table 5.4: Optimization to obtaining quinolone A1-3.

In the meantime, a procedure using molybdenum hexacarbonyl ($Mo(CO)_6$,) by Ghosh *et al*. (2018), was attempted (Table 5.4, expt 2) [316]. The method encourages the use of Pd-NHC for the best yield of 94%. Due to the unavailability of Pd-NHC, $PdCl_2$ was used alongside triethylamine (Et_3N), however, the reaction did not proceed with no consumption of the starting materials. Hence, the procedure using CO was attempted again, using a lower temperature of 75 °C, to prevent decomposition (Table 5.4, expt 3). The reaction took 6 days for the iodinated aniline **11** to be completely reacted. After silica gel flash chromatography, the major product was determined to be the alkyne **A1-4**, by NMR and mass spectrometry. The ^{13}C NMR spectrum indicates the presence of alkyne carbons at 85.6 and 90.6 ppm, and ketone carbon at 176.34 ppm, signifying the CO insertion and Sonogashira have proceeded smoothly. However, the second part of the tandem reaction, the aza-Micheal reaction had not occurred (Appendix L).

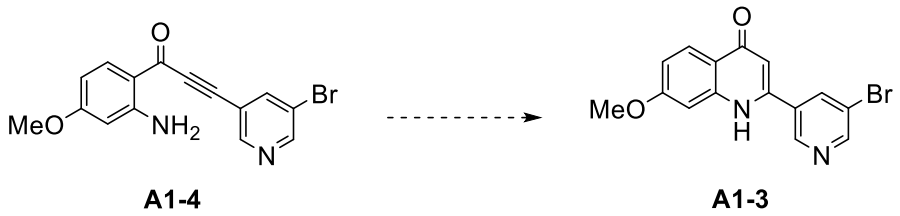

Figure 5.32: Major product A1-4 obtained after carbonylative-Sonogashira reaction. Intramolecular Micheal reaction have to occur to obtain the quinolone **A1-3**.

A change of catalyst to (1,1'-bis(diphenylphosphino)ferrocene)palladium(II) dichloride ($Pd(dppf)Cl_2$) was utilized at 75 °C as well (Table 5.4, expt 4), providing the alkyne **A1-4** with 95% yield. With the concept that the alkyne **A1-4** can be subjected to a base to allow the intramolecular Micheal reaction to proceed to quinolone **A1-3** (Fig. 5.32), further optimizations were carried out to reduce the reaction time by incorporating a XPhos ligand (Table 5.4, expt 5). This led to a quantitative yield of the alkyne **A1-4**, without any improvement in the reaction time. Hence, the same experiment was carried out, while increasing the temperature to 85 °C, completing the reaction in three days, with a quantitative yield (Table 5.4, expt 6).

In hope to achieve a one-pot reaction for the synthesis of quinolone **A1-3**, a stronger base, DBU, was added to the reaction mixture, as Et_3N might not be sufficiently strong for the aza-Micheal reaction. At 75 °C, the reaction was completed in 7 days, with a 50% yield of quinolone **A1-3** (Table 5.4, expt 7). ^1H NMR spectroscopy confirmed the synthesis of quinolone **A1-3** with 7 hydrogen in the downfield region, along with a broad singlet corresponding to the N-H hydrogen (Appendix M). More distinctively, the presence of a singlet at 6.60 ppm relates to the proton alpha to the carbonyl.

Future optimization includes increasing the temperature to 85 °C to speed up the rate of reaction, as well as attempting different catalyst and bases, to assist in the ring closing to obtain a higher yield. Following this, a Suzuki cross-coupling can be carried out, similar to the method in preparing SCR0911, to obtain **SCR0911-A1**.

Discussion

6. Discussion

6.1 Towards affecting the cytochrome *bcc* complex

6.1.1 Repurposing of SCR0911

The docking studies revealed four binding sites of SCR0911 to the *Mtb* cyt-*bcc* model, with the 4th binding site being the most functionally important as it binds at the Q_i site. Additionally, SCR0911 was postulated to bind to the Q_i site in *P. falciparum* [248, 253], and a cryo-EM structure of SCR0911 within the Q_i site of the bovine bc_1 was also produced [254], signifying the significance of this binding site. The binding of SCR0911 at this region would prevent menaquinone binding and hence affect the electron transfer towards the menaquinone at the Q_i site.

Despite having a similar binding region of SCR0911 in the *Mtb* bc_1 model, bovine bc_1 cryo-EM structure and the *P. falciparum* bc_1 model, the interacting residues differ vastly, indicating SCR0911 adoption of a different conformation in *Mtb*. Due to the concern of cardiotoxicity to humans in compounds targeting the cytochrome bc_1, the binding residues of SCR0911 in *Mtb* was analyzed with the sequence alignment data (Fig. 1.16). Only two residues, L31 (Y16 in *P. falciparum*) and L232 (I88 in *P. falciparum*), are conserved in human, L21 and L197, respectively. Other residues interacting with SCR0911 in the *Mtb* model were determined to have dissimilar properties, as shown from the sequence alignment, to the residues found in human bc_1. Residue Q34, containing an amine group, was revealed to be proline in human bc_1, while residues F39 and F45 were revealed to be serine in human bc_1, a polar residue with the capability of forming a hydrogen bond, unlike phenylalanine. Residue F262 corresponds to tyrosine in human bc_1, a polar residue as well. Furthermore, residue Y53, shown to have a hydrogen bonding interaction with SCR0911, corresponds to isoleucine, an aliphatic amino acid, as compared to an aromatic acid with an OH group.

These results indicate that it might be unlikely for SCR0911 to possess this conformation in the human cytochrome bc_1. In addition, as the bovine cytochrome *b* has a 80% sequence homology to human cytochrome *b*, SCR0911 could bind to human bc_1 in a similar fashion as in the bovine crystal structure of cytochrome bc_1. However, the sequence aligment results have shown that residues I39 and A232 in bovine are not conserved in humans and were shown to be A39 and L232, respectively. Despite all the residues being hydrophobic, the larger residues might displace SCR0911 from occupying the Q_i site of cytochrome bc_1.

The synthesis of SCR0911 was carried out following a similar synthetic scheme as published by Charoensutthivarakul *et al*. (2015) [248] with several modifications, such as the synthesis of oxazole **4** directly from benzoic acid **6**. This avoided the synthesis of an isatoic anhydride from the benzoic acid **6**, allowing the reduction of a reaction step and avoided the use of triphosgene, a hazardous chemical.

SCR0911 has displayed its effectiveness in inhibiting the growth of both *M. smegmatis* and *M. bovis* BCG, with an MIC_{50} of 272 μM and 107 μM, respectively. Furthermore, when employing the *M. smegmatis* Δ*bcc* mutant, no inhibition was observed, supporting the cyt-*bcc* complex as its target. It has additionally indicated its success in inhibiting ATP synthesis in both the intracellular assays and *in-vitro* IMVs experiments, highly suggesting the ability of SCR0911 in disrupting the oxidative phosphorylation pathway. The additional ATP synthesis assay of PMVs with succinate have eliminated NADH-dehydrogenase as a target as well. Interestingly, the methylene blue assay indicates that the oxygen consumption was inhibited for SCR0911, which was not observed for Q203, a cytochrome *bcc* inhibitor. Despite the results revealing its inhibitory effect towards the cyt-*bcc* complex, the docking studies and oxygen consumption assay signifies a different mechanism of action of SCR0911 possess, as compared to Q203. Q203 was revealed to bind at the Q_o site, while the docking studies indicate SCR0911 binding at the Q_i site of the cyt-*bcc* complex. Although Q203 has a high potency towards *Mtb* strains, it was established to be bacteriostatic, only becoming bactericidal with the addition of a cyt-*bd* inhibitor [183, 184].

6.1.2 Spectral Analysis with NADH

The development of the novel spectral analysis using NADH came about during the discussion to determine the target of SCR0911. In the 1920s, it was first revealed that the oxidation state of the cytochromes in the ETC causes a change in the spectra across a range of wavelengths [317, 318]. The result is a spectra of these reduced cytochromes, containing heme groups that absorb at specific wavelengths. Previous methods employ sodium dithionite as a reductant to reduce the cytochromes (Fe^{3+} to Fe^{2+}) [72, 186, 224, 314]. For this study, compounds were initially added while using sodium dithionite as a reductant. However, no difference in the reduced spectrum was observed, as sodium dithionite could have reduced the heme groups in the different cytochrome complexes directly, irrespective of the mode of action of the compound. Hence, NADH was employed as an electron donor. Here, two interesting

factors were noticed. Firstly, the reduction of the cytochromes was not immediate, as in the case of using sodium dithionite. The wavelength scan carried out immediately after the addition of NADH reveals no reduction of cytochromes, and the absorbance bands are observed only after three minutes. This suggests the transfer of electrons from NADH to the cyt-aa_3 complex requires time, and the heme groups are not reduced directly. Secondly, when comparing the spectrum of the Δ*bcc M. smegmatis* when utilizing sodium dithionite and NADH, it was found that the absorbance band corresponding to heme *a* (cyt-aa_3 complex) was only observed when sodium dithionite was used as a reductant. When NADH was added to the Δ*bcc M. smegmatis*, the transfer of electrons towards cyt-aa_3 was not possible, and therefore, not reduced. It supports the notion that the transfer of electron occurs through the ETC when incorporating NADH. These two factors support the utilization of the spectral analysis using NADH to identify cytochrome inhibitors.

To validate the study, known cyt-*bcc* inhibitor, Q203 was utilized. Q203 was found to successfully prevent the reduction of the cytochromes in the WT *M. smegmatis* PMVs, but not in the PMVs of Δ*bcc M. smegmatis*, indicating it being a cyt-*bcc*. When SCR0911, a conjectured *Mtb* cyt-*bcc* inhibitor, was employed in this study, no effect on the heme groups was identified. This could be attributed to the different binding sites of SCR0911 and Q203. Q203 is understood to bind to the Q_o site of the cyt-*bcc* complex, while the docking studies indicated SCR0911 binding to the Q_i site [183]. With the binding of Q203 at the Q_o site, it prevents menaquinol binding and impedes the release of electrons from menaquinol to heme b_L, as well as to the iron-sulfur cluster, inhibiting the reduction of the heme groups [72]. Alternatively, SCR0911 at the Q_i site only prevents the attachment of menaquinone at the Q_i site. It still allows the binding of menaquinol at the Q_o site, which in turn permits the transfer of electrons towards the cyt-aa_3 complex. These results in the reduction of the cytochromes, and the absorption bands observed with the addition of SCR0911.

This assay provides further insights into the mechanism of SCR0911, where the transfer of electrons towards the cyt-aa_3 complex could be possible, without the return of electrons to menaquinone, to complete the Q-cycle [72, 319]. This has its repercussions, as it inhibits the creation of a transmembrane electric gradient, which is essential in generating the proton motive force for ATP synthesis [231]. Furthermore, an inhibitor at the Q_i site could result in the accumulation of semi-menaquinone that promotes the reduction of oxygen to superoxide [319, 320].

6.1.3 Analogs of SCR0911

The docking model demonstrates that SCR0911 is surrounded by mycobacterial specific residues, opening the door for the design of new mycobacterial specific SCR0911 analogs. To improve the efficiency of SCR0911, several analogs were designed, especially with modifications on rings A and B, as most interactions are found surroundings rings A and B. **SCR0911-A4** was revealed from the GOLD docking studies to be the most intriguing, as the interaction profile indicates its ability to form an additional hydrogen bonding, with a similar binding interaction to SCR0911. This will hopefully allow a better growth inhibition of *Mtb*.

Conclusion

7. Conclusion

In this study, two separate pathways for the inhibition of mycobacterial species have been described. The first is an antioxidant defense pathway involving *Mt*AhpC, which is found to be critical in INH-resistant TB [102]. The second comprises of the oxidative phosphorylation pathway, that focuses on the cyt-*bcc* complex, where a major amount of endogenous ROS are produced [72, 228].

To understand the importance of the Cys-S_pH containing helix in regards to its catalytic acvity, site-directed mutagenesis was carried out to disrupt the helical movement and to determine the critical residues that allow this helical movement. The results indicate the importance of the synchronized helical movement for the reduction of peroxides, as demonstrated by the mutant *Mb*AhpC$_{F68V}$, which reveals negligible enzymatic activity, and *Mb*AhpC$_{A67D}$, which retains only 64% of WT *Mb*AhpC's activity.

The F68 residue was revealed to be a critical residue for the helical movement and enzymatic activity, as it requires a concerted movement of the three phenylalanine side chains, F51, F68 and F108 for the rigid body movement [107]. Crystallization on *Mb*AhpC$_{A67D/C176S}$ provides insights on the loss of activity from the A67D mutation, as alteration on the helix containing the peroxidatic cysteine can be observed. Additionally, the loop contributing to the hydrophobic interactions for oligomerization was as well shifted. These resulted in the loss of oligomerization, and decreased in enzymatic activity. Nevertheless, reduction of peroxides was still possible, as the disulfide bond is still in close proximity, allowing binding of peroxides.

On the second pathway of interest, SCR0911 was found to be a cyt-*bcc* complex inhibitor. With an MIC_{50} of 272 μM and 107 μM in *M. smegmatis* and *M. bovis* BCG respectively, it portrayed no inhibition in the Δ*bcc M. smegmatis* strains. Further on-target assays were carried out which have established SCR0911's ability to inhibit ATP synthesis, indicating its effect on the oxidative phosphorylation pathway. The novel spectral analysis approach utilizing NADH have additionally agree with the docking studies of SCR0911 binding to the Q_i site, unlike Q203, which binds to the Q_o site, thus allowing reduction of the cyt-aa_3. The binding at the Q_i site would result in the collapse of the proton motive force, and additionally result in more superoxide formation.

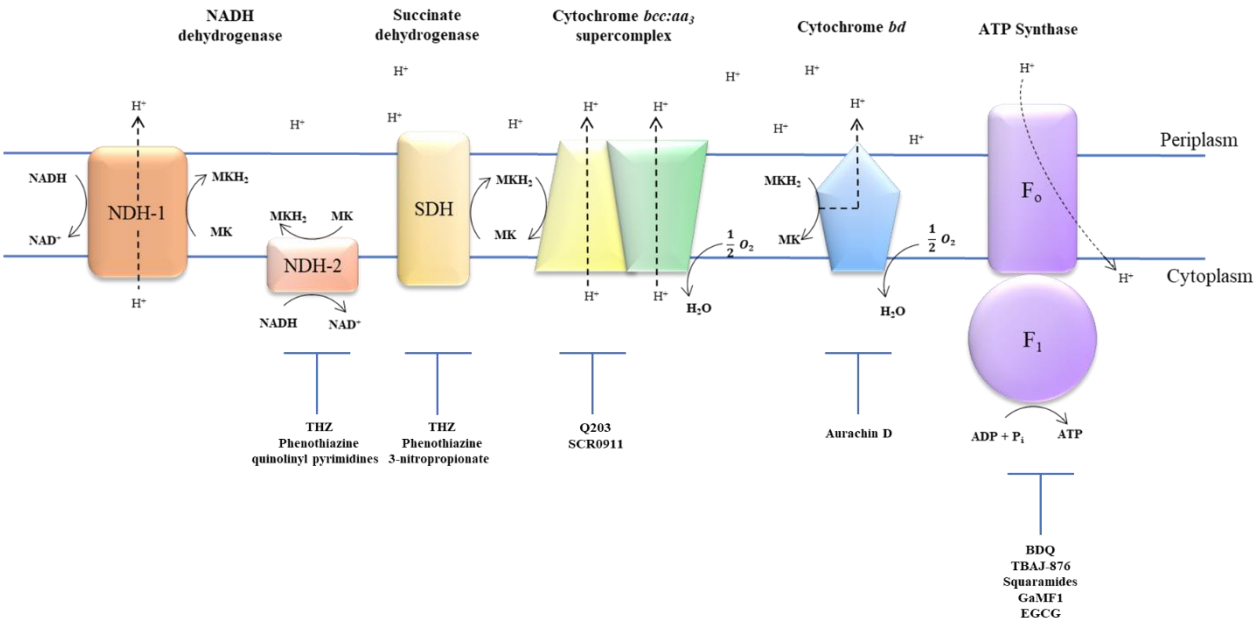

Figure 6.1: The complexes involved in the ETC of *Mtb*. ATP synthesis could be blocked at different points in the oxidative phosphorylation pathway. Several known inhibitors of the complexes are outlined in the figure.

To meet the Sustainable Development Goals and Stop TB Strategy [2], efforts from research groups around the world have allowed the discovery of new TB drugs (Fig. 6.1). SCR0911 with a different mechanism of action might contribute to the combination therapy along with the novel drugs targeting the ETC. This may increase the possibility of combatting the drug-resistant TB strains. Additionally, studies have identified structural scaffolds of SCR0911 to be cyt-*bd* inhibitors, indicating its potential to inhibit both cyt-*bcc* and cyt-*bd* complex [249].

This research has provided insights into the structure-function of *Mt*AhpC, while identifying SCR0911 as a lead compound targeting the cyt-*bcc* complex. Herein, a concept to stimulate the pathogen to kill itself with endogenous ROS production, while removing its ability to reduce the oxidative species was unveiled.

Future works will include *in silico* structure-based studies to identify compounds that specifically target residue F68 in *Mt*AhpC, as well as the design of analogs for SCR0911 to allow a better binding at the Q_i site. This could not only cause the breakdown of the proton motive force, but results in an excess of endogenous ROS.

References

1. World Health Organization. *Global tuberculosis report 2017*. 2017; Available from: http://apps.who.int/iris/bitstream/handle/10665/259366/9789241565516-eng.pdf;jsessionid=943BED7667B61C4C09C823E8FAB77AD3?sequence=1.
2. World Health Organization. *Global tuberculosis report 2016*. 2016; Available from: http://www.who.int/tb/publications/global_report/en/.
3. Pai, M., et al., *Tuberculosis.* Nature Review Disease Primers, 2016. **2**: p. 16076.
4. Gomez, J.E. and J.D. McKinney, *M. tuberculosis persistence, latency, and drug tolerance.* Tuberculosis, 2004. **84**(1): p. 29-44.
5. Houben, R.M.G.J. and P.J. Dodd, *The Global Burden of Latent Tuberculosis Infection: A Re-estimation Using Mathematical Modelling.* PLOS Medicine, 2016. **13**(10): p. e1002152.
6. Koul, A., et al., *The challenge of new drug discovery for tuberculosis.* Nature, 2011. **469**: p. 483.
7. Kumar, A., et al., *Redox homeostasis in mycobacteria: the key to tuberculosis control?* Expert Reviews in Molecular Medicine, 2011. **13**: p. e39.
8. Al-Orainey, I.O., *Diagnosis of latent tuberculosis: Can we do better?* Annals of Thoracic Medicine, 2009. **4**(1): p. 5-9.
9. Getahun, H., et al., *Latent Mycobacterium tuberculosis Infection*. Vol. 372. 2015. 2127-35.
10. Sacchettini, J.C., E.J. Rubin, and J.S. Freundlich, *Drugs versus bugs: in pursuit of the persistent predator Mycobacterium tuberculosis.* Nat Rev Micro, 2008. **6**(1): p. 41-52.
11. World Health Organization. *Global tuberculosis report 2015*. 2015; Available from: http://apps.who.int/iris/handle/10665/191102.
12. Bucher, H.C., et al., *Isoniazid prophylaxis for tuberculosis in HIV infection: a meta-analysis of randomized controlled trials.* Aids, 1999. **13**(4): p. 501-507.
13. Daley, C.L., et al., *An Outbreak of Tuberculosis with Accelerated Progression among Persons Infected with the Human Immunodeficiency Virus.* New England Journal of Medicine, 1992. **326**(4): p. 231-235.
14. Corbett, E.L., et al., *The growing burden of tuberculosis: Global trends and interactions with the hiv epidemic.* Archives of Internal Medicine, 2003. **163**(9): p. 1009-1021.
15. Mugusi, F., et al., *HIV co-infection, CD4 cell counts and clinical correlates of bacillary density in pulmonary tuberculosis.* The International Journal of Tuberculosis and Lung Disease, 2006. **10**(6): p. 663-669.
16. Padmapriyadarsini, C., G. Narendran, and S. Swaminathan, *Diagnosis & treatment of tuberculosis in HIV co-infected patients.* The Indian journal of medical research, 2011. **134**(6): p. 850.
17. Aaron, L., et al., *Tuberculosis in HIV-infected patients: a comprehensive review.* Clinical Microbiology and Infection, 2004. **10**(5): p. 388-398.
18. Varghese, G.M., et al., *The Twin Epidemics of Tuberculosis and HIV.* Current Infectious Disease Reports, 2013. **15**(1): p. 77-84.

19. Marais, B.J., *The global tuberculosis situation and the inexorable rise of drug-resistant disease.* Advanced Drug Delivery Reviews, 2016. **102**: p. 3-9.
20. Connolly, L.E., P.H. Edelstein, and L. Ramakrishnan, *Why Is Long-Term Therapy Required to Cure Tuberculosis?* PLoS Medicine, 2007. **4**(3): p. e120.
21. Islam, T., et al., *Drug-resistant tuberculosis in the WHO Western Pacific Region.* Western Pacific surveillance and response journal: WPSAR, 2014. **5**(4): p. 34.
22. Blumberg, H.M. and J.D. Ernst, *The Challenge of Latent TB Infection.* JAMA, 2016. **316**(9): p. 931-933.
23. Joshi, J.M., *Tuberculosis chemotherapy in the 21(st) century: Back to the basics.* Lung India : Official Organ of Indian Chest Society, 2011. **28**(3): p. 193-200.
24. Bhat, Z.S., et al., *Drug targets exploited in Mycobacterium tuberculosis: Pitfalls and promises on the horizon.* Biomedicine & Pharmacotherapy, 2018. **103**: p. 1733-1747.
25. Almeida Da Silva, P.E. and J.C. Palomino, *Molecular basis and mechanisms of drug resistance in Mycobacterium tuberculosis: classical and new drugs.* Journal of Antimicrobial Chemotherapy, 2011. **66**(7): p. 1417-1430.
26. Dheda, K., et al., *The epidemiology, pathogenesis, transmission, diagnosis, and management of multidrug-resistant, extensively drug-resistant, and incurable tuberculosis.* The lancet Respiratory medicine, 2017. **5**(4): p. 291-360.
27. World Health Organization. *End TB Strategy*. 2015; Available from: http://www.who.int/tb/End_TB_brochure.pdf?ua=1.
28. Uplekar, M., et al., *WHO's new end TB strategy.* The Lancet, 2015. **385**(9979): p. 1799-1801.
29. Mitchison, D.A., *Role of individual drugs in the chemotherapy of tuberculosis.* The International Journal of Tuberculosis and Lung Disease, 2000. **4**(9): p. 796-806.
30. Botha, F., et al., *Early bactericidal activity of ethambutol, pyrazinamide and the fixed combination of isoniazid, rifampicin and pyrazinamide (Rifater) in patients with pulmonary tuberculosis.* South African Medical Journal, 1996. **86**(2).
31. Diacon, A.H., et al., *The Diarylquinoline TMC207 for Multidrug-Resistant Tuberculosis.* New England Journal of Medicine, 2009. **360**(23): p. 2397-2405.
32. Gler, M.T., et al., *Delamanid for Multidrug-Resistant Pulmonary Tuberculosis.* New England Journal of Medicine, 2012. **366**(23): p. 2151-2160.
33. Hoffmann, H., et al., *Delamanid and bedaquiline resistance in Mycobacterium tuberculosis ancestral Beijing genotype causing extensively drug-resistant tuberculosis in a Tibetan refugee.* American journal of respiratory and critical care medicine, 2016. **193**(3): p. 337-340.
34. Nguyen, T.V.A., et al., *Bedaquiline Resistance: Its Emergence, Mechanism, and Prevention.* Clinical Infectious Diseases, 2018. **66**(10): p. 1625-1630.
35. Sharma, S. and A. Mohan, *Extrapulmonary tuberculosis.* Indian Journal of Medical Research, 2004. **120**: p. 316-353.
36. Sepkowitz, K.A., *How contagious is tuberculosis?* Clinical Infectious Diseases, 1996. **23**(5): p. 954-962.

37. Simmons, J.D., et al., *Immunological mechanisms of human resistance to persistent Mycobacterium tuberculosis infection.* Nature Reviews Immunology, 2018.
38. Zahrt, Thomas C., *Molecular mechanisms regulating persistent Mycobacterium tuberculosis infection.* Microbes and Infection, 2003. **5**(2): p. 159-167.
39. Sakamoto, K., *The Pathology of Mycobacterium tuberculosis Infection.* Veterinary Pathology, 2012. **49**(3): p. 423-439.
40. van Crevel, R., T.H.M. Ottenhoff, and J.W.M. van der Meer, *Innate Immunity to Mycobacterium tuberculosis.* Clinical Microbiology Reviews, 2002. **15**(2): p. 294-309.
41. Dannenberg, A.M., Jr., *Delayed-type hypersensitivity and cell-mediated immunity in the pathogenesis of tuberculosis.* Immunology Today, 1991. **12**(7): p. 228-233.
42. Chai, Q., Y. Zhang, and C.H. Liu, *Mycobacterium tuberculosis: An Adaptable Pathogen Associated With Multiple Human Diseases.* Frontiers in Cellular and Infection Microbiology, 2018. **8**: p. 158.
43. Lenaerts, A., C.E. Barry III, and V. Dartois, *Heterogeneity in tuberculosis pathology, microenvironments and therapeutic responses.* Immunological reviews, 2015. **264**(1): p. 288-307.
44. Dormans, J., et al., *Correlation of virulence, lung pathology, bacterial load and delayed type hypersensitivity responses after infection with different Mycobacterium tuberculosis genotypes in a BALB/c mouse model.* Clinical & Experimental Immunology, 2004. **137**(3): p. 460-468.
45. Silva Miranda, M., et al., *The Tuberculous Granuloma: An Unsuccessful Host Defence Mechanism Providing a Safety Shelter for the Bacteria?* Clinical and Developmental Immunology, 2012. **2012**: p. 14.
46. Flynn, J.L., *Immunology of tuberculosis and implications in vaccine development.* Tuberculosis, 2004. **84**(1): p. 93-101.
47. Ramakrishnan, L., *Revisiting the role of the granuloma in tuberculosis.* Nature Reviews Immunology, 2012. **12**: p. 352.
48. Russell, D.G., et al., *Foamy macrophages and the progression of the human TB granuloma.* Nature immunology, 2009. **10**(9): p. 943-948.
49. Ehlers, S. and U.E. Schaible, *The Granuloma in Tuberculosis: Dynamics of a Host–Pathogen Collusion.* Frontiers in Immunology, 2012. **3**: p. 411.
50. Nunes-Alves, C., et al., *In search of a new paradigm for protective immunity to TB.* Nat Rev Micro, 2014. **12**(4): p. 289-299.
51. Kim, M.J., et al., *Caseation of human tuberculosis granulomas correlates with elevated host lipid metabolism.* EMBO Molecular Medicine, 2010. **2**(7): p. 258.
52. Dheda, K., et al., *Lung Remodeling in Pulmonary Tuberculosis.* The Journal of Infectious Diseases, 2005. **192**(7): p. 1201-1210.
53. Knechel, N.A., *Tuberculosis: pathophysiology, clinical features, and diagnosis.* Critical care nurse, 2009. **29**(2): p. 34-43.
54. Smith, I., *Mycobacterium tuberculosis pathogenesis and molecular determinants of virulence.* Clinical microbiology reviews, 2003. **16**(3): p. 463-496.

55. Parekh, M.J. and N.W. Schluger, *Treatment of latent tuberculosis infection.* Therapeutic advances in respiratory disease, 2013. **7**(6): p. 351-356.
56. Dutta, N.K. and P.C. Karakousis, *Latent tuberculosis infection: myths, models, and molecular mechanisms.* Microbiology and Molecular Biology Reviews, 2014. **78**(3): p. 343-371.
57. Qian, X., et al., *Risk factors for extrapulmonary dissemination of tuberculosis and associated mortality during treatment for extrapulmonary tuberculosis.* Emerging Microbes & Infections, 2018. **7**(1): p. 102.
58. Health, M.o. *Tuberculosis*. 2017; Available from: https://www.moh.gov.sg/content/moh_web/home/diseases_and_conditions/t/tuberculosis.html.
59. Singel, K.L. and B.H. Segal, *NOX2-dependent regulation of inflammation.* Clinical science (London, England : 1979), 2016. **130**(7): p. 479-490.
60. Hurst, J.K., *What really happens in the neutrophil phagosome?* Free Radical Biology and Medicine, 2012. **53**(3): p. 508-520.
61. Goldblatt, D., *Recent advances in chronic granulomatous disease.* Journal of Infection, 2014. **69**: p. S32-S35.
62. Segal, B.H., et al., *Chronic granulomatous disease: lessons from a rare disorder.* Biology of Blood and Marrow Transplantation, 2011. **17**(1): p. S123-S131.
63. Bustamante, J., et al., *Germline CYBB mutations that selectively affect macrophages in kindreds with X-linked predisposition to tuberculous mycobacterial disease.* Nature Immunology, 2011. **12**(3): p. 213-221.
64. Shastri, M.D., et al., *Role of Oxidative Stress in the Pathology and Management of Human Tuberculosis.* Oxidative medicine and cellular longevity, 2018. **2018**: p. 7695364-7695364.
65. Nyström, T., *Role of oxidative carbonylation in protein quality control and senescence.* The EMBO Journal, 2005. **24**(7): p. 1311-1317.
66. Traoré, D.A.K., et al., *Structural and functional characterization of 2-oxo-histidine in oxidized PerR protein.* Nature Chemical Biology, 2009. **5**(1): p. 53-59.
67. Ezraty, B., et al., *Oxidative stress, protein damage and repair in bacteria.* Nature Reviews Microbiology, 2017. **15**(7): p. 385-396.
68. Van Acker, H. and T. Coenye, *The role of reactive oxygen species in antibiotic-mediated killing of bacteria.* Trends in microbiology, 2017. **25**(6): p. 456-466.
69. Belenky, P., et al., *Bactericidal Antibiotics Induce Toxic Metabolic Perturbations that Lead to Cellular Damage.* Cell Reports, 2015. **13**(5): p. 968-980.
70. Imlay, J.A., *Pathways of oxidative damage.* Annual Reviews in Microbiology, 2003. **57**(1): p. 395-418.
71. Messner, K.R. and J.A. Imlay, *Mechanism of superoxide and hydrogen peroxide formation by fumarate reductase, succinate dehydrogenase, and aspartate oxidase.* Journal of Biological Chemistry, 2002. **277**(45): p. 42563-42571.

72. Gong, H., et al., *An electron transfer path connects subunits of a mycobacterial respiratory supercomplex.* Science, 2018. **362**(6418): p. eaat8923.
73. Wiseman, B., et al., *Structure of a functional obligate complex III2IV2 respiratory supercomplex from Mycobacterium smegmatis.* Nature Structural & Molecular Biology, 2018. **25**(12): p. 1128-1136.
74. Laborde, J., et al., *Synthesis, oxidation potential and anti–mycobacterial activity of isoniazid and analogues: insights into the molecular isoniazid activation mechanism.* ChemistrySelect, 2016. **1**(2): p. 172-179.
75. Jenkins, H.E., M. Zignol, and T. Cohen, *Quantifying the Burden and Trends of Isoniazid Resistant Tuberculosis, 1994–2009.* PLOS ONE, 2011. **6**(7): p. e22927.
76. Bardou, F., et al., *Mechanism of isoniazid uptake in Mycobacterium tuberculosis.* Microbiology, 1998. **144**(9): p. 2539-2544.
77. Zhang, Y., T. Garbe, and D. Young, *Transformation with katG restores isoniazid-sensitivity in Mycobacterium tuberculosis isolates resistant to a range of drug concentrations.* Molecular microbiology, 1993. **8**(3): p. 521-524.
78. Timmins, G.S. and V. Deretic, *Mechanisms of action of isoniazid.* Molecular microbiology, 2006. **62**(5): p. 1220-1227.
79. Ghiladi, R.A., et al., *Correlation between Isoniazid Resistance and Superoxide Reactivity in Mycobacterium tuberculosis KatG.* Journal of the American Chemical Society, 2005. **127**(38): p. 13428-13442.
80. Zhao, X., et al., *Hydrogen Peroxide-Mediated Isoniazid Activation Catalyzed by Mycobacterium tuberculosis Catalase−Peroxidase (KatG) and Its S315T Mutant.* Biochemistry, 2006. **45**(13): p. 4131-4140.
81. Rickman, K.A., et al., *Isoniazid: Radical-induced oxidation and reduction chemistry.* Bioorganic & Medicinal Chemistry Letters, 2013. **23**(10): p. 3096-3100.
82. Timmins, G.S., et al., *Nitric oxide generated from isoniazid activation by KatG: source of nitric oxide and activity against Mycobacterium tuberculosis.* Antimicrobial agents and chemotherapy, 2004. **48**(8): p. 3006-3009.
83. Zhang, Y., *THE MAGIC BULLETS AND TUBERCULOSIS DRUG TARGETS.* Annual Review of Pharmacology and Toxicology, 2005. **45**(1): p. 529-564.
84. Rawat, R., A. Whitty, and P.J. Tonge, *The isoniazid-NAD adduct is a slow, tight-binding inhibitor of InhA, the Mycobacterium tuberculosis enoyl reductase: Adduct affinity and drug resistance.* Proceedings of the National Academy of Sciences of the United States of America, 2003. **100**(24): p. 13881-13886.
85. Silva, M.S.N., et al., *Mutations in katG, inhA, and ahpC Genes of Brazilian Isoniazid-Resistant Isolates of Mycobacterium tuberculosis.* Journal of Clinical Microbiology, 2003. **41**(9): p. 4471-4474.
86. Jena, L., et al., *Computational approach to understanding the mechanism of action of isoniazid, an anti-TB drug.* International Journal of Mycobacteriology, 2014. **3**(4): p. 276-282.

87. Zhang, Y., et al., *The catalase-peroxidase gene and isoniazid resistance of Mycobacterium tuberculosis.* Nature, 1992. **358**(6387): p. 591.
88. Winder, F. and P. Collins, *Inhibition by isoniazid of synthesis of mycolic acids in Mycobacterium tuberculosis.* Microbiology, 1970. **63**(1): p. 41-48.
89. Heym, B., et al., *Implications of multidrug resistance for the future of short-course chemotherapy of tuberculosis: a molecular study.* The Lancet, 1994. **344**(8918): p. 293-298.
90. Shekar, S., et al., *Detecting Novel Genetic Variants Associated with Isoniazid-Resistant Mycobacterium tuberculosis.* PLOS ONE, 2014. **9**(7): p. e102383.
91. Bollela, V.R., et al., *Detection of katG and inhA mutations to guide isoniazid and ethionamide use for drug-resistant tuberculosis.* The international journal of tuberculosis and lung disease : the official journal of the International Union against Tuberculosis and Lung Disease, 2016. **20**(8): p. 1099-1104.
92. Saint-Joanis, B., et al., *Use of site-directed mutagenesis to probe the structure, function and isoniazid activation of the catalase/peroxidase, KatG, from Mycobacterium tuberculosis.* Biochemical Journal, 1999. **338**(3): p. 753-760.
93. Heym, B., et al., *Missense mutations in the catalase-peroxidase gene, katG, are associated with isoniazid resistance in Mycobacterium tuberculosis.* Molecular microbiology, 1995. **15**(2): p. 235-245.
94. Diaz, G.A. and L.G. Wayne, *Isolation and characterization of catalase produced by Mycobacterium tuberculosis.* American Review of Respiratory Disease, 1974. **110**(3): p. 312-319.
95. Pym, A.S., et al., *Regulation of catalase–peroxidase (KatG) expression, isoniazid sensitivity and virulence by furA of Mycobacterium tuberculosis.* Molecular Microbiology, 2001. **40**(4): p. 879-889.
96. Master, S.S., et al., *Oxidative stress response genes in Mycobacterium tuberculosis: role of ahpC in resistance to peroxynitrite and stage-specific survival in macrophages.* Microbiology, 2002. **148**(10): p. 3139-3144.
97. Akaki, T., et al., *Comparative roles of free fatty acids with reactive nitrogen intermediates and reactive oxygen intermediates in expression of the anti-microbial activity of macrophages against Mycobacterium tuberculosis.* Clinical and Experimental Immunology, 2000. **121**(2): p. 302-310.
98. Gengenbacher, M. and S.H.E. Kaufmann, *Mycobacterium tuberculosis: success through dormancy.* FEMS Microbiology Reviews, 2012. **36**(3): p. 514-532.
99. Sala, C., et al., *The katG mRNA of Mycobacterium tuberculosis and Mycobacterium smegmatis is processed at its 5' end and is stabilized by both a polypurine sequence and translation initiation.* BMC Molecular Biology, 2008. **9**: p. 33-33.
100. Wilson, T.M., G.W. de Lisle, and D.M. Collins, *Effect of inhA and katG on isoniazid resistance and virulence of Mycobacterium bovis.* Molecular microbiology, 1995. **15**(6): p. 1009-1015.

101. Pym, A.S., B. Saint-Joanis, and S.T. Cole, *Effect of katG mutations on the virulence of Mycobacterium tuberculosis and the implication for transmission in humans.* Infection and immunity, 2002. **70**(9): p. 4955-4960.
102. Sherman, D.R., et al., *Compensatory AhpC Gene Expression in Isoniazid-Resistant Mycobacterium tuberculosis.* Science, 1996. **272**(5268): p. 1641-1643.
103. Wilson, T.M. and D.M. Collins, *ahpC, a gene involved in isoniazid resistance of the Mycobacterium tuberculosis complex.* Molecular microbiology, 1996. **19**(5): p. 1025-1034.
104. Springer, B., et al., *Silencing of Oxidative Stress Response in Mycobacterium tuberculosis: Expression Patterns of ahpC in Virulent and Avirulent Strains and Effect of ahpC Inactivation.* Infection and immunity, 2001. **69**(10): p. 5967-5973.
105. Hugo, M., R. Radi, and M. Trujillo, *Thiol-Dependent Peroxidases in Mycobacterium tuberculosis Antioxidant Defense*, in *Understanding Tuberculosis-Deciphering the Secret Life of the Bacilli*. 2012, InTech.
106. Sherman, D.R., et al., *Regulation of the Mycobacterium tuberculosis hypoxic response gene encoding α-crystallin.* Proceedings of the National Academy of Sciences, 2001. **98**(13): p. 7534-7539.
107. Guimarães, B.G., et al., *Structure and Mechanism of the Alkyl Hydroperoxidase AhpC, a Key Element of the Mycobacterium tuberculosis Defense System against Oxidative Stress.* Journal of Biological Chemistry, 2005. **280**(27): p. 25735-25742.
108. Chae, H. and S. Rhee, *A thiol-specific antioxidant and sequence homology to various proteins of unknown function.* BioFactors (Oxford, England), 1994. **4**(3-4): p. 177-180.
109. Wood, Z.A., et al., *Structure, mechanism and regulation of peroxiredoxins.* Trends in Biochemical Sciences, 2003. **28**(1): p. 32-40.
110. Chae, H.Z., T.B. Uhm, and S.G. Rhee, *Dimerization of thiol-specific antioxidant and the essential role of cysteine 47.* Proceedings of the National Academy of Sciences, 1994. **91**(15): p. 7022-7026.
111. Rhee, S.G., H.Z. Chae, and K. Kim, *Peroxiredoxins: A historical overview and speculative preview of novel mechanisms and emerging concepts in cell signaling.* Free Radical Biology and Medicine, 2005. **38**(12): p. 1543-1552.
112. Perkins, A., et al., *The Sensitive Balance Between the Fully Folded and Locally Unfolded Conformations of a Model Peroxiredoxin.* Biochemistry, 2013. **52**(48): p. 8708-8721.
113. Wood, Z.A., et al., *Dimers to Doughnuts: Redox-Sensitive Oligomerization of 2-Cysteine Peroxiredoxins.* Biochemistry, 2002. **41**(17): p. 5493-5504.
114. Barranco-Medina, S., J.-J. Lázaro, and K.-J. Dietz, *The oligomeric conformation of peroxiredoxins links redox state to function.* FEBS Letters, 2009. **583**(12): p. 1809-1816.
115. Parsonage, D., et al., *Analysis of the Link between Enzymatic Activity and Oligomeric State in AhpC, a Bacterial Peroxiredoxin.* Biochemistry, 2005. **44**(31): p. 10583-10592.
116. Nartey, W., et al., *NMR studies reveal a novel grab and release mechanism for efficient catalysis of the bacterial 2-Cys peroxiredoxin machinery.* FEBS Journal, 2015. **282**(23): p. 4620-4638.

117. Poole, L.B., *Bacterial defenses against oxidants: mechanistic features of cysteine-based peroxidases and their flavoprotein reductases.* Archives of Biochemistry and Biophysics, 2005. **433**(1): p. 240-254.
118. Kamariah, N., et al., *Transition steps in peroxide reduction and a molecular switch for peroxide robustness of prokaryotic peroxiredoxins.* Sci Rep, 2016. **6**: p. 37610.
119. Dip, P.V., et al., *Structure, mechanism and ensemble formation of the alkylhydroperoxide reductase subunits AhpC and AhpF from Escherichia coli.* Acta Crystallographica Section D: Biological Crystallography, 2014. **70**(11): p. 2848-2862.
120. Nelson, K.J., et al., *Analysis of the peroxiredoxin family: using active site structure and sequence information for global classification and residue analysis.* Proteins, 2011. **79**(3): p. 947-964.
121. Noichri, Y., et al., *In vivo parameters influencing 2-Cys Prx oligomerization: The role of enzyme sulfinylation*. Vol. 6. 2015. 326-333.
122. Poole, L.B., A. Hall, and K.J. Nelson, *Overview of Peroxiredoxins in oxidant defense and redox regulation.* Current protocols in toxicology / editorial board, Mahin D. Maines (editor-in-chief) ... [et al.], 2011. **CHAPTER**: p. Unit7.9-Unit7.9.
123. Kang, S.W., et al., *2-Cys peroxiredoxin function in intracellular signal transduction: therapeutic implications.* Trends in Molecular Medicine, 2005. **11**(12): p. 571-578.
124. Flohé, L. and J.R. Harris, *Peroxiredoxin systems: structures and functions*. Vol. 44. 2007: Springer Science & Business Media.
125. Nelson, K.J., et al., *Cysteine pKa Values for the Bacterial Peroxiredoxin AhpC.* Biochemistry, 2008. **47**(48): p. 12860-12868.
126. Hillas, P.J., et al., *The AhpC and AhpD Antioxidant Defense System of Mycobacterium tuberculosis.* Journal of Biological Chemistry, 2000. **275**(25): p. 18801-18809.
127. Chauhan, R. and S.C. Mande, *Site-directed mutagenesis reveals a novel catalytic mechanism of Mycobacterium tuberculosis alkylhydroperoxidase C.* Biochemical Journal, 2002. **367**(1): p. 255-261.
128. Wong, C.F., et al., *AhpC of the mycobacterial antioxidant defense system and its interaction with its reducing partner Thioredoxin-C.* Scientific Reports, 2017. **7**: p. 5159.
129. Jaeger, T., et al., *Multiple thioredoxin-mediated routes to detoxify hydroperoxides in Mycobacterium tuberculosis.* Archives of Biochemistry and Biophysics, 2004. **423**(1): p. 182-191.
130. Bryk, R., et al., *Metabolic enzymes of mycobacteria linked to antioxidant defense by a thioredoxin-like protein.* Science, 2002. **295**(5557): p. 1073-1077.
131. Zhang, Z., P.J. Hillas, and P.R.O. de Montellano, *Reduction of Peroxides and Dinitrobenzenes byMycobacterium tuberculosisThioredoxin and Thioredoxin Reductase.* Archives of biochemistry and biophysics, 1999. **363**(1): p. 19-26.
132. Lu, J. and A. Holmgren, *The thioredoxin antioxidant system.* Free Radical Biology and Medicine, 2014. **66**: p. 75-87.
133. Bragg, P., *The respiratory system of Escherichia coli.* Diversity of bacterial respiratory systems, 1980. **1**: p. 115-136.

134. Sassetti, C.M., D.H. Boyd, and E.J. Rubin, *Genes required for mycobacterial growth defined by high density mutagenesis.* Molecular Microbiology, 2003. **48**(1): p. 77-84.
135. Tran, S.L. and G.M. Cook, *The F1Fo ATP Synthase of Mycobacterium smegmatis Is Essential for Growth.* Journal of Bacteriology, 2005. **187**(14): p. 5023-5028.
136. Black, P.A., et al., *Energy metabolism and drug efflux in Mycobacterium tuberculosis.* Antimicrobial agents and chemotherapy, 2014: p. AAC. 02293-13.
137. Rao, S.P.S., et al., *The protonmotive force is required for maintaining ATP homeostasis and viability of hypoxic, nonreplicating Mycobacterium tuberculosis.* Proceedings of the National Academy of Sciences, 2008. **105**(33): p. 11945-11950.
138. Muttucumaru, D.G.N., et al., *Gene expression profile of Mycobacterium tuberculosis in a non-replicating state.* Tuberculosis, 2004. **84**(3): p. 239-246.
139. Wayne, L.G. and L.G. Hayes, *An in vitro model for sequential study of shiftdown of Mycobacterium tuberculosis through two stages of nonreplicating persistence.* Infection and Immunity, 1996. **64**(6): p. 2062-2069.
140. Prosser, G., et al., *The bacillary and macrophage response to hypoxia in tuberculosis and the consequences for T cell antigen recognition.* Microbes and infection, 2017. **19**(3): p. 177-192.
141. Cook, G.M., et al., *Oxidative Phosphorylation as a Target Space for Tuberculosis: Success, Caution, and Future Directions.* Microbiology spectrum, 2017. **5**(3): p. 10.1128/microbiolspec.TBTB2-0014-2016.
142. Watt, I.N., et al., *Bioenergetic cost of making an adenosine triphosphate molecule in animal mitochondria.* Proceedings of the National Academy of Sciences, 2010. **107**(39): p. 16823-16827.
143. Sazanov, L.A., *A giant molecular proton pump: structure and mechanism of respiratory complex I.* Nature Reviews Molecular Cell Biology, 2015. **16**: p. 375.
144. Bald, D., et al., *Targeting Energy Metabolism in Mycobacterium tuberculosis, a New Paradigm in Antimycobacterial Drug Discovery.* mBio, 2017. **8**(2): p. e00272-17.
145. Shi, L., et al., *Changes in energy metabolism of Mycobacterium tuberculosis in mouse lung and under in vitro conditions affecting aerobic respiration.* Proceedings of the National Academy of Sciences, 2005. **102**(43): p. 15629-15634.
146. Velmurugan, K., et al., *Mycobacterium tuberculosis nuoG is a virulence gene that inhibits apoptosis of infected host cells.* PLoS pathogens, 2007. **3**(7): p. e110-e110.
147. Weinstein, E.A., et al., *Inhibitors of type II NADH: menaquinone oxidoreductase represent a class of antitubercular drugs.* Proceedings of the National Academy of Sciences, 2005. **102**(12): p. 4548-4553.
148. Vilchèze, C., et al., *Plasticity of Mycobacterium tuberculosis NADH dehydrogenases and their role in virulence.* Proceedings of the National Academy of Sciences of the United States of America, 2018. **115**(7): p. 1599-1604.
149. Miesel, L., et al., *NADH Dehydrogenase Defects Confer Isoniazid Resistance and Conditional Lethality in Mycobacterium smegmatis.* Journal of Bacteriology, 1998. **180**(9): p. 2459-2467.

150. Bald, D. and A. Koul, *Respiratory ATP synthesis: the new generation of mycobacterial drug targets?* FEMS Microbiology Letters, 2010. **308**(1): p. 1-7.
151. Malhotra, S., S.C. Vedithi, and T.L. Blundell, *Decoding the similarities and differences among mycobacterial species.* PLOS Neglected Tropical Diseases, 2017. **11**(8): p. e0005883.
152. Beites, T., et al., *Plasticity of the Mycobacterium tuberculosis respiratory chain and its impact on tuberculosis drug development.* Nature Communications, 2019. **10**(1): p. 4970.
153. Foo, C.S.-Y., K. Pethe, and A. Lupien, *Oxidative Phosphorylation—an Update on a New, Essential Target Space for Drug Discovery in Mycobacterium tuberculosis.* Applied Sciences, 2020. **10**(7): p. 2339.
154. Bettencourt, M.V., S. Bosne-David, and L. Amaral, *Comparative in vitro activity of phenothiazines against multidrug-resistant Mycobacterium tuberculosis.* International Journal of Antimicrobial Agents, 2000. **16**(1): p. 69-71.
155. He, C.-X., et al., *Synthesis and bio-evaluation of phenothiazine derivatives as new anti-tuberculosis agents.* Chinese Chemical Letters, 2015. **26**(8): p. 951-954.
156. Salie, S., et al., *Novel non-neuroleptic phenothiazines inhibit Mycobacterium tuberculosis replication.* Journal of Antimicrobial Chemotherapy, 2014. **69**(6): p. 1551-1558.
157. Shirude, P.S., et al., *Quinolinyl Pyrimidines: Potent Inhibitors of NDH-2 as a Novel Class of Anti-TB Agents.* ACS Medicinal Chemistry Letters, 2012. **3**(9): p. 736-740.
158. Murugesan, D., et al., *2-Mercapto-Quinazolinones as Inhibitors of Type II NADH Dehydrogenase and Mycobacterium tuberculosis: Structure–Activity Relationships, Mechanism of Action and Absorption, Distribution, Metabolism, and Excretion Characterization.* ACS Infectious Diseases, 2018. **4**(6): p. 954-969.
159. Maklashina, E., G. Cecchini, and S.A. Dikanov, *Defining a direction: electron transfer and catalysis in Escherichia coli complex II enzymes.* Biochimica et biophysica acta, 2013. **1827**(5): p. 668-678.
160. Griffin, J.E., et al., *High-resolution phenotypic profiling defines genes essential for mycobacterial growth and cholesterol catabolism.* PLoS pathogens, 2011. **7**(9).
161. Hartman, T., et al., *Succinate Dehydrogenase is the Regulator of Respiration in Mycobacterium tuberculosis.* PLOS Pathogens, 2014. **10**(11): p. e1004510.
162. Pecsi, I., et al., *Essentiality of Succinate Dehydrogenase in Mycobacterium smegmatis and Its Role in the Generation of the Membrane Potential Under Hypoxia.* mBio, 2014. **5**(4): p. e01093-14.
163. Kröger, A., et al., *Fumarate respiration of Wolinella succinogenes: enzymology, energetics and coupling mechanism.* Biochimica et Biophysica Acta (BBA) - Bioenergetics, 2002. **1553**(1): p. 23-38.
164. Jones, H. and R. Gunsalus, *Regulation of Escherichia coli fumarate reductase (frdABCD) operon expression by respiratory electron acceptors and the fnr gene product.* Journal of bacteriology, 1987. **169**(7): p. 3340-3349.
165. Rustad, T.R., et al., *The enduring hypoxic response of Mycobacterium tuberculosis.* PloS one, 2008. **3**(1): p. e1502-e1502.

166. Boshoff, H.I., et al., *The transcriptional responses of Mycobacterium tuberculosis to inhibitors of metabolism novel insights into drug mechanisms of action.* Journal of Biological Chemistry, 2004. **279**(38): p. 40174-40184.
167. Watanabe, S., et al., *Fumarate Reductase Activity Maintains an Energized Membrane in Anaerobic Mycobacterium tuberculosis.* PLOS Pathogens, 2011. **7**(10): p. e1002287.
168. Rutter, J., D.R. Winge, and J.D. Schiffman, *Succinate dehydrogenase – Assembly, regulation and role in human disease.* Mitochondrion, 2010. **10**(4): p. 393-401.
169. Hards, K., et al., *Two for the price of one: Attacking the energetic-metabolic hub of mycobacteria to produce new chemotherapeutic agents.* Prog Biophys Mol Biol, 2020. **152**: p. 35-44.
170. Alston, T.A., L. Mela, and H.J. Bright, *3-Nitropropionate, the toxic substance of Indigofera, is a suicide inactivator of succinate dehydrogenase.* Proceedings of the National Academy of Sciences, 1977. **74**(9): p. 3767-3771.
171. Eoh, H. and K.Y. Rhee, *Multifunctional essentiality of succinate metabolism in adaptation to hypoxia in Mycobacterium tuberculosis.* Proceedings of the National Academy of Sciences, 2013. **110**(16): p. 6554-6559.
172. Borisov, V.B., et al., *The cytochrome bd respiratory oxygen reductases.* Biochimica et biophysica acta, 2011. **1807**(11): p. 1398-1413.
173. Jasaitis, A., et al., *Electrogenic Reactions of Cytochrome bd.* Biochemistry, 2000. **39**(45): p. 13800-13809.
174. Matsoso, L.G., et al., *Function of the cytochrome bc1-aa3 branch of the respiratory network in mycobacteria and network adaptation occurring in response to its disruption.* Journal of bacteriology, 2005. **187**(18): p. 6300-6308.
175. Lee, H.J., et al., *Functional proton transfer pathways in the heme–copper oxidase superfamily.* Biochimica et Biophysica Acta (BBA) - Bioenergetics, 2012. **1817**(4): p. 537-544.
176. Mascolo, L. and D. Bald, *Cytochrome bd in Mycobacterium tuberculosis: A respiratory chain protein involved in the defense against antibacterials.* Progress in Biophysics and Molecular Biology, 2020. **152**: p. 55-63.
177. Safarian, S., et al., *Structure of a bd oxidase indicates similar mechanisms for membrane-integrated oxygen reductases.* Science, 2016. **352**(6285): p. 583-586.
178. Safarian, S., et al., *Active site rearrangement and structural divergence in prokaryotic respiratory oxidases.* Science, 2019. **366**(6461): p. 100-104.
179. Sviriaeva, E., et al., *Features and Functional Importance of Key Residues of the Mycobacterium tuberculosis Cytochrome bd Oxidase.* ACS Infectious Diseases, 2020.
180. Shepherd, M., *The CydDC ABC transporter of Escherichia coli: new roles for a reductant efflux pump.* Biochemical Society Transactions, 2015. **43**(5): p. 908-912.
181. Georgiou, C.D., H. Fang, and R.B. Gennis, *Identification of the cydC locus required for expression of the functional form of the cytochrome d terminal oxidase complex in Escherichia coli.* Journal of bacteriology, 1987. **169**(5): p. 2107-2112.

182. Lu, P., et al., *The anti-mycobacterial activity of the cytochrome bcc inhibitor Q203 can be enhanced by small-molecule inhibition of cytochrome bd.* Scientific Reports, 2018. **8**(1): p. 2625.
183. Pethe, K., et al., *Discovery of Q203, a potent clinical candidate for the treatment of tuberculosis.* Nature medicine, 2013. **19**(9): p. 1157.
184. Kalia, N.P., et al., *Exploiting the synthetic lethality between terminal respiratory oxidases to kill Mycobacterium tuberculosis and clear host infection.* Proceedings of the National Academy of Sciences, 2017. **114**(28): p. 7426-7431.
185. Cortes, T., et al., *Delayed effects of transcriptional responses in Mycobacterium tuberculosis exposed to nitric oxide suggest other mechanisms involved in survival.* Scientific Reports, 2017. **7**(1): p. 8208.
186. Kana, B.D., et al., *Characterization of the cydAB-encoded cytochrome bd oxidase from Mycobacterium smegmatis.* Journal of bacteriology, 2001. **183**(24): p. 7076-7086.
187. Boshoff, H.I. and C.E. Barry, *Tuberculosis—metabolism and respiration in the absence of growth.* Nature Reviews Microbiology, 2005. **3**(1): p. 70-80.
188. D'mello, R., S. Hill, and R.K. Poole, *The cytochrome bd quinol oxidase in Escherichia coli has an extremely high oxygen affinity and two oxygen-binding haems: implications for regulation of activity in vivo by oxygen inhibition.* Microbiology, 1996. **142**(4): p. 755-763.
189. Matta, S.K. and D. Kumar, *Hypoxia and classical activation limits Mycobacterium tuberculosis survival by Akt-dependent glycolytic shift in macrophages.* Cell death discovery, 2016. **2**: p. 16022-16022.
190. Giuffrè, A., et al., *Cytochrome bd oxidase and bacterial tolerance to oxidative and nitrosative stress.* Biochimica et Biophysica Acta (BBA) - Bioenergetics, 2014. **1837**(7): p. 1178-1187.
191. Lu, P., H. Lill, and D. Bald, *ATP synthase in mycobacteria: Special features and implications for a function as drug target.* Biochimica et Biophysica Acta (BBA) - Bioenergetics, 2014. **1837**(7): p. 1208-1218.
192. Haagsma, A.C., et al., *ATP synthase in slow- and fast-growing mycobacteria is active in ATP synthesis and blocked in ATP hydrolysis direction.* FEMS Microbiology Letters, 2010. **313**(1): p. 68-74.
193. Ballmoos, C.v., G.M. Cook, and P. Dimroth, *Unique Rotary ATP Synthase and Its Biological Diversity.* Annual Review of Biophysics, 2008. **37**(1): p. 43-64.
194. Walker, John E., *The ATP synthase: the understood, the uncertain and the unknown.* Biochemical Society Transactions, 2013. **41**(1): p. 1-16.
195. Preiss, L., et al., *Structure of the mycobacterial ATP synthase Fo rotor ring in complex with the anti-TB drug bedaquiline.* Science Advances, 2015. **1**(4): p. e1500106.
196. Ballmoos, C.v., A. Wiedenmann, and P. Dimroth, *Essentials for ATP Synthesis by F1F0 ATP Synthases.* Annual Review of Biochemistry, 2009. **78**(1): p. 649-672.
197. Guo, H. and J.L. Rubinstein, *Cryo-EM of ATP synthases.* Current Opinion in Structural Biology, 2018. **52**: p. 71-79.

198. Gajadeera, C.S. and J. Weber, *Escherichia coli F1Fo-ATP synthase with ab/δ fusion protein allows analysis of the function of the individual b subunits.* Journal of Biological Chemistry, 2013. **288**(37): p. 26441-26447.
199. Kamariah, N., et al., *Structure and subunit arrangement of Mycobacterial F1FO ATP synthase and novel features of the unique mycobacterial subunit δ.* Journal of Structural Biology, 2019. **207**(2): p. 199-208.
200. Jiang, W., J. Hermolin, and R.H. Fillingame, *The preferred stoichiometry of c subunits in the rotary motor sector of Escherichia coli ATP synthase is 10.* Proceedings of the National Academy of Sciences, 2001. **98**(9): p. 4966-4971.
201. Okuno, D., R. Iino, and H. Noji, *Rotation and structure of FoF1-ATP synthase.* J Biochem, 2011. **149**(6): p. 655-64.
202. Pänke, O., et al., *F-ATPase: specific observation of the rotating c subunit oligomer of EFoEF1.* FEBS Letters, 2000. **472**(1): p. 34-38.
203. Dittrich, M., S. Hayashi, and K. Schulten, *On the mechanism of ATP hydrolysis in F1-ATPase.* Biophysical journal, 2003. **85**(4): p. 2253-2266.
204. Adachi, K., et al., *Stepping rotation of F1-ATPase visualized through angle-resolved single-fluorophore imaging.* Proceedings of the National Academy of Sciences, 2000. **97**(13): p. 7243-7247.
205. Weber, J. and A.E. Senior, *Catalytic mechanism of F1-ATPase.* Biochimica et Biophysica Acta (BBA) - Bioenergetics, 1997. **1319**(1): p. 19-58.
206. Hotra, A., et al., *Deletion of a unique loop in the mycobacterial F-ATP synthase γ subunit sheds light on its inhibitory role in ATP hydrolysis-driven H+ pumping.* The FEBS Journal, 2016. **283**(10): p. 1947-1961.
207. Ragunathan, P., et al., *Solution structure of subunit γ (γ1-204) of the Mycobacterium tuberculosis F-ATP synthase and the unique loop of γ165-178, representing a novel TB drug target.* Journal of Bioenergetics and Biomembranes, 2013. **45**(1): p. 121-129.
208. Ragunathan, P., et al., *The uniqueness of subunit α of mycobacterial F-ATP synthases: An evolutionary variant for niche adaptation.* Journal of Biological Chemistry, 2017. **292**(27): p. 11262-11279.
209. Kamariah, N., et al., *Unique structural and mechanistic properties of mycobacterial F-ATP synthases: Implications for drug design.* Progress in Biophysics and Molecular Biology, 2020. **152**: p. 64-73.
210. Bogdanović, N., et al., *Structure and function of Mycobacterium-specific components of F-ATP synthase subunits α and ε.* Journal of structural biology, 2018. **204**(3): p. 420-434.
211. Biuković, G., et al., *Variations of subunit ε of the Mycobacterium tuberculosis F1Fo ATP synthase and a novel model for mechanism of action of the tuberculosis drug TMC207.* Antimicrobial agents and chemotherapy, 2013. **57**(1): p. 168-176.
212. Joon, S., et al., *The NMR solution structure of Mycobacterium tuberculosis F-ATP synthase subunit ε provides new insight into energy coupling inside the rotary engine.* The FEBS Journal, 2018. **285**(6): p. 1111-1128.

213. Andries, K., et al., *A Diarylquinoline Drug Active on the ATP Synthase of Mycobacterium tuberculosis.* Science, 2005. **307**(5707): p. 223-227.
214. Koul, A., et al., *Diarylquinolines are bactericidal for dormant mycobacteria as a result of disturbed ATP homeostasis.* Journal of Biological Chemistry, 2008. **283**(37): p. 25273-25280.
215. Andries, K., et al., *Acquired resistance of Mycobacterium tuberculosis to bedaquiline.* PloS one, 2014. **9**(7).
216. Hartkoorn, R.C., S. Uplekar, and S.T. Cole, *Cross-resistance between clofazimine and bedaquiline through upregulation of MmpL5 in Mycobacterium tuberculosis.* Antimicrobial agents and chemotherapy, 2014. **58**(5): p. 2979-2981.
217. Guglielmetti, L., et al., *QT prolongation and cardiac toxicity of new tuberculosis drugs in Europe: A Tuberculosis Network European Trialsgroup (TBnet) study.* European Respiratory Journal, 2018: p. 1800537.
218. Sarathy, J.P., et al., *TBAJ-876 Retains Bedaquiline's Activity against Subunits c and ε of Mycobacterium tuberculosis F-ATP Synthase.* Antimicrobial Agents and Chemotherapy, 2019. **63**(10): p. e01191-19.
219. Sarathy, J.P., G. Gruber, and T. Dick, *Re-Understanding the Mechanisms of Action of the Anti-Mycobacterial Drug Bedaquiline.* Antibiotics (Basel, Switzerland), 2019. **8**(4): p. 261.
220. Sarathy, J.P., et al., *TBAJ-876 displays Bedaquiline-like mycobactericidal potency without retaining the parental drug's uncoupler activity.* Antimicrobial Agents and Chemotherapy, 2019: p. AAC.01540-19.
221. Tantry, S.J., et al., *Discovery of Imidazo[1,2-a]pyridine Ethers and Squaramides as Selective and Potent Inhibitors of Mycobacterial Adenosine Triphosphate (ATP) Synthesis.* Journal of Medicinal Chemistry, 2017. **60**(4): p. 1379-1399.
222. Hotra, A., et al., *Discovery of a novel Mycobacterial F-ATP synthase inhibitor and its potency in combination with diarylquinolines.* Angewandte Chemie International Edition, 2020. **n/a**(n/a).
223. Saw, W.-G., et al., *Disrupting coupling within mycobacterial F-ATP synthases subunit ε causes dysregulated energy production and cell wall biosynthesis.* Scientific Reports, 2019. **9**(1): p. 16759.
224. Megehee, J.A., J.P. Hosler, and M.D. Lundrigan, *Evidence for a cytochrome bcc–aa3 interaction in the respiratory chain of Mycobacterium smegmatis.* Microbiology, 2006. **152**(3): p. 823-829.
225. Kao, W.-C., et al., *The obligate respiratory supercomplex from Actinobacteria.* Biochimica et Biophysica Acta (BBA) - Bioenergetics, 2016. **1857**(10): p. 1705-1714.
226. Niebisch, A. and M. Bott, *Purification of a Cytochromebc 1-aa 3 Supercomplex with Quinol Oxidase Activity from Corynebacterium glutamicum. Identification of a Fourth Subunity of Cytochrome aa3 Oxidase and Mutational Analysis of Diheme Cytochrome c1.* Journal of Biological Chemistry, 2003. **278**(6): p. 4339-4346.

227. Magalon, A., R. Arias-Cartin, and A. Walburger, *Chapter Six - Supramolecular Organization in Prokaryotic Respiratory Systems*, in *Advances in Microbial Physiology*, R.K. Poole, Editor. 2012, Academic Press. p. 217-266.
228. Korshunov, S. and J.A. Imlay, *Two sources of endogenous hydrogen peroxide in Escherichia coli.* Molecular Microbiology, 2010. **75**(6): p. 1389-1401.
229. Turrens, J.F. and A. Boveris, *Generation of superoxide anion by the NADH dehydrogenase of bovine heart mitochondria.* Biochemical Journal, 1980. **191**(2): p. 421-427.
230. Piddington, D.L., et al., *Cu, Zn superoxide dismutase of Mycobacterium tuberculosis contributes to survival in activated macrophages that are generating an oxidative burst.* Infection and immunity, 2001. **69**(8): p. 4980-4987.
231. Osyczka, A., C.C. Moser, and P.L. Dutton, *Fixing the Q cycle.* Trends in Biochemical Sciences, 2005. **30**(4): p. 176-182.
232. Quinlan, C.L., et al., *The mechanism of superoxide production by the antimycin-inhibited mitochondrial Q-cycle.* Journal of Biological Chemistry, 2011. **286**(36): p. 31361-31372.
233. Muller, F., A.R. Crofts, and D.M. Kramer, *Multiple Q-Cycle Bypass Reactions at the Qo Site of the Cytochrome bc1 Complex.* Biochemistry, 2002. **41**(25): p. 7866-7874.
234. Millett, F. and B. Durham, *Chapter 5 Use of ruthenium photooxidation techniques to study electron transfer in the cytochrome bc1 complex.* Methods in enzymology, 2009. **456**: p. 95-109.
235. Bouvier, G., et al., *Target Engagement and Binding Mode of an Antituberculosis Drug to Its Bacterial Target Deciphered in Whole Living Cells by NMR.* Biochemistry, 2019. **58**(6): p. 526-533.
236. de Jager, V.R., et al., *Telacebec (Q203), a New Antituberculosis Agent.* New England Journal of Medicine, 2020. **382**(13): p. 1280-1281.
237. Moosa, A., et al., *Susceptibility of Mycobacterium tuberculosis Cytochrome bd Oxidase Mutants to Compounds Targeting the Terminal Respiratory Oxidase, Cytochrome c.* Antimicrobial Agents and Chemotherapy, 2017. **61**(10): p. e01338-17.
238. Scherr, N., et al., *Targeting the Mycobacterium ulcerans cytochrome bc(1):aa(3) for the treatment of Buruli ulcer.* Nature communications, 2018. **9**(1): p. 5370-5370.
239. Moraski, G.C., et al., *Arrival of Imidazo[2,1-b]thiazole-5-carboxamides: Potent Anti-tuberculosis Agents That Target QcrB.* ACS Infectious Diseases, 2016. **2**(6): p. 393-398.
240. Caminero, J.A., et al., *Best drug treatment for multidrug-resistant and extensively drug-resistant tuberculosis.* The Lancet Infectious Diseases, 2010. **10**(9): p. 621-629.
241. Gualano, G., et al., *New Antituberculosis Drugs: From Clinical Trial to Programmatic Use.* Infectious disease reports, 2016. **8**(2): p. 6569-6569.
242. Xavier, A.S. and M. Lakshmanan, *Delamanid: A new armor in combating drug-resistant tuberculosis.* Journal of pharmacology & pharmacotherapeutics, 2014. **5**(3): p. 222-224.
243. Veziris, N., et al., *Rapid emergence of Mycobacterium tuberculosis bedaquiline resistance: lessons to avoid repeating past errors.* European Respiratory Journal, 2017. **49**(3): p. 1601719.

244. Li, Y., F. Sun, and W. Zhang, *Bedaquiline and delamanid in the treatment of multidrug-resistant tuberculosis: Promising but challenging.* Drug Development Research, 2019. **80**(1): p. 98-105.
245. Ramanathan, M.R., C.K. Howell, and J.M. Sanders, *Chapter 28 - Drugs in tuberculosis and leprosy*, in *Side Effects of Drugs Annual*, S.D. Ray, Editor. 2019, Elsevier. p. 321-338.
246. Pushpakom, S., et al., *Drug repurposing: progress, challenges and recommendations.* Nature Reviews Drug Discovery, 2019. **18**(1): p. 41-58.
247. Nzila, A., Z. Ma, and K. Chibale, *Drug repositioning in the treatment of malaria and TB.* Future Medicinal Chemistry, 2011. **3**(11): p. 1413-1426.
248. Charoensutthivarakul, S., et al., *2-Pyridylquinolone antimalarials with improved antimalarial activity and physicochemical properties.* MedChemComm, 2015. **6**(7): p. 1252-1259.
249. Biagini, G.A., et al., *Combination Product*, U.S.P.A.T. OFFICE, Editor. 2019, Liverpool School Of Tropical Medicine: United States of America.
250. Cleghorn, L.A.T., et al., *Identification of Morpholino Thiophenes as Novel Mycobacterium tuberculosis Inhibitors, Targeting QcrB.* Journal of Medicinal Chemistry, 2018. **61**(15): p. 6592-6608.
251. Hong, W.D., et al., *Rational Design, Synthesis, and Biological Evaluation of Heterocyclic Quinolones Targeting the Respiratory Chain of Mycobacterium tuberculosis.* Journal of Medicinal Chemistry, 2017. **60**(9): p. 3703-3726.
252. Biagini, G.A., et al., *Generation of quinolone antimalarials targeting the Plasmodium falciparum mitochondrial respiratory chain for the treatment and prophylaxis of malaria.* Proceedings of the National Academy of Sciences, 2012. **109**(21): p. 8298-8303.
253. Capper, M.J., et al., *Antimalarial 4(1H)-pyridones bind to the Qi site of cytochrome bc1.* Proceedings of the National Academy of Sciences, 2015. **112**(3): p. 755-760.
254. Amporndanai, K., et al., *X-ray and cryo-EM structures of inhibitor-bound cytochrome bc1 complexes for structure-based drug discovery.* IUCrJ, 2018. **5**(2): p. 200-210.
255. Dip, P.V., et al., *Key roles of the Escherichia coli AhpC C-terminus in assembly and catalysis of alkylhydroperoxide reductase, an enzyme essential for the alleviation of oxidative stress.* Biochimica et Biophysica Acta (BBA)-Bioenergetics, 2014. **1837**(12): p. 1932-1943.
256. Dip, P.V., et al., *Structure, mechanism and ensemble formation of the alkylhydroperoxide reductase subunits AhpC and AhpF from Escherichia coli.* Acta Crystallogr D Biol Crystallogr, 2014. **70**(Pt 11): p. 2848-62.
257. Emsley, P. and K. Cowtan, *Coot: model-building tools for molecular graphics.* Acta Crystallographica Section D: Biological Crystallography, 2004. **60**(12): p. 2126-2132.
258. Otwinowski, Z. and W. Minor, *Processing of X-ray diffraction data collected in oscillation mode*, in *Methods in enzymology*. 1997, Elsevier. p. 307-326.

259. Murshudov, G.N., A.A. Vagin, and E.J. Dodson, *Refinement of macromolecular structures by the maximum-likelihood method.* Acta Crystallographica Section D: Biological Crystallography, 1997. **53**(3): p. 240-255.
260. Laskowski, R.A., et al., *PROCHECK: a program to check the stereochemical quality of protein structures.* Journal of Applied Crystallography, 1993. **26**(2): p. 283-291.
261. Ramachandran, G.N., C. Ramakrishnan, and V. Sasisekharan, *Stereochemistry of polypeptide chain configurations.* Journal of Molecular Biology, 1963. **7**(1): p. 95-99.
262. Pettersen, E.F., et al., *UCSF Chimera—A visualization system for exploratory research and analysis.* Journal of Computational Chemistry, 2004. **25**(13): p. 1605-1612.
263. Adams, P.D., et al., *PHENIX: a comprehensive Python-based system for macromolecular structure solution.* Acta Crystallographica Section D: Biological Crystallography, 2010. **66**(2): p. 213-221.
264. Laskowski, R.A. and M.B. Swindells, *LigPlot+: Multiple Ligand–Protein Interaction Diagrams for Drug Discovery.* Journal of Chemical Information and Modeling, 2011. **51**(10): p. 2778-2786.
265. Jones, G., et al., *Development and validation of a genetic algorithm for flexible docking.* Journal of Molecular Biology, 1997. **267**(3): p. 727-748.
266. McCoy, A.J., et al., *Phaser crystallographic software.* Journal of applied crystallography, 2007. **40**(4): p. 658-674.
267. Morris, G.M., et al., *AutoDock4 and AutoDockTools4: Automated docking with selective receptor flexibility.* Journal of computational chemistry, 2009. **30**(16): p. 2785-2791.
268. Raman, M. and K. Martin, *One solution for cloning and mutagenesis: In-Fusion[reg] HD Cloning Plus.* Nat Meth, 2014. **11**(9).
269. Laemmli, U.K., *Cleavage of structural proteins during the assembly of the head of bacteriophage T4.* nature, 1970. **227**(5259): p. 680-685.
270. DeLano, W.L., *PyMOL*. 2002.
271. Waterhouse, A., et al., *SWISS-MODEL: homology modelling of protein structures and complexes.* Nucleic acids research, 2018. **46**(W1): p. W296-W303.
272. Camacho, C., et al., *BLAST+: architecture and applications.* BMC bioinformatics, 2009. **10**: p. 421-421.
273. Remmert, M., et al., *HHblits: lightning-fast iterative protein sequence searching by HMM-HMM alignment.* Nature Methods, 2012. **9**(2): p. 173-175.
274. Wallace, A.C., R.A. Laskowski, and J.M. Thornton, *LIGPLOT: a program to generate schematic diagrams of protein-ligand interactions.* Protein Engineering, Design and Selection, 1995. **8**(2): p. 127-134.
275. Gopal, P. and T. Dick, *The new tuberculosis drug Perchlozone® shows cross-resistance with thiacetazone.* International Journal of Antimicrobial Agents, 2015. **45**(4): p. 430-433.
276. Moreira, W., D.B. Aziz, and T. Dick, *Boromycin Kills Mycobacterial Persisters without Detectable Resistance.* Frontiers in Microbiology, 2016. **7**(199).

277. Chong, S.M.S., et al., *Antituberculosis Activity of the Antimalaria Cytochrome bcc Oxidase Inhibitor SCR0911*. ACS Infectious Diseases, 2020. **6**: p. 725–737.
278. Gengenbacher, M., et al., *Nutrient-starved, non-replicating Mycobacterium tuberculosis requires respiration, ATP synthase and isocitrate lyase for maintenance of ATP homeostasis and viability.* Microbiology, 2010. **156**(1): p. 81-87.
279. Li, M., et al., *Indolylalkyltriphenylphosphonium Analogues Are Membrane-Depolarizing Mycobactericidal Agents.* ACS medicinal chemistry letters, 2017. **8**(11): p. 1165-1170.
280. Benetoli, L.O.d.B., et al., *Effect of temperature on methylene blue decolorization in aqueous medium in electrical discharge plasma reactor.* Journal of the Brazilian Chemical Society, 2011. **22**(9): p. 1669-1678.
281. Zhai, J., et al., *Boronic acid functionalized boron dipyrromethene fluorescent probes: preparation, characterization, and saccharides sensing applications.* Analytical chemistry, 2012. **84**(23): p. 10214-10220.
282. Zhao, C.-J., et al., *Methanol-promoted Borylation of Arylamines: A simple and green synthetic method to Arylboronic acids and Arylboronates.* Synlett, 2014. **25**(11): p. 1577-1584.
283. Sieber, J.D. and J.P. Morken, *Asymmetric Ni-catalyzed conjugate allylation of activated enones.* Journal of the American Chemical Society, 2008. **130**(14): p. 4978-4983.
284. Tomoaki, M., et al., *Novel azalide and azalactam derivatives and process for the production of the same*. 2004, Meiji Seika Kaisha, Ltd.
285. Paterson, I., et al., *Stereocontrolled total synthesis of (+)-concanamycin F: the strategic use of boron-mediated aldol reactions of chiral ketones.* Tetrahedron, 2011. **67**(52): p. 10119-10128.
286. Shen, H. and K.P.C. Vollhardt, *Remarkable Switch in the Regiochemistry of the Iodination of Anilines by N-Iodosuccinimide: Synthesis of 1, 2-Dichloro-3, 4-diiodobenzene.* Synlett, 2012. **2012**(02): p. 208-214.
287. Middleton, D.S. and A. Stobie, *1,2,3,4-tetrahydro-1-naphthalenamine compounds useful in therapy*. 2000, Pfizer Ltd.
288. Hinsberger, S., et al., *Discovery of Novel Bacterial RNA Polymerase Inhibitors: Pharmacophore-Based Virtual Screening and Hit Optimization.* Journal of Medicinal Chemistry, 2013. **56**(21): p. 8332-8338.
289. Wu, C., P.A. Miller, and M.J. Miller, *Syntheses and studies of amamistatin B analogs reveals that anticancer activity is relatively independent of stereochemistry, ester or amide linkage and select replacement of one of the metal chelating groups.* Bioorg Med Chem Lett, 2011. **21**(9): p. 2611-5.
290. Pavlidis, V.H. and P.J. Perry, *The Synthesis of a Novel Series of Substituted 2-Phenyl-4H-3,1-benzoxazin-4-ones.* Synthetic Communications, 1994. **24**(4): p. 533-548.
291. Jiang, H., et al., *Study on the tandem synthesis of optically active 2-substituted 4 (or 5)-phenyl-1, 3-oxazolines.* Tetrahedron, 2013. **69**(9): p. 2150-2156.

292. Howard, N., et al., *Application of Fragment Screening and Fragment Linking to the Discovery of Novel Thrombin Inhibitors.* Journal of Medicinal Chemistry, 2006. **49**(4): p. 1346-1355.
293. Raboisson, P., et al., *Novel potent and selective αvβ3/αvβ5 integrin dual antagonists with reduced binding affinity for human serum albumin.* European Journal of Medicinal Chemistry, 2006. **41**(7): p. 847-861.
294. Müller, S., et al., *An improved one-pot procedure for the synthesis of alkynes from aldehydes.* Synlett, 1996. **1996**(6): p. 521-522.
295. Agejas-Chicharro, F.J., et al., *Pyridyl derivatives and their use as mGlu5 antagonists*. 2011, Google Patents.
296. Torii, S., et al., *Syntheses of chromones and quinolones via pd-catalyzed carbonylation of o-iodophenols and anilines in the presence of acetylenes.* Tetrahedron, 1993. **49**: p. 6773–6784.
297. Chong, S.M.S., N. Kamariah, and G. Grüber, *Critical residues of helix a2 for catalytic efficiency of Mycobacterial Alkylhydroperoxide reductase subunit C.* FEBS letters, manuscript in review.
298. Wong, C.F., *Novel Insights into the N-terminus of Mycobacterium Tuberculosis Alkyl-hydroperoxide Reductase Subunit C (AhpC)*, in *Nanyang Technological University*. 2017.
299. Diederichs, K. and P.A. Karplus, *Better models by discarding data?* Acta Crystallographica Section D: Biological Crystallography, 2013. **69**(7): p. 1215-1222.
300. Matthews, B.W., *Solvent content of protein crystals.* Journal of molecular biology, 1968. **33**(2): p. 491-497.
301. Garman, E.F., *Radiation damage in macromolecular crystallography: what is it and why should we care?* Acta Crystallographica Section D, 2010. **66**(4): p. 339-351.
302. Biolabs, N.E. *Guidelines for PCR Optimization with Phusion High-Fidelity DNA Polymerase*. 2017 2017 [cited 2017 8 August]; Available from: https://www.neb.com/protocols/2012/06/01/guidelines-for-pcr-optimization-with-phusion-high-fidelity-dna-polymerase.
303. Roy, A., A. Kucukural, and Y. Zhang, *I-TASSER: a unified platform for automated protein structure and function prediction.* Nature protocols, 2010. **5**(4): p. 725-738.
304. Yang, J., et al., *The I-TASSER Suite: protein structure and function prediction.* Nat Meth, 2015. **12**(1): p. 7-8.
305. Zhang, Y., *I-TASSER server for protein 3D structure prediction.* BMC Bioinformatics, 2008. **9**: p. 40-40.
306. Nakamura, Y. and K. Mori, *New syntheses of the rice moth and stink bug pheromones by employing (2R, 6S)-7-acetoxy-2, 6-dimethyl-1-heptanol as a building block.* Bioscience, biotechnology, and biochemistry, 2000. **64**(8): p. 1713-1721.
307. Bobileva, O., et al., *Synthesis and evaluation of (E)-2-(5-phenylpent-2-en-4-ynamido)cyclohex-1-ene-1-carboxylate derivatives as HCA2 receptor agonists.* Bioorg Med Chem, 2017. **25**(16): p. 4314-4329.

308. Schoenberg, A., I. Bartoletti, and R. Heck, *Palladium-catalyzed carboalkoxylation of aryl, benzyl, and vinylic halides.* The Journal of Organic Chemistry, 1974. **39**(23): p. 3318-3326.
309. Zhao, J., et al., *An Aryl to Imidoyl Palladium Migration Process Involving Intramolecular C− H Activation.* Journal of the American Chemical Society, 2007. **129**(16): p. 5288-5295.
310. Budzik, B., et al., *Benzimidazolones which have activity at MI receptor*. 2007, Glaxo Group Limited.
311. Kundu, S., et al., *Bedaquiline Targets the ε Subunit of Mycobacterial F-ATP Synthase.* Antimicrobial Agents and Chemotherapy, 2016. **60**(11): p. 6977-6979.
312. Lamprecht, D.A., et al., *Turning the respiratory flexibility of Mycobacterium tuberculosis against itself.* Nature Communications, 2016. **7**(1): p. 12393.
313. Hards, K., et al., *Bactericidal mode of action of bedaquiline.* Journal of Antimicrobial Chemotherapy, 2015. **70**(7): p. 2028-2037.
314. Hards, K., et al., *Alternate quinone coupling in a new class of succinate dehydrogenase may potentiate mycobacterial respiratory control.* FEBS Letters, 2019. **593**(5): p. 475-486.
315. Bloch, D.A., et al., *Heme/heme redox interaction and resolution of individual optical absorption spectra of the hemes in cytochrome bd from Escherichia coli.* Biochimica et Biophysica Acta (BBA)-Bioenergetics, 2009. **1787**(10): p. 1246-1253.
316. Ghosh, P., A.K. Nandi, and S. Das, *Carbonylative Sonogashira annulation sequence: One-pot synthesis of 4-quinolone and 4H-chromen-4-one derivatives.* Tetrahedron Letters, 2018. **59**(21): p. 2025-2029.
317. Keilin, D., *Cytochrome and respiratory enzymes.* Proceedings of the Royal Society of London. Series B, Containing Papers of a Biological Character, 1929. **104**(730): p. 206-252.
318. Jones, C.W. and R.K. Poole, *10 The Analysis of Cytochromes*, in *Methods in Microbiology*, T. Bergan, Editor. 1985, Academic Press. p. 285-328.
319. Crofts, A.R., et al., *Proton pumping in the bc1 complex: A new gating mechanism that prevents short circuits.* Biochimica et Biophysica Acta (BBA) - Bioenergetics, 2006. **1757**(8): p. 1019-1034.
320. Muller, F.L., et al., *Architecture of the Qo Site of the Cytochrome bc1 Complex Probed by Superoxide Production.* Biochemistry, 2003. **42**(21): p. 6493-6499.

Author's publication related to this project

- **Chong, S. S. M.;** Malathy S. S. M.; Sarathy, J. P.; Williams, Z. C.; Harold, L. K.; Cook, G. M.; Dick, T.; Pethe, K.; Bates, R. W.; Grüber, G., Anti-tuberculosis activity of the anti-malaria cytochrome *bcc* oxidase inhibitor SCR0911. ACS infectious diseases, 2020. **6**, 725–737. doi: 10.1021/acsinfecdis.9b00408.
- **Chong, S. S. M.;** Kamariah, N.; Grüber, G., Critical residues of helix α2 for catalytic efficiency of Mycobacterial Alkylhydroperoxide reductase subunit C. FEBS Letters, 2020. doi:10.1002/1873-3468.13864.

Posters and Abstracts

- **Chong, S. S. M.;** Shin, J.; Kamariah, N.; Grüber, G., Mechanistic insights into the helical displacement of *Mycobacterium tuberculosis* AhpC for TB-drug discovery. Gordon Research Conference on Tuberculosis Drug Discovery and Development. Spain, Castelldefels.
- **Chong, S. S. M.;** Bates, R. W.; Grüber, G., Effecting the antioxidant defenses of *Mycobacteium tuberculosis* for tuberculosis disease. TOPNET 1st Annual Symposium. From crisis to cures: New approaches to TB Drug discovery. Singapore.
- **Chong, S. S. M.;** Bates, R. W.; Grüber, G., Effecting the antioxidant defenses of *Mycobacteium tuberculosis* for tuberculosis disease. The Pure and Applied Chemistry International Conference (PACCON) 2018, chemistry towards a sustainable future. Thailand, Hat Yai.
- **Chong, S. S. M.;** Grüber, G., Effecting the antioxidant defenses of *Mycobacteium tuberculosis* for tuberculosis disease. EMBO courses and workshops: structural and biophysical methods for biological macromolecules in solution. Singapore.

Appendix

Appendix A

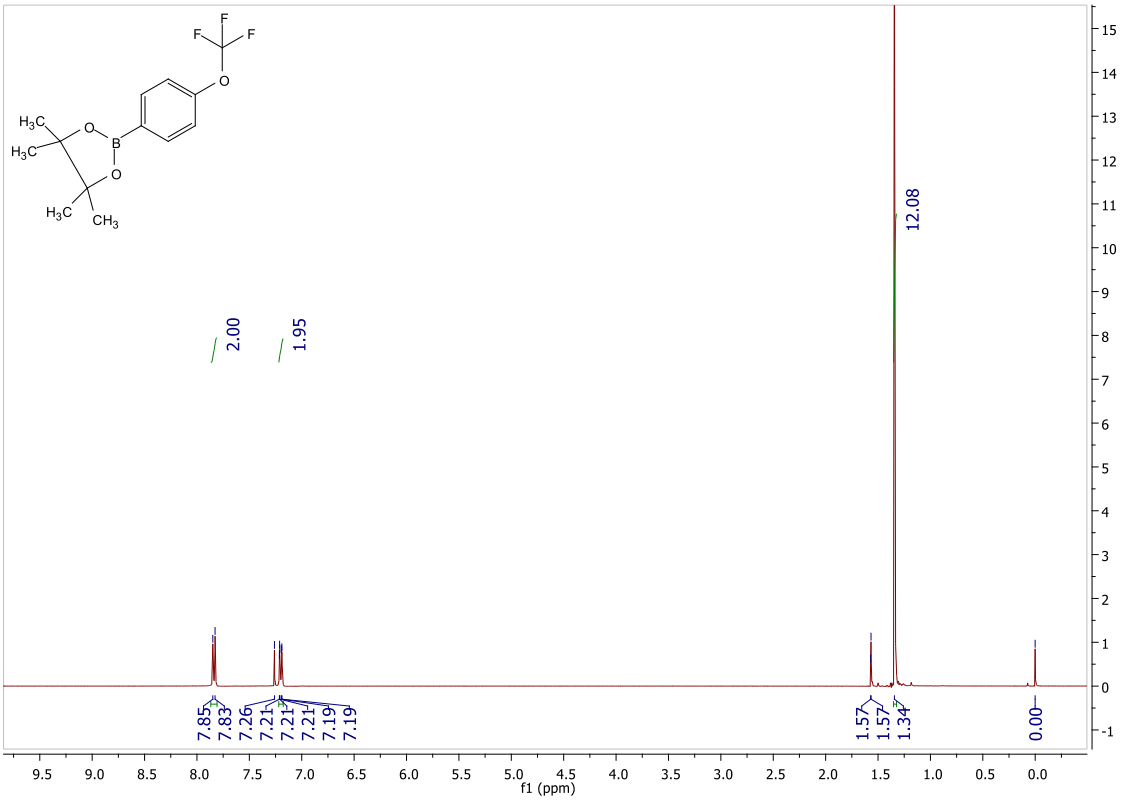

^{1}H NMR spectrum of 4,4,5,5-Tetramethyl-2-(4-(trifluoromethoxy)phenyl)-1,3,2-dioxaborolane **2**

Appendix B

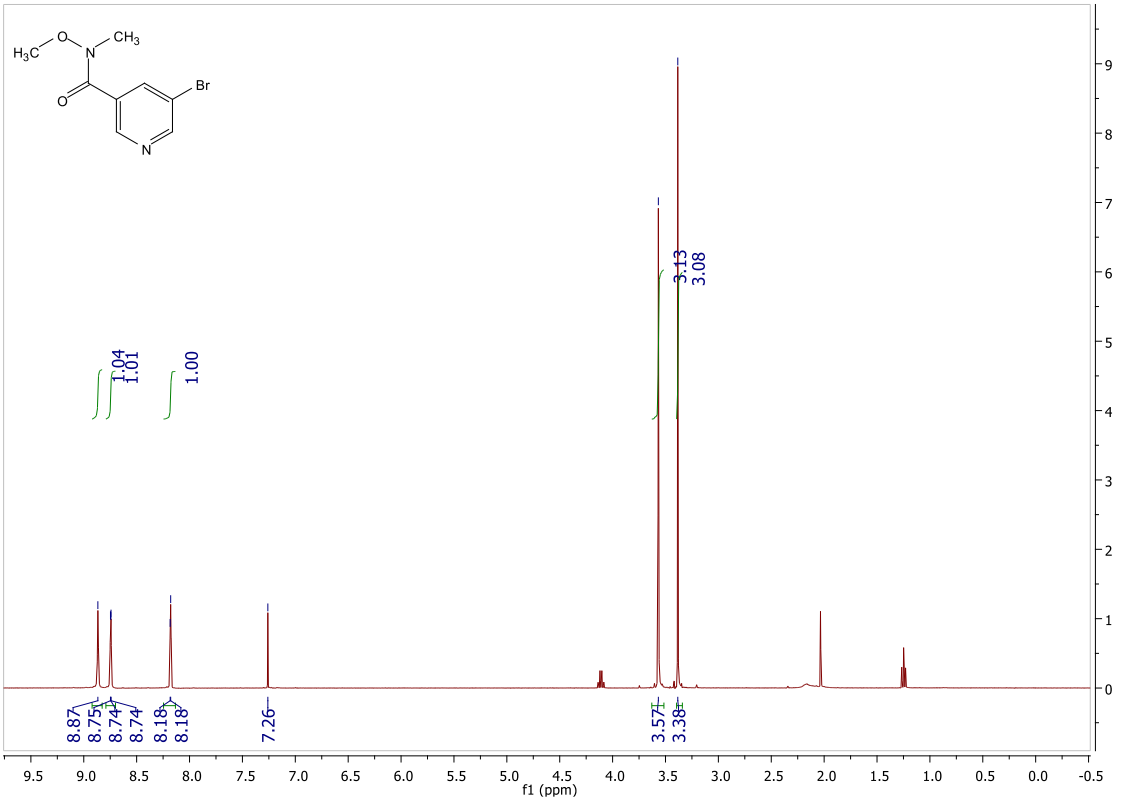

^{1}H NMR spectrum of 5-Bromo-N-methoxy-N-methylnicotinamide **9**

Appendix C

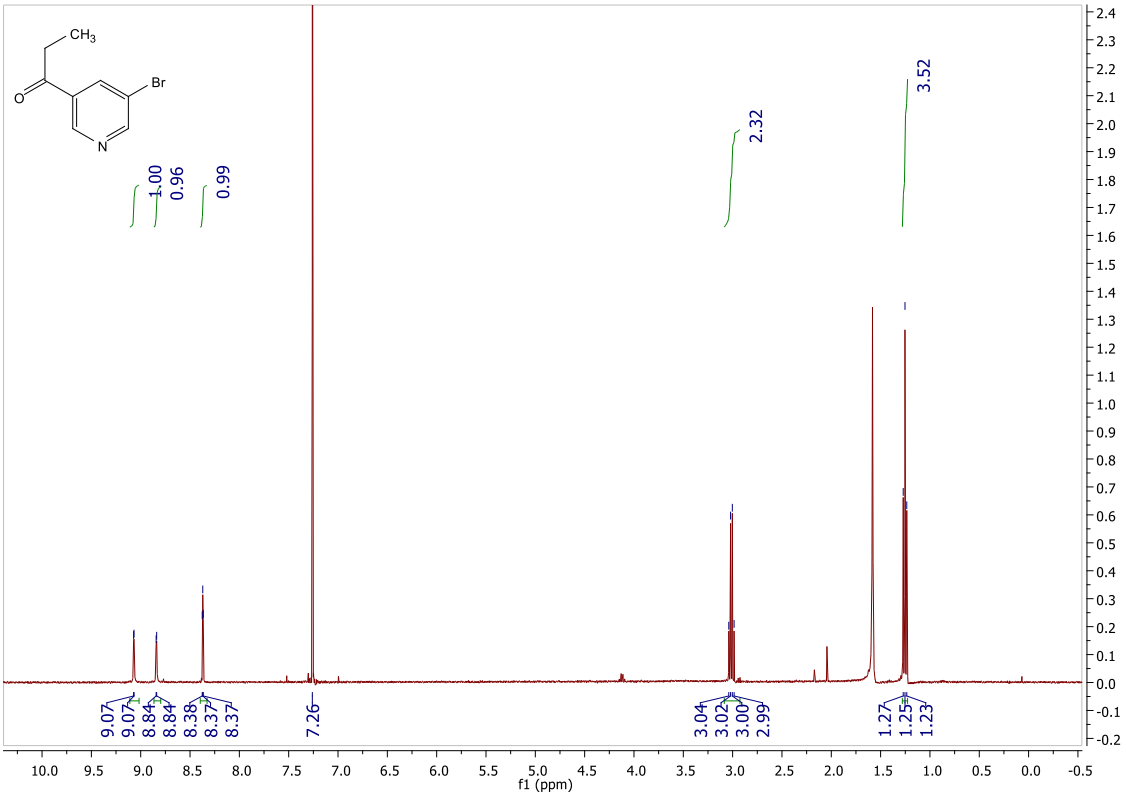

^{1}H NMR spectrum of 1-(5-Bromopyridin-3-yl)propan-1-one **3**

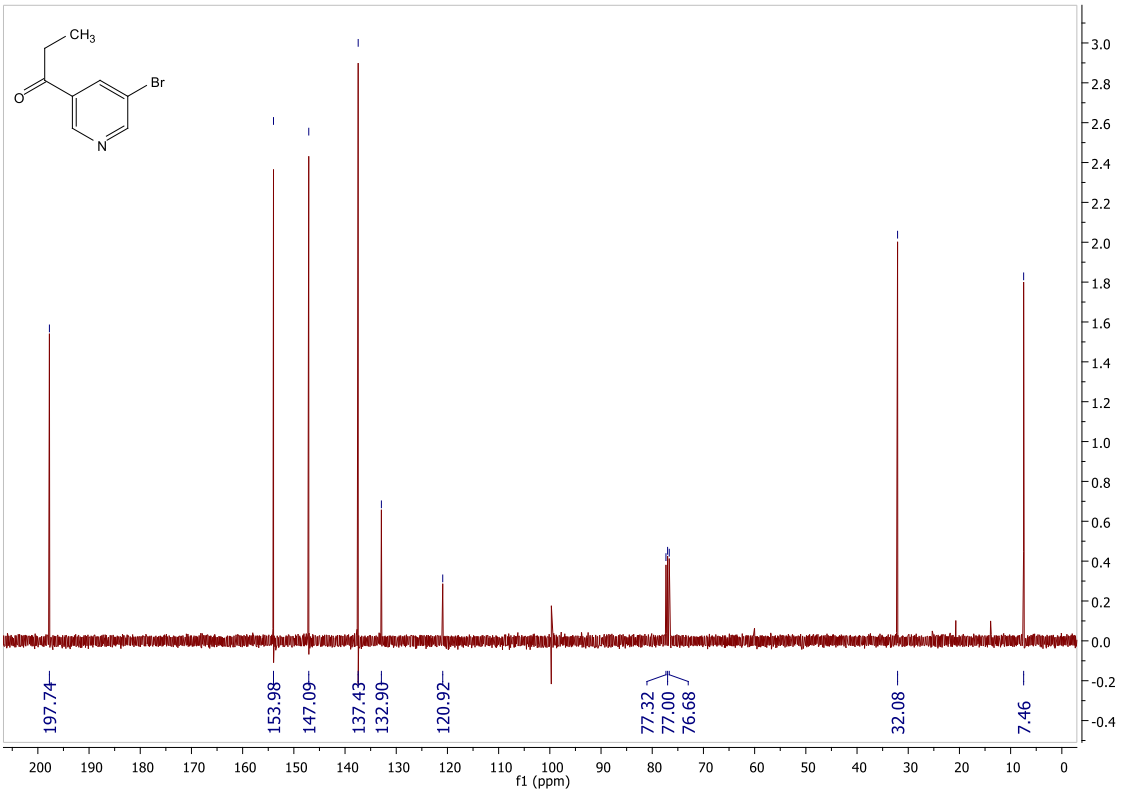

^{13}C NMR spectrum of 1-(5-Bromopyridin-3-yl)propan-1-one **3**

Appendix D

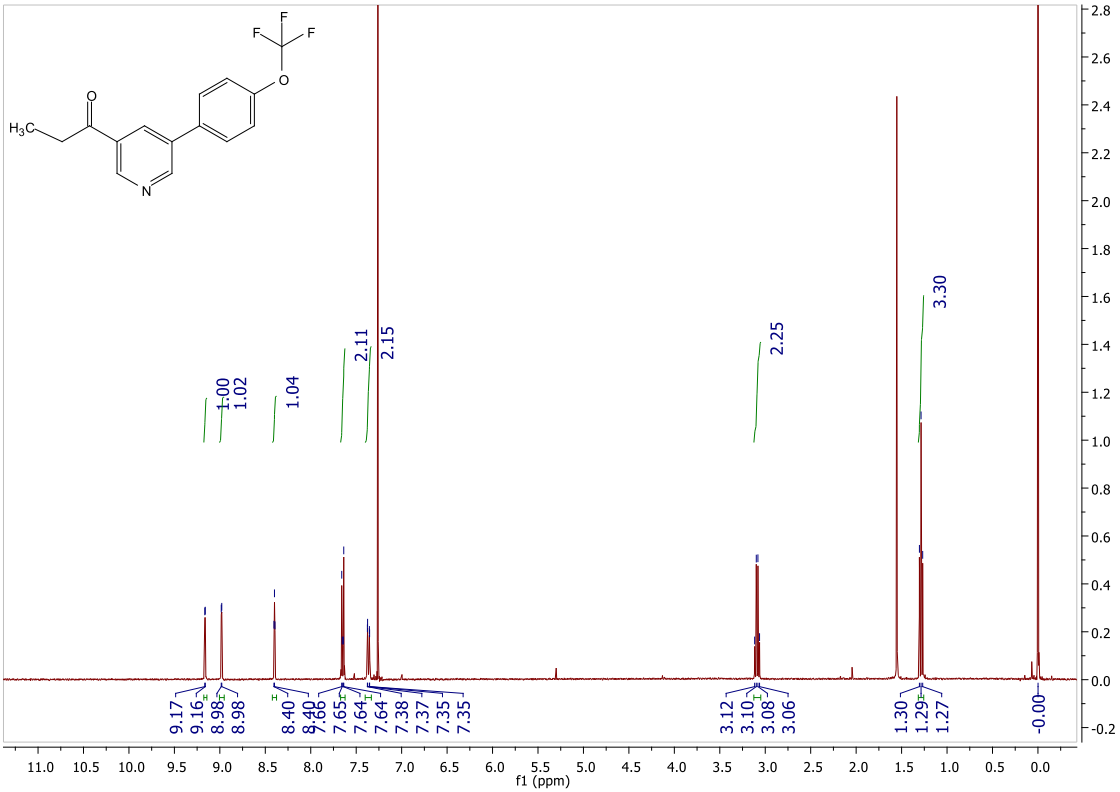

^{1}H NMR spectrum of 1-(5-(4-(Trifluoromethoxy)phenyl)pyridin-3-yl)propan-1-one **1**

Appendix E

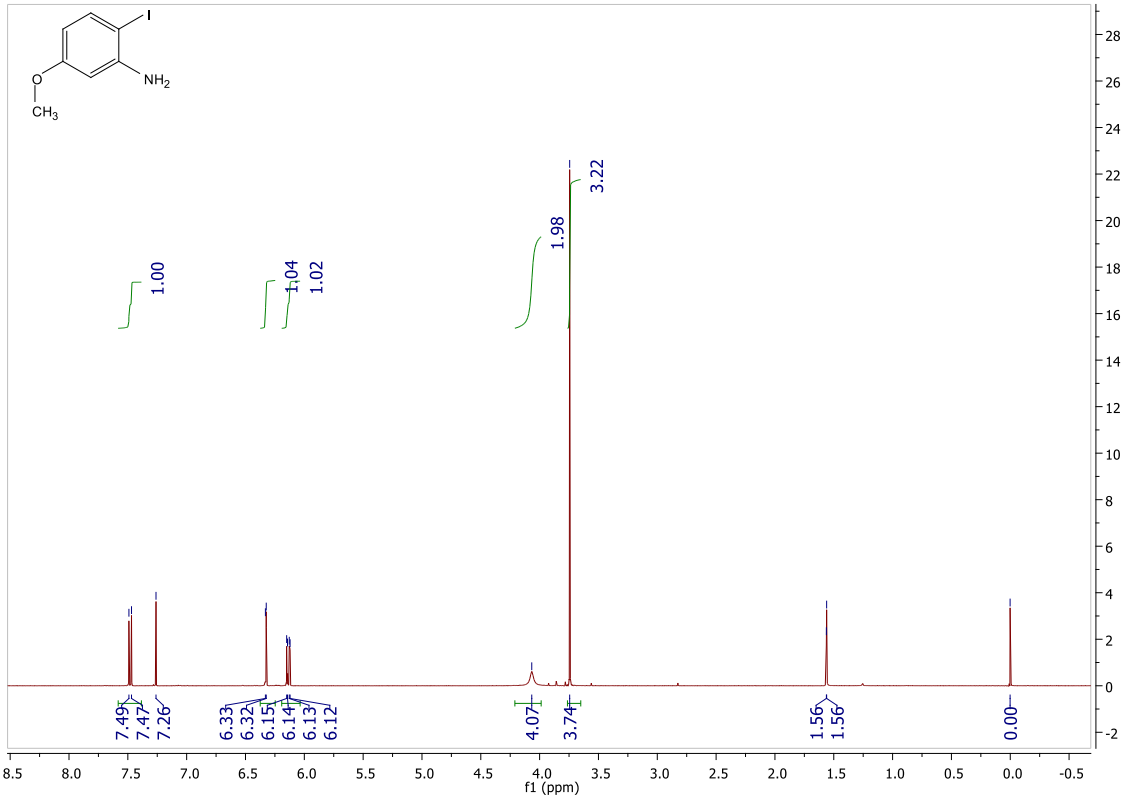

^{1}H NMR spectrum of 2-Iodo-5-methoxyaniline **11**

Appendix F

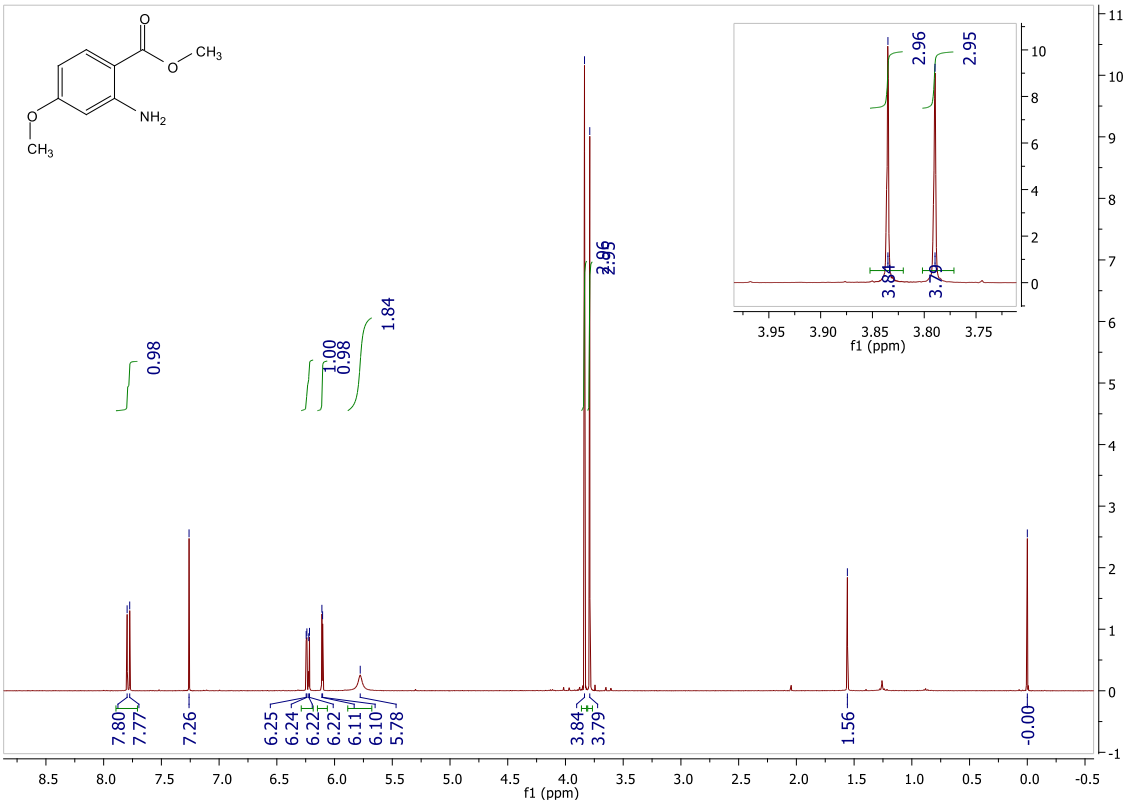

[1]H NMR spectrum of Methyl 2-amino-4-methoxybenzoate **12**

Appendix G

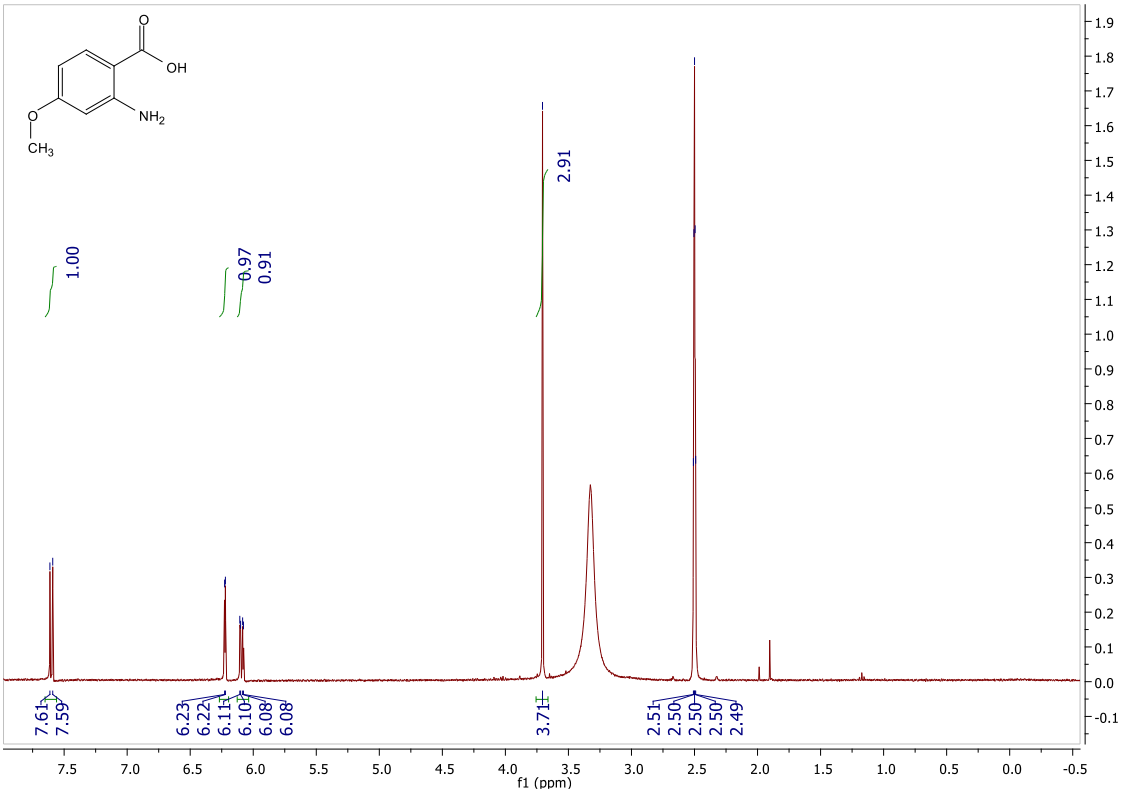

[1]H NMR spectrum of 2-Amino-4-methoxybenzoic acid **6**

Appendix H

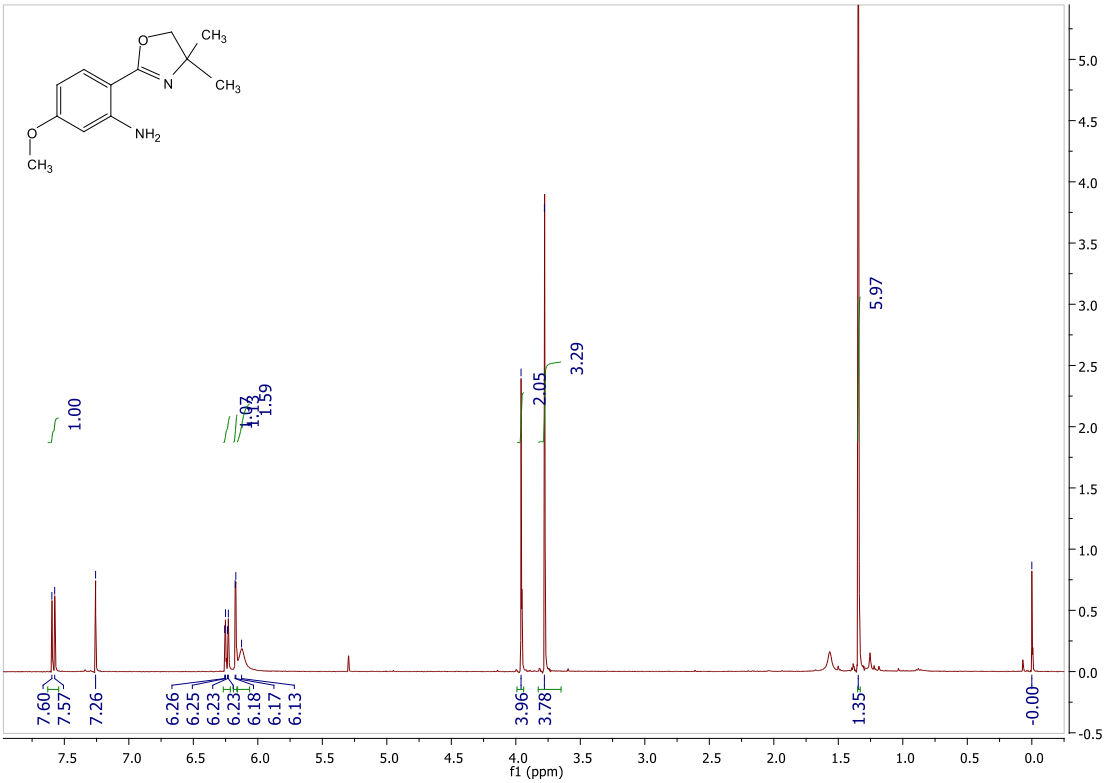

^{1}H NMR spectrum of 2-(4,4-Dimethyl-4,5-dihydrooxazol-2-yl)-5-methoxyaniline **4**

Appendix I

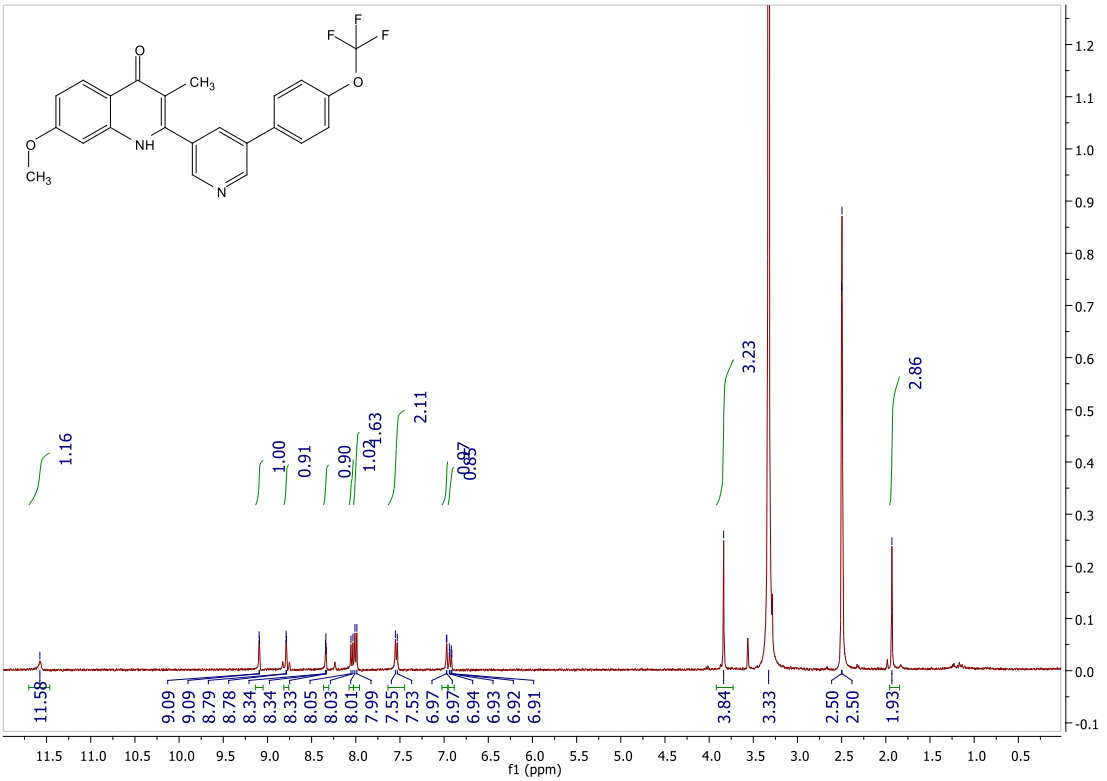

^{1}H NMR spectrum of 7-methoxy-3-methyl-2-(5-(4-(trifluoromethoxy)phenyl)pyridin-3-yl)quinolin-4(1H)-one **SCR0911**

Appendix J

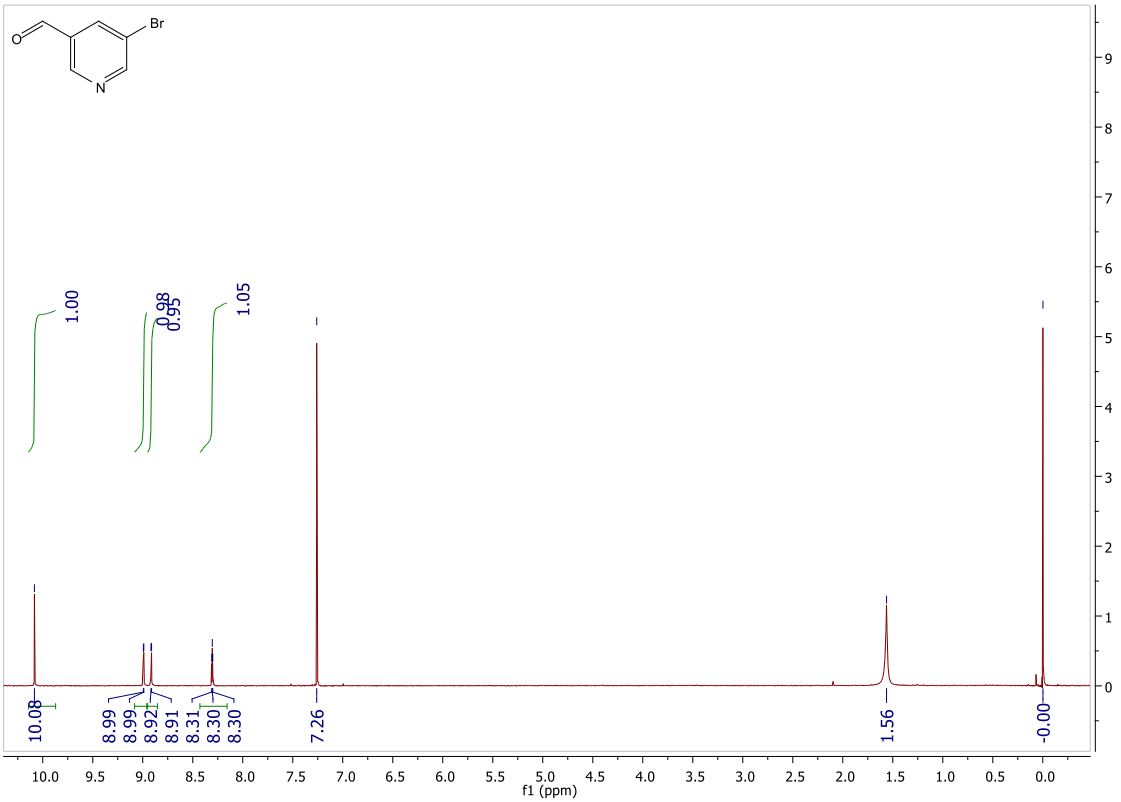

^{1}H NMR spectrum of 5-bromonicotinaldehyde **A1-1**

Appendix K

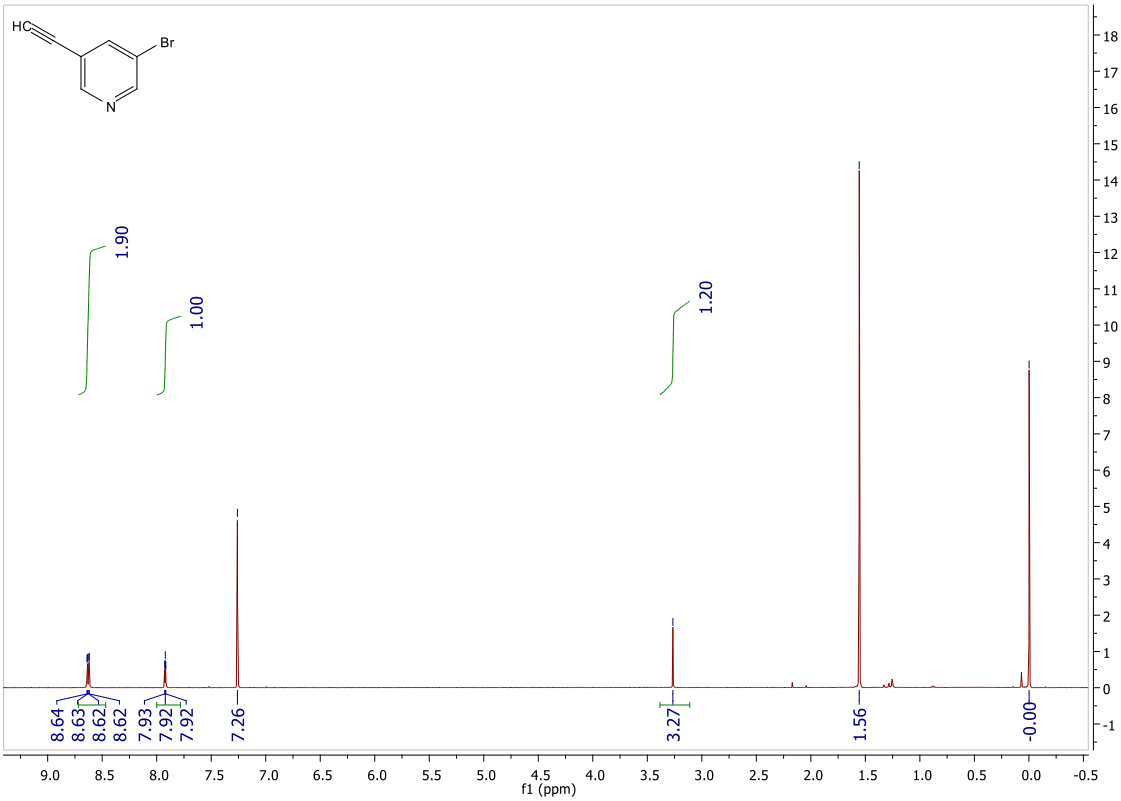

^{1}H NMR spectrum of 3-bromo-5-ethynylpyridine **A1-2**

Appendix L

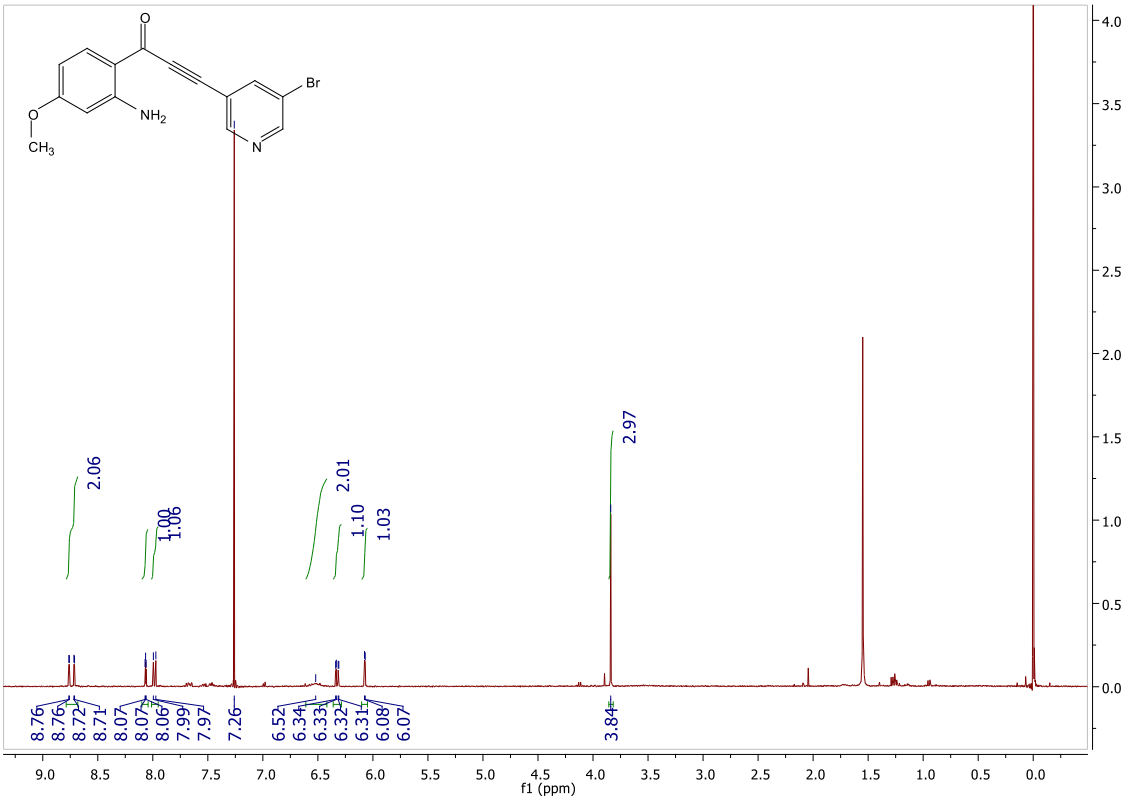

^{1}H NMR spectrum of 1-(2-amino-4-methoxyphenyl)-3-(5-bromopyridin-3-yl)prop-2-yn-1-one **A1-4**

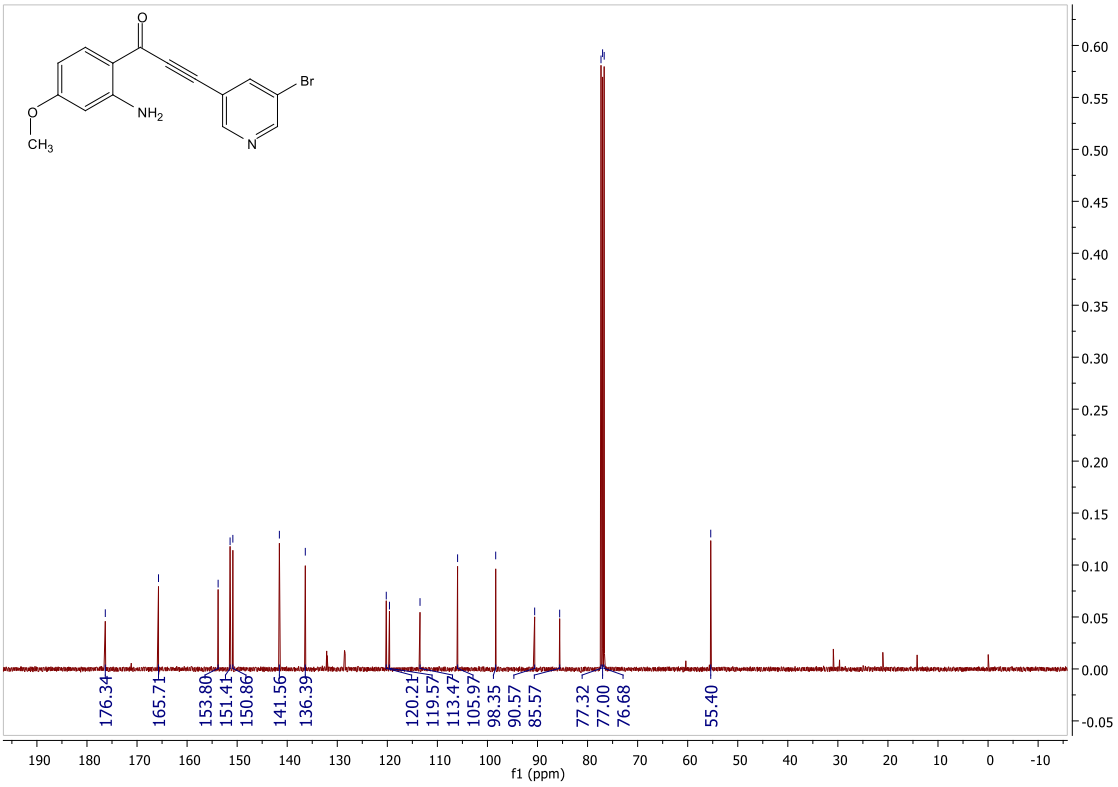

^{13}C NMR spectrum of 1-(2-amino-4-methoxyphenyl)-3-(5-bromopyridin-3-yl)prop-2-yn-1-one **A1-4**

Appendix M

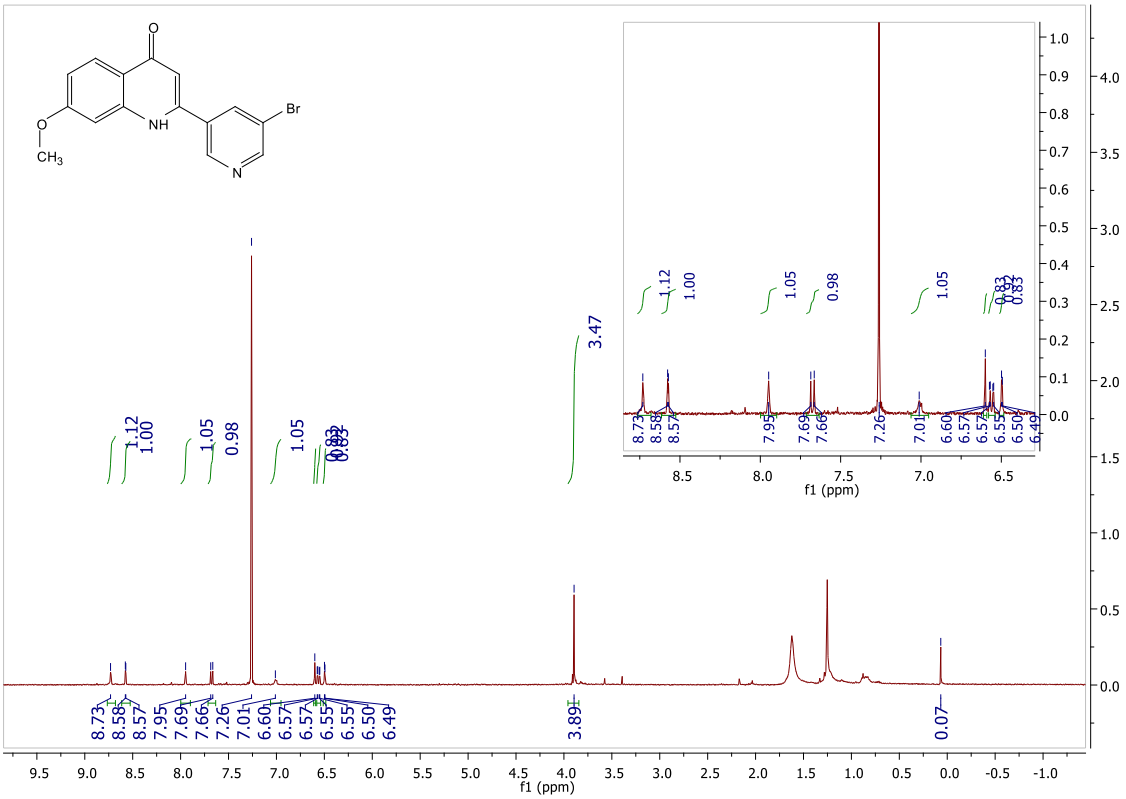

^{1}H NMR spectrum of 2-(5-bromopyridin-3-yl)-7-methoxyquinolin-4(1H)-one **A1-3**